UNIVERSITY OF OKLAHOMA

GRADUATE COLLEGE

Characterization and Control of Spatial Correlations in Entangled Twin Beams

A dissertation
submitted to the graduate faculty
in partial fulfillment of the requirements for
the degree of

DOCTOR OF PHILOSOPHY

by

Gaurav Nirala
Norman, Oklahoma
2024

Downloaded from SHAREOK. Persistent Handle URL: https://hdl.handle.net/11244/340250

Characterization and Control of Spatial Correlations in Entangled Twin Beams

A DISSERTATION APPROVED FOR THE
HOMER L. DODGE DEPARTMENT OF PHYSICS AND ASTRONOMY

BY THE COMMITTEE CONSISTING OF

Dr. Alberto M. Marino, Chair

Dr. Doerte Blume

Dr. Arne Schwettmann

Dr. Bruno Uchoa

Dr. Samual Cheng

Chapter 4 and 6 Copyright by AAAS 2023.
Chapter 5 Copyright by IOP Publishing 2021.
All other chapters Copyright by Gaurav Nirala 2024.
All Rights Reserved.

Dedication

I dedicate this thesis to all the people who knowingly and unknowingly inspired me to consciously add value in life ...
... and to educators like Prof. Mullen,
who are a constant reminder of what it means to pursue science in its purest form.

Acknowledgments

We shall not cease from exploration
And the end of all our exploring
Will be to arrive where we started
And know the place for the first time.

— T. S. Eliot in 'Little Gidding'

First and foremost, I would like to thank my advisor, Prof. Alberto Marino, for giving me an opportunity to become a part of his research group at OU and learn quantum optics firsthand. He worked hard and tirelessly to ensure we had all we needed to run our experiments smoothly, and his continued guidance was instrumental in making the research presented in this dissertation a reality.

My early days in the quantum optics lab were enriched by Ashok Kumar's sincere and patient guidance. His strong work ethic and sincerity have inspired me ever since. Later in my PhD, I was fortunate to collaborate with my senior colleague and friend, Siva. Our discussions on physics were some of the most intellectually stimulating experiences I've had. I will always miss the lengthy discussions on science, religion, and especially philosophy with my colleague and dear friend Saesun. I thank my colleague and friend Umang for his constant help and companionship, especially over the last year of my PhD. I am grateful to Daida for happily giving me her time and joyful company at Pepe Delgados and Haystack Cafe.

Beyond the lab, I extend my gratitude towards all the people who made this journey possible in various ways:

- To Prof. Mullen for teaching graduate courses on Statistical Mechanics and Quantum Hybrid Systems. His way of approaching essential questions in physics has had a lasting impact on me. I wish to have encountered educators like him earlier in my career.
- To Chad, Alex, and Berry at OU physics department machine and electronic shop. Their constant technical support was critical to keep the projects running at times.
- To Prof. Schwettmann, who painstakingly corrected many typos in this dissertation and helped make it more readable, and to Tim for setting up a well-written latex dissertation format (which I have adapted here).

The path to completing this PhD has been long and arduous. During this time, I was fortunate to have the company and support of my very close friends Audi, Geo, and Vishal. I am infinitely indebted to my partner in life, Jaya, who saw all the ups and downs while listening and supporting me every step of the way. I thank Jugal, Shashi, and Hadi for enriching my time in Norman with many memorable weekends and beautiful outdoor experiences.

Abstract

Our understanding and ability to manipulate quantum correlations in non-classical states of light will be a determining factor in realizing the next generation of quantum technologies. Over the last several decades, we witnessed the wide-scale use of sensing and communication technologies, such as RADAR/LiDAR, radio, and fiber-optics telecommunications, that were based on classical conceptions of electromagnetic fields. Harnessing the power of the counter-intuitive phenomenon of quantum superposition and entanglement, quantum theory promises a transformative leap in capabilities that lies beyond such classical approaches. The early success of quantum secure communication, quantum computers, advanced gravitational-wave detectors, and quantum random number generators offer a glimpse into the immense potential offered by quantum mechanics. This dissertation investigates the manipulation of quantum correlations in light, particularly focusing on the spatial degrees of freedom, to propel the development of next-generation quantum technologies.

Quantum states of light, known as twin beams, intrinsically linked through quantum correlations, form the cornerstone of this exploration. These bipartite entangled beams of light are at the heart of several quantum sensing applications and are natural candidates to encode and exchange quantum information. Their generation via the nonlinear parametric process of four-wave mixing leads to temporal (energy conservation) and spatial (momentum conservation) correlations in the quantum regime. Notably, the conservation of transverse momentum in the fields during the process implies that the spatial properties of the input photons determine the distribution of spatial correlations in the generated entangled photons, thus providing a practical way to engineer the correlated spatial modes. After characterizing the entanglement within the spatial as well as spatio-temporal degrees of freedom of the twin beams via a direct imaging technique, this dissertation delves into the extensive engineering of spatial correlations of the fields generated through four-wave mixing.

Our approach of using a deliberately phase-structured input field to drive the four-wave mixing leads to the creation of spatially structured quantum states. The degree of control demonstrated via the phase manipulation implies that this approach can be tailored to the specific requirements of quantum sensing and imaging applications. The abundance of spatial modes in the multimode twin beams that utilize the vastness of the Hilbert space associated with spatial modes, coupled with precise control over their correlations, unlocks possibilities for high-dimensional quantum communication protocols, leading to ultra-secure and high-capacity quantum teleportation and communication.

Contents

Dedication iv

Acknowledgments v

Abstract vi

1 Introduction 1
- 1.1 Why Study Spatial Correlations in Quantum States . . . 1
- 1.2 Summary of the Dissertation . . . 4

2 Quantum Mechanical Description of Light 6
- 2.1 Classical Picture . . . 6
- 2.2 Quantum Picture . . . 9
- 2.3 Number Operator and Fock States . . . 11
- 2.4 Field Quadratures, Coherent States and Shot Noise Limit . . . 14
- 2.5 Phase Space Description of Light . . . 17
- 2.6 Squeezed States of Light . . . 22

3 Generation and Measurement of Squeezed Light 32
- 3.1 Non-linear Optical Processes . . . 32
- 3.2 Two-mode Squeezing via Four-wave Mixing . . . 35
- 3.3 Measurement of Noise Properties . . . 39

4 Spatial Properties of Twin Beams Generated in FWM 44
- 4.1 Pump Momentum and Far Field Correlations . . . 45
- 4.2 Longitudinal Phase Matching and Near Field Correlations . . . 46
- 4.3 FWM Hamiltonian in Spatial Variables . . . 47
- 4.4 FWM Biphoton Wavefunction . . . 51
- 4.5 Einstein-Podolsky-Rosen Correlations in the Spatial Domain . . . 53

5 Measurement of Spatial Properties and EPR Correlations 56
- 5.1 Role of Bright Beams in Spatial Correlation Measurement . . . 56
- 5.2 Imaging Setup for Spatial Correlation Measurements . . . 58
- 5.3 Frame Acquisition and Image Processing . . . 60
- 5.4 Near and Far Field Spatial Squeezing . . . 63
- 5.5 Certification of EPR Correlations using Bright Beams . . . 65

6 Information Encoding in Twin Beams **69**
6.1 Effect of Pump Momentum on Spatial Correlations 69
6.2 FWM with Modified Pump and Correlation Measurement 73
6.3 Information Encoding with Engineered Correlations 77
6.4 Control of the Degree of Correlation via Quadrature Selection 79
6.5 Spatial Auto-Correlation in Twin Beams 81
6.6 Security of Encoded Information 84

7 Future Directions and Conclusions **89**
7.1 Spatial Eigenmodes of FWM 89
7.2 Outlook and Conclusions 93

Appendices **97**

A Hologram preparation for spatial light modulator **97**

B Fourier transform using MATLAB **100**

C Saturation absorption spectroscopy layout **101**

Bibliography **112**

CHAPTER 1

Introduction

Spatial information is all around us. From traffic signs to QR codes, and from emojis to camera pictures, humans as a species find it very useful to organize, convey, and distribute information using spatial patterns. The effectiveness of spatial patterns lies in their inherent ability to bypass the limitations of language and transmit/encode large amounts of information. A complex set of instructions can be condensed into a simple map, allowing for quick and clear navigation. Similarly, we often visualize complex data sets through charts and graphs, which gives us insight that might be concealed in raw numbers. The widespread usefulness of spatial information is aptly summarized in the proverb: "A picture is worth a thousand words". Upon analyzing an image or a pattern on a micro scale, one may however conclude that each individual part (i.e. dot or pixel) of an image shares a relation to nearby ones. It is this relation between different neighboring parts of an image where the information is truly present.

Such an identification of 'what and where' information is, seems necessary[1] if we wish to store and share it as efficiently as possible. This is ultimately reflected as an important aspect of our everyday life in the current information age, where we need to process and communicate increasingly larger and larger amounts of information efficiently. To do so, some of the key tools and techniques that we have developed rely on the unique properties of light. LASERs, CCD cameras, holographic displays and light modulators, optical fibers, and free space optical communication, all are engineered to harness the beneficial properties of light, which for us has become an indispensable medium to collect, display, and distribute information.

A unification of novel properties of light with spatial information in the quantum regime reflects one of the main themes of this dissertation. Here, we describe at length our experimental and theoretical studies of the generation, characterization and manipulation of spatial correlations in quantum optical states of light suitable for emerging applications in quantum communication and sensing.

1.1 Why Study Spatial Correlations in Quantum States

The usefulness of certain quantum states can be understood by their ability to produce patterns or correlations that cannot be reproduced by a classical state. To see the utility of the non-classical behavior of these correlations, let us consider an example of their applicability. Using a certain bipartite (two-part) quantum state, Alice and Bob can individually generate a string of numbers based on the measurements on their part of the state. These strings of numbers have the form

1.1 Why Study Spatial Correlations in Quantum States

{01000101010010100110...} for Alice and {01000101010010100110...} for Bob[1]. Upon comparing their strings, Alice and Bob find that while each string is completely random, they are also perfectly correlated. Additionally, if they repeat their experiment with measurements in a different basis, they find the same pattern even if they are at long distance apart from each other. In other words, they have stumbled upon a physical phenomenon in which there is no way to predict the next individual realization while being completely certain that it is going to be same for both regardless of their separation. This phenomenon highlights the inherent unpredictable nature combined with 'entangledness' afforded by the quantum theory.

Based on the use of an entangled state, the ability of two distant parties to produce random yet correlated sequence of numbers has been put to use in the field of quantum cryptography. For example, using clever adaptations of the phenomenon outlined above, quantum key distribution protocols (such as the BB84[2] or Ekert[3] protocol) can establish secret keys (sequence of random numbers) between two parties for exchanging encrypted messages in a way that is mathematically proven to be secure[4]. Even in the absence of entanglement, the randomness offered by quantum theory via quantum superposition or vacuum noise is useful towards generating true random numbers using devices known as quantum random number generators (QRNGs)[5]. Currently, QRNG devices are being actively developed for applications in quantum Monte-Carlo simulations, cryptography and quantum computation.

Given the unique benefits of quantum correlations in quantum states, there are a number of reasons to study them in terms of spatial variables. Here we highlight two of them.

Quantum Communication in Higher Dimensions: Consider an entangled state, known as the Einstein-Podolsky-Rosen (EPR) state, given by

$$|\text{EPR}\rangle = \int d\boldsymbol{x}\, |\boldsymbol{x}, \boldsymbol{x}\rangle = \int d\boldsymbol{p}\, |\boldsymbol{p}, -\boldsymbol{p}\rangle\,. \tag{1.1}$$

Such an EPR state describes an ideal bipartite system which displays perfect correlations/anti-correlations in terms of the position/momentum continuous variables of the system. An optical implementation of the EPR state utilizing position and momentum [2] correlations in photons would allow Alice and Bob to exchange information much more efficiently and securely[6–8]. This can be seen via a visualization of the properties of an ideal optical EPR state shown in figure 1.1. Here, Alice and Bob make measurements on the EPR state by capturing image 1 and image 2, respectively. While comparing these two images, they find that the intensity of a point in image 1 is correlated with the intensity of a corresponding point located at the same spatial position in image 2 (see figure 1.1). Moreover, they also find that the intensity distribution in each image is a uniformly distributed random distribution. In other words, a spatially entangled EPR state can be thought of as composed of a large number of quantum correlated pairs with each pair localized to an independent spatial region and thus, providing a multi-dimensional quantum system to exchange information. This dissertation will give details on the practical implementation of an optical EPR source in the lab along with its characterization by measuring position and momentum correlations in the quantum regime.

Quantum Imaging and Sensing: Bipartite or two-part quantum optical states (such as the EPR state described above) with a large number of spatial modes, are also immensely beneficial in the

[1] We are referring to the entangled Bell state of the form $|\text{HH} + \text{VV}\rangle/\sqrt{2}$, where 'H' and 'V' denote horizontal and vertical polarization of entangled photons. Here, the notation $|\text{HH}\rangle \equiv |\text{H}\rangle_{\text{Alice}} \otimes |\text{H}\rangle_{\text{Bob}}$.

[2] For the optical state, we are referring to transverse spatial variables which are the position and momentum degrees of freedom of the photons in the plane perpendicular to the propagation direction.

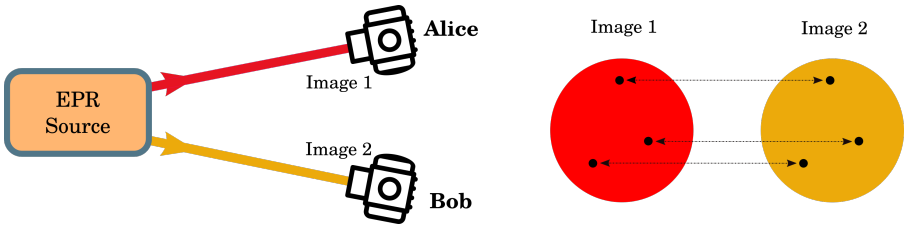

Figure 1.1: An ideal (optical) EPR state with correlations in spatial variables. An EPR source emits two quantum correlated optical beams, one for Alice and one for Bob. They independently take images of their portion of the EPR state and find the resulting images to be point-to-point correlated in terms of the intensity distribution. Also, the spatial intensity distribution in each image is found to be completely random.

fields of quantum imaging and sensing[9,10], in addition to their applicability in higher-dimensional quantum communication. Due to correlated photon statistics in the paired spatial modes between the two parts, one part of the state can be used for detection while the other acts as a reference. A comparison in the detection of the two parts, labeled as detection A and B in figure 1.2, can provide more information in the presence of quantum correlations than by using an equivalent classical state[11]. Additionally, different spatial modes of the quantum state may not interact

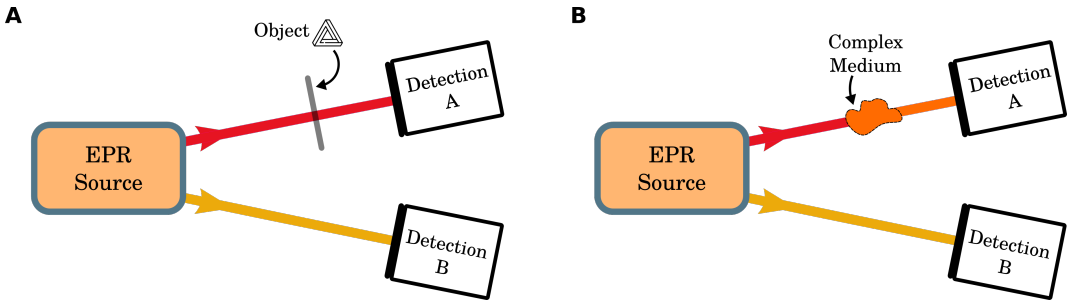

Figure 1.2: Use of spatially correlated quantum states in quantum imaging and sensing. For a bipartite spatially correlated quantum state, one part of the state acts as a reference while the other part interacts with (A) an object or (B) a complex medium. After detection, a comparison between the results of detection A and B can provide more information than an equivalent classical state based detection due to the photon correlations present in the spatial modes. Depending on the nature of the interaction, some of the spatial modes can be transformed into other spatial modes or are irreversibly lost to the environment. This can lead to changes in the spatial composition of the quantum state. This can be seen in (B) where the composition of the spatial modes in detection A has changed due to an interaction with the complex medium. One may achieve a more efficient detection in such scenarios using a quantum state with selectively correlated spatial modes.

equally with the object to be imaged[12], or in the case of sensing in a complex environment, the information contained in certain spatial modes may be transferred to other spatial modes[13]. A prior characterization along with the engineering of the spatial modes can be a useful approach in such scenarios that would allow one to extract information more efficiently with the use of specific spatial modes based on the interaction. Later chapters of this dissertation describe this approach of modifying quantum correlated spatial modes in a bipartite quantum optical state.

At present, we see a rise in real-world applications based on quintessential quantum phenomena, such as quantum superposition and entanglement, which is often regarded as the advent of a second quantum revolution. Building on it, our scientific and technical community has increasingly focused on certain key areas that are poised to greatly benefit from the ongoing quantum revolution within

the next two to three decades. These are broadly categorized as quantum computing, quantum sensing (including quantum imaging), and quantum communication[14]. Although quantum computers could be the most fruitful area in the scope of impactful applications, they will certainly have a longer timeline to reach maturity for the first real-life applications[15,16]. On the other hand, we are already witnessing the deployment of real-world quantum technologies in the areas of communication and sensing including but not limited to discrete[17] and continuous-variable[18] quantum key distribution, quantum satellite communication[19], space and terrestrial atomic clocks[20,21], quantum imaging of biological cells[22] and quantum-enhanced gravitational wave detectors[23,24]. We anticipate that our exploration of spatial correlations in quantum optical states presented in this dissertation will be fruitful towards the practical use of spatial quantum correlations in emerging quantum communication and sensing applications.

1.2 Summary of the Dissertation

This dissertation is subdivided into seven chapters. The first few chapters provide the motivation and necessary background to discuss spatial correlations in two-mode squeezed states of light followed by details of their theoretical and experimental studies leading to this dissertation. Toward the end, we summarize our ongoing and possible future works followed by some supplemental material in appendices.

Chapter 1 gives a broad motivation for the relevance of the research work discussed in this dissertation. In chapter 2, we first provide the theoretical framework necessary to understand squeezed states of light. Beginning with the classical description of light, we introduce the quantum picture with the quantization of a multimode electromagnetic field in a confined volume. Building upon the concepts of vacuum fluctuations, coherent states, and number states, we describe the reduced noise properties of single-mode and two-mode squeezed states using a phase space description of light.

Chapter 3 details the generation of squeezed states of light using non-linear interactions such as spontaneous parametric down-conversion (SPDC) and four-wave mixing (FWM). We also provide a connection between the two-mode squeezing operation and the non-linear generation process. Focusing on the FWM process in Rb vapor, we discuss the generation of probe and conjugate twin beams in a stimulated non-collinear FWM setup along with a general overview of the phase-matching condition. Finally, we introduce the intensity-difference (ID) measurement and how it characterizes the temporal quantum correlations between the probe and the conjugate photons by measuring ID squeezing. We also provide relevant details of homodyne detection for later reference.

Chapter 4 lays out an intuitive picture for understanding the position (near field) and momentum (far field) correlations in the twin beams as dictated by the phase matching along the propagation direction and momentum conservation in the transverse plane, respectively. We further support our arguments by subsequently developing a quantitative description of the spatial correlations using a suitable interaction Hamiltonian describing the FWM process. In the end, using appropriately derived theoretical expressions, a concise argument on why spatial Einstein-Podolsky-Rosen (EPR) entanglement is expected in the FWM process is provided.

Chapter 5 details the experimental measurement of near and far field correlations in the twin beams using a specialized low-noise CCD camera. We describe how the acquired data is processed to extract position and momentum correlations and obtain a verification of EPR entanglement. We also report on the measurements of spatial squeezing in the near and the far field which are used to show inseparability (and hence, entanglement) in terms of the spatial degrees of freedom.

Collectively, our results indicate a generation of hyperentanglement (involving temporal and spatial variables) in the FWM process. The results discussed in this chapter are part of our publication in the IOP Quantum Science and Technology Journal.

Chapter 6 focuses on our latest experiment towards the control of spatial correlations in twin beams generated in FWM. Here, we develop a more detailed understanding of how the pump angular spectrum affects the distribution of spatial correlations in the far field and provide details of our experimental implementation in which we systematically modify the pump momentum using a hologram (to engineer correlations in a desired way). We discuss the experimental results comparing them to the corresponding simulations and highlight the fact that such an engineering of the spatial correlations can be seen as a novel way to securely encode information in the twin beams. Based on the phenomenon of phase-conjugation in the FWM process, we also discuss our results in which we are able to vary how strongly the probe and conjugate beams appear to be correlated in the measurements. Toward the end of the chapter, we comment on the security aspects of the encoded information based on the experimental data and how it can be improved further based on certain experimental parameters. The results presented here are part of our publication in the Journal of Science Advances.

Finally, in chapter 7, we provide a broader framework of fundamental or Schmidt modes of a non-linear process. We discuss our preliminary work in identifying spatial Schmidt modes in the FWM process for a Gaussian input pump field and verify their validity using previous experimental data. After highlighting their importance for better quantum communication and sensing, we give a future outlook along with concluding remarks.

CHAPTER 2

Quantum Mechanical Description of Light

Light is an electromagnetic phenomenon. A vast majority of optical phenomena, such as the diffraction and interference of light, propagation of light in waveguides as well as the interaction of lasers with prisms, lenses, and mirrors, are adequately explained by Maxwell's theory of electromagnetism. However, this classical description of light fails to provide a satisfactory explanation of, for example, the black-body radiation or the noise characteristics of optical states generated via specific nonlinear interactions. The quantum theory of light requires the introduction of photons as the *quanta* of electromagnetic fields. The idea of quantization, put forward by Planck and Einstein, eventually led to the birth of quantum mechanics during the first half of the 19th century [25]. The modern theory of quantum coherence was developed around the 1960s by Glauber, Sudarshan, Wolf, Mandel, and others. Concepts related to the coherent states, photon number states, and quasiprobability distributions developed during this period and combined with the invention of the laser by Maiman [26] eventually led to several pioneering quantum optics experiments in the 1970s. Observation of antibunching of photons in resonance fluorescence [27,28] and detection of sub-Poissonian statistics with newly generated squeezed states of light [29] firmly established quantum optics as an area of study we know today. This chapter introduces all the necessary concepts to appreciate the quantum nature of squeezed states of light. A theoretical description of single and two-mode squeezed states of light is then provided towards the end of the chapter.

2.1 Classical Picture

We begin by solving Maxwell's equations in a finite volume with the appropriate boundary conditions. In the absence of sources (charges and currents), Maxwell's equations take the form [30]

$$\boldsymbol{\nabla} \cdot \mathbf{D} = 0, \qquad \boldsymbol{\nabla} \cdot \mathbf{B} = 0, \tag{2.1}$$

$$\boldsymbol{\nabla} \times \mathbf{E} + \frac{\partial \mathbf{B}}{\partial t} = 0, \qquad \boldsymbol{\nabla} \times \mathbf{H} - \frac{\partial \mathbf{D}}{\partial t} = 0, \tag{2.2}$$

where the fields are dependent on position and time, i.e. $(\boldsymbol{r}, t)$, variables[1]. In the case of uniform isotropic linear media, we can write $\mathbf{D} = \varepsilon \mathbf{E}$ and $\mathbf{B} = \mu \mathbf{H}$ where ε and μ are the permittivity and permeability of the medium respectively. Assuming the $\mathbf{E}(\boldsymbol{r}, t)$ and $\mathbf{B}(\boldsymbol{r}, t)$ fields have harmonic

[1] Boldface notation is used throughout this dissertation to represent vectors.

dependence in time, these can be expanded as

$$\mathbf{E}(\boldsymbol{r},t) = \frac{1}{\sqrt{2\pi}} \int d\omega\ \mathbf{E}(\boldsymbol{r},\omega)\ e^{-i\omega t}$$
$$\mathbf{B}(\boldsymbol{r},t) = \frac{1}{\sqrt{2\pi}} \int d\omega\ \mathbf{B}(\boldsymbol{r},\omega)\ e^{-i\omega t}. \tag{2.3}$$

Using (2.2) and (2.3), the frequency dependent $\mathbf{E}(\boldsymbol{r},\omega)$ and $\mathbf{B}(\boldsymbol{r},\omega)$ amplitudes satisfy the following equations

$$\boldsymbol{\nabla} \times \mathbf{E}(\boldsymbol{r},\omega) - i\omega \mathbf{B}(\boldsymbol{r},\omega) = 0, \qquad \boldsymbol{\nabla} \times \mathbf{B}(\boldsymbol{r},\omega) + i\varepsilon\mu\omega \mathbf{E}(\boldsymbol{r},\omega) = 0. \tag{2.4}$$

Here, the zero divergence equations in (2.1) can be obtained by applying the divergence operator on (2.4). Combining the above two equations into one by the method of elimination, we get the Helmholtz wave equation

$$(\boldsymbol{\nabla}^2 + \varepsilon\mu\omega^2) \begin{bmatrix} \mathbf{E}(\boldsymbol{r},\omega) \\ \mathbf{B}(\boldsymbol{r},\omega) \end{bmatrix} = 0. \tag{2.5}$$

A solution to the Helmholtz wave equation can be obtained as the electromagnetic plane waves of the form

$$\mathbf{E}(\boldsymbol{r},t) = \tilde{\boldsymbol{\epsilon}}\, \mathcal{E}_{\boldsymbol{k}} e^{i(\boldsymbol{k}\cdot\boldsymbol{r}-\omega t)} + \ c.c. \quad \text{and} \quad \mathbf{B}(\boldsymbol{r},t) = \frac{\boldsymbol{k}\times\tilde{\boldsymbol{\epsilon}}}{k}\, \mathcal{B}_{\boldsymbol{k}} e^{i(\boldsymbol{k}\cdot\boldsymbol{r}-\omega t)} + \ c.c., \tag{2.6}$$

where the wave vector $\boldsymbol{k}$ points in the direction of wave propagation with magnitude $|\boldsymbol{k}| = \sqrt{\mu\varepsilon\omega^2}$ and $\tilde{\boldsymbol{\epsilon}}$ is the polarization unit vector. The wave amplitudes $\mathcal{E}$ and $\mathcal{B}$ are complex numbers (c-numbers) in general. The phrase 'c.c.' stands for complex conjugate of the previous term which is added to represent the measured values of electric and magnetic fields (real quantities). The phase velocity, v, of the wave is

$$v = \frac{\omega}{k} = \frac{1}{\sqrt{\varepsilon\mu}}\ , \tag{2.7}$$

where $k = |\boldsymbol{k}|$. The factor $\sqrt{\varepsilon\mu}$ is related to the speed of light, c $(= \frac{1}{\sqrt{\varepsilon_0\mu_0}})$, as

$$\sqrt{\varepsilon\mu} = c/n\ , \tag{2.8}$$

where n is the refractive index of the medium. Using (2.4) and (2.6), one can show that the electric and magnetic field amplitude are related as $\mathcal{B}_{\boldsymbol{k}} = \mathcal{E}_{\boldsymbol{k}}/c$ in vacuum. A general free-space solution $\boldsymbol{\Psi}$ for $\mathbf{E}$ and $\mathbf{B}$ fields can be constructed using a Fourier superposition of the plane waves in (2.6), i.e.,

$$\boldsymbol{\Psi}_{\mathbf{E}}(\boldsymbol{r},t) = \left(\frac{1}{\sqrt{2\pi}}\right)^{3/2} \int d\boldsymbol{k}\ \mathcal{E}(\boldsymbol{k})\, \tilde{\boldsymbol{\epsilon}}_{\boldsymbol{k}}\ e^{i(\boldsymbol{k}\cdot\boldsymbol{r}-\omega(k)t)} + \ c.c.$$
$$\boldsymbol{\Psi}_{\mathbf{B}}(\boldsymbol{r},t) = \left(\frac{1}{\sqrt{2\pi}}\right)^{3/2} \int d\boldsymbol{k}\ \mathcal{B}(\boldsymbol{k})\, (\tilde{\boldsymbol{k}}\times\tilde{\boldsymbol{\epsilon}}_{\boldsymbol{k}})\ e^{i(\boldsymbol{k}\cdot\boldsymbol{r}-\omega(k)t)} + \ c.c., \tag{2.9}$$

where $\tilde{\boldsymbol{k}}$ is the wave unit vector and $\omega(k)$ is evaluated using (2.7).

2.2 Classical Picture

The energy density for the electromagnetic field is

$$u = \frac{1}{2}\left(\varepsilon \mathbf{E}\cdot\mathbf{E} + \frac{1}{\mu}\mathbf{B}\cdot\mathbf{B}\right), \tag{2.10}$$

and the corresponding Hamiltonian $\mathcal{H}$, or classical field energy within a box of volume V has the form[31,32]

$$\mathcal{H} = \frac{1}{2}\int_V dV\left(\varepsilon \mathbf{E}\cdot\mathbf{E} + \frac{1}{\mu}\mathbf{B}\cdot\mathbf{B}\right). \tag{2.11}$$

For a single mode field at frequency ω given in (2.6), it can be shown that the expression for $\mathcal{H}$ can be simplified to

$$\begin{aligned}\mathcal{H} &= \varepsilon V\left(\mathcal{E}_{\boldsymbol{k}}\mathcal{E}^*_{\boldsymbol{k}} + \mathcal{E}^*_{\boldsymbol{k}}\mathcal{E}_{\boldsymbol{k}}\right) &(2.12)\\ &= \omega^2\left(a_{\boldsymbol{k}}a^*_{\boldsymbol{k}} + a^*_{\boldsymbol{k}}a_{\boldsymbol{k}}\right) &(2.13)\\ &= 2\omega^2|a_{\boldsymbol{k}}|^2, &(2.14)\end{aligned}$$

where $\mathcal{E}_{\boldsymbol{k}} = \omega a_{\boldsymbol{k}}/\sqrt{\varepsilon V}$. Here, we assume the volume V to be a rectangular box with perfectly reflective walls which leads to periodic boundary conditions on $\boldsymbol{k}$ and therefore, $\int_V dV e^{\pm i(\boldsymbol{k}-\boldsymbol{k}')\cdot\boldsymbol{r}} = \delta_{\boldsymbol{k}\boldsymbol{k}'}V$. The amplitude $\mathcal{E}$ (and hence, $\mathcal{B}, a$) are c-numbers and therefore commute. The equation (2.14) accounts for the energy of a single mode field. A general solution for multimode field can be obtained as[31,32]

$$\mathcal{H} = \sum_{\boldsymbol{k}} 2\omega_k^2|a_{\boldsymbol{k}}|^2. \tag{2.15}$$

The conversion of integral to summation is due to the discreteness of k-modes. In the expressions (2.14) and (2.15), we have suppressed a summation over the polarization degrees of freedom for simplicity. We now introduce a pair of real canonical variables, $q_{\boldsymbol{k}}$ and $p_{\boldsymbol{k}}$, defined as

$$\begin{aligned}q_{\boldsymbol{k}} &= a_{\boldsymbol{k}} + a^*_{\boldsymbol{k}}\\ p_{\boldsymbol{k}} &= \omega_k(a_{\boldsymbol{k}} - a^*_{\boldsymbol{k}})/i. &(2.16)\end{aligned}$$

Rewriting $\mathcal{H}$ in terms of q and p variables gives

$$\mathcal{H} = \frac{1}{2}\sum_{\boldsymbol{k}}\left(p^2_{\boldsymbol{k}} + \omega_k^2 q^2_{\boldsymbol{k}}\right). \tag{2.17}$$

Hence, the total energy of the electromagnetic field is the sum of many independent oscillators one for each $\boldsymbol{k}$-mode (equivalent to harmonic oscillator with unit mass). It is also worth noting that, apart from some scale factors, electric and magnetic fields play the roles of canonical position and momentum variables[33]. Using (2.6) and (2.16), a classical expression for the multimode $\mathbf{E}$ and $\mathbf{B}$ fields, confined to volume V, in terms of the q and p variables can be given as

$$\begin{aligned}\mathbf{E}(\boldsymbol{r},t) &= \frac{1}{\sqrt{\varepsilon V}}\sum_{\boldsymbol{k}}\omega_k a_{\boldsymbol{k}}\,\tilde{\boldsymbol{\epsilon}}_{\boldsymbol{k}}\; e^{i(\boldsymbol{k}\cdot\boldsymbol{r}-\omega t)} + \;c.c.\\ &= \frac{1}{2\sqrt{\varepsilon V}}\sum_{\boldsymbol{k}}\left(\omega_k q_{\boldsymbol{k}} + ip_{\boldsymbol{k}}\right)\,\tilde{\boldsymbol{\epsilon}}_{\boldsymbol{k}}\; e^{i(\boldsymbol{k}\cdot\boldsymbol{r}-\omega t)} + \;c.c.\\ \mathbf{B}(\boldsymbol{r},t) &= \frac{1}{2\sqrt{\varepsilon V}}\sum_{\boldsymbol{k}}\left(q_{\boldsymbol{k}} + i\frac{p_{\boldsymbol{k}}}{\omega_k}\right)\left(\boldsymbol{k}\times\tilde{\boldsymbol{\epsilon}}_{\boldsymbol{k}}\right)\; e^{i(\boldsymbol{k}\cdot\boldsymbol{r}-\omega t)} + \;c.c.. &(2.18)\end{aligned}$$

In the above expression of **E** and **B** fields, we see that q and p variables are related to real and imaginary (or in-phase and out-of-phase) components of the corresponding field amplitudes.

2.2 Quantum Picture

In the quantum mechanical description of electromagnetic fields, we assign the q and p variables to corresponding Hilbert space operators, $\hat{q}$ and $\hat{p}$, which do not commute. The traditional hat or caret ('^') notation is used to distinguish them from the classical equivalent variables. These operators must satisfy the canonical commutation relations[34]

$$[\hat{q}_{\boldsymbol{k}}, \hat{p}_{\boldsymbol{k}'}] = i\hbar\delta_{\boldsymbol{k}\boldsymbol{k}'}\hat{\mathbb{I}}, \tag{2.19}$$

$$[\hat{q}_{\boldsymbol{k}}, \hat{q}_{\boldsymbol{k}'}] = 0, \tag{2.20}$$

$$[\hat{p}_{\boldsymbol{k}}, \hat{p}_{\boldsymbol{k}'}] = 0, \tag{2.21}$$

where $\mathbb{I}$ is the identity operator. The corresponding Hamiltonian of the electromagnetic field confined to a volume V is

$$\hat{\mathcal{H}} = \frac{1}{2}\sum_{\boldsymbol{k}} \left(\hat{p}_{\boldsymbol{k}}^2 + \omega_k^2 \hat{q}_{\boldsymbol{k}}^2\right). \tag{2.22}$$

The energy of the field is the eigenspectrum of the $\hat{\mathcal{H}}$ operator and is discrete. The eigenvalues of the $\hat{q}$ and $\hat{p}$ Hermitian operators are, however, continuous. Algebraically, it easier to deal with the set of non-Hermitian operators, similar to classical c-number analogues a and a^*, defined as

$$\hat{a}_{\boldsymbol{k}} = \frac{1}{\sqrt{2\hbar\omega_k}}\left(\omega_k \hat{q}_{\boldsymbol{k}} + i\hat{p}_{\boldsymbol{k}}\right), \tag{2.23}$$

$$\hat{a}_{\boldsymbol{k}}^\dagger = \frac{1}{\sqrt{2\hbar\omega_k}}\left(\omega_k \hat{q}_{\boldsymbol{k}} - i\hat{p}_{\boldsymbol{k}}\right). \tag{2.24}$$

These are known as the 'creation' and 'annihilation' operators of the field, respectively. The '†' symbol represents the Hermitian conjugate of the corresponding operator. Inverting (2.23) and (2.24) for the $\hat{q}$ and $\hat{p}$ operators, we get

$$\hat{q}_{\boldsymbol{k}} = \sqrt{\frac{\hbar}{\omega_k}}\left(\frac{\hat{a}_{\boldsymbol{k}} + \hat{a}_{\boldsymbol{k}}^\dagger}{\sqrt{2}}\right), \tag{2.25}$$

$$\hat{p}_{\boldsymbol{k}} = \sqrt{\hbar\omega_k}\left(\frac{\hat{a}_{\boldsymbol{k}} - \hat{a}_{\boldsymbol{k}}^\dagger}{i\sqrt{2}}\right). \tag{2.26}$$

Using (2.19-2.21), $\hat{a}_{\boldsymbol{k}}$ and $\hat{a}_{\boldsymbol{k}}^\dagger$ satisfy the following commutation relations

$$[\hat{a}_{\boldsymbol{k}}, \hat{a}_{\boldsymbol{k}'}^\dagger] = \delta_{\boldsymbol{k}\boldsymbol{k}'}\hat{\mathbb{I}}, \tag{2.27}$$

$$[\hat{a}_{\boldsymbol{k}}, \hat{a}_{\boldsymbol{k}'}] = 0, \tag{2.28}$$

$$[\hat{a}_{\boldsymbol{k}}^\dagger, \hat{a}_{\boldsymbol{k}'}^\dagger] = 0. \tag{2.29}$$

2.2 Quantum Picture

Operator $\hat{\mathcal{H}}$ can also be rewritten in terms of $\hat{a}$ and $\hat{a}^\dagger$ operators as

$$\hat{\mathcal{H}} = \sum_{\boldsymbol{k}} \frac{\hbar\omega_k}{2} \left(\hat{a}_{\boldsymbol{k}} \hat{a}^\dagger_{\boldsymbol{k}} + \hat{a}^\dagger_{\boldsymbol{k}} \hat{a}_{\boldsymbol{k}} \right) \tag{2.30}$$

$$= \sum_{\boldsymbol{k}} \hbar\omega_k \left(\hat{a}^\dagger_{\boldsymbol{k}} \hat{a}_{\boldsymbol{k}} + \frac{1}{2} \right). \tag{2.31}$$

Comparing (2.31) with (2.17), we see an additional contribution of $\hbar\omega/2$ for each $\boldsymbol{k}$-mode. This is often referred to as the *zero-point energy* of a quantum mechanical mode. Since, even in the ground state, a quantum mechanical oscillator does not come to a complete rest, non-zero energy contributions from all modes are expected. This represents a fundamental problem in quantum electromagnetic theories resulting in an infinite energy contribution due to the unbounded set of modes[35].

To obtain time evolution of various operators, we use the Heisenberg picture to determine the operator evolution that reads

$$\frac{d\hat{O}}{dt} = \frac{i}{\hbar}[\hat{\mathcal{H}}, \hat{O}], \tag{2.32}$$

where is $\hat{O}$ is an arbitrary operator. For the annihilation operator $\hat{a}_{\boldsymbol{k}}$, this becomes

$$\frac{d\hat{a}_{\boldsymbol{k}}}{dt} = \frac{i}{\hbar}[\hat{\mathcal{H}}, \hat{a}_{\boldsymbol{k}}] \tag{2.33}$$

$$= \left[\sum_{\boldsymbol{l}} i\omega_l \hat{a}^\dagger_{\boldsymbol{l}} \hat{a}_{\boldsymbol{l}}, \hat{a}_{\boldsymbol{k}} \right] \tag{2.34}$$

$$= -i\omega_k \hat{a}_{\boldsymbol{k}}. \tag{2.35}$$

The above equation has a solution of the form

$$\hat{a}_{\boldsymbol{k}}(t) = \hat{a}_{\boldsymbol{k}} e^{-i\omega_k t}, \tag{2.36}$$

where $\hat{a}_{\boldsymbol{k}} \equiv \hat{a}_{\boldsymbol{k}}(0)$. Similarly, one can evaluate the time evolution of the creation operator as $\hat{a}^\dagger_{\boldsymbol{k}}(t) = \hat{a}^\dagger_{\boldsymbol{k}} e^{i\omega_k t}$. Using the expressions of $\hat{q}_{\boldsymbol{k}}$ and $\hat{p}_{\boldsymbol{k}}$ from (2.25, 2.26) in the (2.18), we get the following expressions for the field operators in the quantum picture,

$$\hat{\mathbf{E}}(\boldsymbol{r}, t) = \sum_{\boldsymbol{k}} \sqrt{\frac{\hbar\omega_k}{2\varepsilon V}}\, \hat{a}_{\boldsymbol{k}}\, \tilde{\boldsymbol{\epsilon}}_{\boldsymbol{k}}\, e^{i(\boldsymbol{k}\cdot\boldsymbol{r} - \omega_k t)} + \ H.c.\ , \tag{2.37}$$

$$\hat{\mathbf{B}}(\boldsymbol{r}, t) = \sum_{\boldsymbol{k}} \sqrt{\frac{\hbar}{2\omega_k \varepsilon V}}\, \hat{a}_{\boldsymbol{k}}\, (\boldsymbol{k} \times \tilde{\boldsymbol{\epsilon}}_{\boldsymbol{k}})\, e^{i(\boldsymbol{k}\cdot\boldsymbol{r} - \omega_k t)} + \ H.c.\ , \tag{2.38}$$

where the term $H.c.$ stands for Hermitian conjugate. For a rectangular volume V, the above expression can be seen as the superposition of plane waves (one for each k-mode). The Hermitian field operator $\hat{\mathbf{E}}$ is often written as

$$\hat{\mathbf{E}}(\boldsymbol{r}, t) = \hat{\mathbf{E}}^{(+)}(\boldsymbol{r}, t) + \hat{\mathbf{E}}^{(-)}(\boldsymbol{r}, t) \tag{2.39}$$

where $\hat{\mathbf{E}}^{(-)}(\boldsymbol{r},t) = [\hat{\mathbf{E}}^{(+)}(\boldsymbol{r},t)]^\dagger$. The $\hat{\mathbf{E}}^{(+)}(\boldsymbol{r},t)$ part is called the positive frequency part of the field (i.e. it oscillates as $e^{-i\omega t}$ for $\omega > 0$) and consists of only the annihilation operators. This decomposition is related to how photon detectors interact with the electromagnetic field and to the fact that the $\hat{\mathbf{E}}^{(+)}$ part of the field operator contains the annihilation operator. As we will see in the following section, the annihilation operator is associated with the removal of a photon and, therefore, corresponds to absorption of photons by a photodetector. This was first put forward by Glauber in the quantum theory of optical coherence[36,37].

2.3 Number Operator and Fock States

The creation ($\hat{a}^\dagger_{\boldsymbol{k}}$) and annihilation ($\hat{a}_{\boldsymbol{k}}$) operators introduced in section 2.2 are non-Hermitian operators. However, these appear together in the Hamiltonian as $\hat{a}^\dagger\hat{a}$. This new operator is Hermitian and is known as the number operator $\hat{n}_{\boldsymbol{k}}$, i.e.,

$$\hat{n}_{\boldsymbol{k}} = \hat{a}^\dagger_{\boldsymbol{k}}\hat{a}_{\boldsymbol{k}}. \tag{2.40}$$

Consider the Hamiltonian of the $\boldsymbol{k}^{th}$-mode (for a given $\boldsymbol{k}$) in terms of the number operator as

$$\hat{\mathcal{H}}_{\boldsymbol{k}} = \hbar\omega_k\left(\hat{n}_{\boldsymbol{k}} + \frac{1}{2}\right). \tag{2.41}$$

From (2.41), one can see that the eigenstates of the number operator are the same as the energy eigenstates of the Hamiltonian. Therefore, one can define

$$\hat{n}_{\boldsymbol{k}}\left|n_{\boldsymbol{k}}\right\rangle = n_{\boldsymbol{k}}\left|n_{\boldsymbol{k}}\right\rangle, \tag{2.42}$$

with the corresponding eigenvalues as $n_{\boldsymbol{k}}$. Using the Hamiltonian $\hat{\mathcal{H}}_{\boldsymbol{k}}$, we have

$$\hat{\mathcal{H}}_{\boldsymbol{k}}\left|n_{\boldsymbol{k}}\right\rangle = \hbar\omega_k\left(n_{\boldsymbol{k}} + \frac{1}{2}\right)\left|n_{\boldsymbol{k}}\right\rangle. \tag{2.43}$$

The energy eigenstate $|n_{\boldsymbol{k}}\rangle$ is known as the photon number state or the Fock state with the corresponding energy eigenvalue given by (2.43).

With respect to the number state, the $\hat{a}_{\boldsymbol{k}}$ and $\hat{a}^\dagger_{\boldsymbol{k}}$ have the following relations

$$\begin{aligned}\hat{a}_{\boldsymbol{k}}\left|n_{\boldsymbol{k}}\right\rangle &= \sqrt{\hat{n}_{\boldsymbol{k}}}\ \left|n_{\boldsymbol{k}}-1\right\rangle \\ \hat{a}^\dagger_{\boldsymbol{k}}\left|n_{\boldsymbol{k}}\right\rangle &= \sqrt{\hat{n}_{\boldsymbol{k}}+1}\ \left|n_{\boldsymbol{k}}+1\right\rangle,\end{aligned} \tag{2.44}$$

which justifies their corresponding nomenclature as they lower or raise the photon number occupation $n_{\boldsymbol{k}}$ by 1. If we now define the ground state according to

$$\hat{a}_{\boldsymbol{k}}\left|0_{\boldsymbol{k}}\right\rangle = 0, \tag{2.45}$$

then using the commutation relation $[\hat{a}_{\boldsymbol{k}}, \hat{a}^\dagger_{\boldsymbol{k}}] = \hat{\mathbb{I}}$, we have

$$\hat{a}^\dagger_{\boldsymbol{k}}\left|0_{\boldsymbol{k}}\right\rangle = \left|1_{\boldsymbol{k}}\right\rangle, \tag{2.46}$$

that is, addition of a single photon into the $\boldsymbol{k}^{th}$-mode. We can continue this process to obtain a n-photon state in the same mode as

$$|n_{\boldsymbol{k}}\rangle = \frac{(\hat{a}^{\dagger}_{\boldsymbol{k}})^{n_{\boldsymbol{k}}}}{\sqrt{n_{\boldsymbol{k}}}} |0_{\boldsymbol{k}}\rangle \,. \tag{2.47}$$

We see that the number of photons in a given $\boldsymbol{k}^{th}$-mode is unbounded. Since photons are spin-1 bosons and obey Bose-Einstein statistics, an arbitrary large number of photons can occupy the same quantum state.

We use the following notation for a multimode photon number state

$$\begin{aligned} |\{n\}_{\boldsymbol{k}}\rangle &\equiv |n_1, n_2, n_3 \ldots\rangle \\ &= |n_1\rangle\, |n_2\rangle\, |n_3\rangle \ldots \\ &= \prod_{\boldsymbol{k}} |n_{\boldsymbol{k}}\rangle \,. \end{aligned} \tag{2.48}$$

Similarly, multimode vacuum and single photon states are represented as $|\{0\}_{\boldsymbol{k}}\rangle$ and $|\{1\}_{\boldsymbol{k}}\rangle$ which contain 0 and 1 photon in all the modes, respectively. The multimode number states have the following completeness and orthogonality relations

$$\hat{\mathbb{I}} = \prod_{\boldsymbol{k}} \langle\{n\}_{\boldsymbol{k}}|\{n\}_{\boldsymbol{k}}\rangle \,, \tag{2.49}$$

$$\langle\{n\}_{\boldsymbol{k}}|\{m\}_{\boldsymbol{k}}\rangle = \prod_{\boldsymbol{k}} \delta_{n_{\boldsymbol{k}} m_{\boldsymbol{k}}}. \tag{2.50}$$

Using the Hamiltonian in (2.41), one calculate the energy of a multimode Fock state as

$$\hat{\mathcal{H}}\, |\{n\}_{\boldsymbol{k}}\rangle = E\, |\{n\}_{\boldsymbol{k}}\rangle \,, \tag{2.51}$$

where

$$E = \sum_{\boldsymbol{k}} \hbar\omega_k \left(n_{\boldsymbol{k}} + \frac{1}{2}\right). \tag{2.52}$$

All multimode Fock states can be generated by applying the creation operators on the multimode vacuum state, i.e.

$$|\{n\}_{\boldsymbol{k}}\rangle = \prod_{\boldsymbol{k}} \frac{(\hat{a}^{\dagger}_{\boldsymbol{k}})^{n_{\boldsymbol{k}}}}{\sqrt{n_{\boldsymbol{k}}}} |\{0\}_{\boldsymbol{k}}\rangle \,. \tag{2.53}$$

At this point, we introduce variance of an observable, O, which measures the fluctuations or noise in the observable around the mean for a given quantum state. It is defined as

$$\begin{aligned} \langle(\Delta\hat{O})^2\rangle &\equiv \langle\hat{O}^2\rangle - \langle\hat{O}\rangle^2 \\ &= \langle\Delta^2\hat{O}\rangle \end{aligned} \tag{2.54}$$

where $\hat{O}$ is the corresponding operator and $\langle\hat{O}\rangle = \langle\psi|\hat{O}|\psi\rangle$ is the mean value, which implies that the variance is a state dependent quantity. A related and useful noise operator is often defined as

$$\delta\hat{O} = \hat{O} - \langle\hat{O}\rangle. \tag{2.55}$$

The photon number fluctuations in an electromagnetic field (or optical state) are crucial to distinguish between the classical and quantum optical fields. Mandel introduced[38] a useful parameter

$$Q_{\mathrm{M}} = \frac{\langle \Delta^2 \hat{n} \rangle - \langle \hat{n} \rangle}{\langle \hat{n} \rangle} \tag{2.56}$$

to characterize[2] the non-classicality of a quantum state, known as Mandel Q-parameter (Q_{M}). Since Fock states are the eigenstates of the number operator, the variance of the number operator vanishes for Fock states which leads to $Q_{\mathrm{M}} = -1$ for the Fock states. The importance of negative Q_{M} values will become clear in the later sections when we discuss coherent and squeezed states of light.

Apart from the energy fluctuations of a given state, one can also study the variance (or noise) of $\hat{q}_{\boldsymbol{k}}$ and $\hat{p}_{\boldsymbol{k}}$ operators. Since these operators do not commute for any given k-mode, their variances are related by the Heisenberg uncertainty principle. In order to show this, we first note that the expectation values of $\hat{a}_{\boldsymbol{k}}$ and $\hat{a}^{\dagger}_{\boldsymbol{k}}$ vanish for the Fock states. Thus,

$$\langle \{n\}_{\boldsymbol{l}} | \hat{a}_{\boldsymbol{k}} | \{n\}_{\boldsymbol{l}} \rangle = \langle \{n\}_{\boldsymbol{l}} | \hat{a}_{\boldsymbol{k}} | \{n\}_{\boldsymbol{l}} \rangle = 0 \quad \text{for all } \boldsymbol{k}. \tag{2.57}$$

Using (2.23) and (2.24), the $\hat{q}_{\boldsymbol{k}}$ and $\hat{p}_{\boldsymbol{k}}$ operators are obtained as addition and subtraction of the $\hat{a}_{\boldsymbol{k}}$ and $\hat{a}^{\dagger}_{\boldsymbol{k}}$ which implies that

$$\langle \{n\}_{\boldsymbol{l}} | \hat{q}_{\boldsymbol{k}} | \{n\}_{\boldsymbol{l}} \rangle = \langle \{n\}_{\boldsymbol{l}} | \hat{p}_{\boldsymbol{k}} | \{n\}_{\boldsymbol{l}} \rangle = 0 \quad \text{for all } \boldsymbol{k}. \tag{2.58}$$

This means that the observed eigenvalues of $\hat{q}_{\boldsymbol{k}}$ and $\hat{p}_{\boldsymbol{k}}$ operators are both positive and negative with equal probability for a Fock state. However, the second order moments of these operators do not vanish for a Fock state and are equal to

$$\langle \{n\}_{\boldsymbol{l}} | \hat{q}^2_{\boldsymbol{k}} | \{n\}_{\boldsymbol{l}} \rangle = \frac{\hbar}{\omega_k} \left(n_{\boldsymbol{k}} + \frac{1}{2} \right) \tag{2.59}$$

and

$$\langle \{n\}_{\boldsymbol{l}} | \hat{p}^2_{\boldsymbol{k}} | \{n\}_{\boldsymbol{l}} \rangle = \hbar \omega_k \left(n_{\boldsymbol{k}} + \frac{1}{2} \right). \tag{2.60}$$

From (2.54, 2.58-2.60), one can conclude that

$$\left\langle \Delta^2 \hat{q}_{\boldsymbol{k}} \right\rangle \left\langle \Delta^2 \hat{p}_{\boldsymbol{k}} \right\rangle = \frac{\hbar^2}{4} \left(n_{\boldsymbol{k}} + \frac{1}{2} \right)^2. \tag{2.61}$$

This is consistent with the general uncertainty relation for any two Hermitian operators $\hat{A}$ and $\hat{B}$, which states[39] that the following relation must be satisfied,

$$\langle \Delta^2 \hat{A} \rangle \langle \Delta^2 \hat{B} \rangle \geq \left(\frac{1}{2i} \left\langle [\hat{A}, \hat{B}] \right\rangle \right)^2, \tag{2.62}$$

where the equality sign holds for certain states that are known as the 'minimum uncertainty states' for the canonical position and momentum variables. Using (2.19), one can further simplify (2.62) for the $\hat{q}_{\boldsymbol{k}}$ and $\hat{p}_{\boldsymbol{k}}$ operators as

$$\left\langle \Delta^2 \hat{q}_{\boldsymbol{k}} \right\rangle \left\langle \Delta^2 \hat{p}_{\boldsymbol{k}} \right\rangle \geq \frac{\hbar^2}{4}. \tag{2.63}$$

[2]Here the multimode notation is suppressed for clarity. In general, for a multimode state, Q_{M} will be mode dependent.

The relation (2.63) is known as the Heisenberg uncertainty relation[34]. A comparison between (2.61) and (2.63) reveals that the multimode vacuum state $|\{0\}_{\boldsymbol{k}}\rangle$ (i.e. $n_{\boldsymbol{k}} = 0$ for all $\boldsymbol{k}$) is the only Fock state that is a minimum uncertainty state. For multimode states, it may be more useful to think of 'minimum uncertainty modes' defined as modes for which the equality sign in (2.63) holds.

2.4 Field Quadratures, Coherent States and Shot Noise Limit

The Hermitian $\hat{q}_{\boldsymbol{k}}$ and $\hat{p}_{\boldsymbol{k}}$ operators defined in section 2.2 have unequal dimensions. These are often replaced with the $\hat{X}_{\boldsymbol{k}}$ and $\hat{Y}_{\boldsymbol{k}}$ operators which are defined as

$$\hat{X}_{\boldsymbol{k}} \equiv \frac{\hat{a}_{\boldsymbol{k}} + \hat{a}^\dagger_{\boldsymbol{k}}}{\sqrt{2}} = \sqrt{\frac{\omega_k}{\hbar}}\,\hat{q}_{\boldsymbol{k}}, \tag{2.64}$$

$$\hat{Y}_{\boldsymbol{k}} \equiv \frac{\hat{a}_{\boldsymbol{k}} - \hat{a}^\dagger_{\boldsymbol{k}}}{i\sqrt{2}} = \frac{1}{\sqrt{\hbar\omega_k}}\,\hat{p}_{\boldsymbol{k}}. \tag{2.65}$$

As one can see from the above definitions, the two Hermitian quadrature operators are essentially the same as $\hat{q}_{\boldsymbol{k}}$ and $\hat{p}_{\boldsymbol{k}}$ but are scaled to be dimensionless. Using the commutation relations (2.27-2.29), we get

$$[\hat{X}_{\boldsymbol{k}},\, \hat{Y}_{\boldsymbol{k}'}] = i\delta_{\boldsymbol{k}\boldsymbol{k}'}\hat{\mathbb{I}}, \tag{2.66}$$

$$[\hat{X}_{\boldsymbol{k}}, \hat{X}_{\boldsymbol{k}'}] = 0, \tag{2.67}$$

$$[\,\hat{Y}_{\boldsymbol{k}},\, \hat{Y}_{\boldsymbol{k}'}] = 0. \tag{2.68}$$

Since $\hat{X}$ and $\hat{Y}$ do not commute, the Heisenberg uncertainty relation for these quadrature operators is

$$\langle \Delta^2 \hat{X}_{\boldsymbol{k}} \rangle \langle \Delta^2 \hat{Y}_{\boldsymbol{k}} \rangle \geq \frac{1}{4}\,. \tag{2.69}$$

It may be useful now to represent a single mode electric field operator using the quadrature operators as

$$\hat{E}_{\boldsymbol{k}}(\boldsymbol{r}, t) = \sqrt{\frac{\hbar\omega_k}{2\varepsilon V}}\,\left(\hat{a}_{\boldsymbol{k}}\; e^{i(\boldsymbol{k}\cdot\boldsymbol{r} - \omega_k t)} + \hat{a}^\dagger_{\boldsymbol{k}}\; e^{-i(\boldsymbol{k}\cdot\boldsymbol{r} - \omega_k t)}\right) \tag{2.70}$$

$$= \mathscr{E}_{\boldsymbol{k}}\left(\hat{X}_{\boldsymbol{k}}\cos(\omega_{\boldsymbol{k}} t - \phi) + \hat{Y}_{\boldsymbol{k}}\sin(\omega_{\boldsymbol{k}} t - \phi)\right), \tag{2.71}$$

where $\mathscr{E}_{\boldsymbol{k}} = \sqrt{\hbar\omega_k/\varepsilon V}$ and $\phi = \boldsymbol{k}\cdot\boldsymbol{r}$. For brevity, we have assumed a fixed polarization and omitted the unit polarization vector. In (2.71), the presence of cos and sin terms tells us that the $\hat{X}_{\boldsymbol{k}}$ and $\hat{Y}_{\boldsymbol{k}}$ associated field components are oscillating out of phase by 90° with respect to each other (and, hence, the name 'quadratures'). Depending on the phase reference, these are also sometimes referred to as the 'in-phase' and 'out-of-phase' quadrature operators and are very useful in extracting phase dependent information of the field. Applying these operators on a Fock state, however, reveals

$$\langle n_{\boldsymbol{k}}|\hat{X}_{\boldsymbol{k}}|n_{\boldsymbol{k}}\rangle = \langle n_{\boldsymbol{k}}|\hat{Y}_{\boldsymbol{k}}|n_{\boldsymbol{k}}\rangle = 0, \tag{2.72}$$

$$\langle n_{\boldsymbol{k}}|\hat{X}^2_{\boldsymbol{k}}|n_{\boldsymbol{k}}\rangle = \langle n_{\boldsymbol{k}}|\hat{Y}^2_{\boldsymbol{k}}|n_{\boldsymbol{k}}\rangle = n_{\boldsymbol{k}} + \frac{1}{2}, \tag{2.73}$$

which points to the fact that Fock states represent electromagnetic fields that do not have a phase dependent behavior. In the classical picture, the electromagnetic field has a well-defined amplitude and phase. Also, the field produced by a monochromatic single mode laser seems to be 'coherent' (i.e. well-defined phase and amplitude). Therefore, one may look for appropriate corresponding quantum states of such fields.

Glauber[40] put forward a new class of states, known as coherent states and denoted by $|\alpha\rangle$, which are defined using the following eigenvalue equation[3]

$$\hat{a}\,|\alpha\rangle = \alpha\,|\alpha\rangle\,, \tag{2.74}$$

where α is a complex number. Assuming that a normalized solution exists for the above equation, the coherent state can be represented in terms of the Fock basis as[40]

$$|\alpha\rangle = e^{-\frac{1}{2}|\alpha|^2} \sum_{n=0}^{\infty} \frac{|\alpha|^n}{\sqrt{n!}}\,|n\rangle\,. \tag{2.75}$$

To look for the phase behavior of a coherent state, we calculate the mean values of the quadrature operators as

$$\langle\alpha|\hat{X}|\alpha\rangle = \sqrt{2}\;\mathfrak{Re}[\alpha], \tag{2.76}$$

$$\langle\alpha|\hat{Y}|\alpha\rangle = \sqrt{2}\;\mathfrak{Im}[\alpha]. \tag{2.77}$$

For $\alpha = |\alpha|e^{i\theta}$, we have

$$\alpha = \mathfrak{Re}[\alpha] + i\,\mathfrak{Im}[\alpha] \tag{2.78}$$

$$= \frac{1}{\sqrt{2}}\left(\langle\hat{X}\rangle_{|\alpha\rangle} + i\,\langle\hat{Y}\rangle_{|\alpha\rangle}\right), \tag{2.79}$$

where the subscript $|\alpha\rangle$ denotes expectation value with respect to the coherent state and $\mathfrak{Re}/\mathfrak{Im}$ denotes the real/imaginary part of a complex number. In other words, the quadrature expectation values give information about the real and imaginary parts of the complex amplitude of the field. Therefore, we can estimate the phase of a coherent state as

$$\theta = \tan^{-1}\left(\frac{\langle\hat{Y}\rangle_{|\alpha\rangle}}{\langle\hat{X}\rangle_{|\alpha\rangle}}\right). \tag{2.80}$$

The intensity of the state, that is, the average photon occupation is given by

$$\bar{n} = \langle\alpha|\hat{n}|\alpha\rangle \tag{2.81}$$

$$= |\alpha|^2. \tag{2.82}$$

This is like a classical field where the intensity is given by the square of amplitude $|\alpha|$ of the field. Here in (2.81), we have assumed ergodicity to replace the time average with the ensemble average. One can also evaluate the photon number variance as

$$\langle\Delta^2\hat{n}\rangle_{|\alpha\rangle} = \langle\hat{n}^2\rangle_{|\alpha\rangle} - \langle\hat{n}\rangle^2_{|\alpha\rangle} \tag{2.83}$$

$$= (|\alpha|^4 + |\alpha|^2) - |\alpha|^4 \tag{2.84}$$

$$= |\alpha|^2, \tag{2.85}$$

[3] As we will be mostly discussing fields and operators corresponding to a particular $\boldsymbol{k}$-mode, we will be dropping the subscript $\boldsymbol{k}$ for the rest of the chapter to simplify notation.

which implies that the fractional photon number uncertainty ($\Delta n \equiv \sqrt{\langle \Delta^2 \hat{n} \rangle}$) decreases with average photon number as

$$\frac{\Delta n}{\bar{n}} = \frac{1}{\sqrt{\bar{n}}}. \tag{2.86}$$

Based on the properties of the bright coherent states (i.e. large $\bar{n}$), one might say that they are just like classical states as (i) their expectation values for amplitude and phase match with that of a classical electric field, and (ii) the fractional uncertainty in photon number decreases with higher intensity. Indeed, bright coherent states are often approximated with classical fields in order to simplify calculations.

However, despite their near classical behavior, they represent a quantum description of classical states. Exploring their quadrature noise behavior, we find

$$\langle \Delta^2 \hat{X} \rangle_{|\alpha\rangle} = \langle \Delta^2 \hat{Y} \rangle_{|\alpha\rangle} = \frac{1}{2}, \tag{2.87}$$

for all α. Therefore, coherent states are minimum uncertainty states with fluctuation properties identical to the vacuum state $|0\rangle$ (which is itself a coherent state with zero amplitude). In contrast to the behavior of number states whose quadrature noise scale linearly with amplitude as shown in (2.59) and (2.60), coherent states can have arbitrary large values of $|\alpha|$ without any noise penalty in the quadratures. As evident from (2.75), a coherent state is a superposition of Fock states and the probability of finding n photons in the field is

$$p_n = |\langle n|\alpha\rangle|^2 \tag{2.88}$$

$$= e^{-|\alpha|^2} \sum_{n=0}^{\infty} \frac{|\alpha|^{2n}}{n!} \tag{2.89}$$

$$= e^{-\bar{n}} \frac{\bar{n}^n}{n!}, \tag{2.90}$$

which is a Poisson distribution with a mean and corresponding photon number variance $\langle \Delta^2 \hat{n} \rangle$ of $\bar{n}$. This essentially implies that during the detection of a coherent state using a photodetector, the arrival of photons is randomly distributed[41] in time or, in other words, the distribution of photons in a coherent state is uniform. The value of the Mandel parameter Q_{M} for the coherent state is

$$Q_{\mathrm{M}} = \frac{\langle \Delta^2 \hat{n} \rangle_{|\alpha\rangle} - \langle \hat{n} \rangle_{|\alpha\rangle}}{\langle \hat{n} \rangle_{|\alpha\rangle}} \tag{2.91}$$

$$= 0, \tag{2.92}$$

which places them at the boundary of classical and quantum regime in terms of the quantum coherence and photon statistics behavior[38,42]. A related parameter is the Fano factor (F) defined, for a given optical state $|\Psi\rangle$, as[43]

$$\mathrm{F} = \frac{\langle \Delta^2 \hat{n} \rangle_{|\Psi\rangle}}{\langle \Delta^2 \hat{n} \rangle_{|\alpha\rangle}} \tag{2.93}$$

$$= \frac{\langle \Delta^2 \hat{n} \rangle_{|\Psi\rangle}}{\bar{n}}, \tag{2.94}$$

where $\bar{n} = \langle\alpha|\hat{n}|\alpha\rangle = \langle\Psi|\hat{n}|\Psi\rangle$. Thus, it is a ratio quantifying super- or sub-Poissonian behavior[44] in the photon distributions. The photon number states $|n\rangle$ have a Fano factor equal to zero (and $Q_M = -1$) due to vanishing photon number variance. These states display extreme sub-Poissonian behavior and, therefore, are non-classical[38].

From our discussion of the Heisenberg Uncertainty principle and quadrature variance of various optical states, it seems clear that all states of light display some minimal noise features in the quantum theory of light. We also defined a class of 'minimum uncertainty states' with minimal quadrature noise that reach the lower bound of uncertainty principle. Given a equal distribution of noise or uncertainty in the two quadratures, the vacuum and the coherent states saturate this lower bound with their quadrature variance equal to

$$\langle\Delta^2\hat{X}\rangle = \langle\Delta^2\hat{Y}\rangle = \frac{1}{2}. \tag{2.95}$$

We find that this is the minimum amount of noise an optical state is allowed to have without requiring a description based on non-classical probability distributions. Therefore, this lower limit on quadrature variances is known as the quantum noise limit (QNL) or the shot noise limit (SNL).

2.5 Phase Space Description of Light

In our discussion of coherent states, we pointed out that they have the same noise properties as a vacuum state. In fact, the vacuum state is a coherent state with $\alpha = 0$. For non-zero values of α, the coherent state is essentially a displaced vacuum state with non-zero quadrature expectation values given by (2.76) and (2.77). Taking note of the form of a coherent state in (2.79), one can graphically visualize it in a corresponding optical phase space diagram with the two quadratures as the position and momentum axes. Figure 2.1A depicts a coherent state $|\alpha\rangle$ with $\alpha = |\alpha|e^{i\theta}$ in phase space. The fuzzy disc represents the uncertainty region of phase space that gives the probable values of the X and Y quadratures. The uncertainties are symmetric along all directions represented by radial symmetry around the center of the disc with the center given by the average and most probable values of the two quadratures[43]. This fuzzy disk representation can be viewed as a projection of the Wigner quasiprobability distribution which is a 2D Gaussian distribution in phase space for the coherent states. The variance in the two quadratures is equal to $1/2$ (the direction in which variance is evaluated is indicated using small arrows). Since, the variance is the same in all directions, we draw a dashed circle (representing σ^2 of the Gaussian distribution) with a radius of $1/2$. The disc is located at a distance of $\sqrt{2}\,|\alpha|$ from the origin[4] and subtends a positive angle of θ with respect to the X-axis. The angle uncertainty $\Delta\theta$ diminishes with large values of $|\alpha|$, therefore, increasing the phase stability of the state. The noise behavior of the vacuum state, shown in figure 2.1B, is the same as the coherent state but has zero displacement with respect to the origin in phase space. The radial symmetry combined with no displacement lead to complete phase uncertainty of a vacuum state, i.e. $\Delta\theta = 2\pi$.

[4]The distance is a different value than $|\alpha|$ because the real and imaginary parts of α are scaled up by $\sqrt{2}$ to get the corresponding quadrature expectation values. To be precise, let $\langle\hat{X}\rangle_{|\alpha\rangle} = c$ and $\langle\hat{Y}\rangle_{|\alpha\rangle} = d$, then using (2.76) and (2.77), we get

$$(c^2 + d^2)^{1/2} = \sqrt{2}\left([\mathfrak{Re}\{\alpha\}]^2 + [\mathfrak{Im}\{\alpha\}]^2\right)^{1/2} = \sqrt{2}\,|\alpha|. \tag{2.96}$$

2.5 Phase Space Description of Light

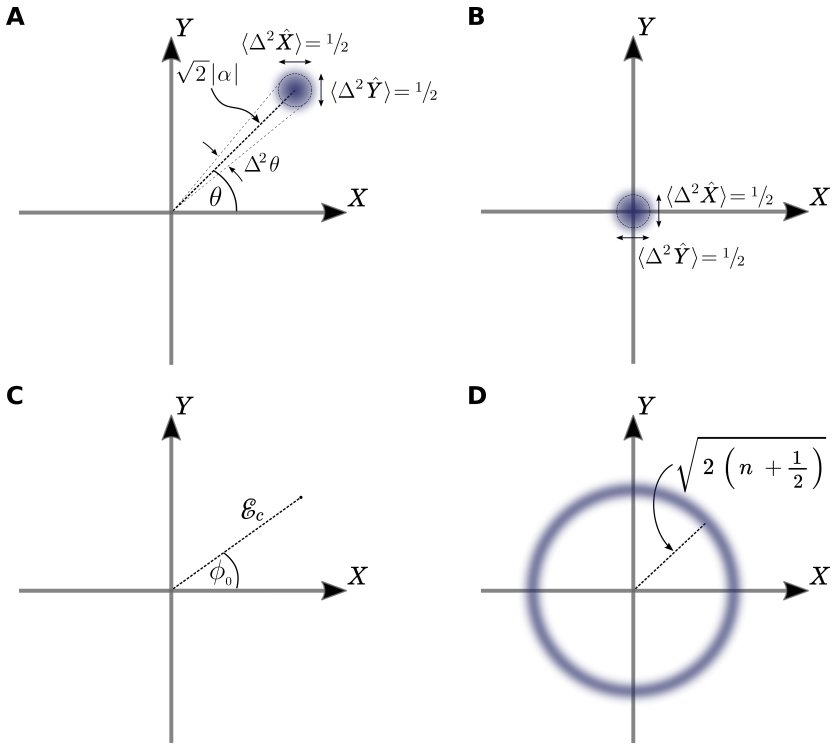

Figure 2.1: Phase space depiction of optical states in terms of the X and Y quadratures. (A) A coherent state $|\alpha\rangle$ with $\alpha = |\alpha|e^{i\theta}$ is portrayed as a blurry disc with radial symmetry. The two quadratures have the same variance of $1/2$ which is the same in all directions and is highlighted using a dashed circle. The phase uncertainty ($\Delta\theta$) of a coherent state decreases as $1/\sqrt{|\alpha|}$. (B) The vacuum state is essentially a coherent state with zero amplitude and is depicted as a the blurry disc at the origin in phase space. Being at the origin, the phase of a vacuum state is undefined and the phase uncertainty is 2π. The blurry disk portrayal of the coherent and vacuum states can be seen as projections of the corresponding Wigner functions[43]. (C) A classical state is portrayed using a single dot in phase space. Since classical states are not constrained by the Heisenberg uncertainty principle, they do not have any fundamental noise associate with them, and hence, are unphysical. (D) A number state in phase space as a simplified version of the Husimi Q-function quasiprobability distribution. The phase of a number state is random due to the radially symmetric distribution around the origin.

Similar to the form of the electric field operator given in (2.70), one can write an equivalent expression for a single mode classical field by replacing various operators with corresponding c-numbers as[41]

$$E(\boldsymbol{r},t) = \frac{\mathcal{E}_c}{\sqrt{2}}\left(a\; e^{i(\boldsymbol{k}\cdot\boldsymbol{r}-\omega t)} + a^*\; e^{-i(\boldsymbol{k}\cdot\boldsymbol{r}-\omega t)}\right) \tag{2.97}$$

$$= \mathcal{E}_c \cos\phi_0\, X(t) + \mathcal{E}_c \sin\phi_0\, Y(t), \tag{2.98}$$

where

$$X(t) = \frac{ae^{-i\omega t} + a^* e^{i\omega t}}{\sqrt{2}}, \tag{2.99}$$

$$Y(t) = \frac{ae^{-i\omega t} - a^* e^{i\omega t}}{i\sqrt{2}} \tag{2.100}$$

and $\phi_0 = -\boldsymbol{k}\cdot\boldsymbol{r}$. Here, $\mathcal{E}_c$ is a real constant that denotes the amplitude of the classical field in phase

space. In other words, the time varying electric field can be decomposed into in-phase $X(t)$ and out-of-phase $Y(t)$ frequency components[45]. The decomposition is similar to the I/Q representation of a time-varying periodic signal and is well-known in electrical signal analysis literature. One can depict the classical expression of the electric field in (2.98) with respect to the quadrature components as shown in figure 2.1C. The state of the field is given by a single point in phase space and has no fundamental quadrature noise associated with it.

A number state $|n\rangle$ can be represented in phase space using a circle[43] since the number state has no phase information. The radius of the circle is given by the amplitude of the state and is proportional to $\sqrt{n}$. In figure 2.1D, we show a simplified phase space representation of the Q-function for state $|n\rangle$ which is a Gaussian distribution in radial direction with a mean equal to the amplitude of the state[43,46] (hence, a finite width ring).

The phase space representation of optical states given here is very useful for visualizing their distribution. However, for quantum states of light, such a representation must be seen as only describing the qualitative behavior of these states in phase space. Mathematically rigorous representations of quantum states have been developed in the form of various quasiprobability distributions[47] dependent on suitable quadrature variables. For a given quantum state, the phase space behavior of certain quasiprobability distributions can be more well-behaved than the rest. For further details on the use of quasiprobability distributions in quantum mechanics, one may consult these references[46,48–51].

In addition to the visualization of the distribution of a state, one can also study the evolution of optical states using the phase space picture. For the time evolution of the quadrature expectation values of a coherent state, we have

$$\langle \hat{X} \rangle_{|\alpha\rangle}(t) = \frac{\alpha e^{-i\omega t} + \alpha^* e^{i\omega t}}{\sqrt{2}} \tag{2.101}$$

$$= \frac{\alpha(\cos\omega t - i\sin\omega t) + \alpha^*(\cos\omega t + i\sin\omega t)}{\sqrt{2}}$$

$$= \langle \hat{X} \rangle_{|\alpha\rangle} \cos\omega t + \langle \hat{Y} \rangle_{|\alpha\rangle} \sin\omega t, \tag{2.102}$$

and similarly,

$$\langle \hat{Y} \rangle_{|\alpha\rangle}(t) = \frac{\alpha e^{-i\omega t} - \alpha^* e^{i\omega t}}{i\sqrt{2}} \tag{2.103}$$

$$= \langle \hat{Y} \rangle_{|\alpha\rangle} \cos\omega t - \langle \hat{X} \rangle_{|\alpha\rangle} \sin\omega t, \tag{2.104}$$

where

$$\langle \hat{X} \rangle_{|\alpha\rangle} \equiv \langle \hat{X} \rangle_{|\alpha\rangle}(t=0) = \frac{\alpha + \alpha^*}{\sqrt{2}}, \tag{2.105}$$

$$\langle \hat{X} \rangle_{|\alpha\rangle} \equiv \langle \hat{X} \rangle_{|\alpha\rangle}(t=0) = \frac{\alpha - \alpha^*}{i\sqrt{2}}. \tag{2.106}$$

The expressions for time evolution in (2.102) and (2.104) can be neatly conveyed in the matrix from as

$$\begin{bmatrix} \langle \hat{X} \rangle_{|\alpha\rangle}(t) \\ \langle \hat{Y} \rangle_{|\alpha\rangle}(t) \end{bmatrix} = \begin{bmatrix} \cos\omega t & \sin\omega t \\ -\sin\omega t & \cos\omega t \end{bmatrix} \begin{bmatrix} \langle \hat{X} \rangle_{|\alpha\rangle} \\ \langle \hat{Y} \rangle_{|\alpha\rangle} \end{bmatrix}. \tag{2.107}$$

Such an evolution of quadrature expectations is equivalent to the time evolution of the corresponding coherent state as $|\alpha(t)\rangle = \left|\alpha(0)e^{-i\omega t}\right\rangle$ which represents a clockwise rotation in phase space[5]. Figure 2.2A shows the time evolution of a coherent state in phase space. The fuzzy disk revolves

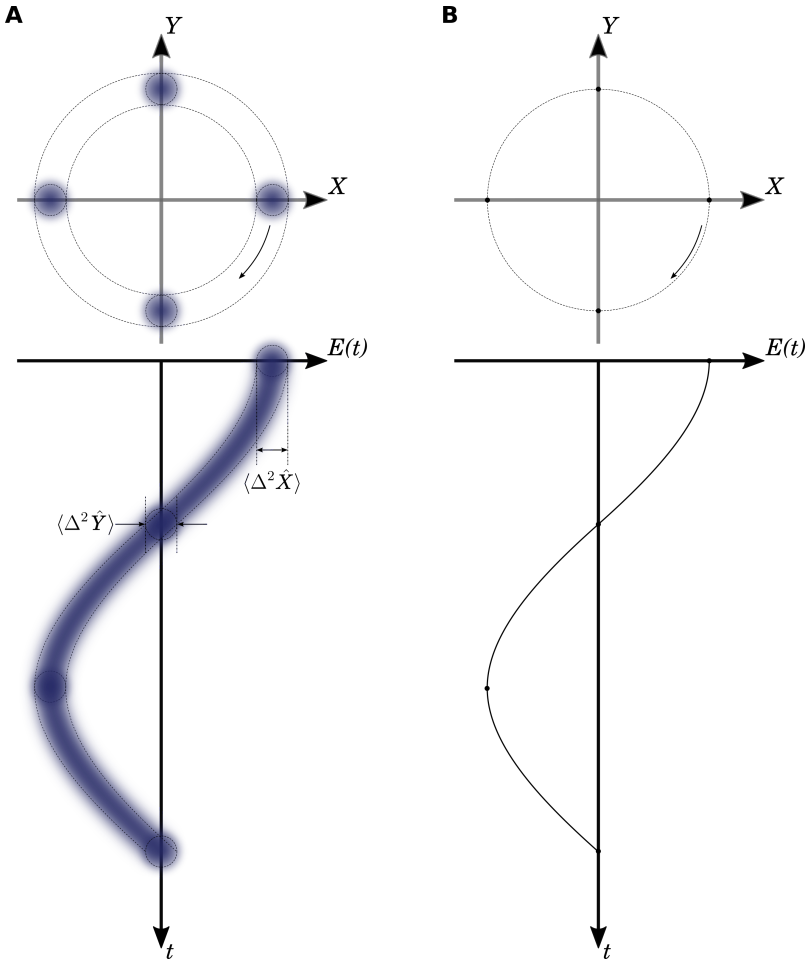

Figure 2.2: Time evolution of a coherent and a classical state. (A) The coherent state rotates clockwise in phase phase with time according to $|\alpha(t)\rangle = \left|\alpha(0)e^{-i\omega t}\right\rangle$. Changes in the value of electric field along the X quadrature with respect to time (or equivalently phase) are shown in the bottom figure. (B) A similar time evolution can be seen for a classical state that has angular frequency ω. In the absence of any inherent noise, the amplitude of the state oscillates between a maximum and a minimum value. For both the figures (A) and (B), we assume that the phase of the initial state is zero with respect to the X-axis.

at a constant distance around the origin with an angular velocity ω. The electric field (and its fluctuations) of the coherent state along the X quadrature is given by the projection of the disk onto the X-axis (see figure 2.2A bottom). At time $t = 0$, we take the amplitude of the state to be aligned with the X-axis (i.e. zero initial phase). Therefore, the amplitude noise of the electric field is the same as the X quadrature noise. After time $t = \pi/2\omega$, equivalent to a clockwise $\pi/2$ phase rotation of the state in phase space, the projection of the amplitude of coherent state goes to zero and we observe the noise in the (initial) Y quadrature of the state. At $t = \pi/\omega$, we again see the

[5] A counter-clockwise rotation of quadrature axes is equivalent to clockwise rotation of the state. For phase space description of time evolution using quadrature axes rotation, see reference [52,53]

X quadrature noise and the negative amplitude of the electric field before restoring back to initial state at $t = 2\pi/\omega$.

In the figure 2.2B, the time evolution of a classical state is shown with the same initial condition and the angular velocity ω. Once again we see the similarities in the behaviors of a coherent and a classical state as the amplitude of the classical field changes periodically between maximum and minimum values, however, without being accompanied by quadrature or field fluctuations. The time evolution of the classical field is essentially the same as that of the coherent state which is expected due to the similarities of the classical quadrature expressions (2.99) and (2.100) with the quadrature expectation values (2.101) and (2.103) in the quantum picture.

Based on our discussion of the phase space description, we saw that one can create a coherent state starting from a vacuum state and displacing it from the origin by α. A relevant operator corresponding to such a transformation is known as the displacement operator $\hat{D}(\alpha)$ and, can be defined as

$$\hat{D}(\alpha) = e^{(\alpha\hat{a}^\dagger - \alpha^*\hat{a})} \tag{2.108}$$

$$= e^{-\frac{1}{2}|\alpha|^2}\, e^{\alpha\hat{a}^\dagger} e^{-\alpha^*\hat{a}} \tag{2.109}$$

$$= e^{\frac{1}{2}|\alpha|^2}\, e^{-\alpha^*\hat{a}}\, e^{\alpha\hat{a}^\dagger}\,, \tag{2.110}$$

where we have used the Baker-Campbell-Hausdorff (BCH) theorem [32] to derive (2.109) and (2.110). Applying the displacement operator on the vacuum state, we get

$$\hat{D}(\alpha)|0\rangle = e^{-\frac{1}{2}|\alpha|^2}\, e^{\alpha\hat{a}^\dagger} e^{-\alpha^*\hat{a}}\, |0\rangle \tag{2.111}$$

$$= e^{-\frac{1}{2}|\alpha|^2}\, e^{\alpha\hat{a}^\dagger}\, |0\rangle$$

$$= e^{-\frac{1}{2}|\alpha|^2} \sum_{n=0}^{\infty} \frac{\alpha^n}{n!} (\hat{a}^\dagger)^n\, |0\rangle$$

$$= |\alpha\rangle\,. \tag{2.112}$$

For the displacement of any general coherent state $|\beta\rangle$, we have

$$\hat{D}(\alpha)\,|\beta\rangle = |\alpha+\beta\rangle\, e^{\frac{1}{2}(\alpha\beta^* - \alpha^*\beta)} \tag{2.113}$$

$$= |\alpha+\beta\rangle\, e^{i\,\Im\mathrm{m}[\alpha^*\beta]}. \tag{2.114}$$

Some of the other useful properties of the displacement operator are

$$\hat{a} + \alpha = \hat{D}^\dagger(\alpha)\hat{a}\hat{D}(\alpha) \tag{2.115}$$

$$\hat{D}^\dagger(\alpha) = \hat{D}(-\alpha) = \hat{D}^{-1}(\alpha). \tag{2.116}$$

Before moving on to a discussion of the squeezed state of light in the next section, we introduce a useful terminology of generalized quadratures X_θ and Y_θ as

$$\hat{X}_\theta = \frac{\hat{a}e^{-i\theta} + \hat{a}^\dagger e^{i\theta}}{\sqrt{2}}, \tag{2.117}$$

$$\hat{Y}_\theta = \hat{X}_{\theta+\frac{\pi}{2}} = \frac{\hat{a}e^{-i\theta} - \hat{a}^\dagger e^{i\theta}}{i\sqrt{2}}. \tag{2.118}$$

Again, one may notice the similarities of expressions (2.99) and (2.100) with (2.117) and (2.118), respectively. Fundamentally, these expression are based on the separation of positive $\hat{\mathbf{E}}^{(+)}$ and negative $\hat{\mathbf{E}}^{(-)}$ frequency parts of the field. Although, such a separation has no physical motivation in the classical picture (it is used for the mathematical convenience of exponential functions); in the quantum picture, the detection mechanism of photons via photo-absorption at the detector exclusively deals with the annihilation operator built into the positive frequency component [37].

2.6 Squeezed States of Light

As we mentioned in section 2.4, the vacuum and the coherent states have the same fixed amount of variance in any given quadrature. This leads to the definition of the SNL due to their minimum noise property following the Heisenberg uncertainty principle. However, it is possible to have quantum optical states with one quadrature noise lower than the SNL at the expense of excess noise in the other quadrature, e.g.

$$\langle \Delta^2 \hat{X} \rangle < \frac{1}{2} \quad \text{and} \quad \langle \Delta^2 \hat{Y} \rangle > \frac{1}{2}\,, \tag{2.119}$$

These states are known as squeezed states of light and, in general, need not be minimum uncertainty states. Figure 2.3 provides a phase space depiction of a few squeezed states of light. A 'zero-mean' vacuum squeezed state that has less uncertainty in the X quadrature is shown in figure 2.3A. The distribution is a fuzzy elliptical disk, commonly referred to as the 'noise ellipse', which is a simplified representation of the Wigner distribution of the squeezed state. Since the Wigner distribution of the squeezed states is also a 2D Gaussian distribution, it can be used to evaluate the variance along any given axis and is shown using a dashed ellipse. The angle of lowest variance below the SNL with

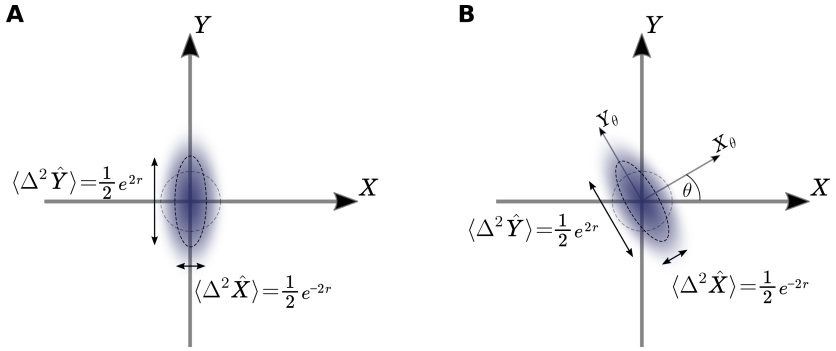

Figure 2.3: Phase space representations of various squeezed states of light. (A) A vacuum squeezed state with lower noise (than SNL) in the X quadrature at the expense of higher noise in the Y quadrature. A dashed ellipse is drawn to represent the variance of the given squeezed state. A dashed circle in the background represents the variance of the vacuum state (i.e. SNL). Since the X quadrature is the squeezing quadrature, the squeezing angle is zero. (B) A vacuum squeezed state that has squeezing along the X_θ quadrature in phase space. Angle θ is equal to half the squeezing phase φ as described in the main text.

respect to the X-axis is known as the *squeezing angle* (denoted here with θ_s) and the corresponding quadrature, oriented along the minor axis of the noise ellipse, is known as the *squeezing quadrature*. The amount of squeezing in the squeezing quadrature, which is simply referred as *squeezing* and

denoted here by 's', is given as

$$s = \frac{\langle \Delta^2 \hat{X}_{\theta_s} \rangle}{\langle \Delta^2 \hat{X} \rangle_{|\alpha\rangle}}, \tag{2.120}$$

where $\langle \Delta^2 \hat{X} \rangle_{|\alpha\rangle}$ denotes the variance of an equivalent (amplitude) coherent state and the expectation value in the numerator is evaluated with respect to the squeezed state. The amount of squeezing is often reported on the decibel logscale and is defined as

$$s_{\text{dB}} = -10 \log_{10} s. \tag{2.121}$$

Hence, squeezing is positive on the dB scale. A related parameter to squeezing is the squeeze parameter r, defined using the following relation

$$e^{-2r} = s. \tag{2.122}$$

Given the $\langle \Delta^2 \hat{X} \rangle_{|\alpha\rangle} = 1/2$, we get

$$\langle \Delta^2 \hat{X}_{\theta_s} \rangle = \frac{1}{2} e^{-2r} \quad \text{and} \quad \langle \Delta^2 \hat{Y}_{\theta_s} \rangle = \frac{1}{2} e^{2r} \tag{2.123}$$

for a vacuum squeezed state (see figure 2.3A).

Earlier we saw that a coherent state $|\alpha\rangle$ can be generated from a vacuum state using the displacement operator $D(\alpha)$. Similarly, a vacuum squeezed state $|\xi\rangle$ can be generated using a squeezing operator $\hat{S}(\xi)$ as

$$\hat{S}(\xi) |0\rangle = |\xi\rangle, \qquad \xi = r e^{i\varphi}, \tag{2.124}$$

where the additional parameter φ is known as *squeezing phase* which determines the squeezing and anti-squeezing directions in phase space. The squeezing operator is a unitary operator and can be defined as

$$\hat{S}(\xi) = \exp\left(\frac{1}{2} \xi^* \hat{a}^2 - \frac{1}{2} \xi \, \hat{a}^{\dagger 2} \right) \tag{2.125}$$

Using the above form of $\hat{S}(\xi)$, we can solve for $|\xi\rangle$ as

$$|\xi\rangle = \exp\left(\frac{1}{2} \xi^* \hat{a}^2 - \frac{1}{2} \xi \, \hat{a}^{\dagger 2} \right) |0\rangle \tag{2.126}$$

$$= \frac{1}{\sqrt{\cosh r}} \sum_{n=0}^{\infty} (-1)^n e^{in\varphi} (\tanh r)^n \frac{\sqrt{(2n)!}}{2^n n!} |2n\rangle . \tag{2.127}$$

Notice that the odd numbered states are absent. The probability of finding the field in a specific $|2m\rangle$ number state is given by

$$p_{2m} = |\langle 2m|\xi\rangle|^2 = \frac{(\tanh r)^{2m}}{\cosh r} \frac{(2m)!}{2^{2m} m!}. \tag{2.128}$$

Therefore, despite the zero mean, a vacuum squeezed state 'contains' photons with an average photon occupancy

$$\langle \hat{n} \rangle_{|\xi\rangle} = \sinh^2 r, \tag{2.129}$$

which is non-zero for $r > 0$. Looking further into the photon statistics properties of the variance and Q_M are

$$\langle \Delta^2 \hat{n} \rangle_{|\xi\rangle} = 2(\sinh^2 r + \sinh^4 r), \tag{2.130}$$

$$Q_M = 1 + 2\sinh^2 r. \tag{2.131}$$

Both of these quantities point toward a super-Poisson or thermal behavior of these states. Therefore, it is not clear if the squeezed states are non-classical in nature. However, explaining certain characteristics of these states in terms of the Glauber-Sudarshan P-distribution, such as the normalized variance along the squeezed quadrature, requires non-positiveness of the distribution and points to the non-classical behavior of squeezed states [54,55].

We can now connect the squeezing angle θ_s with the squeezing phase φ of $|\xi\rangle$ by calculating the quadrature variances $\langle \Delta^2 \hat{X} \rangle_{|\xi\rangle}$ and $\langle \Delta^2 \hat{Y} \rangle_{|\xi\rangle}$. To evaluate these variances, we consider how the squeezing operator transforms the creation and annihilation operators

$$\hat{S}^\dagger(\xi)\, \hat{a}\, \hat{S}(\xi) = \hat{a} \cosh r - \hat{a}^\dagger e^{i\varphi} \sinh r, \tag{2.132}$$

$$\hat{S}^\dagger(\xi)\, \hat{a}^\dagger\, \hat{S}(\xi) = \hat{a}^\dagger \cosh r - \hat{a}\, e^{-i\varphi} \sinh r. \tag{2.133}$$

These transformations are known as the Bogoliubov transformations [56] and preserve the commutation relation between the creation and annihilation operators. Using these transformations and the unitarity of $\hat{S}(\xi)$, one can evaluate

$$\langle \xi |\, \hat{a}\, | \xi \rangle = \langle 0 | \hat{S}^\dagger(\xi)\, \hat{a}\, \hat{S}(\xi) | 0 \rangle \tag{2.134}$$

$$\langle \xi |\, \hat{a}^2\, | \xi \rangle = \langle 0 | \hat{S}^\dagger(\xi)\, \hat{a}\, \hat{S}(\xi)\, \hat{S}^\dagger(\xi)\, \hat{a}\, \hat{S}(\xi) | 0 \rangle. \tag{2.135}$$

Using (2.132-2.135), the quadrature variances have the form

$$\langle \Delta^2 \hat{X} \rangle_{|\xi\rangle} = \frac{1}{2} \left(\cosh^2 r + \sinh^2 r - 2 \sinh r \cosh r \cos\varphi \right) \tag{2.136}$$

$$\langle \Delta^2 \hat{Y} \rangle_{|\xi\rangle} = \frac{1}{2} \left(\cosh^2 r + \sinh^2 r + 2 \sinh r \cosh r \cos\varphi \right). \tag{2.137}$$

For $\varphi = 0$, we get squeezing along the X quadrature and anti-squeezing along the Y quadrature which is the vacuum squeezed state shown in figure 2.3A. For values of $\varphi \neq 0$ or π, the squeezing quadrature X_{θ_s} is neither along X or Y. It can be shown that if we rotate the quadratures by an angle of $\theta = \varphi/2$ (counter-clockwise, assuming $\varphi > 0$) in phase space, we get

$$\langle \Delta^2 \hat{X}_{\theta=\varphi/2} \rangle_{|\xi\rangle} = \frac{1}{2} e^{-2r}, \tag{2.138}$$

$$\langle \Delta^2 \hat{Y}_{\theta=\varphi/2} \rangle_{|\xi\rangle} = \frac{1}{2} e^{2r}. \tag{2.139}$$

This implies $\theta_s = \varphi/2$. With respect to θ_s, we can rewrite the generalized quadrature variance as

$$\langle \Delta^2 \hat{X}_\theta \rangle_{|\xi\rangle} = \frac{1}{2} e^{-2r} \cos^2(\theta - \theta_s) + \frac{1}{2} e^{2r} \sin^2(\theta - \theta_s). \tag{2.140}$$

Figure 2.3B depicts the corresponding vacuum squeezed state $|\xi\rangle$ with $\xi = re^{i\varphi}$, that is rotated at an angle in phase space. The angle θ of the generalized quadrature X_θ is taken to be θ_s.

A more general class of states with non-zero amplitudes are the squeezed coherent states. These states can be obtained by displacing the squeezed state $|\xi\rangle$ in phase space with the displacement operator, i.e.

$$|\alpha, \xi\rangle = \hat{D}(\alpha)\hat{S}(\xi)\,|0\rangle\,, \tag{2.141}$$

where $|\alpha, \xi\rangle$ is the squeezed coherent state with $\alpha = |\alpha|e^{i\phi}$ and $\xi = re^{i\varphi}$. Some of the relevant operator expectation values and properties are

$$\langle\hat{a}\rangle_{|\alpha,\xi\rangle} = \alpha, \quad \langle\hat{a}^2\rangle_{|\alpha,\xi\rangle} = \alpha^2 - e^{i\varphi}\cosh r \sinh r \tag{2.142}$$

$$\langle\hat{n}\rangle_{|\alpha,\xi\rangle} = |\alpha|^2 + \sinh^2 r, \quad \langle\hat{X}_\theta\rangle_{|\alpha,\xi\rangle} = \frac{\alpha e^{-i\theta} + \alpha^* e^{i\theta}}{\sqrt{2}} \tag{2.143}$$

$$\langle\Delta^2\hat{X}_{\frac{\varphi}{2}}\rangle_{|\alpha,\xi\rangle} = \frac{1}{2}e^{-2r}, \quad \langle\Delta^2\hat{X}_{\frac{\varphi}{2}+\frac{\pi}{2}}\rangle_{|\alpha,\xi\rangle} = \frac{1}{2}e^{2r}, \quad \langle\Delta^2\hat{X}_{\frac{\varphi}{2}}\rangle_{|\alpha,\xi\rangle}\langle\Delta^2\hat{X}_{\frac{\varphi}{2}+\frac{\pi}{2}}\rangle_{|\alpha,\xi\rangle} = \frac{1}{4}. \tag{2.144}$$

Based on these properties, one would expect the photon statistics of the squeezed coherent states to be the same as the squeezed vacuum states, as the displacement operator does not alter the noise ellipse in phase space. However, the Mandel parameter Q_M can be negative. It can be shown that for $\{\phi, \varphi\} \approx 0$, Q_M is negative for large amplitude coherent squeezed states[55]. In other words, there are values of $\{\alpha, \xi\}$ for which the photon statistics of a squeezed coherent state is sub-Poissonian. This also implies that squeezing as a quantum mechanical effect can be obtained with large number of photons in the field and is, therefore, suitable for showing macroscopic quantum mechanical effects[54].

Figures 2.4A and 2.4B show the phase space distribution of two squeezed coherent states that are squeezed along the X and Y quadrature, i.e. $|\alpha| \neq 0$ and φ equal to 0 and π, respectively. The electric field corresponding to the X and Y quadratures can be evaluated via projections along the X and Y-axes. The time-evolution of these states in phase space can be visualized by a clockwise rotation of the noise ellipse around the origin with angular velocity ω as shown in the figure. During such a rotation, the relative angle between the displacement vector and the minor axis of the noise ellipse remains constant. This can be seen from the fact that time evolution of the squeezed coherent state $|\alpha(t), \xi(t)\rangle$ has the form[57]

$$|\alpha(t), \xi(t)\rangle = e^{-\frac{1}{2}i\omega t}\left|\alpha(0)e^{-i\omega t}, \xi(0)e^{-2i\omega t}\right\rangle. \tag{2.145}$$

Since $\varphi(t)$ evolves as $\varphi - 2\omega t$, the minor/major axes rotate as $e^{-i\omega t}$ which is the same rate as the amplitude rotation. The time evolution of the electric field in the X quadrature is shown at the bottom of figure 2.4 for both states. Since $|\alpha| \neq 0$, the mean electric field also oscillates between a maximum and a minimum along with its variance. Here we take the amplitude of the coherent squeezed states to be aligned with the X quadrature at $t = 0$. For the optical state in figure 2.4A, the minor axis of the noise ellipse is in the direction of the amplitude. It leads to a lower amplitude noise and a higher phase noise in the electric field during time evolution. The condition is reversed for the state shown in 2.4B as the minor axis in now aligned with the out-of-phase Y quadrature. For this reason, these states are often referred to as amplitude-squeezed and phase-squeezed coherent states, respectively.

We now introduce the two-mode squeezed states (TMSS) of light that are generated, like the single mode squeezed states discussed above, via non-linear interactions between light and matter. In

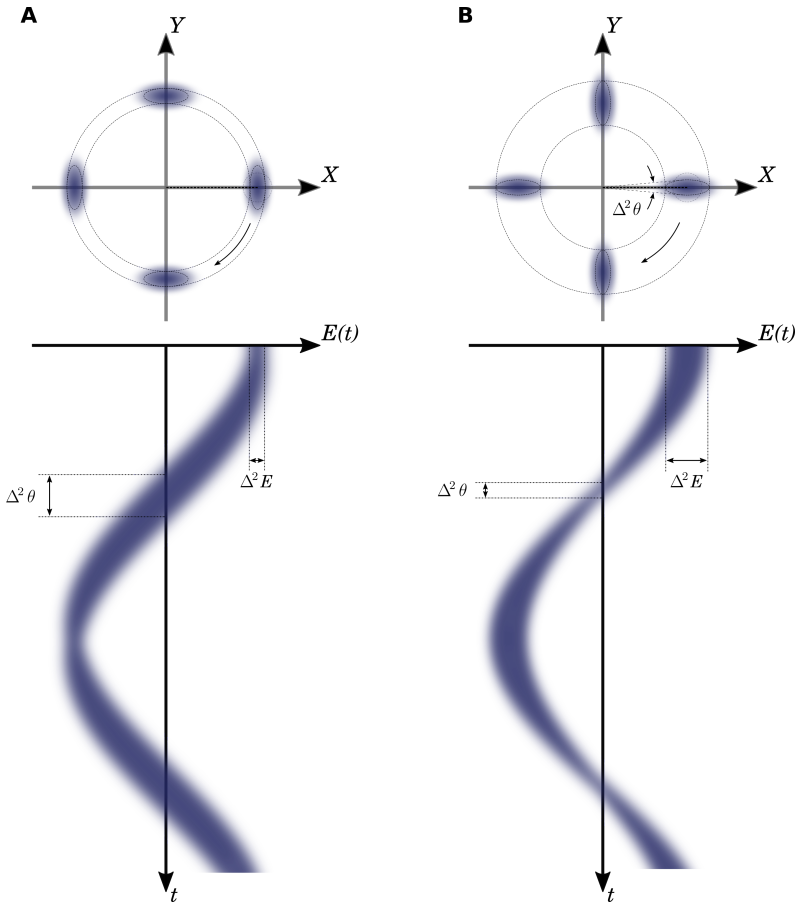

Figure 2.4: Phase space representations of squeezed coherent states and their time evolution. (A) A squeezed coherent state with non-zero amplitude and squeezing along the X quadrature. The electric field along the X quadrature is shown in the bottom figure. During the time evolution, the noise ellipse rotates around the origin while maintaining its orientation with respect to the displacement vector (represented using a dashed line). Since the minor axis of the ellipse is aligned with the amplitude direction, we see less amplitude noise in the electric field. (B) Phase space distribution of a squeezed coherent state with squeezing along the Y quadrature. Although, the time evolution is similar to the state in (A), the orientation of the noise ellipse leads to higher amplitude noise and lower phase noise in the electric field (compared to a coherent state with the same amplitude). A dashed circle in the background in (A) and (B) represents a variance equal to the vacuum state (i.e. SNL).

the case of non-degenerate spontaneous parametric down-conversion (SPDC) and FWM, a discussion of TMSS naturally leads to the idea of entanglement between the two modes of light involved in the non-linear process. In this dissertation, we denote these modes as 'a' and 'b' with the commutation relations between corresponding operators given as

$$[\hat{a}, \hat{a}^\dagger] = [\hat{b}, \hat{b}^\dagger] = \hat{\mathbb{I}}, \tag{2.146}$$

$$[\hat{a}, \hat{b}] = [\hat{a}, \hat{b}^\dagger] = 0. \tag{2.147}$$

The non-degeneracy in the modes can be either in terms of frequency (the signal and idler modes in type-I SPDC or the probe and conjugate modes in FWM) or polarization (as in type-II SPDC). Mathematically, a two-mode squeezed state $|\xi_{ab}\rangle$ is generated by applying the two mode squeezing

operator $\hat{S}_{ab}(\xi)$ on a two-mode vacuum state $|0_a\rangle\,|0_b\rangle$ as

$$|\xi_{ab}\rangle = \hat{S}_{ab}(\xi)\,|0,0\rangle \tag{2.148}$$

$$= e^{(\xi\hat{a}^\dagger\hat{b}^\dagger - \xi^*\hat{a}\hat{b})}\,|0,0\rangle\,, \tag{2.149}$$

where $|0,0\rangle \equiv |0_a\rangle\,|0_b\rangle$. As before, we solve for $|\xi_{ab}\rangle$

$$|\xi_{ab}\rangle = \hat{S}_{ab}(\xi)\,|0,0\rangle \tag{2.150}$$

$$= \exp\Big(e^{i\varphi}\tanh r\;\hat{a}^\dagger\hat{b}^\dagger\Big)\exp\Big[-(\ln\cosh r)(\hat{a}^\dagger\hat{a}+\hat{b}^\dagger\hat{b}+\hat{\mathbb{I}})\Big]\exp\Big(-e^{i\varphi}\tanh r\;\hat{a}\hat{b}\Big)\,|0,0\rangle \tag{2.151}$$

$$= \frac{1}{\cosh r}\exp\Big(e^{i\varphi}\tanh r\;\hat{a}^\dagger\hat{b}^\dagger\Big) \tag{2.152}$$

$$= \frac{1}{\cosh r}\sum_{n=0}^{\infty} e^{in\varphi}\tanh^n r\,|n,n\rangle\,, \tag{2.153}$$

where we have used the BCH-theorem for the SU(1,1) group[58,59] in (2.151). The probability p_{mn} of finding m photons in mode a and n photons in mode b is

$$p_{mn} = \delta_{nm}\frac{\tanh^{2n} r}{\cosh^2 r}. \tag{2.154}$$

This implies that if we find k photons in one of the modes then the other mode also must have k photons and points to perfect photon correlations between the two modes. The photon correlations can be used for 'heralding' specific number of photons in one of the modes based on the detection of photons in the other mode. In practice, two-mode squeezed states, with an optimized generation of the two-photon state $|1,1\rangle$, have been used as heralded single-photon sources[60,61].

To see the photon statistics of the individual modes and the amount of correlation between them, we consider how $\hat{a}$ and $\hat{b}$ change under the action of the two mode squeezing operator (via the two-mode Bogoliubov transformations). For the sake of clarity, we define

$$\hat{a}(\xi) \equiv \hat{S}^\dagger_{ab}(\xi)\,\hat{a}\,\hat{S}_{ab}(\xi), \qquad \hat{b}(\xi) \equiv \hat{S}^\dagger_{ab}(\xi)\,\hat{b}\,\hat{S}_{ab}(\xi), \tag{2.155}$$

$$\hat{a}^\dagger(\xi) \equiv \hat{S}^\dagger_{ab}(\xi)\,\hat{a}^\dagger\,\hat{S}_{ab}(\xi), \qquad \hat{b}^\dagger(\xi) \equiv \hat{S}^\dagger_{ab}(\xi)\,\hat{b}^\dagger\,\hat{S}_{ab}(\xi). \tag{2.156}$$

The two-mode Bogoliubov transformations for these operators are

$$\hat{a}(\xi) = \hat{a}\cosh r + \hat{b}^\dagger\,e^{i\varphi}\sinh r, \tag{2.157}$$

$$\hat{a}^\dagger(\xi) = \hat{a}^\dagger\cosh r + \hat{b}\,e^{-i\varphi}\sinh r, \tag{2.158}$$

$$\hat{b}(\xi) = \hat{b}\cosh r + \hat{a}^\dagger\,e^{i\varphi}\sinh r, \tag{2.159}$$

$$\hat{b}^\dagger(\xi) = \hat{b}^\dagger\cosh r + \hat{a}\,e^{-i\varphi}\sinh r. \tag{2.160}$$

As a result of the two-mode squeezing interaction, the mean photon number in both the modes is non-zero as

$$\langle\hat{a}^\dagger\hat{a}\rangle_{|\xi_{ab}\rangle} = \langle\hat{b}^\dagger\hat{b}\rangle_{|\xi_{ab}\rangle} = \sinh^2 r. \tag{2.161}$$

However, the mean values of the X and Y quadrature of each mode are zero[6], i.e.

$$\langle \hat{X}_a \rangle_{|\xi_{ab}\rangle} = \langle \hat{Y}_a \rangle_{|\xi_{ab}\rangle} = 0. \tag{2.162}$$

The quadrature variances in each mode are larger than the SNL, i.e.

$$\langle \Delta^2 \hat{X}_{a/b} \rangle_{|\xi_{ab}\rangle} = \langle \Delta^2 \hat{Y}_{a/b} \rangle_{|\xi_{ab}\rangle} = \frac{1}{2} + \sinh^2 r. \tag{2.163}$$

The amount of correlation between the modes a and b is

$$\langle \hat{a}\hat{b} \rangle_{|\xi_{ab}\rangle} = \cosh r \sinh r \, e^{i\varphi}, \tag{2.164}$$

which is non-zero for $r > 0$. This non-zero correlation leads to non-classical properties of the TMSS as well as entanglement between the two modes[55]. To show the squeezing behavior of the TMSS, we begin by considering joint quadratures between modes a and b. We define

$$\hat{X}_\pm = \frac{\hat{X}_a \pm \hat{X}_b}{\sqrt{2}}, \tag{2.165}$$

$$\hat{Y}_\pm = \frac{\hat{Y}_a \pm \hat{Y}_b}{\sqrt{2}}. \tag{2.166}$$

and evaluate the change in the variance of these quadratures as a result of the two-mode squeezing. Prior to squeezing, the joint state was a two-mode vacuum state $|0,0\rangle$. Hence,

$$\langle \Delta^2 \hat{X}_\pm \rangle_{|0,0\rangle} = \langle \Delta^2 \hat{Y}_\pm \rangle_{|0,0\rangle} = \frac{1}{2}, \tag{2.167}$$

which is expected. We now evaluate the joint quadrature variances for a two-mode squeezed state.

In order to simplify the calculations, we assume the phase $\varphi = 0$ which makes ξ a real number. However, this assumption does not change the nature of quantum correlation between the two modes. First, we evaluate

$$\langle \Delta^2 \hat{X}_- \rangle_{|\xi_{ab}\rangle} = \langle \xi_{ab}|\hat{X}_-^2|\xi_{ab}\rangle - \langle \xi_{ab}|\hat{X}_a|\xi_{ab}\rangle^2 \tag{2.168}$$

$$= \langle \hat{S}_{ab}^\dagger(\xi)\, \hat{X}_-^2\, \hat{S}_{ab}(\xi) \rangle_{|0,0\rangle} \tag{2.169}$$

$$= \left\langle \left(\hat{S}_{ab}^\dagger(\xi)\, \hat{X}_-\, \hat{S}_{ab}(\xi) \right)^2 \right\rangle_{|0,0\rangle} \tag{2.170}$$

$$= \langle \hat{X}_-^2(\xi) \rangle_{|0,0\rangle}, \tag{2.171}$$

where $\hat{X}_-(\xi) = \hat{S}_{ab}^\dagger(\xi)\, \hat{X}_-\, \hat{S}_{ab}(\xi)$. In (2.170), we used the fact that $\hat{S}_{ab}(\xi)$ is a unitary operator. To

[6] Notice that we evolve the operators using the Heisenberg picture to simplify calculations, i.e.

$$\langle \hat{X}_a \rangle_{|\xi_{ab}\rangle} = \langle \xi_{ab}|\hat{X}_a|\xi_{ab}\rangle = \langle 0,0|\hat{X}_a(\xi)|0,0\rangle = \langle \hat{X}_a(\xi) \rangle_{|0,0\rangle},$$

where $\hat{X}(\xi_{ab}) = \hat{S}_{ab}^\dagger(\xi)\, \hat{X}\, \hat{S}_{ab}(\xi)$.

evaluate $\hat{X}_-(\xi_{ab})$, we use the two-mode Bogoliubov transformations (2.157-2.160) as

$$\hat{X}_-(\xi) = \hat{S}^\dagger_{ab}(\xi)\left(\frac{\hat{X}_a - \hat{X}_b}{\sqrt{2}}\right)\hat{S}_{ab}(\xi), \tag{2.172}$$

$$= \hat{S}^\dagger_{ab}(\xi)\left(\frac{\hat{a}+\hat{a}^\dagger-\hat{b}-\hat{b}^\dagger}{2}\right)\hat{S}_{ab}(\xi) \tag{2.173}$$

$$= \frac{\hat{a}(\xi)+\hat{a}^\dagger(\xi)-\hat{b}(\xi)-\hat{b}^\dagger(\xi)}{2} \tag{2.174}$$

$$= \frac{1}{2}\left[\cosh r\,(\hat{a}+\hat{a}^\dagger)+\sinh r\,(\hat{b}+\hat{b}^\dagger)-\cosh r\,(\hat{b}+\hat{b}^\dagger)-\sinh r\,(\hat{a}+\hat{a}^\dagger)\right] \tag{2.175}$$

$$= \frac{1}{2}\left[e^{-r}\,(\hat{a}+\hat{a}^\dagger)-e^{-r}\,(\hat{b}+\hat{b}^\dagger)\right] \tag{2.176}$$

$$= e^{-r}\left[\frac{\hat{a}+\hat{a}^\dagger-\hat{b}+\hat{b}^\dagger}{2}\right] \tag{2.177}$$

$$= e^{-r}\hat{X}_-. \tag{2.178}$$

Using the above result in (2.171), we get

$$\langle\Delta^2\hat{X}_-\rangle_{|\xi_{ab}\rangle} = e^{-2r}\langle\hat{X}_-^2\rangle_{|0,0\rangle} \tag{2.179}$$

$$= \frac{1}{2}e^{-2r}, \tag{2.180}$$

which implies that the joint quadrature X_- in $|\xi_{ab}\rangle$ is squeezed. This result along with the variances of the all other joint quadratures can be summarized as

$$\langle\Delta^2\hat{X}_\pm\rangle_{|\xi_{ab}\rangle} = \frac{1}{2}e^{\pm 2r}, \qquad \langle\Delta^2\hat{Y}_\pm\rangle_{|\xi_{ab}\rangle} = \frac{1}{2}e^{\mp 2r}. \tag{2.181}$$

Therefore, for $\varphi = 0$, a TMSS exhibits squeezing in 'amplitude-difference' and 'phase-sum' quadratures while the 'amplitude-sum' and 'phase-difference' quadratures are anti-squeezed. Figure 2.5 shows the phase space representation of a two mode squeezed state corresponding to $\varphi = 0$. The individual a and b modes, shown in figures 2.5A and 2.5B, respectively, are thermal (and have $Q_M > 1$) with quadrature variances greater than the SNL. However, in phase space of joint X and Y quadratures, we see variance below the SNL in X_- and Y_+ as shown in figures 2.5C and 2.5D. Such a reduction of noise in the joint quadratures is also sufficient to show EPR entanglement [62–64] (for a pure state) and inseparability [65] (via DGCZ criterion) between the quadratures of modes a and b. We provide a detailed discussion on the EPR entanglement criterion in chapter 4 that relies on reduced variances in the joint variables.

The fundamental nature of two-mode squeezing remains the same for non-zero values of φ. This can be seen if we rewrite the $\hat{S}_{ab}$ as

$$\hat{S}_{ab}(\xi) = \exp\left(\xi\hat{a}^\dagger\hat{b}^\dagger - \xi^*\hat{a}\hat{b}\right) \tag{2.182}$$

$$= \exp\left(\frac{\xi^*}{2}\hat{c}^2 - \frac{\xi}{2}\hat{c}^{\dagger 2}\right)\exp\left(-\frac{\xi^*}{2}\hat{d}^2 + \frac{\xi}{2}\hat{d}^{\dagger 2}\right), \tag{2.183}$$

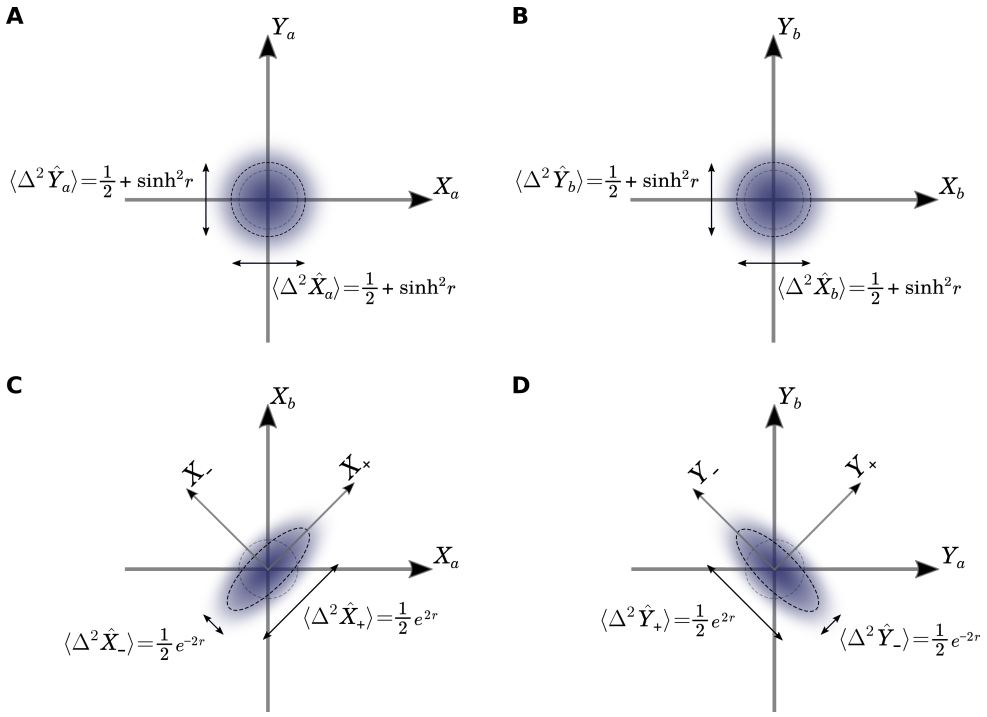

Figure 2.5: Phase space representations of a two-mode squeezed state with $\varphi = 0$. (A) and (B) show the distribution of modes a and b in their corresponding phase space. Both modes individually have higher variance in quadratures than the vacuum state. The noise distribution, however, is the same in all directions (radially symmetric). (C) and (D) show the same state in phase space corresponding to joint quadratures of X and Y, respectively. In this representation, we find $|\xi_{ab}\rangle$ to be squeezed along the amplitude-difference (X_-) and phase-sum (Y_+) quadratures. A dashed circle in the background in all figures represents variance equal to the SNL.

where $\xi = re^{i\varphi}$, $\hat{c} = (\hat{a} - \hat{b})/2$ and $\hat{d} = (\hat{a} + \hat{b})/2$. One can show that the first and second operators in (2.183) lead to squeezing (anti-squeezing) along $X_{-,\theta_s}(Y_{-,\theta_s})$ and $Y_{+,\theta_s}(X_{+,\theta_s})$ quadratures where $\theta_s = \varphi/2$.

One can also generate two-mode squeezed states in which the mean amplitude of each mode is non-zero. These two-mode squeezed coherent states, denoted as $|\alpha, \beta; \xi_{ab}\rangle$, can be generated by displacing the two-mode squeezed state as

$$|\alpha, \beta; \xi_{ab}\rangle = \hat{D}_a(\alpha)\hat{D}_b(\beta)\,|\xi_{ab}\rangle \tag{2.184}$$

$$= \hat{D}_a(\alpha)\hat{D}_b(\beta)\hat{S}_{ab}\,|0,0\rangle\,, \tag{2.185}$$

$$\tag{2.186}$$

where $\hat{D}_a(\alpha)$ and $\hat{D}_b(\beta)$ are the displacement operators acing on modes a and b, respectively. Some of the relevant expectation values and properties of $|\alpha, \beta; \xi_{ab}\rangle$ are

$$\langle\hat{a}\rangle = \alpha, \qquad \langle\hat{b}\rangle = \beta, \tag{2.187}$$

$$\langle\hat{a}^\dagger\hat{a}\rangle = |\alpha|^2 + \sinh^2 r, \qquad \langle\hat{b}^\dagger\hat{b}\rangle = |\beta|^2 + \sinh^2 r, \tag{2.188}$$

$$\langle\hat{a}^2\rangle = \alpha^2, \qquad \langle\hat{b}^2\rangle = \beta^2. \tag{2.189}$$

If modes a and b contain large number of photons, the state $|\alpha, \beta; \xi_{ab}\rangle$ is often referred as the bright two-mode squeezed state (BTMSS). The relevant correlation properties between the bright

two modes are

$$\langle \hat{a}^\dagger \hat{b} \rangle = \alpha^* \beta, \qquad \langle \hat{b}^\dagger \hat{a} \rangle = \beta^* \alpha, \tag{2.190}$$

$$\langle \hat{a}\hat{b} \rangle = \langle \hat{b}\hat{a} \rangle = \alpha\beta + e^{i\varphi} \sinh r \cosh r. \tag{2.191}$$

Here all the expectation values in (2.187-2.191) are taken with respect to the $|\alpha, \beta; \xi_{ab}\rangle$ state.

CHAPTER 3

Generation and Measurement of Squeezed Light

The generation as well as characterization of squeezed states of light is, at present, of high interest because of their low noise and entanglement properties. A most notable use of the low noise aspects of vacuum squeezed states is in the gravitational interferometers[52] such as the Advanced-LIGO interferometers[23], VIRGO[66] and Geo600[24]. Similarly, the shared quantum correlations between the modes of a TMSS are being utilised in upcoming technological applications such as quantum sensing[67–69], quantum communication[6,70,71] and quantum computation[72,73]. Historically, after the development of the quantum theory of optical coherence in the 1960s by Glauber, Cahill, Sudarshan and others[37], a detailed mathematical formalism of the squeezed states of light as 'an equivalence class of minimum-uncertainty states' was given by Stoler[74,75]. Later, Yuen[76] and Caves[77] realized their potential for useful applications such as noiseless amplification and quantum-enhanced interferometry.

The first experimental observation of squeezed states of light was by Slusher *et al.*[27] at AT&T Bell Labs in 1985. They used a sodium atomic vapor as a non-linear medium to implement a non-degenerate FWM process. This was followed by the generation of single mode squeezed light using a non-linear MgO:$LiNbO_3$ crystal in an optical parametric oscillator (OPO) by Wu *et al.*[78] in 1986. Since then, continuous improvements in efficient detectors with low-noise electronics and higher quality optics has led to observation of squeezing up to 9 dB using atomic vapors, 7 dB using non-linear optical fibers[79] and 15 dB using non-linear crystals[80]. The two-mode squeezed states discussed in this dissertation, are generated using the non-linearity in atomic ^{85}Rb vapor. This chapter will provide the essential details of the non-linear FWM process that is used to generate a BTMSS consisting of bright probe and conjugate 'twin beams', followed by the measurement techniques used to help verify and optimize the quantum correlations in these twin beams.

3.1 Non-linear Optical Processes

In chapter 2, we mentioned that the two-mode squeezed states of light are generated via certain non-linear interactions between light and matter that lead to pairwise photon creation as well as entanglement in the two modes. In order to see how a non-linear interaction may lead to photon generation at new frequencies, we first study the electric response of a medium in the presence of external electric fields within the framework of classical optics.

When an external electric field is applied on a medium, the charge distribution inside becomes distorted, i.e. the medium acquires an electric dipole moment. This electric response or polarization

$P(\boldsymbol{r},t)$ of a medium, defined as the amount of dipole moment per unit volume, can expanded as a power series in terms of the electric field

$$P(\boldsymbol{r},t) = \varepsilon_0 \left[\chi^{(1)}E(\boldsymbol{r},t) + \chi^{(2)}E^2(\boldsymbol{r},t) + \chi^{(3)}E^3(\boldsymbol{r},t) + \dots\right], \tag{3.1}$$

$$= P^{(1)}(\boldsymbol{r},t) + P^{(2)}(\boldsymbol{r},t) + P^{(3)}(\boldsymbol{r},t) + \dots \tag{3.2}$$

$$= P^{(1)}(\boldsymbol{r},t) + P^{(\mathrm{NL})}(\boldsymbol{r},t)\ , \tag{3.3}$$

where $\chi^{(n)}$ is the nth order non-linear susceptibility of the medium. $P^{(1)}(\boldsymbol{r}) = \varepsilon_0\chi^{(1)}E(\boldsymbol{r},t)$ is the linear response of the medium and is responsible for absorption, refraction and transmission of the medium and $P^{(\mathrm{NL})}(\boldsymbol{r},t)$ refers to the higher order terms that are dependent on the quadratic or higher powers of the electric field. Working with Maxwell's equations in media, one can obtain the following wave equation[81]

$$\nabla^2 E(\boldsymbol{r},t) - \frac{1}{c^2}\frac{\partial^2 E(\boldsymbol{r},t)}{\partial t^2} = \frac{1}{\varepsilon_0 c^2}\frac{\partial^2 P(\boldsymbol{r},t)}{\partial t^2}. \tag{3.4}$$

Substituting (3.3) in (3.4), we get

$$\nabla^2 E(\boldsymbol{r},t) - \frac{1}{c^2}\frac{\partial^2 E(\boldsymbol{r},t)}{\partial t^2} = \frac{1}{\varepsilon_0 c^2}\frac{\partial^2}{\partial t^2}\left(P^{(1)}(\boldsymbol{r},t) + P^{(\mathrm{NL})}(\boldsymbol{r},t)\right) \tag{3.5}$$

$$\Rightarrow \quad \nabla^2 E(\boldsymbol{r},t) - \frac{(1+\chi^{(1)})}{c^2}\frac{\partial^2 E(\boldsymbol{r},t)}{\partial t^2} = \frac{1}{\varepsilon_0 c^2}\frac{\partial^2 P^{(\mathrm{NL})}(\boldsymbol{r},t)}{\partial t^2} \tag{3.6}$$

$$\Rightarrow \quad \nabla^2 E(\boldsymbol{r},t) - \frac{n^2}{c^2}\frac{\partial^2 E(\boldsymbol{r},t)}{\partial t^2} = \frac{1}{\varepsilon_0 c^2}\frac{\partial^2 P^{(\mathrm{NL})}(\boldsymbol{r},t)}{\partial t^2}, \tag{3.7}$$

where $\varepsilon_r = (1+\chi^{(1)})$ and $n^2 = \varepsilon_r\mu_r$. Here, we have assumed the magnetic response of the medium to be the same as vacuum, i.e. $\mu_r = 1$. The final differential equation obtained in (3.7), is an inhomogeneous wave equation with the right hand side term given by $P^{(\mathrm{NL})}(\boldsymbol{r},t)$ acting as source term. Since $P^{(\mathrm{NL})}$ contains higher order electric field terms, it can generate new frequencies via the non-linear interaction depending on the input frequencies and the non-linear response of the medium.

For example, consider an input electric field that is the sum of electric fields at two different frequencies, incident on a $\chi^{(2)}$ medium as

$$E(t) = (E_p\, e^{-i\omega_p t} + c.c.) + (E_s\, e^{-i\omega_s t} + c.c.), \tag{3.8}$$

where E_p and E_s are the complex amplitudes of the fields at frequencies ω_p and ω_s, respectively. Here, we ignore the spatial dependence of the fields for simplicity. Considering $\chi^{(2)}$ non-linearity of the medium, the second order non-linear response $P^{(2)}(t)$ has the form

$$P^{(2)}(t) = \chi^{(2)}E^2(t) \tag{3.9}$$

$$= \varepsilon_0\chi^{(2)}\left[E_p^2\, e^{-2i\omega_p t} + E_s^2\, e^{-2i\omega_s t} + 2E_pE_s e^{-i(\omega_p+\omega_s)t} + \underline{2E_pE_s^* e^{-i(\omega_p-\omega_s)t}} + c.c.\right]$$
$$+ 2\varepsilon_0\chi^{(2)}\left[|E_p|^2 + |E_s|^2\right], \tag{3.10}$$

where the term *c.c.* in (3.10) implies complex conjugate of all the previous terms. All the terms in the expression for $P^{(2)}(t)$ describe a physical process including the second harmonic generation at

$2\omega_p$ and $2\omega_s$, and sum frequency generation at $\omega_p + \omega_s$. The underlined term in (3.10) represents the down-conversion process in which the field at the difference frequency $\omega_i = \omega_p - \omega_s$ is generated. As the E_p field propagates through the non-linear medium, it can then amplify the field at ω_s in the presence of generated frequency ω_i. In other words, a $\chi^{(2)}$ medium can generate a field at a new frequency as well as amplify an input 'seed' at ω_s in the presence of a third (E_p) field at ω_p. Such frequency down-conversion ($\omega_i, \omega_s < \omega_p$) process is known stimulated parametric down-conversion (PDC). Here, we see that even from the perspective of classical optics, non-linear interactions are valuable as they can generate optical fields at new frequencies. The down-conversion process, however, can still occur even in the absence of any seed field at ω_s. From the quantum description of light given in chapter 2, we concluded that even in the absence of any field excitations (i.e. photons), the vacuum field fluctuations are present at all the frequencies. These fluctuating fields can themselves act as seed to generate photons at new frequencies[82,83]. Such a 'vacuum stimulated' process is known spontaneous parametric down-conversion (SPDC). The PDC process is often implemented in non-centrosymmetric crystals (no inversion symmetry) that have a non-zero $\chi^{(2)}$ susceptibility. Some of the non-linear crystals with a large $\chi^{(2)}$ are β-barium borate (BBO), potassium titanyl phosphate (KTP) and lithium niobate ($LiNbO_3$).

After reviewing how non-linear interactions generate new fields by frequency- or wave-mixing in classical non-linear optics, we can now connect them to the generation of photon pairs in the quantum picture. Recall that the two-mode squeezing operator we introduced in chapter 2 has the form

$$\hat{S}(\xi) = \exp\left(\xi\, \hat{a}^\dagger \hat{b}^\dagger - \xi^* \hat{a}\hat{b}\right), \tag{3.11}$$

where $\xi = re^{i\varphi}$ is a complex parameter, $\hat{a}$, $\hat{b}$ are the annihilation operators for modes a and b, respectively. Since the squeezing operator is unitary, it can be recast in the following form as a time evolution operator

$$\hat{S}(\xi) = \exp\left(-\frac{i}{\hbar}\hat{\mathcal{H}}\, t\right), \tag{3.12}$$

where

$$\hat{\mathcal{H}} = i\hbar g\, (e^{i\varphi}\hat{a}^\dagger \hat{b}^\dagger) + H.c. \quad \text{and} \quad gt = r. \tag{3.13}$$

In other words, the squeezing operation $\hat{S}(\xi)$ can be realized by the Hamiltonian given in (3.13). As can be seen via the form of the Hamiltonian, it denotes a non-linear interaction which leads to photon pair generation (and annihilation) for the modes a and b. For the process of SPDC mentioned above, the constant g which denotes the strength of the interaction, is proportional to[31]

$$g \propto \chi^{(2)}\, E_p, \tag{3.14}$$

which is in agreement with the classical picture described in (3.10). Here, E_p denotes the amplitude of the pump beam, from which the pair of photons are generated (or decay into). Figure 3.1A depicts the quantum picture of the SPDC process in a $\chi^{(2)}$ medium along with the corresponding energy conversion in the optical fields, shown in figures 3.1B. In SPDC, a pump photon at frequency ω_p interacting with the $\chi^{(2)}$ non-linear medium splits into two photons at much lower frequencies, and hence, the name 'down-conversion'. These new photons, known as signal and idler photons,

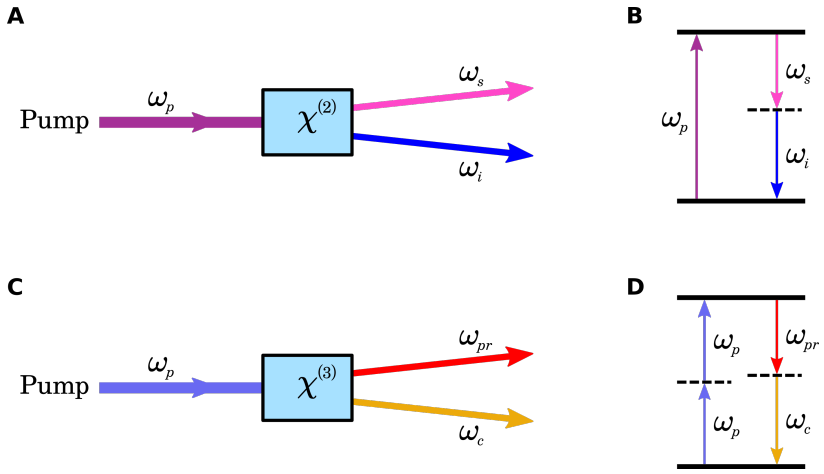

Figure 3.1: Physical processes involving $\chi^{(2)}$ and $\chi^{(3)}$ non-linear susceptibilities. (A) and (B) give schematic diagrams representing SPDC and FWM processes with (B) and (D) as their corresponding energy level diagrams, respectively. During SPDC, a $\chi^{(2)}$ process, a photon at pump frequency ω_p is converted into a pair of photons at frequencies ω_s and ω_i while, in FWM, two pump photons are simultaneously converted into a pair of photons at ω_{pr} and ω_c via the $\chi^{(3)}$ non-linearity of the medium. Both, SPDC and FWM are parametric processes which implies that total energy in the optical field before and after the process is conserved.

have frequencies ω_s and ω_i, respectively, such that $\hbar\omega_p = \hbar\omega_s + \hbar\omega_i$. This is similar to the process of FWM, shown in figure 3.1C and 3.1D, where two pump photons at ω_p are simultaneously converted into a pair of probe and conjugate photons at ω_{pr} and ω_c, respectively, inside a $\chi^{(3)}$ non-linear medium such that $2\hbar\omega_p = \hbar\omega_{pr} + \hbar\omega_c$. For the FWM process, the interaction Hamiltonian has the same form given in (3.13) with g proportional to[81]

$$g \propto \chi^{(3)} E_p^2. \tag{3.15}$$

For a high-intensity coherent pump field, the intensity of the pump remain unchanged during the propagation through the non-linear media. Therefore, the pump field acts as a reservoir of photons and can be treated as a classical field in the interaction Hamiltonian.

3.2 Two-mode Squeezing via Four-wave Mixing

The two-mode squeezed states of light, which are central to the main theme of this dissertation, are generated using FWM in hot atomic Rb vapor. In general, atomic vapors as non-linear media, unlike certain crystals, are fundamentally centrosymmetric (i.e. have inversion symmetry). As a result of which, all the even order susceptibilities $\chi^{(2n)}$ are zero. This can be seen using (3.9), as under inversion symmetry we have

$$\begin{aligned} -P^{(2)}(t) &= \chi^{(2)}[-E(t)]^2 && (3.16)\\ &= \chi^{(2)}[E(t)]^2 && (3.17)\\ &= P^{(2)}(t), && (3.18) \end{aligned}$$

which implies $\chi^{(2)} = 0$. Hence, atomic vapors have the lowest order of non-linearity given by the $\chi^{(3)}$ susceptibility. As we mentioned in the previous section, the $\chi^{(3)}$ susceptibility is responsible

for the FWM process inside a non-linear media. In this section, we will describe why the field interactions during the FWM process, mediated via $\chi^{(3)}$, have an interaction Hamiltonian given by (3.13).

The pump, probe and conjugate electric fields inside the atomic non-linear medium must satisfy the wave equation derived in the previous section

$$\nabla^2 E(\boldsymbol{r},t) - \frac{n^2}{c^2}\frac{\partial^2 E(\boldsymbol{r},t)}{\partial t^2} = \frac{1}{\varepsilon_0 c^2}\frac{\partial^2 P^{(\mathrm{NL})}(\boldsymbol{r},t)}{\partial t^2}, \tag{3.19}$$

To look at the behavior of each (pump, probe and conjugate) frequency component, we write the respective electric field as

$$E_n(\boldsymbol{r},t) = A_n(z)e^{ik_n z}e^{-i\omega_n t} \tag{3.20}$$

where the subscript $n = \{p, pr, c\}$ for the pump, probe and conjugate fields, respectively. Here, we take the fields to be propagating along the z-direction inside the non-linear medium with A_n as the complex amplitude. Under the slowly varying amplitude approximation

$$\left|\frac{d^2}{dz^2}A_n(z)\right| \ll \left|k_n\frac{dA_n(z)}{dz}\right|, \qquad \text{for all } n, \tag{3.21}$$

which implies that the fractional change in A_n over a λ distance is much smaller than unity, the wave equation for the field at ω_n takes the following simpler form

$$\frac{d}{dz}A_n(z) = i\frac{\omega_n}{2\varepsilon_0 n_n c}P_n e^{-ik_n z}. \tag{3.22}$$

where P_n is the non-linear response of the medium at frequency ω_n. For the FWM process, P_n has the form[81]

$$P_n \equiv P(\omega_n = \omega_i + \omega_j - \omega_k) = 6\chi^{(3)}(\omega_n = \omega_i + \omega_j - \omega_k)A_i(z)A_j(z)A_k^*(z)\, e^{i(k_i+k_j-k_k)z}. \tag{3.23}$$

Here, the pump field is accounted twice which is expected as the FWM process involves two pump photons[1]. Using (3.23) in (3.22) with the condition of co-propagating beams, the probe and the conjugate fields in FWM are characterized by the following coupled first-order differential equations

$$\frac{d}{dz}A_{pr}(z) = i\frac{3\,\omega_{pr}\chi^{(3)}_{pr}}{\varepsilon_0 n_{pr} c}A_p^2\, A_c^*(z)\, e^{i\Delta k z}, \tag{3.28}$$

$$\frac{d}{dz}A_c(z) = i\frac{3\,\omega_c\chi^{(3)}_{c}}{\varepsilon_0 n_{c} c}A_p^2\, A_{pr}^*(z)\, e^{i\Delta k z}. \tag{3.29}$$

[1]Explicitly, the four cases of ω_n are

$$\omega_{p_1} = \omega_{pr} + \omega_c - \omega_{p_2} \tag{3.24}$$

$$\omega_{p_2} = \omega_{pr} + \omega_c - \omega_{p_1} \tag{3.25}$$

$$\omega_{pr} = \omega_{p_1} + \omega_{p_2} - \omega_c \tag{3.26}$$

$$\omega_c = \omega_{p_1} + \omega_{p_2} - \omega_{pr}. \tag{3.27}$$

In the case where the two pump photons are degenerate, we have $\omega_{p_1} = \omega_{p_2} = \omega_p$.

Here we have assumed the pump field to remain undepleted which implies $\frac{d}{dz}A_p(z) = 0$. The quantity Δk is the wave vector mismatch or the phase mismatch in the fields. For an efficient generation of fields at new frequencies in the non-linear process, the phase matching condition, $\Delta k = 0$, must be satisfied. We can now introduce the quantum picture in a phenomenological way by replacing the probe and conjugate amplitudes with the corresponding operators[84] as

$$A_{pr}(z) \rightarrow \hat{a}(z), \tag{3.30}$$

$$A_c(z) \rightarrow \hat{b}(z). \tag{3.31}$$

Using the above substitutions in (3.28) and (3.29), we get

$$\frac{d}{dz}\hat{a}(z) = i\eta_{pr}\,\hat{b}^\dagger(z), \tag{3.32}$$

$$\frac{d}{dz}\hat{b}(z) = i\eta_{c}\,\hat{a}^\dagger(z), \tag{3.33}$$

where

$$\eta_{pr} = \frac{3\,\omega_{pr}\chi^{(3)}_{pr}}{\varepsilon_0 n_{pr} c}A_p^2\,e^{i\Delta kz}, \tag{3.34}$$

$$\eta_{c} = \frac{3\,\omega_{c}\chi^{(3)}_{c}}{\varepsilon_0 n_{c} c}A_p^2\,e^{i\Delta kz}. \tag{3.35}$$

In the limit of $\eta_{pr} = \eta_c = \eta$, the solution to (3.32) and (3.33) has the familiar form of

$$\hat{a}(z) = \hat{a}\cosh(|\eta|z) + \hat{b}^\dagger\,e^{i\zeta}\sinh(|\eta|z) = \hat{S}^\dagger_{ab}(\eta z)\,\hat{a}\,\hat{S}_{ab}(\eta z), \tag{3.36}$$

$$\hat{b}(z) = \hat{b}\cosh(|\eta|z) + \hat{a}^\dagger\,e^{i\zeta}\sinh(|\eta|z) = \hat{S}^\dagger_{ab}(\eta z)\,\hat{b}\,\hat{S}_{ab}(\eta z), \tag{3.37}$$

where $\eta = |\eta|e^{i\zeta}$, $\hat{a} \equiv \hat{a}(0)$ and $\hat{b} \equiv \hat{b}(0)$. These are the Bogoliubov transformations introduced

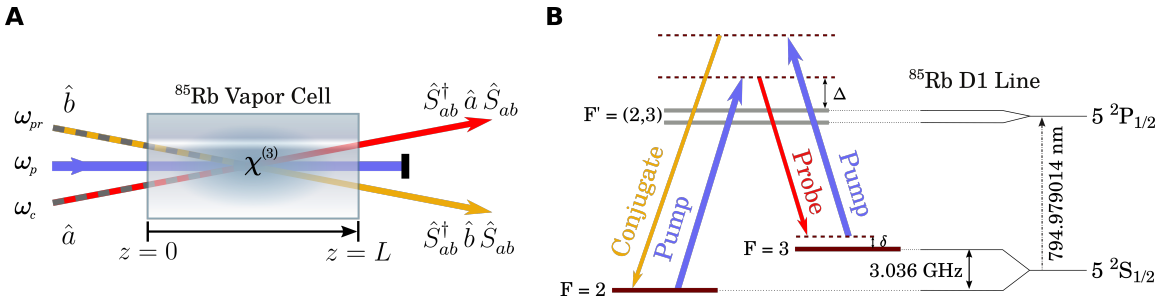

Figure 3.2: Generation of quantum-correlated probe and conjugate fields via FWM in Rb vapor. (A) The probe ($\hat{a}$) and conjugate ($\hat{b}$) modes, which can be vacuum modes before the medium (represented with dashed lines), are transformed into a two-mode squeezed state via the process of FWM inside the Rb vapor cell. (B) The $\chi^{(3)}$ non-linearity is achieved by tuning the relevant optical fields (in a stimulated FWM process, input probe and conjugate fields can have non-zero amplitudes) near the D1 line in ^{85}Rb. Due to the parametric nature of the process, the total energy of the optical fields is conserved which can be seen using the closed form of the double-Λ configuration. The detuning of the pump from the F=2 $\rightarrow$ F'=3 transition is the single photon detuning (Δ) and the two-photon detuning (δ) is given by $\delta = \omega_p - \omega_{pr} - \omega_{\rm HF}$, where $\omega_{\rm HF} = 3.036$ GHz is the hyperfine splitting of the ground state in ^{85}Rb.

in chapter 2 for two-mode squeezed states with corresponding two-mode squeezing operator and Hamiltonian as

$$\hat{S}_{ab}(\xi) = \exp\left(z\eta\,\hat{a}^\dagger\hat{b}^\dagger - z\eta^*\hat{a}\hat{b}\right), \tag{3.38}$$

$$\hat{\mathcal{H}} = i\hbar g'\left(e^{i\zeta}\hat{a}^\dagger\hat{b}^\dagger\right) + H.c., \tag{3.39}$$

where $g't = |\eta|z$. With the substitution of $\eta z = \xi$, these operators are the same as (3.11) and (3.13), respectively. Also, the strength of the interaction g' for the Hamiltonian in (3.39) has the form

$$g' \propto \eta \propto \chi^{(3)}A_p^2. \tag{3.40}$$

The form of the Hamiltonian implies that, via the $\chi^{(3)}$ non-linearity, the FWM process generates two-mode squeezing and entanglement between the probe ($\hat{a}$) and conjugate ($\hat{b}$) modes. Figure 3.2A depicts the generation of quantum-correlated probe and conjugate modes at the frequencies ω_{pr} and ω_c respectively, using a hot ^{85}Rb vapor as a $\chi^{(3)}$ non-linear medium. The $\chi^{(3)}$ non-linearity of Rb vapor is due to the interaction of optical fields with the D1-transition shown in figure 3.2B. The double-Λ configuration of the optical fields conserves the total energy in the optical fields and the destruction of two pump photons is related to a simultaneous creation of a probe and a conjugate photons as a quantum-correlated pair. In this double-Λ configuration, the single photon detuning (Δ) is the detuning of the pump from the F=2 $\rightarrow$ F'=3 transition while the two-photon detuning (δ) is given by $\delta = \omega_p - \omega_{pr} - \omega_{\mathrm{HF}}$, where ω_{HF} is the hyperfine splitting of the ground state in ^{85}Rb as shown in figure 3.2B.

The configuration shown in figure 3.2 is a non-collinear FWM configuration, which implies that the emission of probe and conjugate happens at an angle with respect to the pump beam. This is due to a change in the effective phase-matching condition between the optical field in the presence of a dispersive medium. In the absence of any dispersive effects or refractive index changes, the phase-

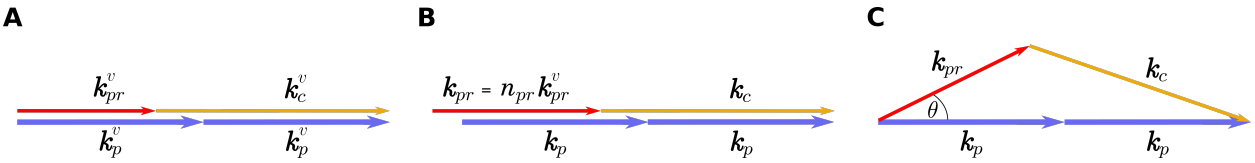

Figure 3.3: Phase-matching condition in the optical fields during a FWM process. (A) The phase-matching for the pump, probe and conjugate fields in free-space. (B) The dispersive effects of the Rb vapor leads to a phase-mismatch between the k-vectors of the fields for the collinear configuration. The effective refractive index n_{pr} for the probe field is larger than 1 for experimentally relevant single and two-photon detunings. The k-vectors of the other fields remain unaffected. (C) The phase-matching condition is restored in the non-collinear configuration of FWM, for a small angle ($\theta \simeq 0.4^\circ$) between the pump and probe k-vectors.

matching condition of the pump, probe and conjugate fields (propagating along the z-direction) is the same as in free space or vacuum which satisfies $\Delta k^v = 2k_p^v - k_{pr}^v - k_c^v = 0$ with $k^v = |\boldsymbol{k}|^v$, as shown in figure 3.3A. Here the superscript 'v' stands for vacuum. In the presence of Rb vapor, the probe field experiences an effective change in the index of refraction with $n_{pr} > 1$ near the optimal two-photon detunings[85]. This leads to a phase-mismatch between the collinearly propagating fields (see figure 3.3B). However, the phase-matching condition is satisfied for a non-collinear configuration shown in figure 3.3C. We use this non-collinear configure with a pump-probe relative angle $\theta \simeq 0.4^\circ$ which has the natural advantage of physical separation between probe and conjugate photons after the cell (due to the slightly different propagation directions). On a microscopic level, i.e. ignoring

the phase accumulation due to propagation through the non-linear medium, the phase-matching condition can be seen as momentum conservation in the optical fields. Due to the parametric nature of the FWM process, the momentum of the pump, probe and conjugate photons must satisfy

$$2\hbar\boldsymbol{k}_p = \hbar\boldsymbol{k}_{pr} + \hbar\boldsymbol{k}_c, \tag{3.41}$$

inside the non-linear medium. Changes in the effective k-vectors due to refractive index changes, therefore, lead to the open-angle (non-collinear) configuration shown in figure 3.3C. Depending on the overall phase-matching over the length of the medium (i.e. Rb vapor cell), the FWM process generates probe and conjugate field within a narrow angular width ($\delta\theta$) which defines the emission angular bandwidth of the process. Hence, the phase-matching condition also governs the spatial distribution of the generated photons for the probe and the conjugate fields. We provide a detailed discussion of the connection between the phase-matching condition and the transverse spatial correlations of photons generated in FWM in chapter 4.

3.3 Measurement of Noise Properties

For an accurate characterization, entanglement verification as well as optimization of the squeezed states generated in FWM, we also need measurement techniques to assess the relevant noise properties. Based on our discussion of the TMSS so far, we saw that individually the probe and conjugate fields have thermal photon statistics, and certain joint quadratures (amplitude difference X_- and phase sum Y_+) have reduced noise. Additionally, due to the pairwise photon generation in the probe and conjugate fields, observables related to the intensity correlations between the two fields can reveal non-classical noise statistics. The measurement reduced noise in the intensity-difference (ID) photocurrent is one of the simplest yet useful method to verify quantum-correlations in twin beams. In this section, we provide details on the ID measurement followed by a brief discussion of the homodyne technique for quadrature noise measurements using bright coherent states as local oscillators.

In our experiments, we work in the bright regime of the FWM process in which the generated bright probe and conjugate beams contain large numbers of correlated photons. To achieve this, we align a weak coherent seed beam with a strong (high intensity) pump beam in the non-collinear configuration shown in figure 3.4. The FWM process amplifies the seed beam into a bright probe beam in addition to generating a bright correlated conjugate beam. We refer to these bright probe and conjugate beams as the 'bright twin beams'. To detect the intensity correlations using an ID

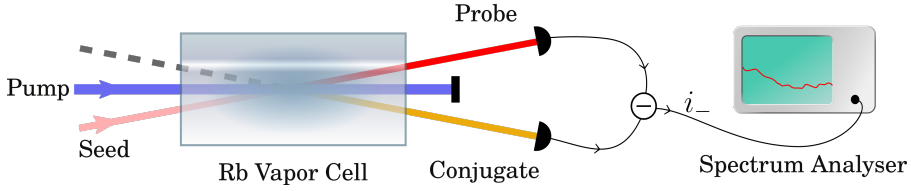

Figure 3.4: ID measurement for the bright twin beams. We seed the probe field to generate bright probe and conjugate twin beams in the FWM process. To measure quantum-correlations between the probe and conjugate photons, we detect each beam with a photodetector and subtract the resulting photocurrents. The noise of the subtracted photocurrent is proportional to the intensity difference noise between the two beams. With the subtracted photocurrent as input to the spectrum analyzer, a noise power spectrum lower than the SNL verifies the non-classical nature of bright twin beams.

measurement (see figure 3.4), each bright beam is detected using an independent photodetector after the Rb vapor cell. Each photodetector produces a photocurrent proportional to the intensity of the detected field and the resulting photocurrents are then electronically subtracted. The ID photocurrent is fed into a spectrum analyzer which gives a real-time noise power spectrum of the input signal. For an ideal measurement (no losses, ideal detection bandwidth and linear response), the observable corresponding to the ID photocurrent has the form

$$i_- \propto \langle \hat{n}_{pr} - \hat{n}_c \rangle, \tag{3.42}$$

$$\Delta^2 i_- \propto \langle \Delta^2 (\hat{n}_{pr} - \hat{n}_c) \rangle. \tag{3.43}$$

To calculate these expectation values, we first note that for a bright twin beam state $|\xi_{ab}; \alpha_a, \beta_b\rangle$, we have

$$|\xi_{ab}; \alpha_a, \beta_b\rangle = \hat{S}_{ab}(\xi)\hat{D}_a(\alpha)\hat{D}_b(\beta)\,|0,0\rangle\,, \tag{3.44}$$

$$\langle \xi_{ab}; \alpha_a, \beta_b|\ \hat{O}\ |\xi_{ab}; \alpha_a, \beta_b\rangle = \langle 0,0|\,\hat{D}_b^\dagger(\beta)\hat{D}_a^\dagger(\alpha)\hat{S}_{ab}^\dagger(\xi)\,\hat{O}\,\hat{S}_{ab}(\xi)\hat{D}_a(\alpha)\hat{D}_b(\beta)\,|0,0\rangle\,, \tag{3.45}$$

where $\hat{O}$ is an arbitrary operator. For the configuration of the FWM in which seeding happens only at the probe frequency, we have $\alpha_a = \alpha$ and $\beta_b = 0$. Using these parameters, the photon occupancy in the probe and the conjugate bright beams and corresponding variances can be evaluated to be

$$\langle \hat{n}_{pr} \rangle = |\alpha|^2 \cosh^2 r + \sinh^2 r \tag{3.46}$$

$$\langle \hat{n}_c \rangle = |\alpha|^2 \sinh^2 r + \sinh^2 r, \tag{3.47}$$

$$\langle \Delta^2 \hat{n}_{pr} \rangle = |\alpha|^2 \cosh^2 r \left[\cosh^2 r + \sinh^2 r\right] + \sinh^2 r \cosh^2 r, \tag{3.48}$$

$$\langle \Delta^2 \hat{n}_c \rangle = |\alpha|^2 \sinh^2 r \left[\cosh^2 r + \sinh^2 r\right] + \sinh^2 r \cosh^2 r \tag{3.49}$$

where all the expectation values are taken with respect to the $|\xi_{ab}; \alpha, 0\rangle$ state. In our experiments, the number of photons in the seed beam is much larger than the spontaneously generated photons, i.e. $|\alpha|^2 \gg \sinh^2 r$. Therefore, we can omit the second terms in all (3.46-3.49) expressions. Similarly, one can evaluate the covariance between $\hat{n}_{pr}$ and $\hat{n}_c$ for the bright twin beam state as

$$\mathrm{Cov}(\hat{n}_{pr}, \hat{n}_c) = \langle \hat{n}_{pr}\hat{n}_c \rangle_{|\xi_{ab};\alpha,0\rangle} - \langle \hat{n}_{pr} \rangle_{|\xi_{ab};\alpha,0\rangle} \langle \hat{n}_c \rangle_{|\xi_{ab};\alpha,0\rangle} \tag{3.50}$$

$$= 2\,|\alpha|^2 \cosh^2 r\, \sinh^2 r. \tag{3.51}$$

Using the expressions (3.46-3.51) in (3.43), we get

$$\Delta^2 i_- \propto \langle \Delta^2 (\hat{n}_{pr} - \hat{n}_c) \rangle_{|\xi_{ab};\alpha,0\rangle} \tag{3.52}$$

$$= \langle \Delta^2 \hat{n}_{pr} \rangle_{|\xi_{ab};\alpha,0\rangle} + \langle \Delta^2 \hat{n}_c \rangle_{|\xi_{ab};\alpha,0\rangle} - 2\mathrm{Cov}(\hat{n}_{pr}, \hat{n}_c) \tag{3.53}$$

$$= |\alpha|^2. \tag{3.54}$$

This implies that the noise present in the intensity difference of the bright twin beams only comes from the input seed beam. To see that such a behavior points to quantum-correlations between the twin beam photons, we replace the bright twin beams with equivalent power coherent states and repeat the ID measurement. For the corresponding coherent state, the variance is equal to the average number of photons. Therefore, we have

$$\left(\Delta^2 i_-\right)_{\mathrm{CS}} \propto \langle \hat{n}_{pr} \rangle + \langle \hat{n}_c \rangle \tag{3.55}$$

$$= |\alpha|^2 (\cosh^2 r + \sinh^2 r). \tag{3.56}$$

Taking the ratio of the two ID measurements, we get

$$s_{\text{ID}} \equiv \frac{\Delta^2 i_-}{(\Delta^2 i_-)_{\text{CS}}} \tag{3.57}$$

$$= \frac{1}{\cosh^2 r + \sinh^2 r}, \tag{3.58}$$

where the subscript CS stands for equivalent coherent state. In other words, the intensity difference squeezing s_{ID} (< 1, for $r > 0$) is related to the joint-quadrature squeezing ($s = \frac{1}{2}e^{-2r}$) for an ideal FWM process (no losses) via the squeeze parameter r. By monitoring $\Delta^2 i_-$ with a spectrum analyzer, we optimized the FWM process as well as verify quantum correlations in the bright twin beams while the noise power spectrum for $\left(\Delta^2 i_-\right)_{\text{CS}}$ measurement provides the SNL. Another parameter we monitor to characterize the FWM is the gain G (defined as the ratio of output and input optical powers) of the probe beam which is equal to $\cosh^2 r$. In terms of the G parameter, we have

$$s_{\text{ID}} = \frac{1}{2G - 1}, \tag{3.59}$$

which is less than one for $G > 1$.

An ID measurement is relatively simple to implement in the lab but is unable to select between different quadratures of the state due to its phase-insensitivity. In order to obtain more detailed information on a given quantum state, such as quadrature entanglement, one of the standard technique is the homodyne detection (HD). It is a phase-sensitive technique that is able to measure noise in any given quadrature and, therefore, is sufficient for full state tomography in most cases[86–88]. In a typical balanced HD setup, the quantum optical state $\hat{E}_{in}$ is combined with a high intensity coherent state, commonly referred to as the local oscillator $\hat{E}_{LO}$, using a 50-50 beam splitter. The two output fields from the beam splitter are then detected using separate photodetectors. We can express the field operators for the incident fields (see figure 3.5B) as

$$\hat{E}_{in}(t) = \mathscr{E}_{in}(\hat{a}_{in}\, e^{-i\omega t} + \hat{a}^\dagger_{in}\, e^{i\omega t}), \tag{3.60}$$

$$\hat{E}_{LO}(t) = \mathscr{E}_{LO}(\hat{a}_{LO}\, e^{-i\omega t} e^{i\phi} + \hat{a}^\dagger_{LO}\, e^{i\omega t} e^{-i\phi}). \tag{3.61}$$

Here ϕ is the phase of the local oscillator which can be controlled independent of the input quantum state to be measured. Note that in a homodyne measurement, the frequency of the local oscillator is matched with the frequency of the input optical state. In order to see what is measured using the detectors at the output ports, we first look at how a beam splitter transforms the input fields.

In the quantum mechanical description of a beam splitter, the input field operators $\hat{u}_1$ and $\hat{u}_2$ are transformed as

$$\begin{pmatrix} \hat{v}_1 \\ \hat{v}_2 \end{pmatrix} = \quad U_{\text{BS}} \quad \begin{pmatrix} \hat{u}_1 \\ \hat{u}_2 \end{pmatrix} \tag{3.62}$$

$$= \begin{pmatrix} t_1 & r_2 \\ r_1 & t_2 \end{pmatrix} \begin{pmatrix} \hat{u}_1 \\ \hat{u}_2 \end{pmatrix}, \tag{3.63}$$

where $\hat{v}_1$, $\hat{v}_2$ are the operator corresponding to the output fields (see figure 3.5A). The transmission and reflection amplitudes of the two sides of the beam splitter are denoted by t_i and r_i, $i = \{1, 2\}$ respectively. The matrix U is a unitary matrix which is equivalent to

$$|t_1|^2 + |r_1|^2 = |t_2|^2 + |r_2|^2 = 1 \quad \text{and} \quad t_1^* r_2 + r_1^* t_2 = 0. \tag{3.64}$$

3.3 Measurement of Noise Properties

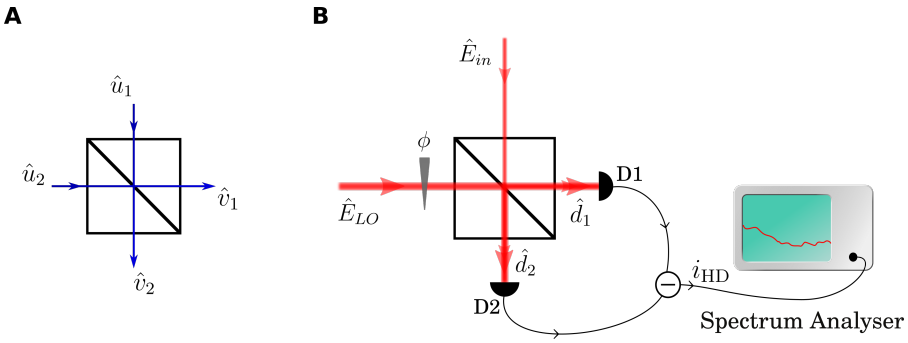

Figure 3.5: Beam splitter in the quantum picture and HD for a quantum optical state. (A) In the quantum picture, a beam splitter transforms the input field operators $\hat{u}_1$ and $\hat{u}_2$ into output field operators $\hat{v}_1$ and $\hat{v}_2$ via a unitary matrix. In the classical picture, beam splitter transformations do not always preserve commutation relations in the field operators. (B) In balanced HD, the input optical state is combined with a strong local oscillator using a 50-50 beam splitter. The two output fields are detected with photodetectors and the subtracted photocurrent i_{HD} is analyzed in terms of spectral noise power. The variance of the i_{HD} is proportional to the variance in the input state quadrature selected using local oscillator phase ϕ.

For a 50-50 beam splitter, U_{BS} has a form equivalent to

$$U_{\mathrm{BS}} = \frac{1}{\sqrt{2}} \begin{pmatrix} 1 & i \\ i & 1 \end{pmatrix}, \tag{3.65}$$

which gives

$$\hat{v}_1 = \hat{u}_1 + i\hat{u}_2 \quad \text{and} \quad \hat{v}_1 = \hat{u}_2 + i\hat{u}_1. \tag{3.66}$$

Using these relations, we evaluate the operators $\hat{d}_1$ and $\hat{d}_2$ corresponding to the field incident on detectors D1 and D2 as

$$\hat{d}_1(t) = \hat{E}^+_{in}(t) + i\hat{E}^+_{LO}(t) \tag{3.67}$$

$$= (\mathscr{E}_{in}\hat{a}_{in} + i\,\mathscr{E}_{LO}\hat{a}_{LO}e^{i\phi})e^{-i\omega t}, \tag{3.68}$$

$$\hat{d}_2(t) = \hat{E}^+_{LO}(t) + i\hat{E}^+_{in}(t) \tag{3.69}$$

$$= (\mathscr{E}_{LO}\hat{a}_{LO} + i\,\mathscr{E}_{in}\hat{a}_{in}e^{i\phi})e^{-i\omega t}. \tag{3.70}$$

Here we only focus on the positive frequency parts of the field operators because only they take part in the detection at the photodetector[36]. After the detection of these fields, we subtract the resulting photocurrents electronically to get i_{HD}, which is proportional to the intensity difference of the two output arms (see figure 3.5B). Using the expressions (3.67-3.70), the i_{HD} has the form

$$i_{\mathrm{HD}} \propto \langle \hat{n}_{\mathrm{D1}} - \hat{n}_{\mathrm{D2}} \rangle \tag{3.71}$$

$$= \langle \hat{d}_1^\dagger \hat{d}_1 - \hat{d}_2^\dagger \hat{d}_2 \rangle \tag{3.72}$$

$$= i \left\langle \hat{E}^{+\dagger}_{in}\hat{E}^+_{LO} - \hat{E}^{+\dagger}_{LO}\hat{E}^+_{in} \right\rangle \tag{3.73}$$

$$= -i \left\langle \mathscr{E}_{in}\hat{a}_{in}\, e^{-i\phi}\, \mathscr{E}_{LO}\hat{a}^\dagger_{LO} - \mathscr{E}_{in}\hat{a}^\dagger_{in}\, e^{i\phi}\, \mathscr{E}_{LO}\hat{a}_{LO} \right\rangle \tag{3.74}$$

$$= -i\,|\alpha_{LO}|\,\mathscr{E}_{in}\langle \hat{a}_{in}\, e^{-i\phi} - \hat{a}^\dagger_{in}\, e^{i\phi} \rangle \tag{3.75}$$

$$= \sqrt{2}\,|\alpha_{LO}|\,\mathscr{E}_{in}\langle \hat{Y}_\phi \rangle, \tag{3.76}$$

where Y_ϕ is a generalized quadrature of the input quantum state. Here, we take the local oscillator to be classical, i.e. $\mathscr{E}_{LO}\hat{a}_{LO}\, e^{-i\phi} = \alpha_{LO}$, in the limit of a high intensity field $\mathscr{E}_{LO} \gg \mathscr{E}_{in}$. Similarly, we have

$$\Delta^2 i_{\mathrm{HD}} \propto \langle \Delta^2(\hat{n}_{\mathrm{D1}} - \hat{n}_{\mathrm{D2}})\rangle \tag{3.77}$$

$$= 2\,|\alpha_{LO}|^2\, \mathscr{E}_{in}^2 \langle \Delta^2 \hat{Y}_\phi \rangle. \tag{3.78}$$

Since Y_ϕ is a generalized quadrature, one can access all other quadratures via a suitable change in the local oscillator phase ϕ. The above expression shows that the variance of i_{HD} photocurrent in a balanced homodyne detection gives the variance of Y_ϕ quadrature and, therefore, is usually fed to a spectrum analyser for the noise power spectrum as shown in figure 3.5B. For the shot noise calibration, the input quantum state is replaced with an equivalent power coherent state.

From the discussion above, we see that the balanced HD will be sufficient for experimental characterization of a single mode squeezed state. In order to see joint quadrature squeezing in twin beam states where the probe and conjugate modes are at different frequencies, one can use the HD detection method with bichromatic local oscillators. In this detection scheme, individual probe and conjugate field quadratures are measured simultaneously with two separate local oscillators (at matching frequencies) via balanced HD. The resulting photocurrents $i_{\mathrm{HD,pr}}$ and $i_{\mathrm{HD,c}}$ are subtracted and the noise in the resulting photocurrent gives information regarding the variance in the joint quadratures. The formal analysis of this method as well as the experimental implementation can be found in refs[89–91].

CHAPTER 4

Spatial Properties of Twin Beams Generated in FWM

The FWM process conserves the energy and momentum between the input and output fields given the parametric nature of the non-linear process. The energy conservation leads to temporal correlations between the probe and conjugate field quadratures (i.e. joint quadrature squeezing). Equivalently, the temporal correlations are also manifested in the generation of photon pairs at the probe and conjugate frequencies[1]. In addition to the quantum correlations in the temporal domain, the twin beams also exhibit spatial quantum correlations in the position and momentum variables of the probe and conjugate photons. An exploration of these spatial correlations is the main theme of this dissertation. As we mentioned in chapter 1, the use of spatial quantum correlations can lead to advancements in quantum imaging[9] (including recording and read-out of spatial patterns beyond the limits set by the shot noise) as well as an increase in sensing and information sharing capacity of quantum networks via spatial mode multiplexing[92].

In this chapter, we will lay out the main concepts to understand and analyze these spatial correlations. We will start with a more detailed discussion on the phase-matching condition along the z-direction as well as the momentum conservation in the transverse plane (plane $\perp$ to the beam propagation) between the input and output optical fields. After developing a simple physical picture

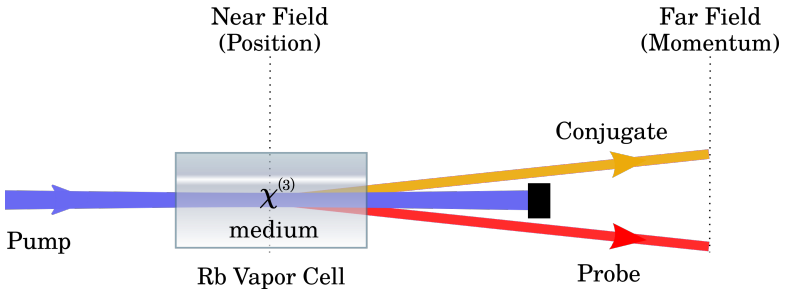

Figure 4.1: Schematic setup for the FWM process. The input pump beam interacts with a $\chi^{(3)}$ non-linear medium composed of Rb atoms to generate probe and conjugate fields. As the probe and conjugate photons are generated together at the same spatial location in the cell, the corresponding fields share position correlations that are revealed in the near field measurements. The generated fields also share momentum correlations due to momentum conservation that are then converted into position (anti-)correlations in the far field via field propagation. In the regime of a large pump size (specifically, Rayleigh range much larger than the Rb cell length), the far field correlations mainly depend on the pump properties while the near field correlations are dominated by spatial bandwidth of the FWM process (related to the inverse of the range of angles over which probe and conjugate photons are emitted).

[1] Similar conclusions are valid for the signal and idler fields generated in a SPDC process (see chapter 3).

regarding the origin of the transverse position and momentum correlations between the generated fields in the near and the far field (see figure 4.1), respectively, along with their dependence on various parameters in a FWM process, we provide a detailed derivation of algebraic expressions for the interaction Hamiltonian and the corresponding FWM two-photon amplitude in the later sections.

4.1 Pump Momentum and Far Field Correlations

During the FWM process, the sum of two input pump photon momenta is equal to the combined momentum of the probe and the conjugate photons following the momentum conservation. In our experiments, the configuration of the FWM process is such that the two pump photons come from a single pump field. Inside the non-linear medium, a field photon with k-vector given as $\boldsymbol{k}$ has momentum equal to $\hbar\boldsymbol{k}$. Expressing the momentum conservation in terms of k-vectors gives $2\boldsymbol{k}_p = \boldsymbol{k}_{pr} + \boldsymbol{k}_c$, where the subscripts p, pr and c stand for the pump, probe and conjugate fields, respectively. To intuitively understand the connection between pump momentum and the nature

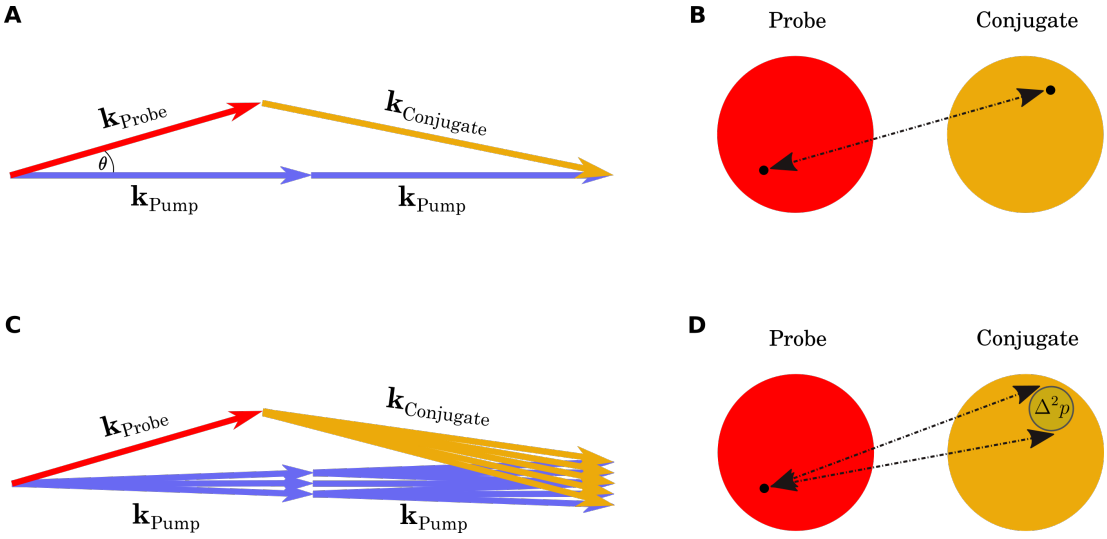

Figure 4.2: Effect of the pump momentum distribution on the far field correlations. (A) For a plane-wave pump (δ-function k-distribution), a given k-vector for the probe is correlated to a single k-vector in the conjugate beam. This leads to point-to-point correlations (B) in the far field. The correlated points are diametrically opposite in the transverse plane (i.e. the plane $\perp$ to pump propagation or the z-direction). This is due to the fact that at the time of generation (in the near field), the probe and conjugate transverse k-vectors are anti-parallel. (C) A broadening in the pump angular spectrum, i.e. a Gaussian distribution, results in one probe k-vector to be correlated with many conjugate k-vectors that give a point-to-area correlation (D) in the far field. Since the conjugate photon can be present anywhere inside the coherence area, the corresponding (conditional) transverse momentum variance is denoted as $\Delta^2 p$.

of far field spatial correlations, first assume a plane-wave pump with δ-function angular spectrum. The angular spectrum of an optical field is given by its transverse k-vector content which ultimately affects the field's angular spread (with respect to the propagation direction) during propagation[2]. Momentum conservation dictates that a pair of pump photons with precisely known k-vectors (δ-function angular spectrum) would generate a pair of probe and conjugate photons with a narrow

[2]We will provide a precise mathematical definition of angular spectrum in section 4.3.

relative angular spectrum. In other words, for a conditional measurement, a given k-vector in the probe will be correlated with only one conjugate k-vector as shown in figure 4.2A. In the case of a non-collinear FWM, the corresponding probe and conjugate photons will then propagate away from the pump beam with their transverse k-vectors oriented in opposite directions (see figure 4.2A). As the generated probe and conjugate fields propagate from the cell position (near field) to the far field, the momentum distribution is mapped to the equivalent position distribution in which a single (transverse) k-vector corresponds to a single point in the far field. Therefore, a point in the probe beam will be correlated to only a single point in the conjugate beam in the far field for a δ-function angular spectrum pump (figure 4.2B). Following this argument, one can subsequently infer that any broadening in the pump angular spectrum (e.g. a Gaussian beam) would lead to a similar spread in far field spatial correlations changing it from a point-to-point to a point-to-area correlation as shown in figures 4.2C and 4.2D. In terms of conditional measurements, the distribution of spatial correlations in the far field gives information about the relative momentum distribution of photons in one of the beams conditioned upon measuring photons with a specific momentum value in the other beam. For a Gaussian pump beam, spatial correlations between the twin beams in the far field have been experimentally shown to exhibit quantum statistics[93,94] within a finite localized region that is often referred to as the 'coherence area'.

4.2 Longitudinal Phase Matching and Near Field Correlations

The position or near field correlations (see figure 4.1) between the probe and the conjugate fields are dependent on the FWM process happening at the Rb vapor cell. Here, the probe and the conjugate photons are generated in close vicinity of each other, and therefore, if the probe photon is detected at a specific location in the near field, the correlated conjugate photon must be present within a small region, known as the 'near field coherence area', around it. An analogous term is the 'biphoton birth zone', defined as the small region inside which twin beam photons are likely to be found (hence, defined in terms of the coincident photon measurements), and is related to the conditional measurement concept of coherence area[95].

To further comment on what determines the size of the coherence area in the near field, we explore the range of angles (between pump-probe k-vectors) over which the phase matching condition is satisfied. For a set of given (fixed) k-vectors for the pump, probe and conjugate fields, a specific angle between the pump and the probe k-vectors leads to an optimal phase matching condition, i.e. $\Delta\boldsymbol{k} = 2\boldsymbol{k}_p - \boldsymbol{k}_{pr} - \boldsymbol{k}_c = 0$ (see figure 4.2A). This condition is known as the perfect phase matching condition during which the generated probe and conjugate fields maintain a fixed phase relation with respect to the pump field (or, equivalently, the non-linear polarization of the medium) and their intensities increase exponentially with the propagation distance[81]. However, the FWM process can also occur with slightly lower efficiency for different pump-probe angles such that

$$\left| e^{i\Delta k_z L} \right| \sim 1. \tag{4.1}$$

where L is the length of the non-linear medium. This implies that there is a finite range of angles for which the FWM phase matching condition is approximately satisfied. Figure 4.3A shows such a scenario where probe k-vectors with different pump-probe angles can participate in the FWM process. The angular bandwidth (or the range of angles) is directly proportional to the range of allowed transverse k-vectors and, as we will show in the following section 4.3, can be quantified using phase mismatch Δk_z along the longitudinal direction. In terms of the conditional measurements,

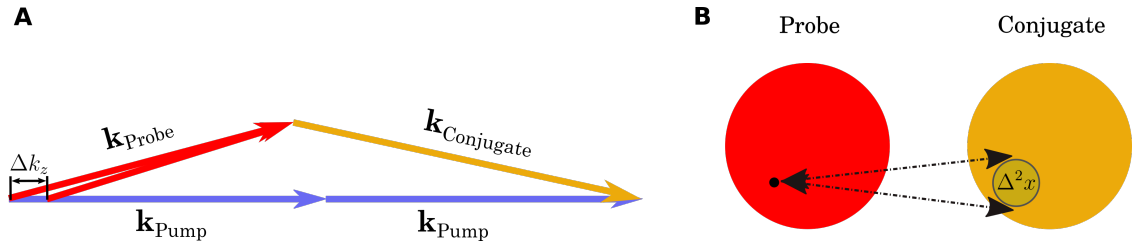

Figure 4.3: Effect of the angular bandwidth of phase matching condition on the near field correlations. (A) The correlated probe and conjugate fields can be generated for a range of pump-probe angles for which the phase matching condition is approximately satisfied. The range of angles corresponds to the uncertainty in the transverse k-vectors (for the probe field) allowed by the process. (B) As the photons are generated in close vicinity, the near field correlations are present in the same part of the probe and conjugate beams. The detection of probe at one point in the near field is correlated with arrival of a conjugate photon over a large area. Here, in the near field, the probe and conjugate beams are shown to be separate for clarity but in experiment, these beams overlap with each other.

we see that a measurement of multiple transverse k-vectors (transverse momentum uncertainty) in the probe field is correlated with the measurement of a single transverse k-vector in the conjugate field. Since the transverse momentum and position variables are related by a Fourier transform, the detection of a probe photon at a given location (hence, large transverse momentum uncertainty) is correlated to the arrival of conjugate photon over a wider area (rather precise k-vector) as shown in figure 4.3B.

4.3 FWM Hamiltonian in Spatial Variables

To develop an analytical expression for the dependence of the spatial correlations between the twin beams on the angular spectrum of the pump as well as the longitudinal phase-matching bandwidth, we need to work with the interaction Hamiltonian of the FWM process expressed in terms of the spatial variables. Here, we start with the following interaction Hamiltonian [31,96],

$$\hat{\mathcal{H}} = i\hbar \int d\boldsymbol{r}\, \chi^{(3)}(\boldsymbol{r}) \hat{E}_p^{(+)}(\boldsymbol{r},t) \hat{E}_p^{(+)}(\boldsymbol{r},t) \hat{E}_{pr}^{(-)}(\boldsymbol{r},t) \hat{E}_c^{(-)}(\boldsymbol{r},t) + H.c.\,, \tag{4.2}$$

where $\chi^{(3)}$ is the third-order susceptibility of the atomic media and $\hat{E}^{(+)}/\hat{E}^{(-)}$ are the positive/negative frequency parts of the electric field operator (see chapter 2 and 3). We here assume that the two required pump photons originate from a single pump field as mentioned earlier. Using the undepleted pump approximation [95], the pump field can be treated as a classical field. This assumption is valid for our experiments as the pump beam with high optical power ($\sim 2\,\text{W}$) essentially acts as a reservoir for probe and conjugate photons ($\sim \mu\text{W}$). As a very small number of pump photons are converted into probe and conjugate photons, the FWM process does not affect the statistics of the pump beam.

If we take the pump to be propagating along the (longitudinal) z-direction, it can be written as

$$E_p^{+}(\boldsymbol{r},t) = E_o(\boldsymbol{\rho},z) e^{i\left(k_p^z z - \omega_p t\right)}, \tag{4.3}$$

where k_p^z denotes the z-component of the pump's k-vector, ω_p is the pump frequency and $\boldsymbol{\rho}$ is the two-dimensional position in the transverse plane at the center of the nonlinear medium. $E_o(\boldsymbol{\rho},z)$

is a complex function representing the slowly varying envelope[3] of the pump's electric field. The waist of the pump is placed at the center of the $\chi^{(3)}$ nonlinear medium (atomic vapor cell) and its transverse spatial distribution is assumed to remain unchanged throughout the length of the nonlinear medium. This assumption is also valid for our experiment, since the Rayleigh range of the pump beam (∼20 m) used is much larger than the length of the Rb cell (12.7 cm). As a result, the slowly varying field envelope is assumed to be independent of z, i.e. $E_o(\boldsymbol{\rho}, z) = E_o(\boldsymbol{\rho})$.

A momentum space (k-space) representation of the field probe and conjugate operators has the form[97]

$$\hat{E}^-_{pr}(\boldsymbol{r}, t) = \left(\frac{1}{2\pi}\right)^{3/2} \int d\boldsymbol{k}_{pr}\, e^{-i(\boldsymbol{k}_{pr}\cdot\boldsymbol{r}-\omega_{pr}t)} \hat{a}^\dagger_{\boldsymbol{k}_{pr}}, \tag{4.4}$$

$$\hat{E}^-_{c}(\boldsymbol{r}, t) = \left(\frac{1}{2\pi}\right)^{3/2} \int d\boldsymbol{k}_{c}\, e^{-i(\boldsymbol{k}_{c}\cdot\boldsymbol{r}-\omega_{c}t)} \hat{b}^\dagger_{\boldsymbol{k}_{c}}, \tag{4.5}$$

where $\hat{a}^\dagger_{\boldsymbol{k}_{pr}}$ ($\hat{b}^\dagger_{\boldsymbol{k}_c}$) is the creation operator for a probe (conjugate) photon with a spatial profile given by a plane wave with $\hbar\boldsymbol{k}$ momentum. Using (4.3), (4.4) and (4.5), the FWM interaction Hamiltonian can be rewritten as

$$\begin{aligned}
\hat{\mathcal{H}} &= i\hbar \left(\frac{1}{2\pi}\right)^3 \iiint d\boldsymbol{r}\, d\boldsymbol{k}_{pr}\, d\boldsymbol{k}_c\, \chi^{(3)}(\boldsymbol{r}) E_o^2(\boldsymbol{\rho}) e^{2i\left(k_p^z z-\omega_p t\right)} e^{-i(\boldsymbol{k}_{pr}\cdot\boldsymbol{r}-\omega_{pr}t)} e^{-i(\boldsymbol{k}_c\cdot\boldsymbol{r}-\omega_c t)} \hat{a}^\dagger_{\boldsymbol{k}_{pr}} \hat{b}^\dagger_{\boldsymbol{k}_c} + H.c. \\
&= i\hbar \left(\frac{1}{2\pi}\right)^3 \iiint d\boldsymbol{r}\, d\boldsymbol{k}_{pr}\, d\boldsymbol{k}_c\, \chi^{(3)}(\boldsymbol{r}) E_o^2(\boldsymbol{\rho})\, e^{i\left(2k_p^z z-\boldsymbol{k}_{pr}\cdot\boldsymbol{r}-\boldsymbol{k}_c\cdot\boldsymbol{r}\right)} e^{-i(2\omega_p-\omega_{pr}-\omega_c)t}\, \hat{a}^\dagger_{\boldsymbol{k}_{pr}} \hat{b}^\dagger_{\boldsymbol{k}_c} + H.c. \\
&= i\hbar\,\Gamma \iiint d\boldsymbol{r}\, d\boldsymbol{k}_{pr}\, d\boldsymbol{k}_c\, E_o^2(\boldsymbol{\rho})\, e^{-i(\boldsymbol{q}_{pr}+\boldsymbol{q}_c)\cdot\boldsymbol{\rho}} e^{i\Delta k_z z} \hat{a}^\dagger_{\boldsymbol{k}_{pr}} \hat{b}^\dagger_{\boldsymbol{k}_c} + H.c.\ ,
\end{aligned} \tag{4.6}$$

where we have assumed that $\chi^{(3)}$ is spatially independent so that it can be taken outside the integral and absorbed into Γ along with the constant factor $(2\pi)^{-3}$, $\Delta k_z = 2k_p^z - k_{pr}^z - k_c^z$ denotes the longitudinal phase-mismatch, and $\boldsymbol{q}_{pr}$ ($\boldsymbol{q}_c$) is the probe (conjugate) k-vector in the transverse plane. In obtaining (4.6), we have assumed the conservation of energy in the optical fields and hence, the angular frequency mismatch ($\Delta\omega = 2\omega_p - \omega_{pr} - \omega_c$) is zero.

Highlighting the dependence of the FWM on the transverse spatial profile of the pump, one can rewrite the interaction Hamiltonian as

$$\hat{\mathcal{H}} = i\hbar\, 2\pi\Gamma \iiint dz\, d\boldsymbol{k}_{pr}\, d\boldsymbol{k}_c \left[\frac{1}{2\pi}\int d\boldsymbol{\rho}\, E_o^2(\boldsymbol{\rho}) e^{-i(\boldsymbol{q}_{pr}+\boldsymbol{q}_c)\cdot\boldsymbol{\rho}}\right] e^{i\Delta k_z z} \hat{a}^\dagger_{\boldsymbol{k}_{pr}} \hat{b}^\dagger_{\boldsymbol{k}_c} + H.c. \tag{4.7}$$

$$= i\hbar\, 2\pi\Gamma \iiint dz\, d\boldsymbol{k}_{pr}\, d\boldsymbol{k}_c\, \mathbb{K}(\boldsymbol{q}_{pr}+\boldsymbol{q}_c) e^{i\Delta k_z z} \hat{a}^\dagger_{\boldsymbol{k}_{pr}} \hat{b}^\dagger_{\boldsymbol{k}_c} + H.c.\ , \tag{4.8}$$

where we have introduced the function $\mathbb{K}$ defined as

$$\mathbb{K}(\boldsymbol{q}_{pr}+\boldsymbol{q}_c) \equiv \frac{1}{2\pi}\int d\boldsymbol{\rho}\, E_o^2(\boldsymbol{\rho}) e^{-i(\boldsymbol{q}_{pr}+\boldsymbol{q}_c)\cdot\boldsymbol{\rho}}, \tag{4.9}$$

which contains all the information of the pump transverse spatial profile and represents the transverse Fourier transform of $E_o^2(\boldsymbol{\rho})$. We further simply this expression by writing the pump's transverse

[3] A slowly varying envelope is the part of the complex amplitude whose variations are small with respect to $\boldsymbol{r}$ and t. More explicitly, the fractional change in amplitude over a time period and distance λ are much smaller than 1.

spatial distribution in momentum space, such that

$$E_o(\boldsymbol{\rho}) = \frac{1}{2\pi}\int d\boldsymbol{q}_p\, \mathcal{E}_o(\boldsymbol{q}_p) e^{i(\boldsymbol{q}_p\cdot\boldsymbol{\rho})}, \tag{4.10}$$

where $\mathcal{E}_o(\boldsymbol{q}_p)$ represents the angular spectrum of the pump, i.e. $\mathcal{F}[E_o(\boldsymbol{\rho})]$. We substitute (4.10) in the expression for $\mathbb{K}$ in (4.9) to rewrite it as

$$\begin{aligned}
\mathbb{K}(\boldsymbol{q}_{pr}+\boldsymbol{q}_c) &= \frac{1}{(2\pi)^3}\int d\boldsymbol{\rho}\left(\int d\boldsymbol{q}_p\, \mathcal{E}_o(\boldsymbol{q}_p) e^{i(\boldsymbol{q}_p\cdot\boldsymbol{\rho})}\int d\boldsymbol{q}'_p\, \mathcal{E}_o(\boldsymbol{q}'_p) e^{i(\boldsymbol{q}'_p\cdot\boldsymbol{\rho})}\right) e^{-i(\boldsymbol{q}_{pr}+\boldsymbol{q}_c)\cdot\boldsymbol{\rho}} \\
&= \frac{1}{(2\pi)^3}\iint d\boldsymbol{q}_p\, d\boldsymbol{q}'_p\, \mathcal{E}_o(\boldsymbol{q}_p)\mathcal{E}_o(\boldsymbol{q}'_p)\int d\boldsymbol{\rho}\, e^{i(\boldsymbol{q}_p+\boldsymbol{q}'_p-\boldsymbol{q}_{pr}-\boldsymbol{q}_c)\cdot\boldsymbol{\rho}} \\
&= \frac{1}{2\pi}\iint d\boldsymbol{q}_p\, d\boldsymbol{q}'_p\, \mathcal{E}_o(\boldsymbol{q}_p)\, \mathcal{E}_o(\boldsymbol{q}'_p)\, \delta(\boldsymbol{q}'_p-(\boldsymbol{q}_{pr}+\boldsymbol{q}_c-\boldsymbol{q}_p)) \\
&= \frac{1}{2\pi}\int d\boldsymbol{q}_p\, \mathcal{E}_o(\boldsymbol{q}_p)\, \mathcal{E}_o(\boldsymbol{q}_{pr}+\boldsymbol{q}_c-\boldsymbol{q}_p) \\
&= \frac{1}{2\pi}\,\Phi(\boldsymbol{q}_{pr}+\boldsymbol{q}_c),
\end{aligned} \tag{4.11}$$

where $\Phi(\boldsymbol{q}_{pr}+\boldsymbol{q}_c) \equiv \int d\boldsymbol{q}_p\, \mathcal{E}_o(\boldsymbol{q}_p)\, \mathcal{E}_o(\boldsymbol{q}_{pr}+\boldsymbol{q}_c-\boldsymbol{q}_p)$ is the convolution of the angular spectra of the two pump photons involved in the FWM process. Equation (4.11) shows that transverse spatial information regarding probe and conjugate fields, represented here by $\mathbb{K}(\boldsymbol{q}_{pr}+\boldsymbol{q}_c)$, is directly related to the convolution function Φ. Substituting the expression of $\mathbb{K}$ in (4.11) back into (4.8) and integrating over the length L of the media (from $-L/2$ to $L/2$) allows us to write the interaction Hamiltonian as

$$\hat{\mathcal{H}} = i\hbar\,\Gamma\iint d\boldsymbol{k}_{pr}\, d\boldsymbol{k}_c\, \Phi(\boldsymbol{q}_{pr}+\boldsymbol{q}_c)\int_{-L/2}^{L/2} dz\, e^{i\Delta k_z z}\hat{a}^\dagger_{\boldsymbol{k}_{pr}}\hat{b}^\dagger_{\boldsymbol{k}_c} + H.c. \tag{4.12}$$

$$= i\hbar L\,\Gamma\iint d\boldsymbol{k}_{pr}\, d\boldsymbol{k}_c\, \Phi(\boldsymbol{q}_{pr}+\boldsymbol{q}_c)\,\mathrm{sinc}(\Delta k_z L/2)\,\hat{a}^\dagger_{\boldsymbol{k}_{pr}}\hat{b}^\dagger_{\boldsymbol{k}_c} + H.c. \tag{4.13}$$

$$= i\hbar L\,\Gamma\iint d\boldsymbol{k}_{pr}\, d\boldsymbol{k}_c\, \mathbb{F}(\boldsymbol{k}_{pr},\boldsymbol{k}_c)\hat{a}^\dagger_{\boldsymbol{k}_{pr}}\hat{b}^\dagger_{\boldsymbol{k}_c} + H.c.\ . \tag{4.14}$$

Here, the two-photon amplitude function

$$\mathbb{F}(\boldsymbol{k}_{pr},\boldsymbol{k}_c) \equiv \Phi(\boldsymbol{q}_{pr}+\boldsymbol{q}_c)\,\mathrm{sinc}(\Delta k_z L/2) \tag{4.15}$$

takes into account the angular spectrum of the pump through function Φ and the phase matching condition through the sinc function. Note that the form of interaction Hamiltonian in (6.6) is very similar to the one for parametric down-conversion (PDC) [95,98,99]. However, in PDC, the function Φ is directly given by the angular spectrum of the single pump photon involved in the process instead of the convolution of the angular spectra of the two pump photons involved in FWM.

The term Δk_z in the argument of the sinc denotes the longitudinal phase-mismatch as shown in figure 4.3A. As we briefly mentioned in section 4.2, Δk_z is related to the allowed range of transverse k-vectors for the probe and conjugate fields. We now develop a more explicit expression of the sinc

4.4 FWM Hamiltonian in Spatial Variables

function for our non-collinear FWM process in the terms of $\boldsymbol{q}_{pr}$ and $\boldsymbol{q}_c$ vectors. We begin with

$$\Delta k_z = 2k_p^z - k_{pr}^z - k_c^z \tag{4.16}$$

$$= 2\sqrt{k_p^2 - q_p^2} - \sqrt{k_{pr}^2 - q_{pr}^2} - \sqrt{k_c^2 - q_c^2} \tag{4.17}$$

$$\simeq 2k_p - \frac{q_p^2}{k_p} - k_{pr} + \frac{q_{pr}^2}{2k_{pr}} - k_c + \frac{q_c^2}{2k_c} \tag{4.18}$$

$$= \frac{q_c^2}{2k_c} + \frac{q_{pr}^2}{2k_{pr}} - \frac{q_p^2}{k_p} - \varphi, \tag{4.19}$$

where $q = |\boldsymbol{q}|$ and $\varphi\,(= k_{pr} + k_c - 2k_p)$ is greater than zero for a non-collinear configuration. In our experiments, the pump-probe angle θ is very small ($\sim 0.4^\circ$), hence $\frac{q_c}{k_c} \simeq \frac{q_c}{k_p}$ and $\frac{q_{pr}}{k_{pr}} \simeq \frac{q_{pr}}{k_p}$. Using momentum conservation in the transverse plane, $2\boldsymbol{q}_p = \boldsymbol{q}_{pr} + \boldsymbol{q}_c$, we have

$$\Delta k_z \simeq \frac{q_c^2}{2k_p} + \frac{q_{pr}^2}{2k_p} - \frac{1}{k_p}\left|\frac{\boldsymbol{q}_{pr} + \boldsymbol{q}_c}{2}\right|^2 - \varphi \tag{4.20}$$

$$= \frac{|\boldsymbol{q}_{pr} - \boldsymbol{q}_c|^2}{4k_p} - \varphi. \tag{4.21}$$

To evaluate φ, one can use the fact that for perfect matching, $\Delta k_z = 0$, which implies

$$\varphi = \frac{|\boldsymbol{q}_{pr} - \boldsymbol{q}_c|^2}{4k_p}. \tag{4.22}$$

Also, using the triangle geometry of the figure 4.2A, we have

$$2k_p \sin\theta = |\boldsymbol{q}_{pr} - \boldsymbol{q}_c| \tag{4.23}$$

$$\Rightarrow \qquad k_p \sin^2\theta = \frac{|\boldsymbol{q}_{pr} - \boldsymbol{q}_c|^2}{4k_p}. \tag{4.24}$$

Using (4.22) and (4.24), we get the following expression

$$\varphi = k_p \sin^2\theta. \tag{4.25}$$

This gives the final form of the sinc function as

$$\operatorname{sinc}\left(\frac{\Delta k_z L}{2}\right) = \operatorname{sinc}\left(\left[\frac{|\boldsymbol{q}_{pr} - \boldsymbol{q}_c|^2}{4k_p} - \varphi\right]\frac{L}{2}\right). \tag{4.26}$$

In the present experiment, $\theta \sim 0.4^\circ$ which is used to set the value of φ. Using (4.15) and (4.26) in (6.6), we write the full interaction Hamiltonian in terms of the transverse spatial coordinates as

$$\hat{\mathcal{H}} = i\hbar L\,\Gamma \iint d\boldsymbol{k}_{pr}\, d\boldsymbol{k}_c\, \Phi(\boldsymbol{q}_{pr} + \boldsymbol{q}_c) \operatorname{sinc}\left(\left[\frac{|\boldsymbol{q}_{pr} - \boldsymbol{q}_c|^2}{4k_p} - \varphi\right]\frac{L}{2}\right) \hat{a}^\dagger_{\boldsymbol{k}_{pr}} \hat{b}^\dagger_{\boldsymbol{k}_c} + H.c.\,. \tag{4.27}$$

Here, we note that the spatial variables appear as the sum and difference in the arguments of two different functions. This is analogous to a system of two massive entangled particles when expressed in terms of the corresponding center of mass and relative coordinates[100]. It is also worth mentioning that a factorization of the two photon amplitude $\mathbb{F}$ into two functions that depend only on $\boldsymbol{q}_{pr}$ and $\boldsymbol{q}_c$ respectively would imply separability of the interaction Hamiltonian and, hence, no spatial entanglement.

4.4 FWM Biphoton Wavefunction

With the final form of interaction Hamiltonian given in (6.6), we derive an expression for the biphoton wavefunction for the generated twin beams using a first order perturbation theory. The combined twin beam state (TBS) of probe and conjugate fields can be written as

$$|\Psi_{\text{TBS}}\rangle = e^{-\frac{i\hat{\mathcal{H}}t}{\hbar}}|\Psi_0\rangle \tag{4.28}$$

$$\simeq \left(1 - \frac{i\hat{\mathcal{H}}t}{\hbar}\right)|\Psi_0\rangle \tag{4.29}$$

$$= |\Psi_0\rangle + C\int\int d\boldsymbol{k}_{pr}\; d\boldsymbol{k}_c \left[\; \mathbb{F}(\boldsymbol{k}_{pr},\boldsymbol{k}_c)\; \hat{a}^\dagger_{\boldsymbol{k}_{pr}}\; \hat{b}^\dagger_{\boldsymbol{k}_c} - \mathbb{F}^*(\boldsymbol{k}_{pr},\boldsymbol{k}_c)\; \hat{a}_{\boldsymbol{k}_{pr}}\; \hat{b}_{\boldsymbol{k}_c}\right]|\Psi_0\rangle \tag{4.30}$$

$$= |\Psi_0\rangle + C\int\int d\boldsymbol{k}_{pr}\; d\boldsymbol{k}_c\; \mathbb{F}(\boldsymbol{k}_{pr},\boldsymbol{k}_c)\; \hat{a}^\dagger_{\boldsymbol{k}_{pr}}\; \hat{b}^\dagger_{\boldsymbol{k}_c}|\Psi_0\rangle \tag{4.31}$$

$$= |\Psi_0\rangle + C\int\int d\boldsymbol{k}_{pr}\; d\boldsymbol{k}_c\; \mathbb{F}(\boldsymbol{k}_{pr},\boldsymbol{k}_c)\; |1'_{\boldsymbol{k}_{pr}}\rangle|1'_{\boldsymbol{k}_c}\rangle\;. \tag{4.32}$$

Here $|\Psi_0\rangle = \left|\{0\}_{\boldsymbol{k}_{pr}},\{0\}_{\boldsymbol{k}_c}\right\rangle$ is the multimode vacuum state, t is the interaction time and $C = tL\,\Gamma$. The notation $\left|1'_{\boldsymbol{k}_o}\right\rangle = |1_{\boldsymbol{k}_o}\rangle\prod_{\boldsymbol{k}\neq\boldsymbol{k}_o}|0_{\boldsymbol{k}}\rangle$ implies that the single photon occupies only the $\boldsymbol{k}_o$-mode and the rest of the modes remain unoccupied. The form of $|\Psi_{\text{TBS}}\rangle$ obtained in (4.32) is the same as the type-I SPDC wavefunction[95,98,99,101–104] with appropriate replacement of the convolution function with the angular spectrum of the pump field. The second term in (4.32) provides relevant information regarding the correlations between probe and conjugate photons as the detection of a probe photon with a fixed momentum ($\boldsymbol{k}_{pr}$) is correlated with the conjugate photons with k-vectors dictated by the convolution and phase-matching functions.

One can get further insight into the probe and conjugate photon emission behavior by examining the ideal scenario where the input pump beam is a plane wave. For a plane wave pump, the transverse spatial profile $E_o(\boldsymbol{\rho})$ is independent of the spatial location, i.e. $E_o(\boldsymbol{\rho}) = A_o$, where A_o is constant. Using the plane wave pump profile in (4.9), we get[4]

$$\Phi(\boldsymbol{q}_{pr}+\boldsymbol{q}_c) = 2\pi\,\mathbb{K}(\boldsymbol{q}_{pr}+\boldsymbol{q}_c) \tag{4.33}$$

$$= \int d\boldsymbol{\rho}\, A_o^2\; e^{-i(\boldsymbol{q}_{pr}+\boldsymbol{q}_c)\cdot\boldsymbol{\rho}} \tag{4.34}$$

$$= (2\pi)^2 A_o^2\,\delta(\boldsymbol{q}_{pr}+\boldsymbol{q}_c). \tag{4.35}$$

Since the a plane wave pump has a precise propagation direction and k-vector (i.e. no momentum uncertainty), the $\mathbb{F}$ function becomes dependent only on the $\boldsymbol{q}_{pr}$ and $\boldsymbol{q}_c$ variables. Using (4.35),

[4] Following the definition of the Fourier transform used here

$$f(x) = \frac{1}{\sqrt{2\pi}}\int dk e^{ikx} g(k)$$
$$\Rightarrow \int dx'\,\delta(x-x')f(x') = \frac{1}{2\pi}\iint dk\,dx'\,e^{ik(x-x')}f(x')$$
$$\Rightarrow \delta(x-x') = \frac{1}{2\pi}\int dk\; e^{ik(x-x')}.$$

we can now calculate the marginal probability amplitude for the probe photons by considering the following expression

$$\int d\boldsymbol{q}_c \, \mathbb{F}(\boldsymbol{q}_{pr}, \boldsymbol{q}_c) = (2\pi)^2 A_o^2 \, \delta(\boldsymbol{q}_{pr} + \boldsymbol{q}_c) \, \text{sinc}\left(\left[\frac{|\boldsymbol{q}_{pr} - \boldsymbol{q}_c|^2}{4k_p} - \varphi\right]\frac{L}{2}\right) \tag{4.36}$$

$$= (2\pi)^2 A_o^2 \, \text{sinc}\left(\left[\frac{|\mathbf{q}_{pr}|^2}{k_p} - \varphi\right]\frac{L}{2}\right). \tag{4.37}$$

The sinc expression in (4.37) provides information about the probability amplitude for the probe

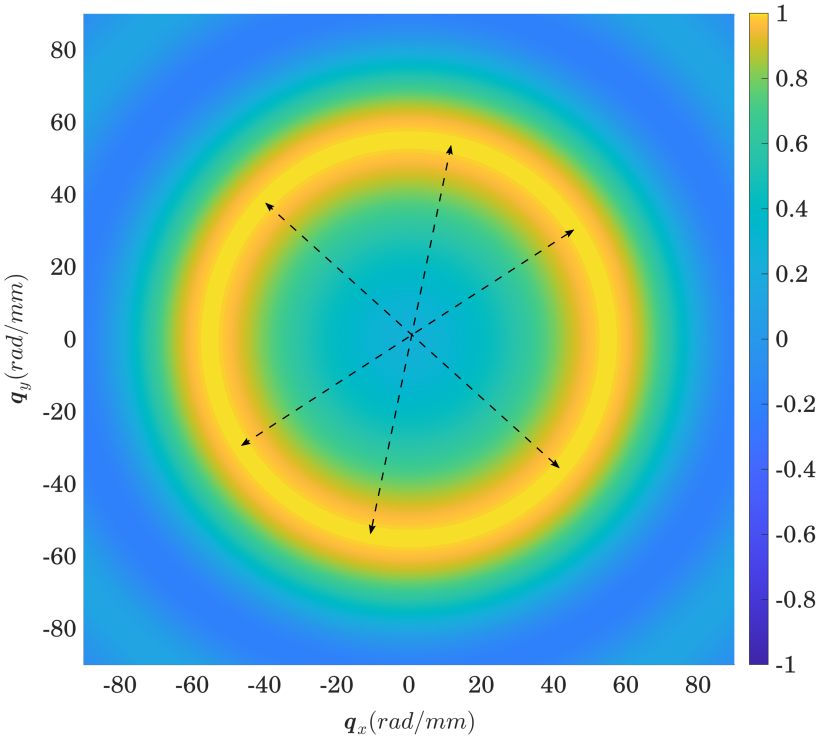

Figure 4.4: Marginal probability amplitude in a far field plane for the probe and conjugate photons. The probe and the conjugate arrive mostly over the bright (yellow) annular region due to optimal phase matching. For a plane wave pump, following momentum conservation in the transverse plane, one can expect point-to-point correlations at diagonally opposite locations indicated via black arrows.

photons as a function of transverse momentum. An identical expression can also be obtained for the conjugate photons as the function is symmetric with respect to transverse momentum variables. Figure 4.4 shows a two-dimensional distribution of the sinc as a function of the horizontal and vertical transverse momentum (of probe/conjugate photons). Since the far field position coordinates scale linearly with the transverse momentum[105], i.e. $\boldsymbol{x}_{far} \propto \boldsymbol{q}/k$, figure 4.4 provides information about the probe or conjugate probability distribution in a far field plane. As we mentioned earlier, for a plane wave pump, the probe and conjugate far field correlations are point-to-point. Therefore, one can expect point-to-point correlations at diagonally opposite regions of the sinc distribution (shown using arrows in figure 4.4). In other words, the arrival of a probe photon at one end of the arrow is correlated with the arrival of a conjugate photon at the other end. The finite width of the annular region points to the fact that the angular phase matching bandwidth for our experimental

parameters is finite and, hence, we expect a finite near field coherence area. In fact, in order to achieve point-to-point correlations in the near field would require a very large spread for the corresponding sinc function in the far field which is in-principle possible in the limit of $L \to 0$.

4.5 Einstein-Podolsky-Rosen Correlations in the Spatial Domain

In general, the non-separability of $|\Psi_{\text{TBS}}\rangle$ in terms of the probe and conjugate spatial variables would indicate the presence of spatial entanglement in the twin beam state. However, in order to develop applications that can take the advantage of the spatial entanglement, a further quantification on the level of entanglement would be necessary. One of the ways to quantify entanglement is via the detection of EPR-type correlations in a given quantum system[106–109]. Here in this section, we provide a brief overview of EPR correlations and why they be should be expected in the transverse spatial degrees of freedom of the photons generated via a FWM process.

The presence of EPR correlations in the position-momentum (spatial) variables was crucial to the original EPR *gedanken* experiment put forward by Albert Einstein, Boris Podolsky and Nathan Rosen in a 1935 paper[110]. Since then, it has become one of the most highly cited and influential papers aimed toward the foundational issues in quantum mechanics as it eventually led to the conception and experimental exploration of entanglement as well as the discovery of non-locality in quantum theory. The proposed thought experiment in this paper considers a pair of particles entangled in terms of the position and momentum eigenstates. An idealized EPR entangled state can be written as

$$|\Psi_{\text{EPR}}\rangle = \int dx\ |x, x\rangle = \int dp\ |p, -p\rangle\,, \tag{4.38}$$

where $|x\rangle$ ($|p\rangle$) is the position (momentum) eigenstates of the position $\hat{x}$ (momentum $\hat{p}$) operator. The state in (4.38) describes a pair of particles with perfect position correlations and momentum anti-correlations. EPR therefore argued that, given that the two entangled particles no longer interact, a measurement of the position for the first particle allows one to precisely infer the position of the second particle. Alternatively, by measuring the momentum of the first particle, one can also predict the precise value of momentum for the second particle. Based on a specific definition of reality[5] for physical variables, they showed that position and momentum variables simultaneously exist for the second particle (which is not directly measured). Since in quantum mechanics, the position and momentum operators do not commute with each other, one can not know the position and momentum of a given particle simultaneously with arbitrary precision. After arriving on a result that was contradictory to quantum mechanics in their analysis, they concluded that "... the quantum mechanical description of the physical reality given by wave functions is not complete".

A critical component of the EPR argument was the principle of 'locality' or 'local realism' which implies that distant particles can not influence each other and, therefore, measurements affect only the immediate surroundings. Combined with the work of J. S. Bell[111] (Bell's inequality published in 1964), numerous experiments have shown[112,113] that the assumption of local realism is not valid for entangled systems. Any measurement performed on the first particle instantaneously affects the state of second particle via the collapse of joint wavefunction regardless of their separation

[5]EPR defined physical reality as[110]
"If, without in any way disturbing a system, we can predict with certainty (i.e., with probability equal to unity) the value of a physical quantity, then there exists an element of physical reality corresponding lo this physical quantity."

(including space-like separation[113,114]). A subsequent measurement made on the second particle gives an outcome that is consistent with the result of the first measurement. In the context of the original EPR article[110], it means that the position or momentum of the second particle becomes precise immediately after the corresponding quantity is measured for the first particle and, since position and momentum are not measured simultaneously, they need not be simultaneous realities for the unmeasured particle.

The existence of an EPR entangled state can be experimentally verified by measuring correlations between the two entangled particles or subsystems. For the ideal EPR state given in (4.38), quantum mechanics predicts the following relations

$$\Delta^2(x_1 - x_2) = \Delta^2(p_1 + p_2) = 0, \tag{4.39}$$

where the subscript 1 and 2 denote the first and second particles, respectively and x/p is the measurement outcome of the position/momentum operator. In general, 1 and 2 can be the two subsystems of the entangled state (based on a partition), between which EPR correlations are measured. The difference/sum measurement of position/momentum outcomes does not show any uncertainty and the EPR correlations lead to an 'apparent' violation of the following Heisenberg inequality

$$\Delta^2_{inf}(x_2 \,|\, x_1)\, \Delta^2_{inf}(p_2 \,|\, p_1) \geq \frac{\hbar^2}{4}, \tag{4.40}$$

where $\Delta^2_{inf}(x_2 \,|\, x_1)$ denotes the *inferred* variance in the position of the second particle conditioned upon position measurements for first particle[6] (and a similar explanation for the inferred momentum variance). For this reason, a violation of the above inequality is also sometimes referred as the EPR criterion for entanglement.

In the terms of an EPR entangled source of light, one can measure the position and momentum properties of the entangled photons in the transverse plane and a violation of (5.8) using inferred position and momentum variances will certify the presence of EPR correlations. For the FWM process considered in our experiments, the transverse position and momentum properties of the generated probe and conjugate photons are given by the two photon amplitude function $\mathbb{F}$ which, in the terms of transverse momenta, has the following form for a plane wave pump

$$\mathbb{F}(\boldsymbol{q}_{pr}, \boldsymbol{q}_c) = (2\pi)^2 A_o^2\, \delta(\boldsymbol{q}_{pr} + \boldsymbol{q}_c)\, \mathrm{sinc}\left(\left[\frac{|\boldsymbol{q}_{pr} - \boldsymbol{q}_c|^2}{4k_p} - \varphi\right]\frac{L}{2}\right). \tag{4.42}$$

The presence of the momentum δ-function immediately tell us about the possibility of spatial EPR correlations in the corresponding FWM twin beam state. As the delta function implies that the knowledge of transverse momentum of one beam will give us the transverse momentum of the other beam precisely. This would result in a zero inferred variance and a violation of (5.8). Although the momentum eigenstates, such as the plane wave mentioned here, are non-normalizable and can not

[6] A precise mathematical definition of the inferred variance can be given as

$$\Delta^2_{inf}(x_2|x_1) = \int dx_2\, P(x_2|x_1)\, x_2^2 - \left(\int dx_2\, P(x_2|x_1)\, x_2\right)^2, \tag{4.41}$$

where $P(x_2|x_1)$ is the conditional probability distribution for variable x_2. From this definition, it is clear that $\Delta^2_{inf}(x_2|x_1)$ is also a function of x_1. However, if the function $P(x_2|x_1)$ is independent of the specific values taken by variable x_1 then $\Delta^2_{inf}(x_2|x_1)$ is a single-valued function and one can evaluate it by using a fixed value of x_1.

be realized in practice, by using a Gaussian pump with large enough waist (depending on the width of the sinc function), one should be able to provide a violation of (5.8). More explicitly, using the transverse electric field profile $E_o(\boldsymbol{\rho}) = A_1 \ \exp\!\left(-\rho^2/2\sigma_p^2\right)$ for the pump beam in (4.33), we get

$$\Phi(\boldsymbol{q}_{pr} + \boldsymbol{q}_c) = \int d\boldsymbol{\rho}\, A_1^2 \ e^{-(\rho^2/\sigma_p^2)} \ e^{-i(\boldsymbol{q}_{pr}+\boldsymbol{q}_c)\cdot\boldsymbol{\rho}} \tag{4.43}$$

$$= A_1^2\, \sigma_p^2\, \pi\, e^{-\sigma_p^2|\boldsymbol{q}_{pr}+\boldsymbol{q}_c|^2/4} \ , \tag{4.44}$$

where σ_p is the width of the pump electric field distribution at the non-linear medium (vapor cell) and $|\boldsymbol{\rho}| = \rho$. We see that for a large pump waist, the inferred transverse momentum variance will scale as $\sim 1/\sigma_p^2$ (also see ref[115]). Using this approach, in the next chapter, we will provide experimental proof of EPR correlations between the probe and conjugate beams in the spatial domain.

CHAPTER 5

Measurement of Spatial Properties and EPR Correlations

In chapter 4, we mentioned that using the FWM non-linear process in the double-Λ configuration, the generation of spatial EPR correlated probe and conjugate photons is possible in the regime of a narrow pump angular spectrum (large waist at the Rb cell). This leads to a reduced size of the coherence area in the far field and can help achieve an apparent violation of the Heisenberg uncertainty principle, i.e., the EPR criterion, in the spatial domain. The degree to which the overall product of conditional position and momentum uncertainties is lowered (which can, in principle, be zero for an ideal EPR state) serves as a quantification benchmark for the level of spatial entanglement between the twin beams. To take advantage of the spatial degrees of freedom for optics based quantum sensing and communication such a prior certification on the level of entanglement is often necessary[116–118].

In this chapter, we will provide details of our twin beam imaging experiment which led to verification of EPR correlations in the transverse position-momentum variables between the probe and conjugate beams[94]. The images of twin beams were acquired using an electron-multiplying CCD (EMCCD) camera and our analysis based on the image intensity correlations led to a direct violation of the EPR criterion for the spatial variables. Moreover, by obtaining spatial quantum squeezing (i.e. temporal squeezing as a function of spatial variables) in both the near and far field, we provide additional evidence towards the presence of hyperentanglement in the spatial and temporal degrees of freedom. Our experimental approach combines the use of bright twin beams to amplify correlated fluctuations with fast image acquisition on the EMCCD camera and is able to show the presence of EPR spatial entanglement with a record low number images (acquired within a small exposure time).

5.1 Role of Bright Beams in Spatial Correlation Measurement

In the quantum picture of FWM discussed in chapter 3, we saw that the FWM process generates a pair of probe and conjugate photons even in the absence of a seed beam. One can also think of these photons as the excitations on the underlying quantum correlated probe and conjugate fields generated in a spontaneous FWM process. In the non-collinear configuration of the FWM, the generated fields are emitted in a (hollow) cone due to the rotational symmetry of the phase-matching condition about the pump propagation direction (see figures 5.1A and 4.4). The correlation properties of these underlying fields were presented in detail in chapter 4. The use of a Gaussian seed beam at the probe frequency then stimulates the FWM process in certain spatial regions inside the emission cone

and generates bright Gaussian probe and conjugate beams (see figure 5.1B), collectively referred to here as the bright twin beams. The overlap of these bright beams with the spatial modes of the underlying spontaneous FWM process can be visualized as the amplification of the spontaneous probe and conjugate fields via bright bichromatic local oscillators[89,90]. It is important to note here

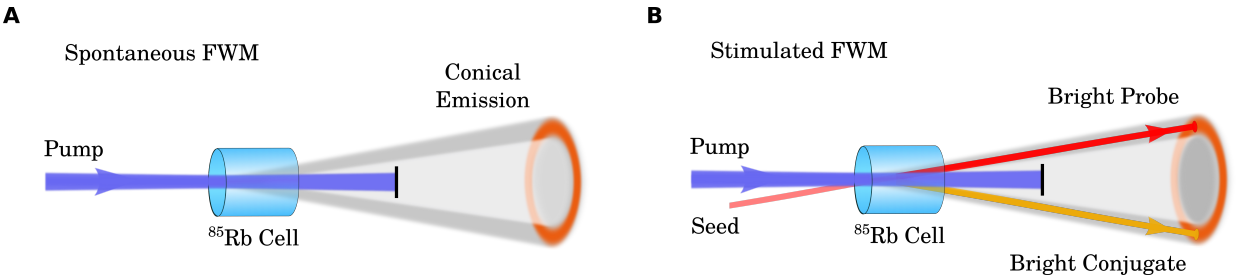

Figure 5.1: Schematic diagrams for (A) spontaneous and (B) stimulated FWM process. In spontaneous FWM, vacuum fields at the probe and conjugate frequency act as seed. The optimal phase matching angle is close to $\sim 0.4^\circ$ resulting in a non-collinear emission of probe and conjugate photons generated at the Rb vapor cell. Due to the rotational symmetry along pump propagation direction, the generated photons are emitted in an hollow cone and the far field distribution (transverse cross section of the conical emission) is an annular ring shown in orange (A and B). Due to having almost same wavelengths, the probe and conjugate emission cones, and hence, their corresponding annular rings spatially overlap. Any individual probe and conjugate photon pair, however, occupy diametrically opposite parts on the annular ring satisfying momentum conservation in the transverse plane (see figure 4.4). (B) In the presence of a seed beam, certain regions of the emission cone become bright via FWM amplification. The photon correlations within these bright regions can be used to study position and momentum correlations of the spontaneously generated fields in the near and far field, respectively.

that by choosing suitable bichromatic local oscillators (i.e. spatial profile and frequency), one can effectively measure the spatial coherence and correlation properties of the spontaneously generated probe and conjugate fields[119,120]. Specifically, in the context of our experiment, the presence of bright beams in the overlap regions effectively acts as a local oscillator and converts the amplitude quadrature fluctuations of the underlying field into the intensity fluctuations.

To see this, we write the field operator as $\hat{a}(\boldsymbol{x}) = |\alpha(\boldsymbol{x})| + \delta\hat{a}(\boldsymbol{x})$, i.e. mean value plus fluctuations, and substitute in the intensity fluctuation operator as

$$\delta\hat{N}(\boldsymbol{x}) = \hat{N}(\boldsymbol{x}) - \langle\hat{N}(\boldsymbol{x})\rangle \tag{5.1}$$

$$= \left(|\alpha(\boldsymbol{x})| + \delta\hat{a}(\boldsymbol{x})\right)^\dagger \left(|\alpha(\boldsymbol{x})| + \delta\hat{a}(\boldsymbol{x})\right) - |\alpha(\boldsymbol{x})|^2 \tag{5.2}$$

$$= |\alpha(\boldsymbol{x})| \left(\delta\hat{a}^\dagger(\boldsymbol{x}) + \delta\hat{a}(\boldsymbol{x})\right) + \delta\hat{a}^\dagger(\boldsymbol{x})\delta\hat{a}(\boldsymbol{x}) \tag{5.3}$$

$$\simeq \sqrt{2}|\alpha(\boldsymbol{x})|\delta\hat{X}(\boldsymbol{x}), \tag{5.4}$$

where $\boldsymbol{x}$ is the location of the transverse plane in the near or far field. By ignoring the contribution of the quadratic fluctuation term in the limit of bright beams ($|\delta\hat{a}|/|\alpha| \ll 1$) in (5.4), we see that amplitude fluctuations in the field are proportional to the photon number/intensity fluctuations. This allows us to measure spatial properties of the correlated field quadratures using the intensity measurements on a CCD camera. For Gaussian bright twin beams with large waist, we can also assume the mean field amplitude to be position independent by restricting the position variable $\boldsymbol{x}$ near the center of the Gaussian. To ensure this, the size of the seed beams is carefully selected for the near and far field measurements. The generation of spatially wide bright beams is also necessary to cover a large number of coherence areas in order to provide a reliable measurement of the spatial correlations[121].

By changing the input power of the seed beam, we are also able to obtain variable control over the optical power of the bright probe and conjugate beams which provides a better to signal-to-noise ratio (SNR) and helps eliminate certain measurement problems for vacuum squeezed states [122,123]. The use of a seed beam facilitates the generation of tunable macroscopic entangled states that have unique applications, such as imaging of biological samples [22,124], Bose-Einstein condensates [125,126] and trapped ions/atoms [127–129] that require better imaging methods with low-intensity thresholds.

5.2 Imaging Setup for Spatial Correlation Measurements

To measure position and momentum spatial correlations, we take images of bright probe and conjugate beams using a high-efficiency electron-multiplying charge-coupled-device (EMCCD) in the near and far field. The experimental setup used for the near and far field measurements is shown in figure 5.2A and 5.2B, respectively. To generate these bright probe and conjugate beams, we use a 532 nm pumped Ti:Sapphire laser to generate a narrow-band pump and a probe (seed) beam close to the D1 transition of ^{85}Rb isotope (∼795 nm). The frequency of pump is blue-detuned from the $5\,^2\mathrm{S}_{1/2}, F{=}2 \longrightarrow 5\,^2\mathrm{P}_{1/2}, F'{=}3$ transition at a single photon detuning (Δ) of 1.18 GHz as shown in figure 5.2 (inset, left). The pump detuning is actively maintained using a saturation-absorption-lock (see appendix C) signal from a separate Rb cell. Using an acousto-optic modulator (AOM), a small portion from the pump beam is red-detuned by 3.04 GHz to generate the input seed probe. This results in an overall two-photon detuning (δ) of 4.27 MHz. The pump and seed probe beams are aligned to intersect at an angle of $\sim 0.4^\circ$ at the center of a 12.7 mm (1/2-inch) long hot Rb vapor cell which acts as a non-linear medium for the FWM process. The temperature of the Rb vapor is stabilized to $(106.0 \pm 0.1)^\circ$C using a proportional-integral (PI) temperature controller (Arroyo TECPak 585). The diameter at the waist of the pump beam is set to be 4.4 mm[1] at the cell center for both the near and far field configurations while the waist of the seed probe beam is 2.0 mm (0.4 mm) for the near (far) field configuration. In the far field setup, a smaller diameter (at the cell) seed beam provides a large bright Gaussian beam in the far field suitable for the corresponding measurements. The pump beam is filtered after the vapor cell using a polarization filter (Semrock BrightLine FF01-842/SP-25) to avoid excessive noise at detectors due to uncorrelated photons. To measure the position correlations between the probe and conjugate beams, we image the cell center (near field) onto the EMCCD sensor by placing 400 mm lenses for both the probe and conjugate beam paths after the cell (figure 5.2A). This leads to a magnification factor of 0.65 which is taken into account during the near field image analysis. For the momentum correlation measurements, we use a 500 mm lens in the probe and conjugate arms which maps the Fourier transform of the cell center at a distance of $2f$ via a f-to-f mapping where the EMCCD is then placed (far field, see figure 5.2B). The f-to-f optical system maps the transverse momentum properties of fields into position ones according to the relation $\boldsymbol{x} = f\boldsymbol{q}/k$, where $\boldsymbol{x}$ is the transverse position at the EMCCD location, f is the focal length of the lens and $\boldsymbol{q}$ is the transverse momentum of the optical field at the cell center.

The EMCCD unit (Princeton Instruments ProEM-HS:512 BX3) has a 16-bit CCD sensor with an active area of 1024×512 pixels with a pixel size of 16×16 μm^2. The active sensor is further subdivided into two regions (each 512×512 pixels) with the first one acting as an image acquisition region and the second as a buffer region for charge storage. The buffer region is never exposed to the incoming photons, which helps reduce unwanted background contributions to the acquired images.

[1] $1/e^2$ diameter or 4σ of the intensity Gaussian profile (for all reported beam diameters in this dissertation).

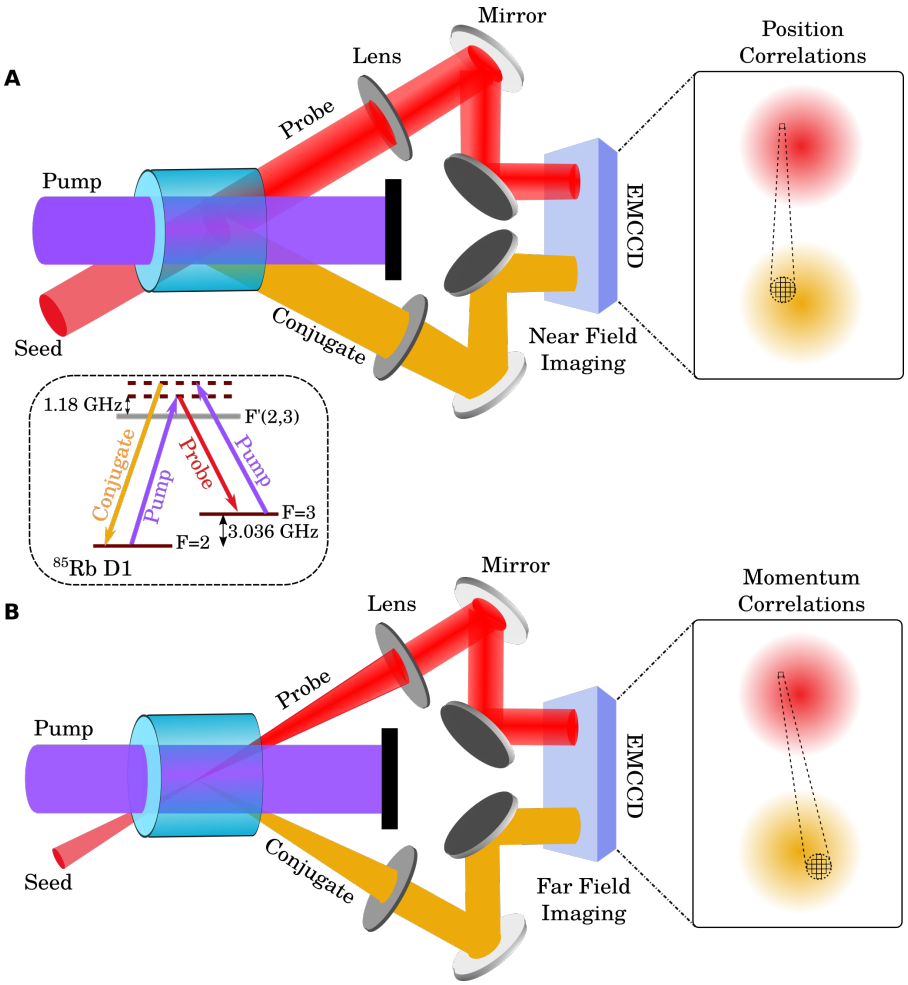

Figure 5.2: Experimental (A) near field and (B) far field setup to measure transverse position and momentum correlations, respectively, in the twin beams. To measure position correlations, the near field (cell center) is mapped to the EMCCD location using a 400 mm lens and, for momentum correlations, a 500 mm lens f-to-f mapping converts the transverse field momentum into transverse position at the EMCCD location ($2f$ distance). The inset on left shows frequencies of the various optical fields near the ^{85}Rb D1 transition in double-Λ configuration. The insets on the right give pictorial representation of relative position and momentum correlations measured in terms of EMCCD pixels of the bright probe and conjugate beam images. Figure adapted from ref[94]. Reproduced with permission.

During our experiments, the temperature of the camera sensor is maintained below -45°C via an in-built thermo-electric Peltier cooler. This significantly reduces the electronic noise of the pixels due to thermal electrons[130]. The quantum efficiency of the EMCCD sensor is $\sim 70\%$. Although the EMCCD unit has an electron multiplier mode, we instead use the low-noise mode more suited for working with bright beams.

To verify spatial EPR correlations as well as hyperentanglement in the spatial temporal degrees of freedom for the spontaneously generated probe and conjugate fields, we must ensure an identical generation of these fields between the near and far field measurements. To achieve this, the pump beam parameters, various frequency detunings and cell temperature remain unchanged during the near and far field measurements. We only vary the seed probe beam waist to overlap bright beams with large number of coherence areas in the near and far field. Since the source cannot be separately

modified for the near and far field measurements, we *a prori* optimize our source with respect to the intensity difference squeezing using single (Δ) and two-photon (δ) detunings. As shown in figure 5.3A and 5.3B, we have an intensity difference squeezing (normalized to the shot noise) of 5.07 dB and 5.75 dB (at ∼200 kHz) in the near and the far field configurations, respectively. It proves that we are able to observe quantum correlations between probe and conjugate beams in the near and far field for our choice of seed beams. The intensity difference squeezing observed here is

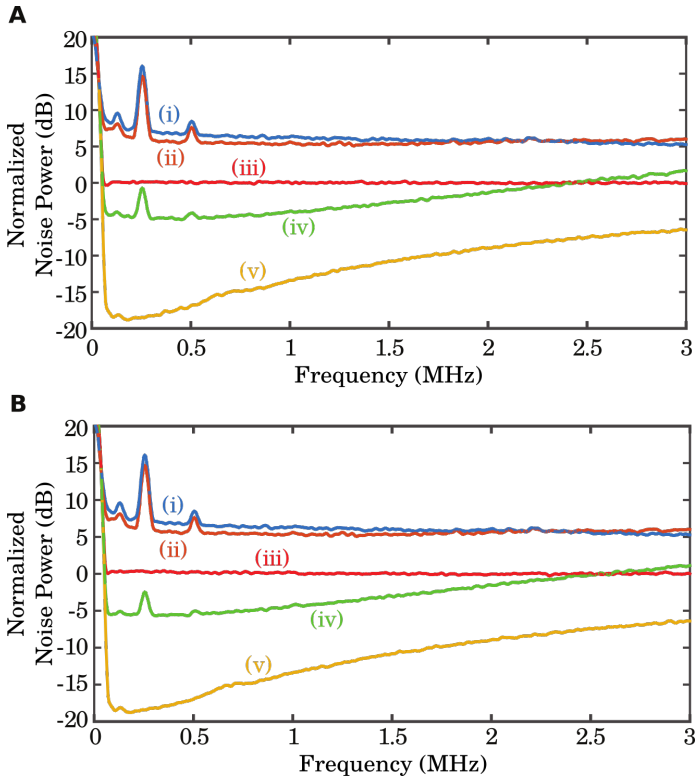

Figure 5.3: Experimental plot of normalized power spectra of the intensity difference noise between bright probe and conjugate beams (iv) in the (A) near and (B) far field configurations which shows temporal squeezing of ∼ 5 dB below shot noise (iii). This represents close to 68% noise reduction compared to coherent (uncorrelated) beams. Individual probe (i) and conjugate (ii) noise power spectra show thermal (super Poisson) behavior. Trace (v) is from the electronic noise of our balanced detector (Thorlabs PDB450A). Figure adapted from ref[94]. Reproduced with permission.

prerequisite for the spatial squeezing (i.e. temporal squeezing confined to certain spatial regions or modes) since it is an average over all spatial regions/pixels overlapping with the bright twin beams. For a more detailed discussion about the relationship between temporal and spatial squeezing see appendix A in ref[94]. The intensity difference squeezing shown here is lower than reported in similar experiments[67,131] in our lab. This is due to the unusually large size of the pump waist at the cell center, which results in lower intensity and, hence, a lower gain[93] for the FWM.

5.3 Frame Acquisition and Image Processing

The spatial correlation properties of the probe and conjugate fields can be characterized via the spatial analysis of field amplitude fluctuations that are converted into intensity fluctuations in the

overlapping bright portions of the probe and conjugate beams as shown in (5.4). For bright probe and conjugate beams, the photon flux can be as high as $\sim 10^{14}$ photons per second limited only by the saturation of the EMCCD device used. This is in contrast with the traditional photon coincidence measurement approach used for SPDC[106,107,132,133] and atomic ensemble based spontaneous FWM[134,135] sources. For bright twin beams, however, the intensity fluctuations are contaminated with classical noise from the laser and other technical noise due to the use of a seed beam. Therefore, in order to extract intensity fluctuations that are quantum correlated, we perform subtraction of consecutive frames containing bright twin beam images acquired via pulsed measurements which helps in classical/technical noise cancellation. The maximum bandwidth of time-frequency correlations generated in our FWM process source is close to 20 MHz[136]. Therefore, a subtraction of two consecutive frame that are separated more than 50 ns in time does impact the quantum correlations.

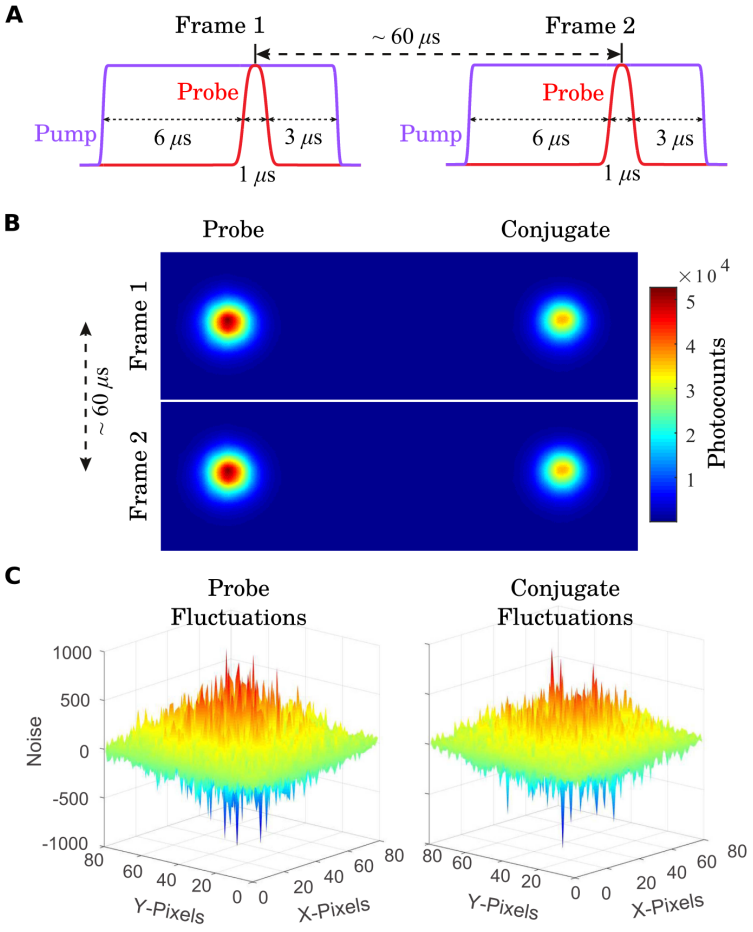

Figure 5.4: Schematic diagram for bright probe and conjugate image acquisition to obtain spatial intensity fluctuations. (A) The pulse timing for the pump and probe, obtained by turning AOMs on and off. (B) Simultaneous measurement of probe and conjugate images in (consecutive) frames 1 and 2 with peak photocounts $\sim 10^4$. Acquisition of Frame 1 and 2 is synchronized with the corresponding pump-probe pulses in (A). (C) Intensity fluctuation images for the probe (left) and conjugate (right) beams obtained from the subtraction Frame 1 - Frame 2. Figure adapted from ref[94]. Reproduced with permission.

Using the kinetic mode feature on our EMCCD device, multiple frames with probe and conjugate

images can be obtained in rapid succession while simultaneously pulsing the pump and seed probe beams. The kinetic mode stores accumulated charges during detection on the CCD sensor providing fast acquisition of two frames within $\sim \mu$s time differences. In our implementation of the kinetic mode, the camera sensor (1024×512 pixels) is divided into 6 frames with each frame ($\sim 170 \times 512$ pixels) containing one exposure for bright probe and conjugate beams. After the acquisition of the first frame, the charge accumulated is shifted at a rate of 300 ns/row. Therefore, to shift the whole frame, the minimum possible time difference between frames is 170×300 ns $= 51$ μs (hence, much higher than 50 ns). This process is repeated 6 times to obtain six images for the probe and conjugate beams on all the frames. As mentioned earlier, we pulse the input beams to intermittently expose the camera sensor to bright twin beams during each frame. The pulsing of inputs is achieved by electronically switching on the probe and the pump AOM for a duration of 1 μs and 10 μs, respectively, using a signal generator. A probe pulse delay of 6 μs after switching on the pump pulse is found to be optimum for to avoid any transient effects in FWM[137]. The timing sequence for two consecutive pump-(seed) probe pulses is shown in figure 5.4A along with the corresponding frames in figure 5.4B. The electronic pulses for probe and pump AOMs are synchronized with the frame acquisition at EMCCD in such a way that the EMCCD acts as a master device and the signal generator for AOMs as a slave. For our experiments, the camera exposure time set to 12 μs (for each frame) and the average time separation between two consecutive frames is ~ 60 μs. One can get an idea of 'macroscopicity' of these measurements by examining the probe and conjugate beams images in figure 5.4B where a pixel near the peak region of the probe (conjugate) has $\sim 5 \times 10^4$ ($\sim 3.5 \times 10^4$) photocounts.

Once all the frames are acquired, they are imported to MATLAB as matrices for further analysis. We first calculate any change in optical power between the frame 2 and 3[2]. For an ideal measurement, the total number of counts (summation over all pixels in the bright regions) in these two frames would be same. Experimentally, however, the output of the Ti:Sapphire laser and coupling efficiency to various optical fiber varies over time and leads to a small but measurable change in twin beam intensity between the two frames. We quantify this change by calculating a 'gain factor' from frame 2 to frame 3 as

$$\text{gain factor} = \frac{\sum'_{\text{frame 3}} \text{ pixel count}}{\sum'_{\text{frame 2}} \text{ pixel count}}, \tag{5.5}$$

where summation of pixel values for a given frame is performed over a $\sim 51 \times 51$ region around the maxima of the Gaussian profile (indicated with a prime over the summation symbol). The gain factor is calculated for both the probe and conjugate regions and is averaged. Frame 2 is then scaled accordingly by multiplying each pixel value with the average gain factor. To account for any frame-to-frame position drift in the probe and/or conjugate images, we crop a larger region ($\sim 121 \times 121$ pixel) around the maximum brightness pixel and align the images between frame 2 and frame 3 using an image registration algorithm in MATLAB with translation as the only allowed degree of freedom[137]. This takes into account the possibility that, from one frame to another, probe and/or conjugate images may drift in the transverse directions due any transient air currents in the beam path. After the translation alignment is preformed, individually for probe and conjugate images, a subtraction between frames yields intensity fluctuations (with minimal DC contribution) for the

[2]We use intensity fluctuations from a subtraction between the second and third frames for all the spatial squeezing as well as correlation analysis reported in this thesis. These frames have the least amount of residual optical background noise and, therefore, give optimal results[137]. It also implies that we get one probe/conjugate intensity fluctuation image per acquisition (6 frames).

probe and conjugate beams as shown in figure 5.4C. These spatial intensity fluctuations provide information about the spatial properties of underlying quantum-correlated probe and conjugate fields while minimizing contamination from classical and technical sources of noise. We also account for any position dependent electronic offset present on the camera sensor by acquiring background images while the camera shutter is closed. The calculated average of these background images is subtracted from all probe and conjugate images prior to the gain factor calculation.

5.4 Near and Far Field Spatial Squeezing

In chapter 4, while explaining the origin of the position correlations in the near field, we mentioned that during the FWM process, the probe and conjugate photons are generated together within a finite volume following energy conservation. This finite generation region for a pair of correlated photons is often termed as the 'biphoton birth zone'[95]. The photon correlation properties in the near field then imply that one can achieve a noise reduction (compared to coherent states) by making intensity difference measurements for the probe and the conjugate fields over spatial regions that were essentially overlapping inside the non-linear medium. In terms of the field quadratures, it was shown in chapter 2 that the amplitude difference quadrature (X_-) is squeezed in the twin beam state which implies correlation between the probe and the conjugate field quadratures. The amplification of these correlated quadratures would lead to intensity correlations, and hence, relative intensity squeezing in the spatially overlapping regions in the near field.

In order to quantify the spatial quantum noise reduction in twin beams (both in the near and far field), we define a noise ratio (NR) as[94]

$$\mathrm{NR} = \frac{\left\langle \Delta^2(\delta P - \delta C)\right\rangle}{\langle P_1 + P_2 + C_1 + C_2\rangle}, \tag{5.6}$$

where (P_1, C_1) and (P_2, C_2) are 80×80 pixel size probe and conjugate images from the consecutive frame 2 and 3, respectively, and have been processed through steps outlined in the previous section. δP and δC represents the subtraction matrices resulting from the $(P_1 - P_2)$ and $(C_1 - C_2)$ operations containing intensity fluctuation information for the probe and conjugate bright beams, respectively (see figure 5.4C). The variance $\Delta^2(\delta P - \delta C)$ is calculated over all the pixel values in a twin beam subtraction image $(\delta P - \delta C)$ and averaged over many acquisitions. This justifies choosing a smaller region (80×80) near the center of the bright regions as the variance is spatially calculated and any contribution due to a change in the spatial profiles of Gaussian bright beams should be minimized. The NR for a coherent state has a value of one as photons do not share temporal correlations following the Poisson distribution[31] and hence, no spatial correlation between δP and δC over a uniform intensity region as well. For a spatially squeezed twin beam state, NR < 1 shows the presence of (relative) sub-Poissonian behavior, i.e. reduced spatial variance due to quantum-correlated fluctuations present within a finite region, in the near and/or the far field. The NR introduced here can be seen as an extension of the Mandel parameter (Q_{M}) in the spatial domain for two modes.

Figure 5.5A shows the experimentally measured NR for twin beams as well as for the equivalent (same optical power) coherent states with respect to the size of superpixel made by grouping (or 'binning') all pixels within a square region. Due to a finite spatial bandwidth of the FWM process (finite Δk_z, see Chapter 4), we do not expect point-to-point correlations in the near field[3]. Given

[3] One can, in-principal, approach such a scenario by using a vapor cell of very small length as the size of near field

5.4 Near and Far Field Spatial Squeezing

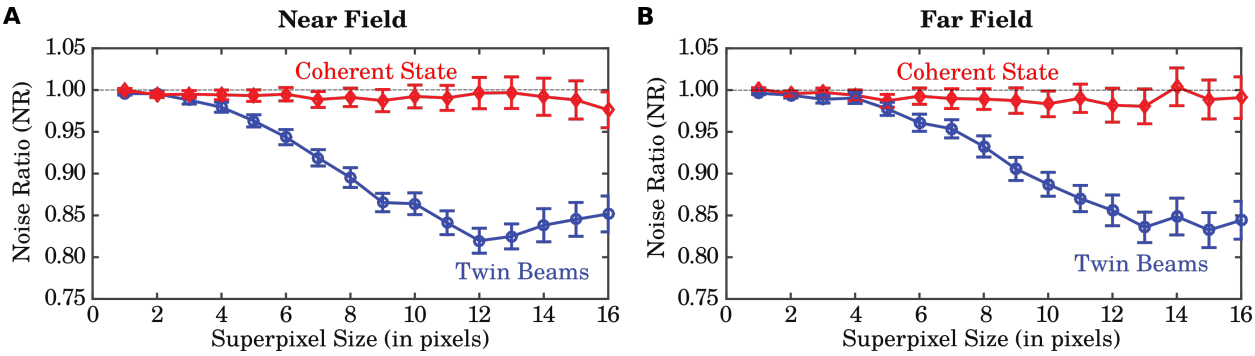

Figure 5.5: Experimental results for the near (A) and far (B) spatial squeezing measurements. We plot the measured noise ratio versus the number of combined pixels (superpixel size) and observe a spatial noise reduction of 0.84 ± 0.02 (0.83 ± 0.02) for the near (far) field for a superpixel size of 15. These results point to the existence of quantum spatial correlations in the twin beams for the transverse position and momentum degrees of freedom. The mean and the standard deviation of mean is calculated over the NR of 200 acquisitions (200 frame pairs). Figure adapted from ref[94]. Reproduced with permission.

that the correlated probe and conjugate fluctuations are spread over an area larger than a pixel, we group the individual pixels into a superpixel and assign it the sum of all individual pixel values. This effectively accounts for the spread in correlations for finite size coherence area and provides a measure of spatial noise reduction as a function of measurements over differently sized regions[141]. From the experimental results shown in figure 5.5A, we see an increasing reduction of the NR for twin beams with respect to the superpixel size until it saturates to a value of ~ 0.82. The 12×12 size of superpixel where NR saturates is slightly bigger larger than the near field coherence area in our experiment (see the next section). The NR for the equivalent coherent states, generated via splitting the seed beam on a 50/50 beamsplitter, stays constant at 1 within the error bars.

We see a similar behavior of the NR for the far field as shown in figure 5.5B. The expected spatial correlations here are due to the momentum correlations between the probe and the conjugate photons during the pair generation process, i.e. conservation of momentum in the transverse plane. Since the width of the pump beam is large, the transverse momentum uncertainty is relatively small. By using the momentum conservation, one can see that the twin beam momenta are oriented in the opposite direction in the transverse plane (see figure 4.2). As the transverse momentum is mapped to transverse position at the camera in the far field (see section 5.3), the correlated regions, and hence the intensity fluctuation lie in opposite sides of the twin beams with respect to the center (or the pump beam center) as shown in figure 5.2. To see the spatial noise reduction in this scenario, we rotate the conjugate intensity fluctuation (δC) image by 180° before subtracting is from the corresponding probe image (δP) which spatially aligns the correlated fluctuations in the two images. As mentioned the section 4.5, due to the finite waist of the pump beam at the nonlinear medium, the coherence area in the far field also has a finite size and, therefore, we do not expect point-to-point correlations in the corresponding far field (momentum) imaging. The corresponding NR in figure 5.5B for twin beams shows a gradual reduction of the spatial intensity noise in the subtraction image ($\delta P - \delta C$) at higher superpixel sizes. The NR saturates to a value of $\sim$0.83 below the classical limit at 13×13 superpixel size while the coherent state NR stays at the classical limit.

Although we will discuss the existence of spatial EPR entanglement in the next section, an

coherence area is proportional to $L^{1/2}$, where L is the length of non-linear medium[132,138–140] (see chapter 4).

alternative way to show the entanglement in the spatial correlations is using the inseparability criterion, which is based on the total (and unconditional) noise properties of the non-commuting position and momentum degrees of freedom. This criterion states that the addition of position-sum and momentum-difference variances must be bounded below by a certain value for separable states. Specifically, the inseparability parameter I must satisfy the the following relation [65]

$$I = \langle \Delta^2 \hat{R} \rangle + \langle \Delta^2 \hat{P} \rangle \geq 2, \tag{5.7}$$

where $\hat{R} = (\hat{\boldsymbol{r}}_{pr} - \hat{\boldsymbol{r}}_c)$ and $\hat{P} = (\hat{\boldsymbol{p}}_{pr} - \hat{\boldsymbol{p}}_c)$. The $\hat{\boldsymbol{r}}$ and $\hat{\boldsymbol{p}}$ are the photon transverse position and momentum operators for the bright twin beams, respectively and all variances are normalized to the corresponding shot noise. A violation of the above inequality indicates the presence of entanglement in the spatial degrees of freedom due to the inseparability of the joint quantum state in terms of position and momentum variables. When the analysis is performed in the near and far field, the two NRs correspond to $\langle \Delta^2 \hat{R} \rangle$ and $\langle \Delta^2 \hat{P} \rangle$, respectively. Based on our near and far field measurements, we find that a minimum value of I (the sum of the two NRs) is 1.67 ± 0.03, which verifies the presence of spatial entanglement in the bright twin beams.

5.5 Certification of EPR Correlations using Bright Beams

The EPR criterion introduced in chapter 4 is based on the measurement of relative uncertainties in the transverse position and momentum variables that show an apparent violation of the Heisenberg Uncertainty principle. For the simplicity of notation, we rewrite the EPR criterion in the vector form as

$$\Delta^2_{inf}(\boldsymbol{r}_c \,|\, \boldsymbol{r}_{pr})\, \Delta^2_{inf}(\boldsymbol{p}_c \,|\, \boldsymbol{p}_{pr}) \geq \frac{\hbar^2}{4}, \tag{5.8}$$

where $\Delta^2_{inf}(\boldsymbol{r}_c \,|\, \boldsymbol{r}_{pr})$ ($\Delta^2_{inf}(\boldsymbol{p}_c \,|\, \boldsymbol{p}_{pr})$) is the inferred variance of the conjugate photon position $\boldsymbol{r}_c$ (momentum $\boldsymbol{p}_c$) conditioned upon the measurement of the probe photon position $\boldsymbol{r}_{pr}$ (momentum $\boldsymbol{p}_{pr}$) in the near (far) field transverse plane. To calculate these position and momentum uncertainties, we first evaluate the spatial cross-correlation[4] between the probe and conjugate intensity fluctuation images using the following matrix expression

$$\mathrm{Corr}(i,j) = \frac{\sum\limits_{m,n} \delta P_{mn}\, \delta C_{(m-i)(n-j)}}{\sqrt{\left(\sum\limits_{m,n} \delta P^2_{mn}\right)\left(\sum\limits_{m,n} \delta C^2_{mn}\right)}}, \tag{5.9}$$

where δP and δC are 80×80 pixel regions cropped around the maximum intensity region in the probe and conjugate fluctuation images, respectively. The summation is done over all the values of the $\delta P/\delta C$ matrix elements, i.e. $1 \leq m, n \leq 80$. This approach to evaluate the spatial cross-correction is similar to overlaying one image over the other and evaluating the sum of all overlapping pixel correlations[5] and repeating the process again with a different amount of offset between the images.

[4] Instead of referring to the correlation between probe and conjugate beams simply as 'correlation', we prefer using the term 'cross-correlation' in order to distinguish it from the self or auto-correlations of the probe/conjugate beam with itself.

[5] A correlation between two pixels is just multiplication of the corresponding pixel values.

Similar to the evaluation of NR for the far field, the conjugate fluctuation images are rotated by 180°, prior to the evaluation of (5.9) for far field measurements, in order to account for momentum anti-correlation between the twin beams resulting from the phase matching condition.

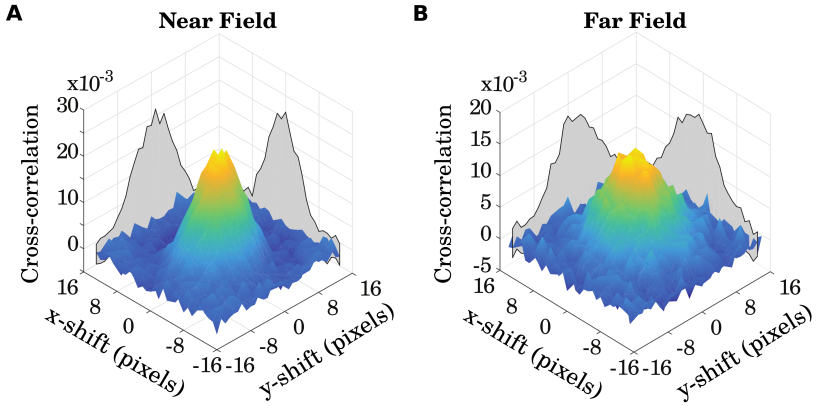

Figure 5.6: Experimental results showing the distribution of the spatial cross-correlation, evaluated using (5.9), between probe and conjugate intensity fluctuation images in the (A) near and the (B) far fields. The distributions are approximately Gaussian with peak a located at the zero offset. The standard deviation of these distributions are related to relative position and momentum uncertainties of the twin beams in the near and far field, respectively. Together these results point to the existence of EPR spatial correlations in the twin beams for the transverse position and momentum degrees of freedom. The plots shown here for spatial correlations are averaged over 200 acquisitions (frame pairs) both for the near and the far field. Figure adapted from ref[94]. Reproduced with permission.

The evaluated spatial cross-correlations between probe and conjugate beams, according to (5.9), are shown in figure 5.6. Both the near and far field spatial cross-correlations are roughly 2D Gaussian distributions with a central peak and a finite width. An approximately Gaussian nature of the cross-correlations implies that the region over which the spatial cross-correlation are distributed, i.e. the coherence area, is finite with a higher level of correlation at smaller offsets between the probe and conjugate images (see also chapter 4). For brevity, in the following description we also define the conditional uncertainty of a variable in terms of the standard deviation, i.e. $\Delta \boldsymbol{r} = \sqrt{\Delta^2(\boldsymbol{r}_c \,|\, \boldsymbol{r}_{pr})}$ and $\Delta \boldsymbol{p} = \sqrt{\Delta^2(\boldsymbol{p}_c \,|\, \boldsymbol{p}_{pr})}$. The distribution of the near and far field spatial correlations shown in figure 5.6 is proportional the conditional probability distributions $P(\boldsymbol{r}_c \,|\, \boldsymbol{r}_{pr})$ and $P(\boldsymbol{p}_c \,|\, \boldsymbol{p}_{pr})$, respectively. Their widths, given by the standard deviation σ of the Gaussian distributions (figure 5.6A and 5.6B), provide information about the conditional uncertainties in the transverse position $\Delta \boldsymbol{r}$ and the transverse momentum $\Delta \boldsymbol{p}$ degrees of freedom. To check the validity of these results, we also repeat this experiment with equivalent optical power coherent beams and perform the same data processing steps. The spatial cross-correlation plot for fluctuation images obtained using coherent pulses result in a distribution that is uniformly zero with no correlation peak, similar to the one shown in ref[93].

To extract the value of $\Delta \boldsymbol{r}$ and $\Delta \boldsymbol{p}$ from the distribution shown in figure 5.6, we use a 2D Gaussian function of the form $A\, e^{-\left[(x-x_0)^2/2\sigma_x^2 + (y-y_0)^2/2\sigma_y^2\right]}$, where A is constant, and fit the experimental plots using A, x_0, y_0, σ_x, and σ_y as parameters. From the fitting, we get the values of $\sigma_x = (4.27 \pm 0.10)$ pixels and $\sigma_y = (3.52 \pm 0.08)$ pixels for the near field, and $\sigma_x = (4.78 \pm 0.13)$ pixels and $\sigma_y = (4.90 \pm 0.13)$ pixels for the far field within the 95% confidence intervals of the fits. To calculate $\Delta \boldsymbol{r}$ and $\Delta \boldsymbol{p}$ from these standard deviations, we need to factor in the transformation performed by the optical elements for the near and far field imaging (see section 5.2). For the near

field, we take into account the magnification factor (M) of 0.65 which gives $\Delta \boldsymbol{r} = \boldsymbol{\sigma} s/M$, where $\boldsymbol{\sigma} = \{\sigma_x, \sigma_y\}$ and $s = 16\,\mu m$ is the linear pixel size of camera sensor. Similarly, for the far field we have the relation $\Delta \boldsymbol{p} = \hbar \Delta \boldsymbol{q} = \frac{\hbar k}{f} \boldsymbol{\sigma} s$, where $\lambda = 795$ nm and $f = 500$ mm is the focal length of the lens used to perform the f-to-f optical transformation. After taking these transformation into account, we calculate the R.H.S. of (5.8) along the x and y-directions as

$$\begin{aligned}(\Delta r_x)^2(\Delta p_x)^2 &= (1.62 \pm 0.12) \times 10^{-2}\hbar^2 < \hbar^2/4,\\ (\Delta r_y)^2(\Delta p_y)^2 &= (1.15 \pm 0.08) \times 10^{-2}\hbar^2 < \hbar^2/4.\end{aligned} \tag{5.10}$$

These results provide an experimental violation of the EPR criterion by more than an order of magnitude and verify the existence of spatial correlations in the bright twin beams with macroscopic number of photons. The results shown in (5.10) are obtained using the fits of the plots shown in figure 5.6 (average of 200 acquisitions).

As mentioned earlier, one advantage of bright beams is to be able to provide better signal-to-noise ratio in our measurements. Therefore, it should be possible to achieve an EPR certification via a statistically significant violation of the EPR criterion using fewer images. In order to analyze the scaling of the EPR violation with the number of images/acquisitions in the experiment, we use a confidence level parameter (C)[142] defined as

$$C_i = \left| \frac{1/4 - (\Delta r_i)^2(\Delta p_i)^2}{\delta_i} \right|, \tag{5.11}$$

where $i = \{x, y\}$ and δ_i is the standard deviation in the estimation of the product $(\Delta r_i)^2(\Delta p_i)^2$. In the following analysis, a violation of EPR criterion by more than 5 standard deviations, i.e. $C > 5$, is considered to be statistically significant. To calculate C, we calculate the near and far field spatial correlation, shown in figure 5.6, over N acquisitions and obtain the product $(\Delta r_i)^2(\Delta p_i)^2$. Therefore, for a total of 200 acquisitions, we have $200/N$ values of C corresponding to N acquisitions. That is, for $N = 5$, we have 40 different values of C, for $N = 10$, 20 different values of C, and so on. For each N, all the C values are averaged over to obtain a more accurate value. For δ, we use the 68% confidence interval from the 2D Gaussian fit and use error propagation to account for averaging. Figure 5.7A shows the scaling of confidence parameter C with the number of acquisitions N. The blue and green data points represent the values of C along the x and y axis, respectively. The dashed line represents the fit of function $C = b\sqrt{N}$, where b is a constant. Using the fit, we observe that C indeed scales as $\sqrt{N}$ which is expected. As shown in figure 5.7A, we have a statistically significant violation of EPR criterion even for 5 acquisitions. The variance product $(\Delta r_i)^2(\Delta p_i)^2$ is essentially constant as a function of N with a slight increase for low values (see figure 5.7B) of N due to noise in the spatial cross-correlations affecting the quality of the Gaussian fits. Here again we see the presence of EPR entanglement for $N = 5$. From the behavior of C with respect to $\sqrt{N}$, it is clear that a statistically violation of the EPR criterion is, in principle, possible with even with one acquisition. This is relatively novel when compared to $\geq 10^4$ images[132,142] or about three order of magnitude longer integration time[143] needed for photon pair experiments.

In the last two sections, we verified the presence of spatial entanglement in the twin beams using two distinct entanglement criterion. We saw a significantly larger violation of the EPR criterion even though it is more stringent than the inseparability criterion. This is because EPR correlations are purely spatial in nature and directly quantify the spatial quantum entanglement in our source. The inseparability criterion, on the other hand, quantifies quantum correlations that are dependent on both temporal and spatial degrees of freedom. We provide a more detailed discussion

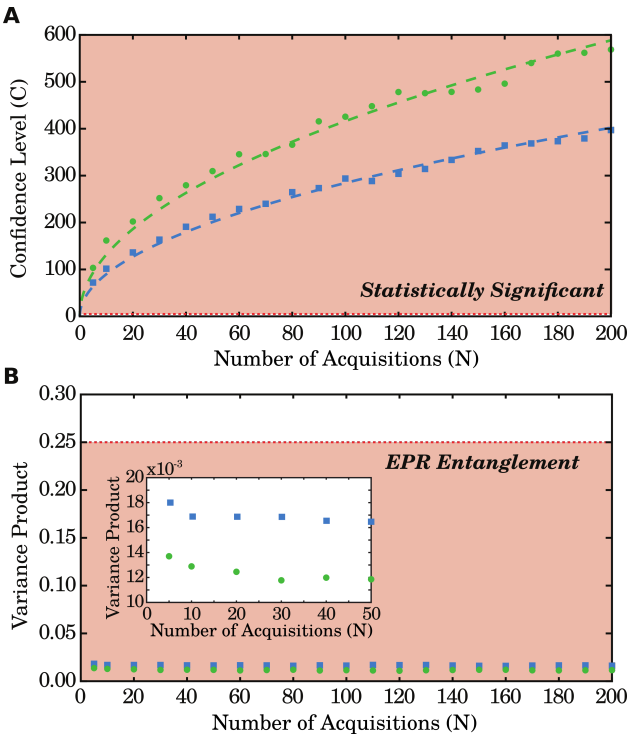

Figure 5.7: Behavior of confidence level parameter and the product $(\Delta r_i)^2(\Delta p_i)^2$ with respect to the number of acquisitions (N) used to get one variance product $(\Delta r_i)^2(\Delta p_i)^2$. The blue squares and green circles represent the analysis along x and y axis, respectively. (A) $\sqrt{N}$ scaling of confidence level expected from the dependence of signal-to-noise ratio on number of data points. The dashed lines represent the fit to curve $b\sqrt{N}$, with b as a fit parameter. The region above the red dotted line (near the bottom) corresponds to statistically significant violation of the EPR criterion. Based on the behavior of the fits, we see that it is possible to obtain EPR certification even with a single acquisition. (B) The position and momentum variance product $(\Delta r_i)^2(\Delta p_i)^2$ stays almost constant with respect N. The inset shows a zoom-in near the region of $N < 50$. Figure adapted from ref[94]. Reproduced with permission.

on the interplay between spatial and temporal squeezing in the appendix A in ref[94]. While the inseparability criterion does not provide a pure measure of the spatial degrees of freedom, it does point to the presence of entanglement in multiple degrees of freedom. The results discussed in this chapter, combined with previously reported results of quadrature entanglement [91,144] using the same FWM source, point to the presence of hyperentanglement in the spatial and temporal degrees of freedom in the generated twin beams.

CHAPTER 6

Information Encoding in Twin Beams

The generation of a large number of quantum-correlated photons with the ability to tune their spatio-temporal properties can be crucial for technologies utilizing spatial modes of light to encode information. The infinite dimensionality of the Hilbert space corresponding to the spatial degree of freedom promises to have a substantial impact on quantum information science by enabling protocols that provide higher density and better security of the information encoded [6,7,92,145,146]. Additionally, a high degree of control of the spatial properties of quantum-correlated photons would pave the way for real-world applications of quantum-enhanced spatial sensing, imaging [12,147] as well as direct encoding and transmission of secure information [148,149]. In this chapter, we describe and implement a scheme to control and engineer the spatial correlations in twin beams by taking advantage of their dependence on the momentum distribution of the input pump beam. By suitably modifying the momentum distribution of the input photons required for the non-linear process of four-wave mixing, we show [71] that it is possible to achieve an on-demand distribution of the spatial correlations for the generated twin beams. We later expand on this scheme and use it as a novel way to securely encode information in the twin beams such that it is only accessible via the joint measurements of the twin beams.

6.1 Effect of Pump Momentum on Spatial Correlations

We introduced the non-linear process of FWM in the earlier chapters and showed that two photons from the input pump field are simultaneously converted into a pair of correlated probe and conjugate photons. As a result of conservation of momentum between the input and output fields in the transverse plane, the momentum (far field) correlations between the probe and conjugate photons are dictated by the momentum distribution of the pump field. It is, therefore, natural to ask if one can modify the distribution of the far field correlations in a controlled way by modifying the pump momentum. In chapter 4, we derived an expression proving that, in the limit of weak focusing of

the pump beam[1], any broadening of the pump angular spectrum[2] leads to a corresponding spread in the relative transverse momentum correlations between the twin beams that are mapped to relative position correlations in the far field. Our preliminary experiments[151,152] indicated that going beyond such a spread requires additional modifications of the angular spectrum of the pump.

However, in order to further distribute these correlations in a desired way, one requires the knowledge of the exact dependence of the twin beam cross-correlation function on the pump momentum distribution in the FWM process. In other words, how the angular spectrum of the input pump beam (given by $\mathcal{E}(\boldsymbol{q}_p) = \mathcal{F}[E_o(\boldsymbol{\rho})]$, where $E_o(\boldsymbol{\rho})$ is the spatial profile of pump beam at the non-linear medium) affects the cross-correlation distribution function defined as

$$c_{\text{cross}}(\boldsymbol{x}_1, \boldsymbol{x}_2) \quad \equiv \quad \left\langle \delta\hat{N}_{pr}(\boldsymbol{x}_1; z_f)\, \delta\hat{N}_c(\boldsymbol{x}_2; z_f) \right\rangle . \tag{6.5}$$

Here $\boldsymbol{x}_1$ and $\boldsymbol{x}_2$ are the position coordinates in the far field transverse plane which is located at a distance of z_f along the z-axis. The function c_{cross}, which can be measured using spatial imaging of the twin beams in the far field, effectively captures the transverse momentum correlations between them. In order to derive the required connection between c_{cross} and $\mathcal{E}(\boldsymbol{q}_p)$, we take the interaction Hamiltonian of FWM as a starting point. By making some reasonable approximations in chapter 4, we showed that the interaction Hamiltonian has the form

$$\hat{\mathcal{H}} = i\hbar L\, \Gamma \iint d\boldsymbol{k}_{pr}\, d\boldsymbol{k}_c\, \mathbb{F}(\boldsymbol{k}_{pr}, \boldsymbol{k}_c) \hat{a}^\dagger_{\boldsymbol{k}_{pr}} \hat{b}^\dagger_{\boldsymbol{k}_c} + H.c.\,. \tag{6.6}$$

Using this interaction Hamiltonian and applying a first order perturbative expansion, we had also shown that the twin beam state $|\Psi_{\text{TBS}}\rangle$ for the probe and conjugate fields can be written as

$$|\Psi_{\text{TBS}}\rangle = e^{-\frac{i\hat{\mathcal{H}}t}{\hbar}} |\Psi_0\rangle \tag{6.7}$$

$$\simeq |\Psi_0\rangle + C \iint d\boldsymbol{k}_{pr}\; d\boldsymbol{k}_c\; \mathbb{F}(\boldsymbol{k}_{pr}, \boldsymbol{k}_c)\; \hat{a}^\dagger_{\boldsymbol{k}_{pr}}\, \hat{b}^\dagger_{\boldsymbol{k}_c} |\Psi_0\rangle\,, \tag{6.8}$$

where $|\Psi_0\rangle = \left|\{0\}_{\boldsymbol{k}_{pr}}, \{0\}_{\boldsymbol{k}_c}\right\rangle$ is the multimode vacuum state and C is constant (see section 4.4). The two-photon amplitude function $\mathbb{F}(\boldsymbol{k}_{pr}, \boldsymbol{k}_c) \equiv \Phi(\boldsymbol{q}_{pr} + \boldsymbol{q}_c)\, \text{sinc}(\Delta k_z L/2)$ dictates the spatial correlations between the probe and conjugate photons (the expression for $|\Psi_{\text{TBS}}\rangle$ in (6.8) can also be written in the single photon Fock basis, see chapter 4).

[1] The weak focusing limit[150] of a Gaussian beam in the context of a non-linear process can be defined as $z_R \gg L$, where z_R is the Rayleigh range of the beam and L is the length of the non-linear medium.

[2] The width of the pump angular spectrum is inversely proportional to width of the pump at the non-linear medium as

$$g(k) \equiv \mathcal{F}[f(x)] \tag{6.1}$$

$$= \frac{1}{\sqrt{2\pi}} \int dx\; e^{-ikx} f(x) \tag{6.2}$$

$$= \frac{1}{\sqrt{2\pi}} \int dx\; e^{-ikx} A_0\, e^{-x^2/2\sigma^2} \tag{6.3}$$

$$= \frac{A_0}{\sigma'}\; e^{-k^2/2\sigma'^2} \tag{6.4}$$

where $\sigma' = 1/\sigma$. Here we see that for a Gaussian beams of width σ, the angular spectrum is also a Gaussian with a width $1/\sigma$.

Using $|\Psi_{\text{TBS}}\rangle$, we can now calculate the expectation value of any near or far field observable. In general, for any observable A, the expectation value of the corresponding operator $\hat{A}$ is (up to first order expansion)

$$\begin{aligned}
\langle\Psi_{\text{TBS}}|\hat{A}|\Psi_{\text{TBS}}\rangle \simeq{}& \langle\Psi_0|\,\hat{A}\,|\Psi_0\rangle + C\iint d\boldsymbol{k}_{pr}\; d\boldsymbol{k}_c\; \mathbb{F}(\boldsymbol{k}_{pr},\boldsymbol{k}_c)\langle\Psi_0|\,\hat{A}\,\hat{a}^\dagger_{\boldsymbol{k}_{pr}}\,\hat{b}^\dagger_{\boldsymbol{k}_c}|\Psi_0\rangle \\
&+ C^*\iint d\boldsymbol{k}_{pr}\; d\boldsymbol{k}_c\; \mathbb{F}^*(\boldsymbol{k}_{pr},\boldsymbol{k}_c)\langle\Psi_0|\,\hat{b}_{\boldsymbol{k}_c}\;\hat{a}_{\boldsymbol{k}_{pr}}\;\hat{A}\,|\Psi_0\rangle \\
&+ |C|^2\iint d\boldsymbol{k}_{pr}\, d\boldsymbol{k}_c \iint d\boldsymbol{k}'_{pr}\, d\boldsymbol{k}'_c\; \mathbb{F}(\boldsymbol{k}_{pr},\boldsymbol{k}_c)\;\mathbb{F}^*(\boldsymbol{k}'_{pr},\boldsymbol{k}'_c)\langle\Psi_0|\,\hat{b}_{\boldsymbol{k}'_c}\;\hat{a}_{\boldsymbol{k}'_{pr}}\hat{A}\;\hat{a}^\dagger_{\boldsymbol{k}_{pr}}\,\hat{b}^\dagger_{\boldsymbol{k}_c}|\Psi_0\rangle \\
={}& \langle\Psi_0|\,\hat{A}\,|\Psi_0\rangle + 2\iint d\boldsymbol{k}_{pr}\, d\boldsymbol{k}_c\; \mathfrak{Re}\left[C\;\mathbb{F}(\boldsymbol{k}_{pr},\boldsymbol{k}_c)\langle\Psi_0|\hat{A}\;\hat{a}^\dagger_{\boldsymbol{k}_{pr}}\;\hat{b}^\dagger_{\boldsymbol{k}_c}|\Psi_0\rangle\right] \\
&+ |C|^2\iint d\boldsymbol{k}_{pr}\, d\boldsymbol{k}_c \iint d\boldsymbol{k}'_{pr}\, d\boldsymbol{k}'_c\; \mathbb{F}(\boldsymbol{k}_{pr},\boldsymbol{k}_c)\,\mathbb{F}^*(\boldsymbol{k}'_{pr},\boldsymbol{k}'_c)\langle\Psi_0|\,\hat{b}_{\boldsymbol{k}'_c}\,\hat{a}_{\boldsymbol{k}'_{pr}}\,\hat{A}\,\hat{a}^\dagger_{\boldsymbol{k}_{pr}}\,\hat{b}^\dagger_{\boldsymbol{k}_c}|\Psi_0\rangle.
\end{aligned} \tag{6.9}$$

As expected, we get three terms in our expansion that are independent, linear and quadratic with respect to the function $\mathbb{F}$.

Since we measure spatial intensity fluctuations of the bright images acquired by the EMCCD, a relevant observable is the cross-correlation between the spatial intensity fluctuations. The far field spatial cross-correlation function c_{cross} defined earlier is related to the transverse momentum correlations as

$$c_{\text{cross}}(\boldsymbol{x}_1,\boldsymbol{x}_2) \equiv \left\langle \delta\hat{N}_{pr}(\boldsymbol{x}_1;z_f)\,\delta\hat{N}_c(\boldsymbol{x}_2;z_f)\right\rangle \tag{6.10}$$

$$\underset{\text{optical system}}{\overset{f-\text{to}-f}{=}} \left\langle \delta\hat{N}_{pr}(\boldsymbol{q}_1;z_o)\,\delta\hat{N}_c(\boldsymbol{q}_2;z_o)\right\rangle \tag{6.11}$$

$$= \left\langle \delta\hat{N}_{pr}(\boldsymbol{q}_1,k_1^z)\,\delta\hat{N}_c(\boldsymbol{q}_2,k_2^z)\right\rangle\Big|_{z=z_0}, \tag{6.12}$$

where $\boldsymbol{x}_1$ and $\boldsymbol{x}_2$ are the transverse measurement positions in the far field, z_f and z_o indicate the far field and near field (Rb cell center) locations along the z-axis, respectively and $\delta\hat{N} = \hat{N} - \langle\hat{N}\rangle$ is the photon number fluctuation operator. To arrive at (6.11), we use the fact that an f-to-f optical system maps the transverse momentum distribution at the cell center to a position distribution in the far field plane at z_f where measurements are performed. Therefore, a photon with transverse momentum $\boldsymbol{q}$ is mapped to spatial location $\boldsymbol{x} = f\boldsymbol{q}/k$ in the far field. In the last expression (6.12), the z-component of the corresponding k-vector is given by $k^z = \sqrt{k - |\boldsymbol{q}|}$. As we explained in chapter 5, in the limit of bright optical fields, the photon number/intensity fluctuations and amplitude quadrature fluctuations are related by

$$\delta\hat{N}(\boldsymbol{x}) \simeq \sqrt{2}\,|\alpha|\delta\hat{X}(\boldsymbol{x}), \tag{6.13}$$

where $|\alpha| = \sqrt{\langle\hat{N}\rangle}$. Using (6.13), we can write the spatial cross-correlation in terms of the quadra-

ture operators as

$$c_{\text{cross}}(\boldsymbol{x}_1,\boldsymbol{x}_2) \overset{\text{bright limit}}{\propto} \left\langle \delta\hat{X}_{pr}(\boldsymbol{x}_1;z_f)\,\delta\hat{X}_c(\boldsymbol{x}_2;z_f)\right\rangle \tag{6.14}$$

$$\overset{\substack{f-\text{to}-f\\ \text{optical system}}}{=} \left\langle \delta\hat{X}_{pr}(\boldsymbol{q}_1;z_o)\,\delta\hat{X}_c(\boldsymbol{q}_2;z_o)\right\rangle \tag{6.15}$$

$$= \left\langle \delta\hat{X}_{pr}(\boldsymbol{q}_1,k_1^z)\,\delta\hat{X}_c(\boldsymbol{q}_2,k_2^z)\right\rangle\Big|_{z=z_0} \tag{6.16}$$

$$= \left\langle \delta\hat{X}_{pr}(\boldsymbol{k}_1)\,\delta\hat{X}_c(\boldsymbol{k}_2)\right\rangle\Big|_{z=z_0}, \tag{6.17}$$

Using (6.12), we can choose a suitable observable 'A' for the present experiment as

$$\hat{A} \equiv \delta\hat{X}_{pr}(\boldsymbol{k}_1)\delta\hat{X}_c(\boldsymbol{k}_2). \tag{6.18}$$

where $\boldsymbol{k}_1$, $\boldsymbol{k}_2$ are the k-vectors mapped to measurement positions $\boldsymbol{x}_1,\boldsymbol{x}_2$ in the far field location $z=z_f$, respectively. Suppressing the k-vector dependence of the quadrature operators for clarity and using $\langle\Psi_{\text{TBS}}|\hat{A}|\Psi_{\text{TBS}}\rangle = \langle\hat{A}\rangle$, the expectation value of $\hat{A}$ can be simplified as

$$\langle\hat{A}\rangle = \langle\delta\hat{X}_{pr}\,\delta\hat{X}_c\rangle \tag{6.19}$$

$$= \left\langle \hat{X}_{pr}\hat{X}_c - \hat{X}_{pr}\langle\hat{X}_c\rangle - \hat{X}_c\langle\hat{X}_{pr}\rangle + \langle\hat{X}_{pr}\rangle\langle\hat{X}_c\rangle\right\rangle \tag{6.20}$$

$$= \langle\hat{X}_{pr}\,\hat{X}_c\rangle. \tag{6.21}$$

Here we used the fact that $\langle\hat{X}\rangle = \langle(\hat{a}+\hat{a}^\dagger)\rangle/\sqrt{2}$ vanishes for $|\Psi_{\text{TBS}}\rangle$ in (6.20). Finally, substituting the final expression of $\langle\hat{A}\rangle$ above in (6.9) with corresponding k-vectors, we get

$$\langle\hat{A}\rangle \simeq \langle\Psi_0|\,\hat{X}_{pr}(\boldsymbol{k}_1)\hat{X}_c(\boldsymbol{k}_2)\,|\Psi_0\rangle + 2\iint d\boldsymbol{k}_{pr}\,d\boldsymbol{k}_c\;\mathfrak{Re}\left[C\,\mathbb{F}(\boldsymbol{k}_{pr},\boldsymbol{k}_c)\langle\Psi_0|\hat{X}_{pr}(\boldsymbol{k}_1)\hat{X}_c(\boldsymbol{k}_2)\,\hat{a}^\dagger_{\boldsymbol{k}_{pr}}\hat{b}^\dagger_{\boldsymbol{k}_c}|\Psi_0\rangle\right]$$
$$+ |C|^2\iint d\boldsymbol{k}_{pr}\,d\boldsymbol{k}_c\iint d\boldsymbol{k}'_{pr}\,d\boldsymbol{k}'_c\,\mathbb{F}(\boldsymbol{k}_{pr},\boldsymbol{k}_c)\,\mathbb{F}^*(\boldsymbol{k}'_{pr},\boldsymbol{k}'_c)\langle\Psi_0|\,\hat{b}_{\boldsymbol{k}'_c}\,\hat{a}_{\boldsymbol{k}'_{pr}}\hat{X}_{pr}(\boldsymbol{k}_1)\hat{X}_c(\boldsymbol{k}_2)\,\hat{a}^\dagger_{\boldsymbol{k}_{pr}}\hat{b}^\dagger_{\boldsymbol{k}_c}|\Psi_0\rangle \tag{6.22}$$

$$= \iint d\boldsymbol{k}_{pr}\,d\boldsymbol{k}_c\;\mathfrak{Re}\left[C\;\mathbb{F}(\boldsymbol{k}_{pr},\boldsymbol{k}_c)\langle\Psi_0|\;(\hat{a}_{\boldsymbol{k}_1}\hat{b}_{\boldsymbol{k}_2}+\hat{a}_{\boldsymbol{k}_1}\hat{b}^\dagger_{\boldsymbol{k}_2}+\hat{a}^\dagger_{\boldsymbol{k}_1}\hat{b}_{\boldsymbol{k}_2}+\hat{a}^\dagger_{\boldsymbol{k}_1}\hat{b}^\dagger_{\boldsymbol{k}_2})\;\hat{a}^\dagger_{\boldsymbol{k}_{pr}}\;\hat{b}^\dagger_{\boldsymbol{k}_c}|\Psi_0\rangle\right] \tag{6.23}$$

$$= \iint d\boldsymbol{k}_{pr}\,d\boldsymbol{k}_c\;\mathfrak{Re}\left[C\;\mathbb{F}(\boldsymbol{k}_{pr},\boldsymbol{k}_c)\langle\Psi_0|\;\hat{a}_{\boldsymbol{k}_1}\hat{a}_{\boldsymbol{k}_2}\;\hat{a}^\dagger_{\boldsymbol{k}_{pr}}\;\hat{a}^\dagger_{\boldsymbol{k}_c}|\Psi_0\rangle\right] \tag{6.24}$$

$$= \iint d\boldsymbol{k}_{pr}\,d\boldsymbol{k}_c\;\mathfrak{Re}\left[C\;\mathbb{F}(\boldsymbol{k}_{pr},\boldsymbol{k}_c)\right]\delta_{\boldsymbol{k}_1,\boldsymbol{k}_{pr}}\delta_{\boldsymbol{k}_2,\boldsymbol{k}_c} \tag{6.25}$$

$$= \mathfrak{Re}\left[C\;\Phi(\boldsymbol{q}_1+\boldsymbol{q}_2)\right]\text{sinc}(\Delta k_z L/2). \tag{6.26}$$

Note that in (6.22), only the second term is non-zero. Referring to the expression in (6.26), if correlations are measured within a small region around the optimal direction inside the emission cone of the FWM process then the phase-mismatch (Δk_z) is close to zero and the sinc function can be taken as unity[153,154]. In our experiments, the measurement regions in the far field lie within the bright region of the probe and conjugate beams (acting as effective LOs for quadrature amplitude fluctuations) and represent a smaller region in the full FWM spatial bandwidth (see figure 4.4). This implies that the sinc function can be uniformly taken to be unity for the corresponding spatial

measurements in the far field. The function Φ depends on the convolution of the angular spectrum of the two pump photons involved in FWM, and has the form (see (4.11))

$$\Phi(\boldsymbol{q}_1 + \boldsymbol{q}_2) \equiv \int d\boldsymbol{q}_p \, \mathcal{E}_o(\boldsymbol{q}_p) \, \mathcal{E}_o(\boldsymbol{q}_1 + \boldsymbol{q}_2 - \boldsymbol{q}_p), \tag{6.27}$$

where $\mathcal{E}_o(\boldsymbol{q}_p)$ is the angular spectrum of the pump beam.

Expressing (6.26) in terms of far field position coordinates $(\boldsymbol{x}_1, \boldsymbol{x}_2)$, we get

$$c_{\text{cross}}(\boldsymbol{x}_1, \boldsymbol{x}_2) \overset{\text{bright limit}}{\propto} \left\langle \delta\hat{X}_{pr}(\boldsymbol{x}_1) \delta\hat{X}_c(\boldsymbol{x}_2) \right\rangle \;\propto\; \mathfrak{Re}\left[\Phi(\boldsymbol{x}_1 + \boldsymbol{x}_2)\right], \tag{6.28}$$

where we have taken the constant C ($\propto \chi^{(3)} L\, t$) to be real without the loss of generality, as the phase of the non-linear response $\chi^{(3)}$ of the atomic Rb vapor can be taken as zero and serve as a phase reference to the optical fields involved in the FWM process. We can now conclude that far field correlations between probe and conjugate photons depend on the angular spectrum of the pump beam with the exact functional dependence outlined in (6.28). One can, therefore, control the way correlations are distributed in the far field via a suitable modification of the pump beam. Recall that for a plane wave pump, a non-zero correlation between probe and conjugate photons is possible only if $-\boldsymbol{x}_1 = \boldsymbol{x}_2$ (or $\boldsymbol{q}_1 + \boldsymbol{q}_2 = 0$) which implies a strict conservation of transverse momentum. However, for a finite size pump beam, a non-zero correlation is possible for $-\boldsymbol{x}_1 \approx \boldsymbol{x}_2$ (up to the uncertainty in transverse momentum). Hence, we define $\boldsymbol{\xi}_+ = \boldsymbol{x}_1 + \boldsymbol{x}_2$ and $\boldsymbol{x}_1 = \boldsymbol{x}$ to rewrite (6.28) as,

$$c_{\text{cross}}(\boldsymbol{x}_1, \boldsymbol{x}_2) \overset{\text{bright limit}}{\propto} \left\langle \delta\hat{X}_{pr}(-\boldsymbol{x}) \delta\hat{X}_c(\boldsymbol{x} + \boldsymbol{\xi}_+) \right\rangle \;\propto\; \mathfrak{Re}\left[\Phi(\boldsymbol{\xi}_+)\right]. \tag{6.29}$$

Equation (6.29), highlights an important aspect of the correlation function c_{cross} which is that it is translationally invariant with respect to $\boldsymbol{x}$ and that the cross-correlation depends only on the relative distance $\boldsymbol{\xi}_+$. The value $\boldsymbol{x} = 0$ (i.e. $\boldsymbol{q} = 0$) is located at the center of the sinc ring (see figure 4.4) which is also the geometric center of the pump beam in the far field. We take advantage of this translation symmetry in our data analysis by averaging the c_{cross} over all the experimentally available values of $\boldsymbol{x}$. This averaging leads to a significant improvement in the signal-to-noise ratio for the measured correlation functions.

6.2 FWM with Modified Pump and Correlation Measurement

To control the distribution of the spatial correlations in the far field, we spatially structure the high power pump beam prior to the FWM process to achieve a desired angular spectrum. The angular spectrum of pump can be modified via both amplitude and/or phase changes in the input pump electric field. However, in our experiment, we restrict to only phase changes to modify the pump's angular spectrum. We use a spatial light modulator (SLM) device to implement relevant phase changes in the pump electric field. The use of SLM in a phase-only configuration has the advantage of not reducing the power of the pump significantly, as the gain of the FWM and thus the temporal quantum correlations of the twin beams are limited by the pump intensity.

Given a predefined pattern for the cross-correlations, referred to here as 'target', we imprint the required phase distribution on the pump beam in the form of a phase-only computer-generated

hologram (CGH) using the SLM. As shown in figure 6.1, for the chosen target pattern of the University of Oklahoma (OU) logo, we calculate a CGH which is transferred to the SLM device. A $4f$ imaging system, constructed using two identical achromatic 300 mm (Thorlabs AC254-300-B-ML) lenses, maps the SLM plane to the Rb cell location with magnification of 1. Given that the angular spectrum of the pump is a complex quantity, the implemented phase-only CGH has to be designed to produce the calculated amplitude and phase for the pump's angular spectrum. Any deviation will affect the real part of the convolution function and hence the fidelity of the information encoded in the far field spatial correlations. To minimize such deviations, we implement a mixed-region-amplitude-freedom (MRAF) algorithm coupled with conjugate-gradient optimization to calculate the required CGH[155].

For a input Gaussian electric field pump beam with a flat wavefront, the angular spectrum has the form

$$\mathcal{E}_o(\boldsymbol{q}_p) = \frac{1}{2\pi}\int d\boldsymbol{q}_p\, E_o(\boldsymbol{\rho}) e^{-i\boldsymbol{q}_p\cdot\boldsymbol{\rho}}, \tag{6.30}$$

where $\boldsymbol{\rho}$ is the 2D position vector in the transverse plane, $E_o(\boldsymbol{\rho})$ is the Gaussian amplitude of the input pump electric field. After a reflection from SLM, the pump field can be written as

$$\mathcal{E}_o(\boldsymbol{q}_p) = \frac{1}{2\pi}\int d\boldsymbol{q}_p\, E_o(\boldsymbol{\rho}) e^{i\phi(\boldsymbol{\rho})} e^{-i\boldsymbol{q}_p\cdot\boldsymbol{\rho}}, \tag{6.31}$$

where $\phi(\boldsymbol{\rho})$ is the position dependent phase pattern imparted during reflection and hence, the information to modify the angular spectrum is encoded in $\phi(\boldsymbol{\rho})$ by the SLM. Using the convolution theorem, we can drive an alternate form of $\Phi(\boldsymbol{\xi}_+)$ that is more useful in the context of a phase pattern

$$\begin{aligned}
\Phi &= (\mathcal{E}_o \star \mathcal{E}_o) && (6.32)\\
&= \mathcal{F}_f\left[E_o(\boldsymbol{\rho}) e^{i\phi(\boldsymbol{\rho})}\right] \star \mathcal{F}_f\left[E_o(\boldsymbol{\rho}) e^{i\phi(\boldsymbol{\rho})}\right] && (6.33)\\
&= \mathcal{F}_f\left[\left(E_o(\boldsymbol{\rho}) e^{i\phi(\boldsymbol{\rho})}\right)^2\right] = T, && (6.34)
\end{aligned}$$

where $\mathcal{F}_f$ is the Fourier transform[3] and $\star$ denotes the convolution operation. Here, T is the target distribution related to the electric field of pump by above expressions. In (6.34) , we see that the phase imparted to the pump electric should be such that the Fourier transform of the square of the field should be equal to the target distribution. The chosen target distribution of OU logo is a real valued distribution and therefore, the corresponding imaginary part is zero. A detailed account of the implemented algorithm for the phase-only CGH calculation, optimized with respect to the SLM device (Hamamatsu LCOS-SLM X13138), is given in appendix A.

To generate bright twin beams via a stimulated FWM process, for a higher signal-to-noise ratio in the intensity fluctuation measurements, we use a weak probe beam as a seed (see figure 6.1). When

[3]The Fourier transform $g(\boldsymbol{x})$ of an optical field $f(\boldsymbol{\rho})$ can be given as[105,156]

$$\begin{aligned}
g(\boldsymbol{x}) &= \mathcal{F}_f[f(\boldsymbol{\rho})](\boldsymbol{x}) && (6.35)\\
&= \frac{1}{2\pi}\int d\boldsymbol{\rho}\, f(\boldsymbol{\rho})\, e^{-i\frac{2\pi}{\lambda f}\boldsymbol{x}\cdot\boldsymbol{\rho}}, && (6.36)
\end{aligned}$$

where λ is the wavelength of the optical field and f is focal length of the lens.

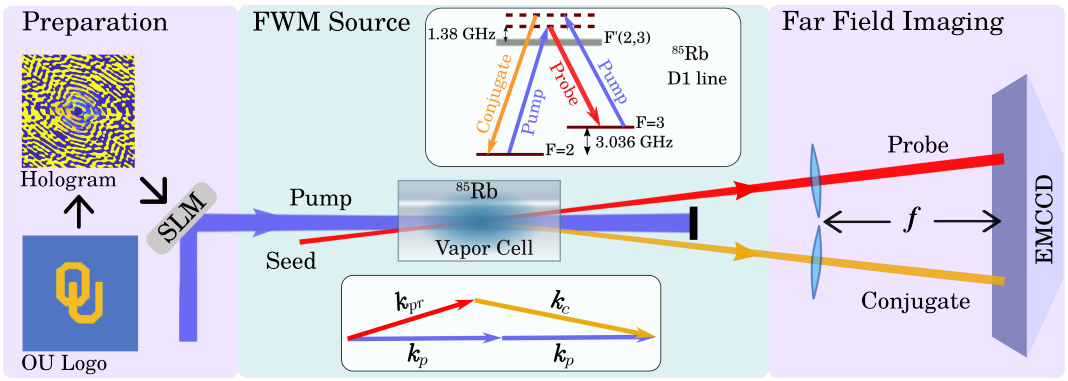

Figure 6.1: Experimental setup for encoding a target pattern in the distribution of the spatial correlations of twin beams. A hot Rb vapor cell is used as the nonlinear medium needed for the FWM process that generates quantum-correlated twin beams. The FWM is based on a double-Λ configuration in the D1 transition of ^{85}Rb atoms, as shown on the top inset. The pump beam, after reflection from the SLM device, acquires a phase which imparts it with the necessary momentum distribution (angular spectrum) for the desired correlation distribution in the far field. From the SLM, the phase-structured pump is then imaged to the center of the cell via a $4f$ optical system. In order to generate bright twin beams, we seed the FWM with an input probe beam to achieve a photon flux of $\sim 10^{14}$ photons/s per output beam, which is limited by saturation of the EMCCD. Finally, the momentum distribution of the probe and the conjugate beams is mapped to a position distribution onto the EMCCD camera in the far field using a f-to-f imaging system. Images acquired by the EMCCD are then used to measure the spatial intensity fluctuations and extract the cross-correlation between the twin beams. The inset at bottom shows the phase-matching for the non-linear geometry used in this experiment which needs to be satisfied for an efficient FWM process. Figure adapted from [71]. Reproduced with permission.

seeded, the FWM amplifies the input probe beam and generates a bright conjugate beam to produce bright twin beams. Tuning the number of photons in the input seed allows us to have a control over the number of correlated photons in the bright twin beams. For the present experiment [71], our non-linear medium is a natural abundance Rb vapor cell (1 inch diameter and 12.7 mm length) which is placed at the intersection of orthogonally polarized pump and probe beams with their beam-waist overlapping at the center of the cell. The $1/e^2$ waist diameter is 4.4 mm for the pump and 0.4 mm for the probe. In the non-collinear geometry, the pump and the probe beams are then made to intersect at an angle of 0.4 degrees inside the cell which is held at a temperature of 114°C. With this configuration, we obtain a gain of ~ 2.6, which is limited by the maximum optical power available for the pump beam.

We implement FWM in a double-Λ configuration in D1 transition of ^{85}Rb and blue-shift the pump frequency to avoid absorption. The pump beam has ~2 W intensity and is blue-detuned by 1.38 GHz from the $F = 2 \rightarrow F' = 3$ transition (see figure 6.1, top inset). Similar to our previous experiments, the input pump field is at much higher intensity than the generated probe and conjugate fields and is essentially acting as a reservoir of photons. It does not share correlations with the probe and conjugate beams within the experimental range of gain values. A small portion of the pump is red-shifted by 3.04 GHz to generate the input seed probe using an acousto-optic modulator. After the Rb vapor cell, a polarization filter is used to filter out the uncorrelated pump beam. However, the phase manipulation of the pump using the SLM results in scattering of a relatively high number of pump photons past the polarization filter and thus reaching our EMCCD sensor. In order to absorb these unwanted pump photons selectively, we place an additional isotopically pure ^{87}Rb 3-inch cell heated to 97°C before the EMCCD camera. We also use a higher than usual one-

photon detuning (Δ =1.38 GHz mentioned above) which lowers the pump transmission to ∼10% through the ^{87}Rb cell. The pump photons are absorbed via the F=1 → F' transition in ^{87}Rb while transmission of probe and conjugate beams remains at ≥ 90%.

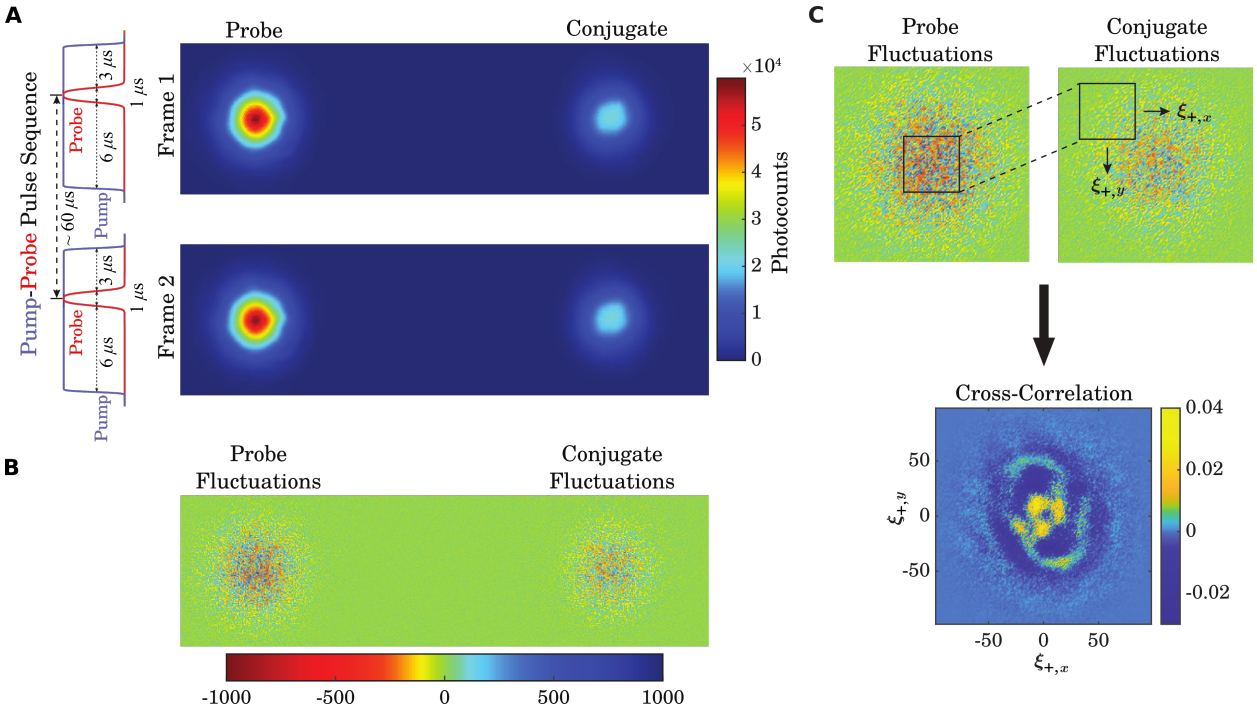

Figure 6.2: Image acquisition for intensity fluctuation measurement in the bright beams and cross-correlation of the corresponding spatial fluctuations. (A) Images of bright probe and conjugate beams in two consecutive frames. The images are acquired using a pump beam modified with the OU logo phase-pattern. The pump-probe pulse sequence which is the same as the one used for EPR experiment, (shown on the left) is synchronized with the acquisition of two consecutive frames of the EMCCD. The separation between two seed probe pulses is ∼60 μs. (B) Intensity fluctuation images for the probe (left) and conjugate (right) beams obtained after a pixel to pixel subtraction between frames 1 and 2. (C) After rotation of one of the fluctuation images, the evaluation of the 2D spatial correlation gives the distribution of the c_{cross} correlation function. The plot of c_{cross} function is in the EMCCD camera pixel basis (pixel size = 16×16 μm^2). The final result shown here is averaged over 2000 acquisitions. Figure adapted from [71]. Reproduced with permission.

In order to measure the momentum correlations as determined by $\Phi(\boldsymbol{\xi}_+)$, the optical Fourier transform mentioned in (6.11) is realized by placing two 500 mm lenses in a f-to-f configuration, one each for the probe and the conjugate beam paths, between the cell and EMCCD as shown in figure 6.1. This configuration maps the transverse momentum correlations at the cell center ($z = z_0$) to transverse position correlations at the EMCCD location ($z = z_f$). The procedure to extract the spatial intensity fluctuations from bright probe and conjugate images is similar to the one used in the EPR-correlation experiment [94] (see chapter 5). We take two frames, each with bright probe and conjugate images, in a rapid succession using the kinetics mode of the EMCCD. The timing sequence for the pump and probe pulses as well as the delay of ∼60 μs between the frames are shown in figure 6.2A. A probe pulse delay of 6 μs with respect to the pump pulse is used to avoid transient effects in the FWM. The active acquisition area on the EMCCD sensor is divided into six frames each with 170 rows × 512 columns. The two successive frames, frame 1 and 2 in figure 6.2A, provide images of the spatial intensity fluctuations in each beam after subtraction (figure 6.2B).

Given that the two consecutive frames are taken with a time difference longer than the inverse of the bandwidth of the FWM process ($\sim 1/20$ MHz $= 50$ ns), the subtraction does not impact the quantum correlations between the twin beam images. The peak intensity region of the probe beam has $\sim 5 \times 10^4$ photocounts per pixel with a corresponding magnitude of intensity fluctuations as $\sim$1000. Before calculating the cross-correlation between the intensity fluctuation images, we rotate one of the image by 180° to account for the transverse momentum anti-correlations between the probe and conjugate beams expressed in the form of a negative position argument in (6.29).

For each acquisition (pair of frames), the cross-correlation evaluation gives the distribution of c_{cross} as a function of the relative distance $\boldsymbol{\xi}_+$ between the fluctuation images. The final result, shown in figure 6.2C is then averaged over many acquisitions for a better signal-to-noise ratio. In principle, one can also directly calculate the convolution between images, without performing any rotations, to arrive at the same result as the two methods are equivalent[4].

6.3 Information Encoding with Engineered Correlations

The entangled twin beams are at the heart of a number of applications in quantum information science and quantum sensing as they provide a natural bipartite system with quantum correlations in multiple degrees of freedom[157]. In particular, the use of spatial quantum correlations is expected to have a substantial impact on emerging quantum information applications, such as the quantum internet[158] and quantum computation[159], due to the infinite dimensionality of the corresponding Hilbert space. In the previous section, we showed that by using a spatially structured pump we can experimentally achieve a desired distribution of spatial correlations in the quantum-correlated twin beams. Our result shows a high degree of control over the spatial properties of the twin beams that can be potentially used as a novel way to encode quantum information in the system. In this section, we further explore the capability of our system to encode information by providing a systematic comparison between target, simulated and experimentally obtained cross-correlations.

To provide these comparisons, we choose two target patterns, more specifically the OU logo and ħ (Planck's constant), to be encoded as far field spatial correlations between the twin beams, as shown in figures 6.3A and 6.3E, respectively. Using the MRAF algorithm, we calculate the optimized 1024×1024 pixels phase holograms (figures 6.3B and 6.3F, see appendix A for algorithm and optimization details). The CGH or phase hologram is the discrete pattern corresponding to continuous phase pattern $\phi(\boldsymbol{\rho})$ mentioned in (6.31). During the CGH calculation, the limited size and resolution of the SLM device are taken into account. Substituting the calculated CGH in expression (6.32), we plot the simulation patterns (in EMCCD pixel basis) taking into account the limited spatial and phase resolution (8-bit) of the SLM as well as finite spatial resolution of the EMCCD. The plots of the simulated patterns (figures 6.3C and 6.3G) are in excellent agreement with the measured cross-correlations (figures 6.3D and 6.3H). Therefore, our results show that by using the present approach of pump modification one can achieve arbitrary distributions in the twin beam spatial correlations. In the past, a similar approach to modify the spatial correlations in the twin beams by exploring the relationship between the spatial properties of the pump and the twin beams has been studied theoretically[160]. In addition, a few SPDC experiments[161,162] have

[4]For functions $f(\boldsymbol{x})$ and $g(\boldsymbol{x})$,

$$[f(\boldsymbol{x}) \star g(\boldsymbol{x})](\boldsymbol{x}) = [f(-\boldsymbol{x}) * g(\boldsymbol{x})](\boldsymbol{x}), \tag{6.37}$$

where $\star$ denotes convolution and $*$ denotes cross-correlation operation.

6.3 Information Encoding with Engineered Correlations

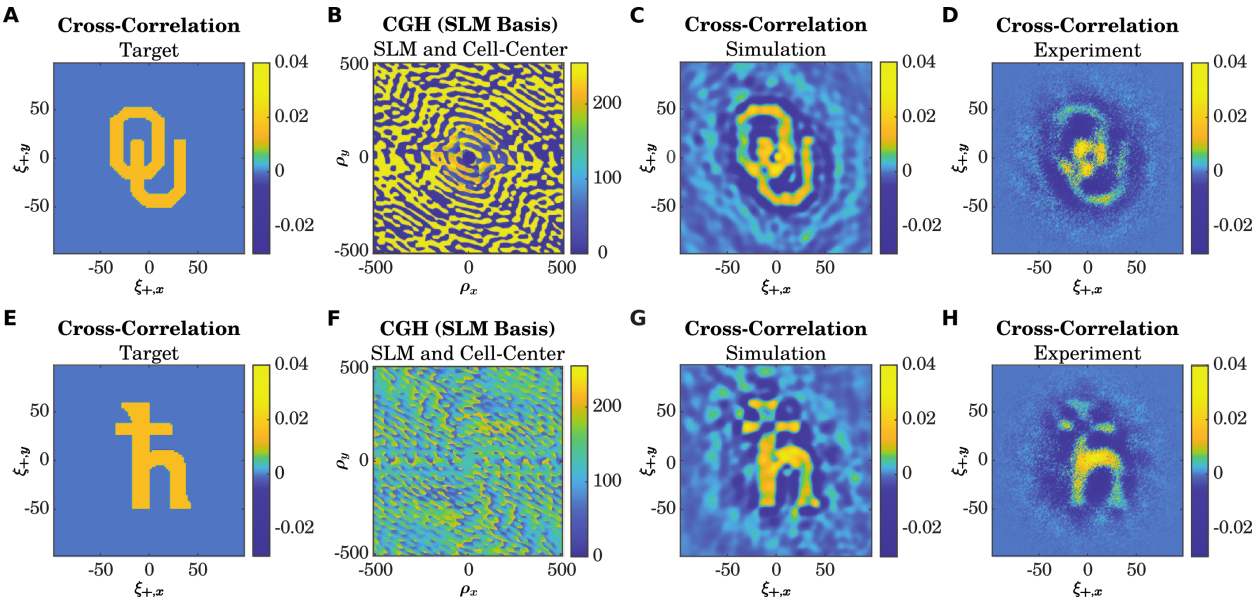

Figure 6.3: Information encoding via control of the spatial correlations in the twin beams along with a comparison of the target patterns (OU logo and ħ) with simulated and experimental results. All figures, except for the CGH, are in the EMCCD pixel basis (pixel size = 16×16 μm^2) in the far field. (A and E) Target patterns according to which the corresponding holograms (B and F) are developed using a MRAF algorithm. The color bar for the CGH figures corresponds to the 8-bit ($2^8 = 256$) phase values from 0 to 2π. The dimensions of the SLM pixels (12.5×12.5 μm^2), its 8-bit phase resolution, the f-to-f mapping and finite resolution of the EMCCD sensor are taken into account while calculating the simulated correlations (C and G) which represent real part of the $\Phi(\boldsymbol{\xi}_+)$ function. The spatial cross-correlations between the probe and conjugate intensity fluctuations show the experimental c_{cross} distributions (D and H). All cross-correlation plots are normalized by the sum of squared-amplitude of all pixel values to provide a better comparison between target and simulation/experimental results. The maximum pixel values are larger in the experimental and simulated correlations compared to the target pattern because of the non-uniform distribution resulting from the non-ideal setup and CGH phase values. One may notice a small rotation (∼5°) in the experimental c_{cross} distributions that is due to optical alignment imperfections. Figure adapted from [71]. Reproduced with permission.

shown that a modification of pump spatial structure leads to a change of the spatial correlation between twin beam photons. In case of the FWM process, similar results with limited modification in spatial correlations have also been observed [141,163–166]. However, the results presented here go beyond these proof-of-principle demonstrations and provide a path towards the redistribution of twin beam spatial correlations as a viable approach for information encoding.

The maximum allowed resolution of a spatial pattern in the spatial correlations for the twin beams is limited by the number of correlated spatial modes supported by the non-linear process. Along with the results achieved in the past [91,119,167], our present findings [71,94] point towards the highly spatially multimode nature of the FWM process. In the context of the present experiment, the resolution of a far field cross-correlation pattern is limited by the size of the far field coherence area which also gives a practical way to estimate the number of independently correlated spatial regions [119]. In chapter 4, we showed that the size of the far field coherence area is inversely proportional to the size of the pump waist at the cell center[5], as shown in section 4.5. In our

[5]The size of the far field coherence area denotes the relative uncertainty in the transverse momentum between the twin beams and, therefore, is equal to the square root of the relative transverse momentum variance (i.e. the standard deviation).

experiments, the size of the pump beam is limited by the maximum output power of the Ti:Sapphire laser used. In addition to these limitations, a significant deviation from the target pattern occurs due to a non-ideal optimization of the CGH. Consequently, we see a degradation of the resolution in the simulated patterns in comparison to the corresponding targets. While comparing the simulated and experimental cross-correlations, there are several factors that lead to additional discrepancies. First, there is a typical decrease in the efficiency of the SLM at higher spatial frequencies[168,169] that limits the spatial bandwidth of the angular spectrum imparted to the pump beam. Second, for a given phase encoding on the pump beam, our simulated pattern based on (6.29) only accounts for the leading order contributions in the FWM process while the experimental cross correlations contain contributions from all the higher order terms. However, despite all these limitations (most of which are technical), we have enough resolution in the present configuration to manipulate a 12× 12 superpixel grid (each superpixel with 10× 10 pixels) with individual superpixel control. If we now consider a simple binary encoding of 0 and 1 (i.e. low and high) for each superpixel, we would be able to encode 144 bits of information in a single pattern. By coupling this scheme with novel spatial light modulators with GHz modulation rates[170], encoding rates exceeding Gbps can be achieved. This point illustrates potential use of engineered correlations in twin beams in the field of continuous variable quantum secure communication[148,149].

The spatial modes of light, as a classical system, have been already used to establish free-space as well as fiber based communication channels[171–173] for high-capacity transmission. However, in the quantum regime, this has been an elusive task due to the limited control and manipulation of spatial correlations. Therefore, an ability to encode and share information using engineered correlations in the spatio-temporal modes of quantum states of light is crucial for emerging applications in quantum communication. For quantum-enhanced imaging and sensing applications, in which the presence of multiple spatial modes can lead to enhanced resolution and sensitivity[68,174,175], engineering of spatial modes can give rise to structured quantum states of light with a mode structure that can be optimized for specific applications[9,176]. At the fundamental level, changes in of spatial correlations via the manipulation of the pump provides a systematic way to study and understand how quantum correlations between various spatial modes of light are generated as a result of a non-linear optical process. This knowledge can be useful in exploring new applications towards quantum information and scalable quantum computation[159]. Our present approach and results show that, by taking advantage of the dependence on pump for such a multimode process, we can effectively introduce quantum correlations between specific spatial modes of the twin beam photons.

6.4 Control of the Degree of Correlation via Quadrature Selection

During the spontaneous (non-collinear) FWM process, the correlated probe and conjugate fields lie within an emission cone similar to the non-collinear type-1 PDC[150]. As we described in detail in chapter 5, the overlapping probe and conjugate emission cones are centered around the pump beam (see figure 5.1) with their angular bandwidth limited by the phase matching condition (see chapter 4). In the far field, a cross-section of the emission cone with the transverse plane is an annular ring with the pump beam at the center. With the use of a coherent seed (probe) beam, in addition to the spontaneously generated probe and conjugate photons, the FWM generates bright probe and conjugate beams. These bright twin beams, localized within a sub-portion of the spontaneous emission region, can be effectively seen as local oscillators (LOs) at mentioned in chapter 5. The generation of these LOs, one for each field, amplifies the corresponding spontaneous

field fluctuations at the overlap regions in the far field, as discussed in (6.13). Since the input seed is a Gaussian beam, the generated bright probe and conjugate beams also have Gaussian profiles. As we modify the angular spectrum of the input pump beam, the (spontaneous) correlated spatial modes in FWM are also modified which leads to a change in the spatial cross-correlation. To clearly see this behaviour, it is important that the Gaussian profiles of bright twin beams do not change with the pump modifications.

In order to achieve this in our experimental setup, we add a constant-phase circular region at the center of the CGH that is large enough for the seed (probe) beam to pass through (see figures 6.3A, 6.3E and 6.4A). Due to a low probe-pump angle (0.4°) and the small (1/2-inch) length of the Rb cell, the bright twin beams remain undistorted while propagating almost collinearly with the pump inside the constant-phase region. Therefore, using a relatively small (compared to the overall CGH) constant phase region, we are able to generate bright Gaussian probe and conjugate beams in the far field with uniform phase. The radius of the constant-phase circular region is kept

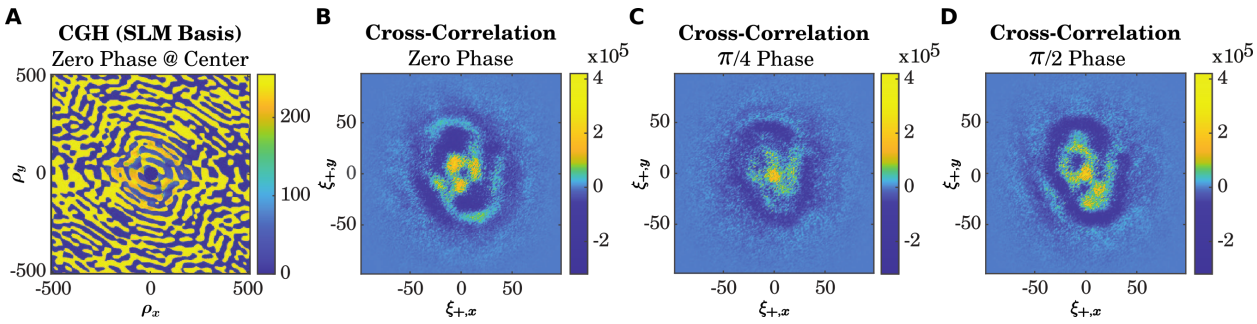

Figure 6.4: Control of the degree of correlations in the far field. All figures except the CGH are in the EMCCD pixel basis. The results show the effect of a phase change of the central circular region on the far field correlations. (A) A CGH to encode information in the form of the OU logo with a zero phase circular region at the center. By choosing suitable phase values for the central region and keeping the rest of CGH same, one can measure spatial correlations between the probe and conjugate quadratures that are (B) positively correlated ($\delta\phi = 0$), (C) uncorrelated ($\delta\phi = \pi/4$) and (D) negatively correlated ($\delta\phi = \pi/2$). Figures (B), (C) and (D) are not normalized. A small clockwise rotation ($\sim 5°$) of the experimental plots is due to optical alignment imperfections. Figure adapted from [71]. Reproduced with permission.

to the smallest possible value such that resulting distortion in the CGH and therefore, in the desired angular distribution for the pump is minimum. An additional advantage of this circular region is the ability to control the relative phase between the probe and conjugate bright beams, which are acting as LOs for the respective field. The relation between the specific phase value of the circular region and the relative phase between the two LOs can be seen using the optical phase-conjugation condition, well known from classical wave optics [81,177–179]. For pump, probe and conjugate fields that are phase matched in a FWM process, the phase-conjugation condition implies

$$2\phi_p = \phi_{pr} + \phi_c, \tag{6.38}$$

where ϕ denotes phase of the respective fields. For example, from the classical picture of FWM with $\phi_p = 0$ (pump with flat wavefront), phase conjugation leads to the generation of a conjugate field such that,

$$E_c(\boldsymbol{\rho}) = E^*_{pr}(\boldsymbol{\rho}), \tag{6.39}$$

in the near field[119]. If we take ϕ_{pr} to be the reference phase for the subsequent analysis and set it to zero, the condition (6.38) then implies that $\phi_c = 0$. Therefore, measurement of intensity correlations in the bright region gives amplitude quadrature correlations for the overlapping probe and conjugate spontaneous fields as shown in (6.29). A modification of the pump phase via CGH implementation while keeping the phase of center region to be zero (i.e no change in LOs relative phase) gives encoded information in the amplitude quadrature correlation as shown in figures 6.3B, 6.3F and 6.2B.

For a local change the phase value of the center region as $\phi_p = \delta\phi$ (and no change in rest of the CGH), the bight conjugate will undergo a phase change of $\phi_c = 2\,\delta\phi$ with respect to the bright probe as given by (6.38). This will effectively changes the conjugate field quadrature to be measured by the bright conjugate to

$$\hat{X}_c^{\phi_c} = \frac{e^{i\phi_c}\ \hat{b}^\dagger + e^{-i\phi_c}\ \hat{b}}{\sqrt{2}}, \tag{6.40}$$

where $\hat{b}$ is the creation operator for conjugate mode. Taking advantage of the relative phase change ϕ_c via introducing $\delta\phi$ at the center of the pump beam, we can now control the degree of correlations in the far field as well. For the CGH corresponding to the OU logo, a change by $\delta\phi = \pi/4$ gives

$$\left\langle \delta\hat{X}_{pr}(-\boldsymbol{x})\,\delta\hat{X}_c^{\pi/2}(\boldsymbol{x}+\boldsymbol{\xi}) \right\rangle = \left\langle \delta\hat{X}_{pr}(-\boldsymbol{x})\,\delta\hat{Y}_c(\boldsymbol{x}+\boldsymbol{\xi}) \right\rangle. \tag{6.41}$$

Since this is a measurement of uncorrelated quadratures of the twin beams, the corresponding cross-correlation should ideally be zero. Similarly for $\delta\phi = \pi/2$, we get

$$\left\langle \delta\hat{X}_{pr}(-\boldsymbol{x})\delta\hat{X}_c^{\pi}(\boldsymbol{x}+\boldsymbol{\xi}) \right\rangle = -\left\langle \delta\hat{X}_{pr}(-\boldsymbol{x})\delta\hat{X}_c(\boldsymbol{x}+\boldsymbol{\xi}) \right\rangle \tag{6.42}$$

$$\propto -\mathfrak{Re}\left[\Phi(\boldsymbol{\xi})\right], \tag{6.43}$$

which is the negative of the correlations between the probe and conjugate amplitude quadratures. Figures 6.4C and 6.4D show the experimentally measured results of cross-correlation for $\delta\phi$ equal to $\pi/4$ and $\pi/2$, respectively. Due to discretization the phase value at the SLM and the center region, we were unable to get uniformly zero cross-correlations in figure 6.4C.

6.5 Spatial Auto-Correlation in Twin Beams

In this chapter so far, we have discussed in detail our approach to encode information in the twin beams generated in the FWM by manipulating the angular spectrum of the pump beam. In terms of experimental execution, precise phase structuring of the pump beam has allowed us to control the distribution as well as the level of cross-correlation between the twin beams. We also expect this approach, that is, encoding information in the form of engineered spatial quantum correlations, to be useful for emerging applications in quantum sensing and computation. However, for the spatial correlations to be a viable solution for the secure transfer of information, we need to further explore if the encoded information is only accessible via a joint measurement of the twin beams, and not from the individual measurements of either beam. While the spatial profiles of the bright twin beams, in principle, should be affected by the phase changes made to the pump beam, we avoid this scenario by passing the seed probe through a constant phase center region as mentioned in the

previous section. This fact is further reflected in the experimental Gaussian images of the bright twin beams, as shown in figure 6.2A.

Considering the spatial properties of the spontaneously generated fields, the spatial modes of the probe and conjugate beams supported by the FWM process are determined by the spatial profile of the pump beam along with the phase matching condition. Therefore, a change in the angular spectrum of the pump, in theory, should affect the spatial correlation of each beam with itself, referred to as the auto-correlation distribution. To further comment on whether one can recover the encoded cross-correlation pattern or any information regarding the pump angular spectrum using the auto-correlations of the probe and/or conjugate beams, we start by deriving an explicit expression for it. In analogy to the definition of the cross-correlation function given in (6.10) and the subsequent derivation, the auto-correlation function $c(\boldsymbol{x}_1, \boldsymbol{x}_2)_{\text{auto}}$ for the probe beam can be defined as

$$c_{\text{auto}}(\boldsymbol{x}_1, \boldsymbol{x}_2) \equiv \left\langle \delta\hat{N}_{pr}(\boldsymbol{x}_1; z_f)\, \delta\hat{N}_{pr}(\boldsymbol{x}_2; z_f) \right\rangle \tag{6.44}$$

$$\overset{\text{bright limit}}{\propto} \left\langle \delta\hat{X}_{pr}(\boldsymbol{x}_1; z_f)\, \delta\hat{X}_{pr}(\boldsymbol{x}_2; z_f) \right\rangle \tag{6.45}$$

$$\overset{\substack{f-\text{to}-f \\ \text{optical system}}}{=} \left\langle \delta\hat{X}_{pr}(\boldsymbol{k}_1)\, \delta\hat{X}_{pr}(\boldsymbol{k}_2) \right\rangle\Big|_{z=z_0}. \tag{6.46}$$

Earlier in section 6.1, we calculated the expectation value for any general operator $\hat{A}$ (see expression 6.9) for $|\Psi_{\text{TBS}}\rangle$. We can now set $\hat{A} = \delta\hat{X}_{pr}(\boldsymbol{k}_1)\, \delta\hat{X}_{pr}(\boldsymbol{k}_2)$ and determine its explicit dependence on the pump angular momentum as

$$\langle \hat{A} \rangle = \langle \delta\hat{X}_{pr}(\boldsymbol{k}_1)\, \delta\hat{X}_{pr}(\boldsymbol{k}_2) \rangle \tag{6.47}$$

$$= \langle \hat{X}_{pr}(\boldsymbol{k}_1)\, \hat{X}_{pr}(\boldsymbol{k}_2) \rangle \tag{6.48}$$

$$= \langle \Psi_0 | \hat{X}_{pr}(\boldsymbol{k}_1) \hat{X}_{pr}(\boldsymbol{k}_2) | \Psi_0 \rangle + 2 \iint d\boldsymbol{k}_{pr} d\boldsymbol{k}_c\, \mathfrak{Re}\Big[C\, \mathbb{F}(\boldsymbol{k}_{pr}, \boldsymbol{k}_c) \langle \Psi_0 | \hat{X}_{pr}(\boldsymbol{k}_1) \hat{X}_{pr}(\boldsymbol{k}_2)\, \hat{a}^\dagger_{\boldsymbol{k}_{pr}} \hat{b}^\dagger_{\boldsymbol{k}_c} | \Psi_0 \rangle \Big]$$
$$+ |C|^2 \iint d\boldsymbol{k}_{pr} d\boldsymbol{k}_c \iint d\boldsymbol{k}'_{pr} d\boldsymbol{k}'_c\, \mathbb{F}(\boldsymbol{k}_{pr}, \boldsymbol{k}_c) \mathbb{F}^*(\boldsymbol{k}'_{pr}, \boldsymbol{k}'_c) \langle \Psi_0 | \hat{b}_{\boldsymbol{k}'_c} \hat{a}_{\boldsymbol{k}'_{pr}} \hat{X}_{pr}(\boldsymbol{k}_1) \hat{X}_{pr}(\boldsymbol{k}_2)\, \hat{a}^\dagger_{\boldsymbol{k}_{pr}} \hat{b}^\dagger_{\boldsymbol{k}_c} | \Psi_0 \rangle$$

$$= \frac{1}{2} \langle \Psi_0 | (\hat{a}_{\boldsymbol{k}_1} \hat{a}^\dagger_{\boldsymbol{k}_2} + \hat{a}^\dagger_{\boldsymbol{k}_1} \hat{a}_{\boldsymbol{k}_2}) | \Psi_0 \rangle$$
$$+ \frac{|C|^2}{2} \iint d\boldsymbol{k}_{pr} d\boldsymbol{k}_c \iint d\boldsymbol{k}'_{pr} d\boldsymbol{k}'_c\, \mathbb{F}(\boldsymbol{k}_{pr}, \boldsymbol{k}_c) \mathbb{F}^*(\boldsymbol{k}'_{pr}, \boldsymbol{k}'_c) \langle \Psi_0 | \hat{b}_{\boldsymbol{k}'_c} \hat{a}_{\boldsymbol{k}'_{pr}} (\hat{a}_{\boldsymbol{k}_1} \hat{a}^\dagger_{\boldsymbol{k}_2} + \hat{a}^\dagger_{\boldsymbol{k}_1} \hat{a}_{\boldsymbol{k}_2}) \hat{a}^\dagger_{\boldsymbol{k}_{pr}} \hat{b}^\dagger_{\boldsymbol{k}_c} | \Psi_0 \rangle$$

$$= \frac{\delta(\boldsymbol{k}_1 - \boldsymbol{k}_2)}{2} + \frac{|C|^2}{2} \iint d\boldsymbol{k}_{pr} d\boldsymbol{k}_c \iint d\boldsymbol{k}'_{pr} d\boldsymbol{k}'_c\, \mathbb{F}(\boldsymbol{k}_{pr}, \boldsymbol{k}_c) \mathbb{F}^*(\boldsymbol{k}'_{pr}, \boldsymbol{k}'_c) \delta(\boldsymbol{k}_c - \boldsymbol{k}'_c)$$
$$\times \left[\delta(\boldsymbol{k}_{pr} - \boldsymbol{k}'_{pr}) \delta(\boldsymbol{k}_1 - \boldsymbol{k}_2) + \delta(\boldsymbol{k}'_{pr} - \boldsymbol{k}_2) \delta(\boldsymbol{k}_{pr} - \boldsymbol{k}_1) + \delta(\boldsymbol{k}'_{pr} - \boldsymbol{k}_1) \delta(\boldsymbol{k}_{pr} - \boldsymbol{k}_2) \right]$$

$$= \frac{\delta(\mathbf{k}_1 - \mathbf{k}_2)}{2} + \frac{|C|^2}{2} B\, \delta(\boldsymbol{k}_1 - \boldsymbol{k}_2) + |C|^2 \int d\boldsymbol{k}_c\, \mathfrak{Re}\left[\mathbb{F}(\boldsymbol{k}_1, \boldsymbol{k}_c) \mathbb{F}^*(\boldsymbol{k}_2, \boldsymbol{k}_c) \right] \tag{6.49}$$

$$= \frac{1}{2}(1 + |C|^2 B) \delta(\boldsymbol{k}_1 - \boldsymbol{k}_2) + |C|^2 \int d\boldsymbol{k}_c\, \mathfrak{Re}\left[\mathbb{F}(\boldsymbol{k}_1, \boldsymbol{k}_c) \mathbb{F}^*(\boldsymbol{k}_2, \boldsymbol{k}_c) \right], \tag{6.50}$$

where $B = \iint d\boldsymbol{k}_{pr} d\boldsymbol{k}_c\, |\mathbb{F}(\boldsymbol{k}_{pr}, \boldsymbol{k}_c)|^2$ is a constant. The first and second delta function terms in (6.49) are due to the pointwise self-correlation of the probe vacuum and the one photon Fock state, respectively, in the far field transverse plane. Since these delta functions do not contain any spatial information, they can be omitted in further analysis. The last term in (6.50) depends on the angular

spectrum of the pump beam, and hence, may provide information regarding the encoded pattern. As mentioned earlier, the measurements are made within the bright region of the probe and conjugate beams and, therefore, we can assume the sinc function is uniformly equal to 1. Using (6.46), (6.50) and the far field mapping of k-vectors, the auto-correlation function $c_{\text{auto}}(\boldsymbol{x}_1, \boldsymbol{x}_2)$ for probe beam can be written as

$$c_{\text{auto}}(\boldsymbol{x}_1, \boldsymbol{x}_2) \overset{\text{bright limit}}{\propto} \int d\boldsymbol{x}_c \, \mathfrak{Re}\left[\Phi(\boldsymbol{x}_1 + \boldsymbol{x}_c)\ \Phi^*(\boldsymbol{x}_2 + \boldsymbol{x}_c)\right], \tag{6.51}$$

where $\boldsymbol{x}_c$ is the position coordinate for conjugate in the far field transverse plane. A derivation of the auto-correlation function for the conjugate beam gives an expression similar to (6.51) with $\boldsymbol{x}_c$ replace by $\boldsymbol{x}_{pr}$. However, the distribution of c_{auto} is independent of these field variables as they are being integrated over.

Since for the auto-correlation, as opposed to the cross-correlation, one should expect correlations between nearby points (i.e. $\boldsymbol{x}_2 \approx \boldsymbol{x}_1$), expression (6.51) can be recast into a more relevant form by defining $\boldsymbol{\xi}_- = \boldsymbol{x}_2 - \boldsymbol{x}_1$, $\boldsymbol{\xi}' = \boldsymbol{x}_1 + \boldsymbol{x}_c$. With these new variables, we rewrite the auto-correlation function as

$$c_{\text{auto}}(\boldsymbol{\xi}_-) \overset{\text{bright limit}}{\propto} \int d\boldsymbol{\xi}' \, \mathfrak{Re}\left[\Phi(\boldsymbol{\xi}')\ \Phi^*(\boldsymbol{\xi}_- + \boldsymbol{\xi}')\right]. \tag{6.52}$$

This equation gives us explicit dependence of the distribution of auto-correlation function on the pump angular spectrum via the function Φ. However, the mapping from Φ to c_{auto} is essentially non-invertible, which makes it impossible, in-general, to reconstruct the the encoded cross-correlation pattern. Figures 6.5A and 6.5B show the plots for the auto-correlation distributions from the

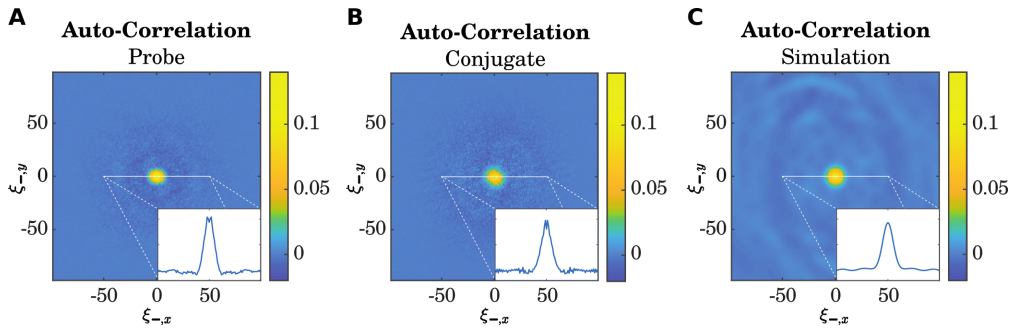

Figure 6.5: Experimental and simulation results for the auto-correlation. Self-correlations in the intensity fluctuations measurements of individual beams provide the auto-correlation distributions for (A) probe and (B) conjugate beams while input pump beam has the phase pattern corresponding to the OU logo. These approximately Gaussian auto-correlations do not reveal any information of the encoded pattern and are in good agreement with simulation of the auto-correlation (C). The small portion at the center of measured auto-correlations is removed as it contains an artificial peak due to prefect correlation of identical images. All figures are in the EMCCD pixel basis. Figure adapted from [71]. Reproduced with permission.

experimental measurements of probe and conjugate intensity fluctuations, respectively, for the case of a structured pump beam with the OU logo phase pattern. It can be seen from these plots that the auto-correlations are very narrow and have an approximately Gaussian distribution that can not be used to recover the encoded information. Using the theoretical derivations developed in the present section, the simulated auto-correlation distribution based on (6.52) and shown in figure 6.5C, closely matches the experimental plots. This proves the validity of our analysis in the

present experiment. Also, the results in figure 6.5 are almost identical to the auto-correlations obtained in the case of no pump beam modification, i.e. no encoded information as discussed in the next section 6.6. Furthermore, in the limit of equally contributing large number of spatial modes, the auto-correlation distribution approaches a delta function, and hence, effectively becomes independent of pump angular spectrum. The detailed derivation of this result is provided in the supplemental material section S4 of ref[71].

A relevant concern here may be regarding what information can be gained about the correlated spatial modes in FWM if measurement are made only one of the beams. With the assumption that overall entangled state is pure, one can estimate the total number of pairwise-correlated spatial modes, known as the Schmidt number, via the coherent mode analysis of one of the beams[180–183].

6.6 Security of Encoded Information

For a highly spatially-multimode twin beam state, the fact that the auto-correlation measurements made on one of the beams do not reveal any information regarding the encoded pattern also implies that the shape of the auto-correlation distribution is relatively insensitive to the exact details of the pump angular spectrum. In other words, by only analyzing correlations in one of the beams, one can not say if a structured pump has been used to generate twin beams with specific encoded information. This is an additional security feature of a secure quantum network utilizing a Hilbert space corresponding to a large number of spatial modes, in which, it becomes difficult for an eavesdropper to figure out when the information is being actively sent. In order to check the uniformity of the auto-correlation distributions against changes in the pump angular spectrum in our FWM process, we plot and compare the auto-correlations for the probe and conjugate beams generated using three different pump angular spectrum. Figure 6.6 shows the CGH phase-patterns, encoded information and corresponding auto-correlations for the cases when the input pump has phase patterns performing no encoding (first row), OU logo encoding (second row) and ħ encoding (last row). While the phase patterns (CGH, first column), hence, the pump angular spectrum and the encoded information (cross-correlation, second column) are quite different for all three cases, the auto-correlations remain narrow Gaussian distributions.

To further quantify, for example, the similarity between auto-correlations in various cases or the amount of information leaked into the auto-correlations, we compare two given correlation distributions using a correlation-coefficient, r, defined as

$$r(A,B) = \frac{\sum_{m,n}(A_{mn} - \bar{A})\,(B_{mn} - \bar{B})}{\sqrt{\left[\sum_{m,n}(A_{mn} - \bar{A})^2\right]\left[\sum_{m,n}(B_{mn} - \bar{B})^2\right]}}\,, \tag{6.53}$$

where A_{mn} and B_{mn} are the matrix elements of the cross/auto-correlation distributions being considered and $\bar{A}$ and $\bar{B}$ are the mean pixel values of the corresponding matrices. For two given images, A and B, the correlation-coefficient provides a measure of similarity between them with values ranging from -1 to 1. For two uncorrelated random images/matrices r has a values close to zero and for identical images $r = 1$. For two similar but anti-correlated images, r has negative values. To compute the values of r, we take the size of the A and B matrices to be 121×121 and centered around the center of the respective correlation distributions.

The results of these comparisons are tabulated in figure 6.7A. The lower half (lower triangle) is removed as r is symmetric with respect to the order of the images. Also, for clarity, we only show the

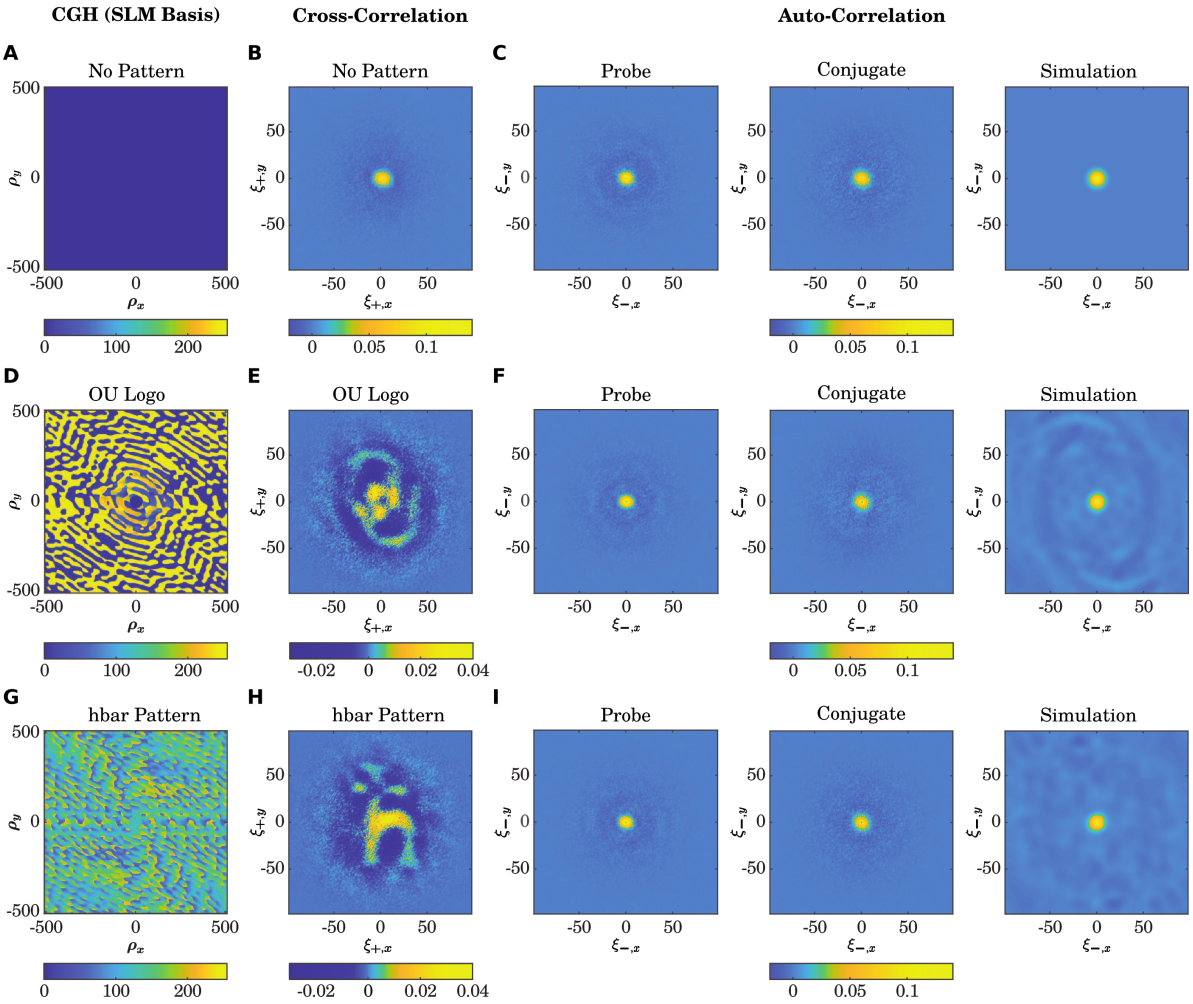

Figure 6.6: Twin beam spatial correlations generated for three different pump angular spectra. Spatial cross-correlations and auto-correlations for the probe and conjugate beams when no pattern is encoded (1st row), the OU logo is encoded (2nd row), and ħ is encoded (3rd row) on the input pump. The corresponding CGH phase patterns are shown in subfigures (A), (D) and (G), respectively. The encoded information, extracted in the form of the cross-correlation (2nd column), is very distinct in all three cases. However, the auto-correlations in (C), (F), and (I) remain unchanged, independent of what information is encoded. The experimental results are also consistent with the corresponding simulations in all three cases. These results demonstrate that each beam by itself does not contain any substantial encoded information, and that one needs a joint measurement on both beams to be able to extract the encoded information. All correlation subfigures are in plotted in the EMCCD basis. The center portion of the measured auto-correlations was removed as it contains an artificial maximum due to the use of the same images to calculate it. Figure adapted from [71]. Reproduced with permission.

relevant comparisons here. Comparing the measured auto-correlations of the probe and conjugate beams in various cases, we find consistently high values of r (≥ 0.78). A large part of the degradation here comes from the removal of the central artificial peak. Given that probe and conjugate auto-correlation are identical in theory, we find a high r-value between them for each individual case. The similarity between the auto-correlation and cross-correlation distributions remains low except when no information is encoded. This is due to the fact that, for the an unmodified pump, all the correlations are approximately Gaussian, which further shows that the Gaussian peak at the

6.6 Security of Encoded Information

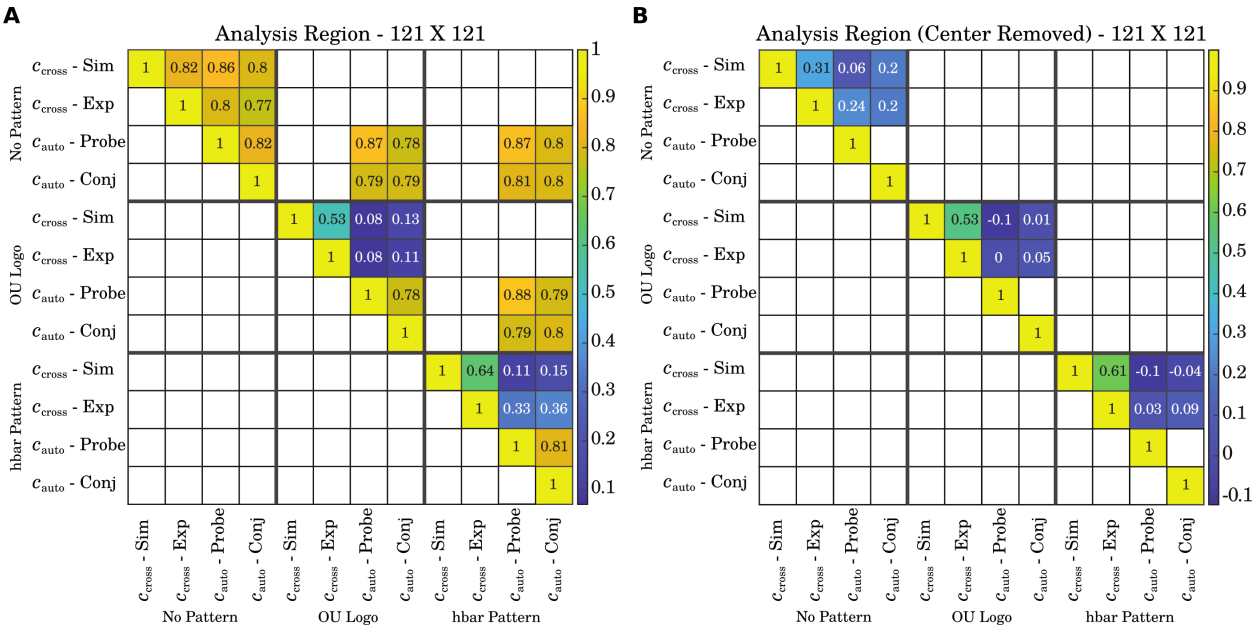

Figure 6.7: Similarity between various auto- and cross-correlation distributions. The correlation-coefficients (r-values) are calculated over a region of 121x121 pixels, which is roughly the size of the region where information is encoded in the form of a spatial pattern. The r values in (A) mainly show the similarity between the different auto-correlation distributions, while the ones on the right (B) show the degree to which information is leaked into the background of the auto-correlations, and is calculated after setting the pixels within a circular region of 10 pixels at the center to zero for the relevant correlation distributions. Figure adapted from [71]. Reproduced with permission.

center of the auto-correlations does not contain any significant information. Additionally, we also provide a comparison between the simulated and experimental cross-correlations for the different pump angular spectra. The relatively low values of r ($\sim$0.6), for the case of OU logo and $\hbar$, is likely from degradation of measured the cross-correlations due loss of higher order spatial frequencies in the phase pattern at the SLM. To see if there might be some information present in the background of the measured the auto-correlations related to the encoded pattern (OU logo or $\hbar$), we take a circular region with a radius of 10 pixels around the center and set it to zero. This effectively removes the central peak at the center of these correlations. Also, to provide a fair comparison with the corresponding cross-correlation, the OU logo and $\hbar$ are also modified using the same procedure. The r-value for the relevant comparisons are tabulated in figure 6.7B. We now find very low r-values between cross-correlation and auto-correlation for these two cases, which experimentally verifies the fact that no relevant encoded information (OU logo or $\hbar$) is present in the corresponding auto-correlation background.

A crucial prerequisite to achieve a practical implementation of a secure quantum network using the twin beams is the presence of temporal quantum correlations between the two modes. Here, referring back to the energy conservation in the optical fields during the FWM process, the intensity fluctuations of the probe and conjugate beams are quantum correlated due to the generation of probe-conjugate photon pairs. As mentioned in the chapter 5, we perform temporal intensity difference measurements to verify the presence of temporal quantum correlations in the twin beams. However, for our present approach to be compatible with current secure quantum communication techniques, the temporal quantum correlation should be preserved [70,184] as we modify the spatial

degrees of freedom to encode information. To confirm this in our experimental setup, we bypass the EMCCD camera and detect bright probe and conjugate beams with a balanced photodiode detector and measure intensity difference squeezing with a spectrum analyzer. Figure 6.8 shows the presence of temporal squeezing with a level of ∼4.5 dB below the shot noise limit. We find similar temporal noise spectra for all three case (i.e no pattern, OU logo and ħ), which shows that the degree of temporal correlations is not affected by the information encoded via manipulation of spatial degrees of freedom. In order to obtain the same level of temporal squeezing, we had to subtract the additional background noise due to scattered pump photons, which becomes significant in the presence of a CGH phase pattern.

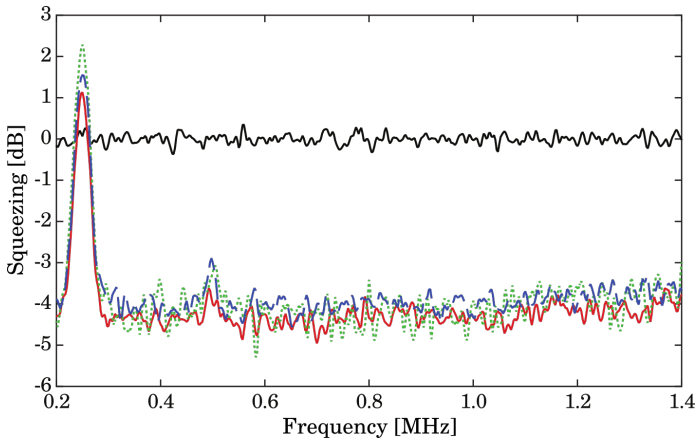

Figure 6.8: Temporal squeezing with a modified pump beam. Quantum correlations in the temporal domain are verified through the presence of intensity difference squeezing. We measure the same level of squeezing, after the subtraction of noise from the scattered pump noise, in all three cases, which shows that it is independent of the spatial modes manipulation. The black trace shows the shot noise level, while the other traces show the intensity difference noise when no information is encoded (red), the OU logo is encoded (green), and ħ is encoded (blue). If we place an additional ^{87}Rb absorption cell before the photodiodes to absorb the scattered pump, we get the same levels of temporal squeezing again without the need to subtract the scattered pump noise, independent of the encoded information. Figure adapted from [71]. Reproduced with permission.

The temporal correlations provide a primary layer of security against any attempt to gain information by an eavesdropper, as such an attempt would inevitably lead to a reduction of the degree of temporal correlations, and hence, the level of intensity difference squeezing [185]. As a result, the presence of an eavesdropper in a quantum communication channel can be checked by monitoring the intensity difference squeezing. More concretely, in the context of CV quantum-key-distribution (QKD), the security of a quantum exchange between two parties, say A and B, depends on the amount of mutual information, I_{AB}, between the two parties [186]. It can then be shown that, for a twin beam purely temporal EPR state, I_{AB} is proportional to the amount of squeezing (logscale, see chapters 2 and 3) in the joint quadratures of the twin beams [187]. The additional advantage of a spatially multimode twin beam state is then to enhance the information capacity and security in a quantum communication channel. The multiple independently correlated spatial modes between the twin beams generated in FWM process [188] can be used to execute a higher dimensional QKD protocol. In this case the mutual information, and hence the security, in a d-dimensional protocol will have an additional scaling of $\log_2 d$ [6,146], where d is directly proportional to the number of spatial modes. As we can see here, for $d > 2$, the higher dimensional protocol will provide better security than a traditional 2-dimensional protocol. A practical way to measure the number of in-

dependent spatial modes is by taking the ratio of the pump size to the size of the independently correlated regions at the center of the cell[95,119] (near-field). The mutual information in our present implementation, therefore, is expected to increase as $\sim 2\log_2(\sigma_p)$ where σ_p is the pump width at the cell center.

In summary, the results presented in this chapter show that we are able to control the distribution of spatial correlations and use it in a novel way to encode information. The degree of control of the spatial correlations in our FWM setup, using a structured pump beam, conveys a substantial advancement over previous experiments with the PDC process[161,162]. Furthermore, the capability to engineer the distribution of the spatial correlations directly at the source can be extended to providing on-demand entanglement between any arbitrary superposition of spatial modes. To date, a similar approach of mode engineering has been used in the time-frequency domain towards the development of devices such as the quantum pulse gate[189] and designing of a single photon source for any given temporal mode[190].

CHAPTER 7

Future Directions and Conclusions

In this dissertation, based on the discussion of spatial correlations in twin beams, we see that our FWM source generates multimode squeezed state of light composed of a large number of spatial modes. We find signatures of it in terms of localized auto-correlations in the probe and conjugate fields as well as in the ability of the FWM process to support relatively complex patterns in their cross-correlations. However, all the correlation information acquired so far is based on and targeted towards conditional measurements (which seems natural because the verification of EPR entanglement require conditional variances). These conditional measurements tell us how a photon is spatially distributed in the transverse plane of the conjugate beam given that the corresponding photon in the probe beam is measured at a specific location.

One may then ask: what is the unconditional distribution of photons in the twin beams? When the pump photons decay into the probe and conjugate photons, are there any preferred spatial modes (or a combination of them)? Given that these spatial modes do exist, what is the nature of the correlations between them and which conservation rules or physical parameters affect them? We aim to provide answers to some of these questions here. The main idea revolves around the (spatial) eigenmode structure, commonly referred to as the Schmidt modes, underlying the FWM process. In this chapter, we provide our preliminary simulation results of their calculation and point to their importance in quantum communication in the first section. Later, we discuss some of the possible future directions and end with our concluding remarks on this dissertation.

7.1 Spatial Eigenmodes of FWM

For a given non-linear process (involved in photon pair generation), the characterization of Schmidt modes is a natural way to identify modes that are pairwise correlated (in a given degree of freedom). More explicitly, in the context of the twin beam wavefunction, the joint probability distribution of one of its relevant (frequency, temporal, or spatial) properties is determined through the (probability) amplitude function $\mathbb{F}$. This function can be decomposed in the form of following summation [140,189,191]

$$\mathbb{F}(\mathrm{x}_a, \mathrm{x}_b) = \sum_i \lambda_i \, u_i(\mathrm{x}_a) \, v_i(\mathrm{x}_b), \tag{7.1}$$

where x is a frequency, time, or space variable. The complex functions u and v, corresponding to the modes of 'a' and 'b', respectively, are known as the Schmidt modes of the process (often also referred as the principal [92] modes or the eigenmodes) and the real, positive factor λ_i's in the summation are the Schmidt values. The single summation index i tells us that the distribution u_m

(in mode a) is only paired with the distribution v_m (in mode b). Therefore, one can visualize this decomposition as an effective diagonalization in the space of all pairwise combinations of the form $u_i(\mathrm{x}_a)v_j(\mathrm{x}_b)$. Since $\mathbb{F}$ is the probability amplitude of a joint probability distribution, we have

$$\iint d\mathrm{x}_a d\mathrm{x}_b \, \mathbb{F}(\mathrm{x}_a, \mathrm{x}_b) = 1 \tag{7.2}$$

$$\Rightarrow \qquad \sum_i \lambda_i^2 = 1, \tag{7.3}$$

which implies that the probability of finding the twin beam photons in the $u_i(\mathrm{x}_a)v_i(\mathrm{x}_b)$ Schmidt pair is given by λ_i^2. Here, we use the orthonormality of Schmidt modes to derive expression (7.3).

Focusing on twin beam correlations in the far field, we can now apply this formalism to the FWM process. Following the expression 4.15 in chapter 4, if we restrict our analysis domain to be within the maximum gain region (see figure 4.4), the sinc function can be taken to be unity. Therefore, for the photon pair generated in the probe and conjugate fields, the two-photon amplitude function $\mathbb{F}$ has the form

$$\mathbb{F}(\boldsymbol{q}_{pr}, \boldsymbol{q}_c) = \Phi(\boldsymbol{q}_{pr} + \boldsymbol{q}_c) \tag{7.4}$$

$$= \int d\boldsymbol{q}_p \, \mathcal{E}(\boldsymbol{q}_p) \, \mathcal{E}(\boldsymbol{q}_{pr} + \boldsymbol{q}_c - \boldsymbol{q}_p), \tag{7.5}$$

where $\mathbf{q}_{pr}$, $\mathbf{q}_c$ and $\mathbf{q}_p$ denote the transverse momentum of the probe, conjugate, and pump fields, respectively, $\mathcal{E}(\boldsymbol{q}_p)$ denotes the angular spectrum of pump and Φ represents the convolution of the angular spectra of the two pump photons. In chapter 4, we calculated the explicit form of the function $\Phi(\boldsymbol{q}_{pr} + \boldsymbol{q}_c)$ for a Gaussian pump beam to be

$$\Phi(\boldsymbol{q}_{pr} + \boldsymbol{q}_c) = A_1^2 \, \sigma_p^2 \, \pi \, e^{-\sigma_p^2 |\boldsymbol{q}_{pr} + \boldsymbol{q}_c|^2/4} \, , \tag{7.6}$$

where A_1 is a constant and σ_p is the waist of the pump beam inside the non-linear medium (near field).

According to the formalism of Schmidt modes given in (7.1), $\mathbb{F}(\boldsymbol{q}_{pr}, \boldsymbol{q}_c)$ can be recast into the form

$$\mathbb{F}(\boldsymbol{q}_{pr}, \boldsymbol{q}_c) = \sum_i \lambda_i \, u_i(\boldsymbol{q}_{pr}) \, v_i(\boldsymbol{q}_c), \tag{7.7}$$

where $u(\boldsymbol{q}_{pr})$ and $v(\boldsymbol{q}_c)$ are the Schmidt modes corresponding to the generated probe and conjugate fields, respectively. Using (7.4), (7.6) and (7.7), we get

$$A_1^2 \, \sigma_p^2 \, \pi \, e^{-\sigma_p^2 |\boldsymbol{q}_{pr} + \boldsymbol{q}_c|^2/4} = \sum_i \lambda_i \, u_i(\boldsymbol{q}_{pr}) \, v_i(\boldsymbol{q}_c). \tag{7.8}$$

A solution of the above equation for u_i and v_i Schmidt modes will give us information about how exactly the spatial modes of the probe and conjugate photons are paired (for a Gaussian pump beam) and that the overall FWM wavefunction can be seen as a superposition of all such pairwise combinations of Schmidt modes. In addition to this, the Schmidt spectrum (composed of various Schmidt values sorted with respect to their magnitude) gives information about the total number of modes as well as the dominant Schmidt modes in the generated fields. Using the method of singular value decomposition (SVD) for complex symmetric matrices[192], the Schmidt modes for

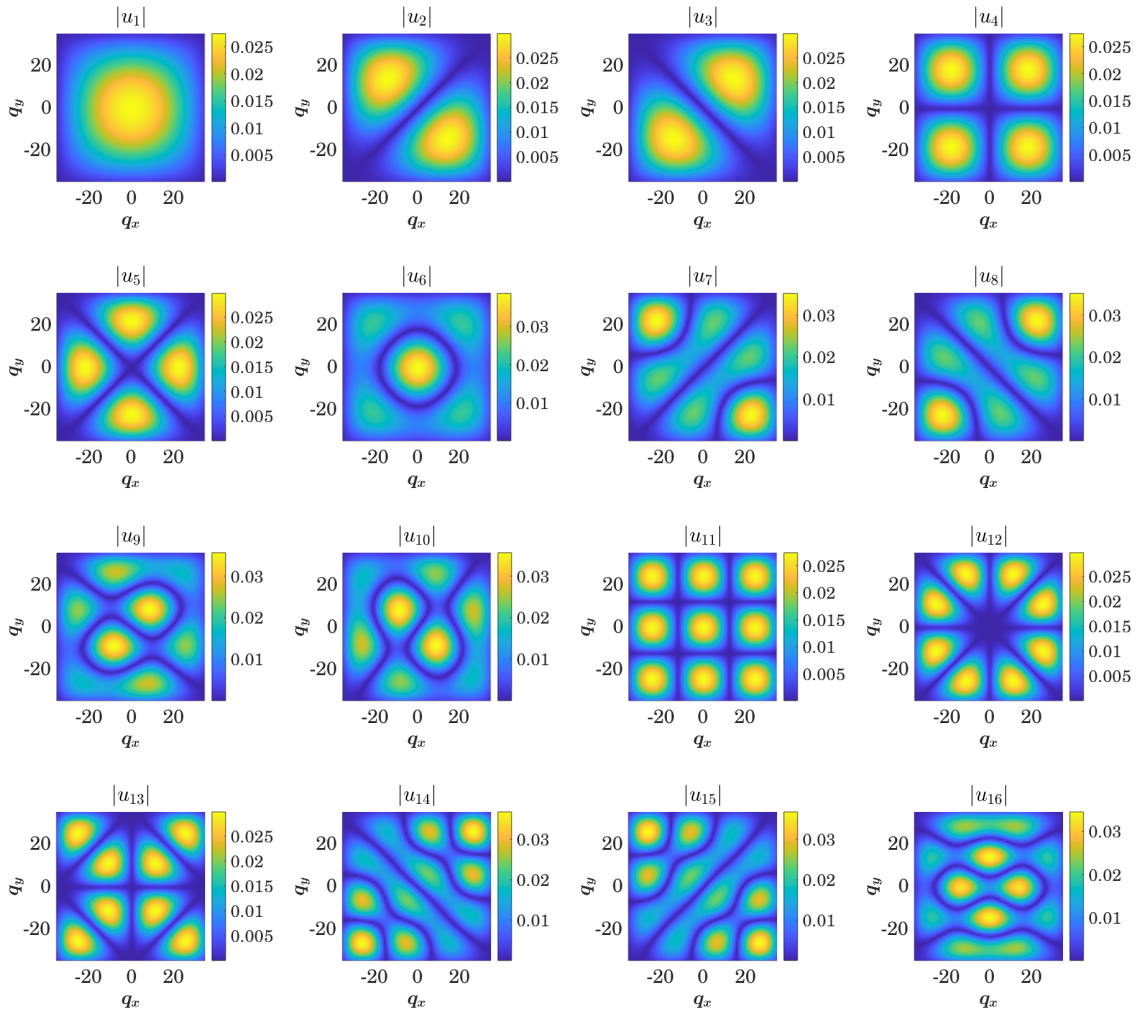

Figure 7.1: Spatial Schmidt mode characterization for a Gaussian input pump field. Based on the computational SVD implementation, the absolute amplitude distribution of the first 16 probe Schmidt modes is shown in decreasing order probability of occurrence. Each mode is normalized such that $\int d\boldsymbol{q}_{pr} u^*(\boldsymbol{q}_{pr})\ u(\boldsymbol{q}_{pr}) = 1$ over the displayed region of 71×71 pixels (with each pixel linear size equivalent to ∼0.2 rad/mm). The amplitude distributions of the conjugate Schmidt modes are the same as the corresponding ones for the probe.

(7.8) can be obtained. Notice that the function Φ is symmetric with respect to the $\boldsymbol{q}_{pr}$ and $\boldsymbol{q}_c$ variables. Therefore, we write it as a symmetric matrix by discretizing the $\boldsymbol{q}_{pr}$ and $\boldsymbol{q}_c$ variables and calculating the u_i and v_i Schmidt modes by implementing SVD in MATLAB.

Based on our computational results, spatial profiles of the absolute amplitude of the first 16 Schmidt modes are shown in figure 7.1 in the order of decreasing Schmidt values. We find that amplitude of a probe (u_i) Schmidt mode is the same as the corresponding conjugate (v_i) Schmidt mode. The phase distribution of the first 8 Schmidt modes for the probe and conjugate fields are shown in figure 7.2A and figure 7.2B, respectively. Some of these modes resemble the distribution of 2D Hermite-Gauss (HG) or Laguerre-Gauss (LG) modes which is expected based on the known literature[150,193]. However, due to the limitation of our SVD implementation, the computed solutions behave differently than HG/LG modes near the boundary.

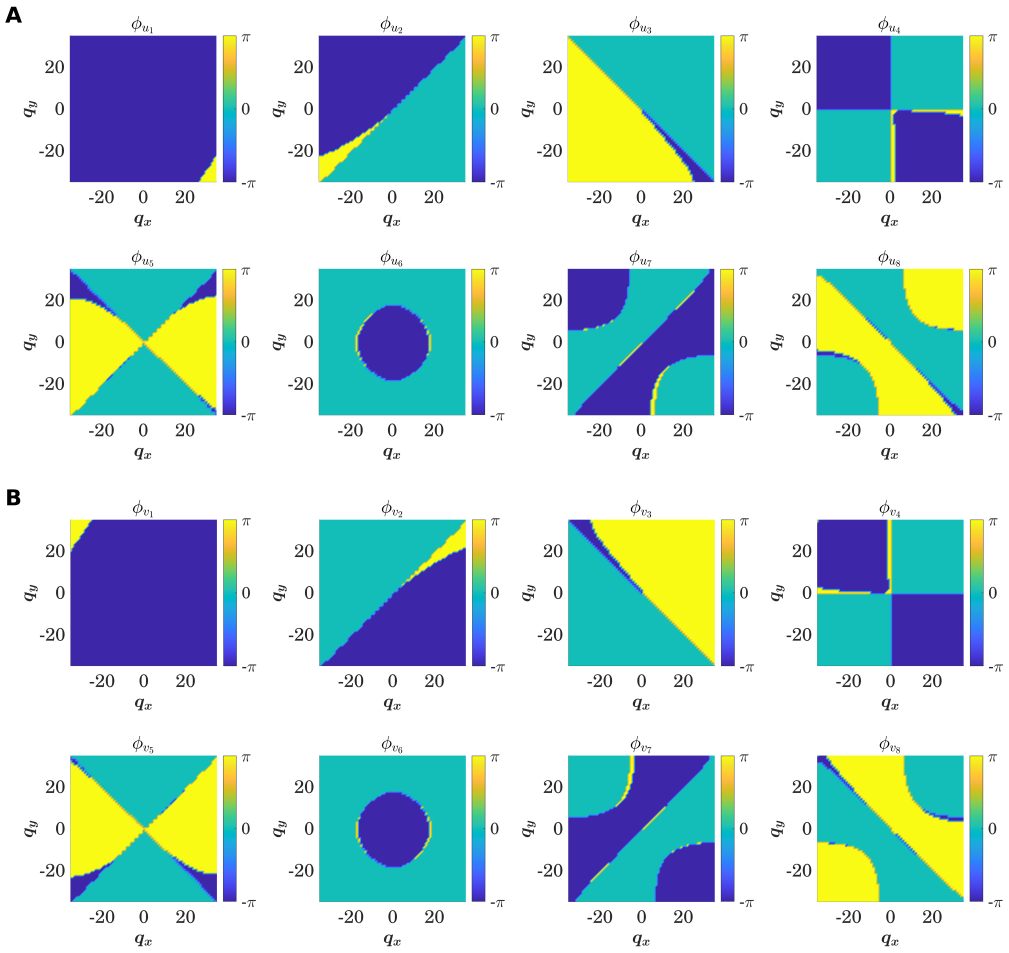

Figure 7.2: Phase distribution of probe and conjugate Schmidt modes for a Gaussian pump field. (A) Phase distribution of the first 8 Schmidt modes for the probe field are shown in decreasing order of probabilities. (B) The phase distribution of the corresponding conjugate Schmidt modes. The phase values in these simulated results are noisy in the regions of small amplitudes. All phase distributions are displayed over a region of 71×71 pixels with the linear size of each pixel equivalent to $\sim 0.2\ rad/mm$.

In order to check the validity of these simulated Schmidt mode results, we use our experimental cross-correlation data which provides the real part of $\Phi(\boldsymbol{q}_{pr}, \boldsymbol{q}_c)$. Since the $\mathfrak{Im}[\Phi]$ is zero for a Gaussian pump, as can be seen from (7.6), the measured cross-correlation has complete information of the required (experimental) two-photon amplitude distribution $\mathbb{F}_{\text{exp}}(\boldsymbol{q}_{pr}, \boldsymbol{q}_c)$. To see if our calculated Schmidt modes represent a valid eigenbasis for $\mathbb{F}_{\text{exp}}$, we use the following projection

$$(\lambda_{\text{exp}})_{ij} = \left| \int \mathbb{F}_{\text{exp}}(\boldsymbol{q}_{pr}, \boldsymbol{q}_c)\ u_i^*(\boldsymbol{q}_{pr}) v_j^*(\boldsymbol{q}_c)\ d\boldsymbol{q}_{pr}\ d\boldsymbol{q}_c \right|, \tag{7.9}$$

where λ_{exp} are experimental Schmidt values resulting from the above projection and $u(\boldsymbol{q}_{pr})$ and $v(\boldsymbol{q}_c)$ are the theoretically calculated Schmidt modes. Figure 7.3A shows the diagonal behavior of the Schmidt values λ_{exp}, which indicates a good match between the simulated and experimental Schmidt modes. We also see a participation of a large number of Schmidt modes (>80) with significant occupation probabilities. To estimate how many spatial modes are expected to participate in an

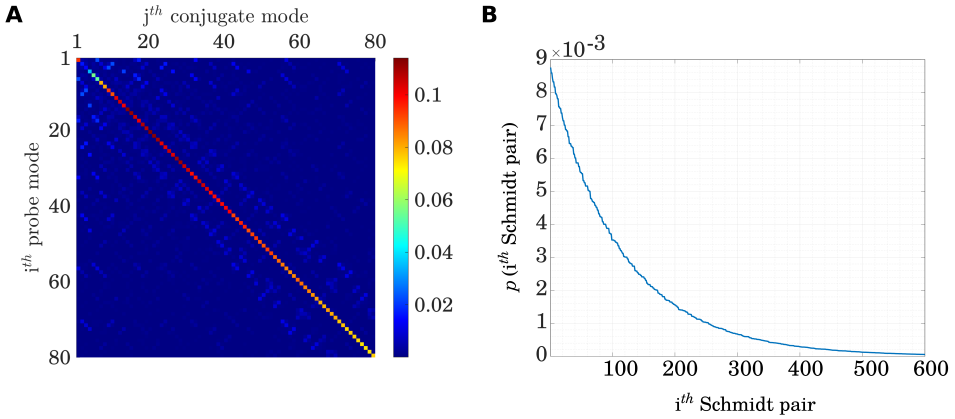

Figure 7.3: Unambiguous verification of the large number of pairwise correlated spatial modes in FWM. (A) The experimental two-photon amplitude $\mathbb{F}_{\text{exp}}(\boldsymbol{q}_{pr}, \boldsymbol{q}_c)$ distribution is projected on the calculated Schmidt basis using expression (7.9). The projected Schmidt values are mostly diagonal which indicates a good match between the simulation and the experiment. We also confirm a large number of Schmidt modes in our experimental data with significant probability of occupation. (B) Exponential decrease in the occupation probability for Schmidt pairs (based on the simulation results). This shows that a large number of Schmidt pairs $u_i(\boldsymbol{q}_{pr})v_i(\boldsymbol{q}_c)$ are expected to participate in the FWM process in the presence of a Gaussian pump with large waist [150].

ideal FWM process, we also calculate the probability of each Schmidt pair (i.e. $p_i = \lambda_i^2$) based on our simulation results. Figure 7.3 plots the distribution of the probability for 600 Schmidt pairs in descending order (of λ_{exp}) and we see an exponential decrease in the occupation probabilities for Schmidt pairs. This is similar to the observed behavior for an SPDC process which has a similar two-photon amplitude function [140,194,195]. These simulation results with supporting experimental evidence provide a direct verification of the fact that FWM is a highly spatially multimode process that generates a large number of quantum-correlated spatial modes. An additional advantage of the Schmidt mode analysis is that one can quantify the amount of entanglement as well as information contained in the correlated spatial modes using the measures of Schmidt number [140] and mutual information via the quantification of the von Neumann entropy [194].

In summary, using the Schmidt mode analysis, we show that the FWM process generates a highly multimode quantum state taking advantage of the infinite dimensional Hilbert space of spatial modes. The generation of a large number pairwise quantum-correlated spatial modes is especially well suited for higher dimensional quantum key distribution (QKD) protocols [6] where the security of a d-dimensional protocol scales as $\log(d)$, where d is proportional to the number of Schmidt modes (assuming the participating modes are equally probable). Additionally, these pairwise correlated spatially entangled states are useful in applications towards the broader field of quantum communication [8] and quantum sensing [196].

7.2 Outlook and Conclusions

With a better understanding of spatial correlations in the twin beams based on the research leading to this dissertation, future research projects may explore the following advanced topics:

- **Engineering of Spatial Schmidt Modes in FWM**
  In chapter 6, we showed that one can control the distribution of the cross-correlation in the

twin beams using a pump beam with a pre-determined angular spectrum. We also discussed that, within the maximum gain region, the two-photon amplitude function $\mathbb{F}(\boldsymbol{q}_{pr}, \boldsymbol{q}_c)$ depends mainly on the properties of the pump beam. Therefore, a change in the angular spectrum of the pump field alters the Schmidt spectrum (obtained from the Schmidt decomposition of the corresponding $\mathbb{F}$ function). Our analysis of the experimental cross-correlation data acquired with a modified pump provides an early verification of this fact as shown in figure 7.4. A more detailed analysis with additional results can be found in the ref[188]. A key advantage of using a structured pump lies in the fact that the corresponding Schmidt spectrum can be tailored towards making the process more efficient if correlations are measured only in certain modes. It is well known that various spatial modes behave differently while propagating in the presence of environmental noise (such as turbulence[197]) or while propagating through multimode fibers[198]. Hence, a structured pump beam can be used to generate correlations between spatial modes with a distribution that is beneficial for a specific application. The modification of Schmidt modes in the time domain is already an active area of research to realize devices like quantum pulse gates[189] and heralded generation of photons with desired temporal properties[190].

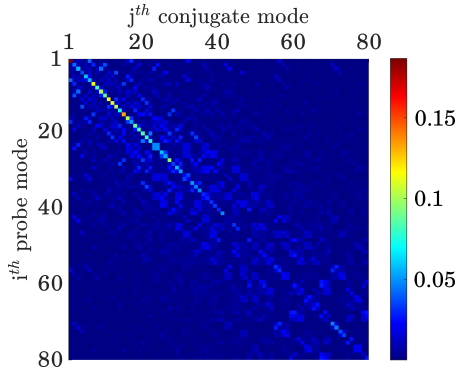

Figure 7.4: Modification of Schmidt modes using the pump angular spectrum. The fundamental eigenmode structure is different when the pump angular spectrum is modified, as evident from the non-diagonal behavior of $\lambda_{\text{exp}}^{\text{OU}}$ (using $\mathbb{F}_{\text{exp}}$ measured for the case of the OU logo) when projected onto the Schmidt basis calculated for the input Gaussian pump beam. One can therefore aim to populate specific Schmidt mode pairs using a modified pump field and effectively engineer Schmidt modes in the spatial domain.

- **Schmidt Mode Decomposition for Non-collinear FWM**
  In our Schmidt mode analysis in section 7.1, we ignored the contribution of the sinc function that accounts for phase-mismatch along the propagation direction and is effectively responsible for the open-angle or non-collinear configuration of the FWM (see chapters 3 and 4). Although the sinc function has a negligible effect on the distribution of the Schmidt modes at the center of the gain region, it dictates their decay behaviors by setting appropriate boundary conditions outside the maximum gain region. In fact, in the absence of a phase-matching function, the resulting Schmidt modes are unbounded along the $\boldsymbol{q}_{pr} = -\boldsymbol{q}_c$ manifold[140]. One can apply the method of SVD to evaluate Schmidt modes of the full $\mathbb{F}_{\text{exp}}(\boldsymbol{q}_{pr}, \boldsymbol{q}_c)$ distribution since it is also a symmetric function with respect to the $\boldsymbol{q}_{pr}$ and $\boldsymbol{q}_c$ variables as shown in section 4.3. However, while maintaining a good resolution in the $\boldsymbol{q}_{pr}$ and $\boldsymbol{q}_c$ variables, it may require decomposition of a matrix of size $\sim 10^6$ using a brute force approach. Further insights from the theoretical analysis of the problem may offer a simpler approach.

- **Higher Order Corrections to Cross-correlations**
  In our calculation of the far field correlations in chapter 6, we perturbatively expand the wave-function $|\Psi_{\text{TBS}}\rangle$ in terms of the interaction Hamiltonian and account only for the zero and first order contributions (see section 6.1). However, there can be contributions to the cross-correlations from higher order terms that can improve the fidelity between the simulated and experimental results (which is ∼0.6 for our current analysis, as shown in chapter 6). In our preliminary work [199], we find that while there is no second-order contribution, there is a non-zero third-order contribution. Improving the fidelity between expected and encoded information is useful for applications such as the quantum secure direct communication [148] with spatial variables. Using the Schmidt mode approach which effectively diagonalizes the interaction Hamiltonian, one could simplify the calculation of the third- or higher order contributions.

In conclusion, we have given a detailed account of our experimental studies of spatial correlations in twin beams generated using the $\chi^{(3)}$ non-linearity in ^{85}Rb vapor. After providing the necessary background, we began by understanding the interaction FWM Hamiltonian expressed in terms of the spatial variables. Based on what was expected from our intuitive picture, for a large size pump beam and a small length Rb cell[1], behavior of the near field correlations in the twin beams is governed by the phase-matching along the propagation direction; while the far field correlations are dependent on the pump angular spectrum following momentum conservation. We showed that for the probe and conjugate transverse position-momentum degrees of freedom, one can expect EPR entanglement. We discussed the details and results of our EPR experiment in which we verify the existence of EPR correlations as well as the inseparability in the spatial variables. Going beyond entanglement verification, we analyzed the exact dependence of far field correlations on the pump angular spectrum and implemented this understanding in our final experiment. We phase-structured the input pump beam to have specific angular spectrum that resulted in encoding of pre-determined spatial patterns in the relative momentum distribution of the twin beams. We also showed that the encoded information is only available via joint measurements and the temporal correlations are also preserved. Towards the end, we introduced the Schmidt modes as the spatial eigenmodes of the FWM process which provide a better understanding of correlated spatial modes in the twin beams.

[1] Explicitly, $z_R \gg L$ or what is known as the weak focusing limit [150].

Appendices

APPENDIX A

Hologram preparation for spatial light modulator

One of the main results described in this dissertation is achieving desired target patterns in the far field spatial correlations of the twin beam using a structured pump beam approach. For a given angular spectrum distribution $\mathcal{E}_o$ of the pump beam, the far field spatial correlation function c_{cross} is dictated by the convolution function Φ as outlined in the following expressions (see chapter 6),

$$c_{\text{cross}}\ (\boldsymbol{\xi}_+) \quad \equiv \quad \left\langle \delta\hat{N}_{pr}(-\boldsymbol{x})\delta\hat{N}_c\left(\boldsymbol{x}+\boldsymbol{\xi}_+\right)\right\rangle \tag{A.1}$$

$$\overset{\text{bright limit}}{\propto} \quad \left\langle \delta\hat{X}_{pr}(-\boldsymbol{x})\delta\hat{X}_c\left(\boldsymbol{x}+\boldsymbol{\xi}_+\right)\right\rangle \tag{A.2}$$

$$\propto \quad \mathfrak{Re}[\Phi(\boldsymbol{\xi}_+)], \tag{A.3}$$

where $\Phi = \mathcal{E}_o \star \mathcal{E}_o$ denotes the convolution of angular of spectrum ($\mathcal{E}_o$) of two pump photons involved in the FWM process. For a predefined target pattern (such as OU logo or $\hbar$) corresponding to the c_{cross} distribution, the goal is to impart the pump beam suitable angular spectrum implied by (A.3). Achieving this desired angular spectrum in the pump field involves applying a suitable phase pattern ϕ at the spatial light modulator (SLM) that is transferred to the pump field upon reflection. Subsequently, the reflected pump beam undergoes a $4f$ imaging system, accurately mapping the field distribution with the phase pattern to the Rb cell center.

The primary objective of hologram preparation is to compute the 2-dimensional phase profile $\phi(\rho)$ for the pump electric field to ensure that E_{out} (equivalent to the function Φ) given as,

$$E_{\text{out}} = \mathcal{E}_o\left(\frac{f\boldsymbol{q}_p}{k}\right) \star \mathcal{E}_o\left(\frac{f\boldsymbol{q}_p}{k}\right) \tag{A.4}$$

$$= \mathcal{F}_f\left[E_o(\boldsymbol{\rho})e^{i\phi(\boldsymbol{\rho})}\right] \star \mathcal{F}_f\left[E_o(\boldsymbol{\rho})e^{i\phi(\boldsymbol{\rho})}\right] \tag{A.5}$$

$$= \mathcal{F}_f\left[\left(E_o(\boldsymbol{\rho})e^{i\phi(\boldsymbol{\rho})}\right)^2\right] = T, \tag{A.6}$$

matches with the target field pattern T (see figure A.1). Here, $\boldsymbol{q}_p$ represents the pump's transverse momentum vector and $\boldsymbol{\rho} = (\rho_1, \rho_2)$ denotes the 2D coordinate in the transverse plane at the cell center. Figure A.1 shows a flowchart to compute an discrete phase matrix or computer generated hologram (CGH) that is iteratively optimized using a cost function. After calculating E_{out} for an initial guess phase using E_{in}, subsequent better values for ϕ can be realized by assigning a cost function to any deviations from the target pattern T and then using a minimization algorithm to

Hologram preparation for spatial light modulator

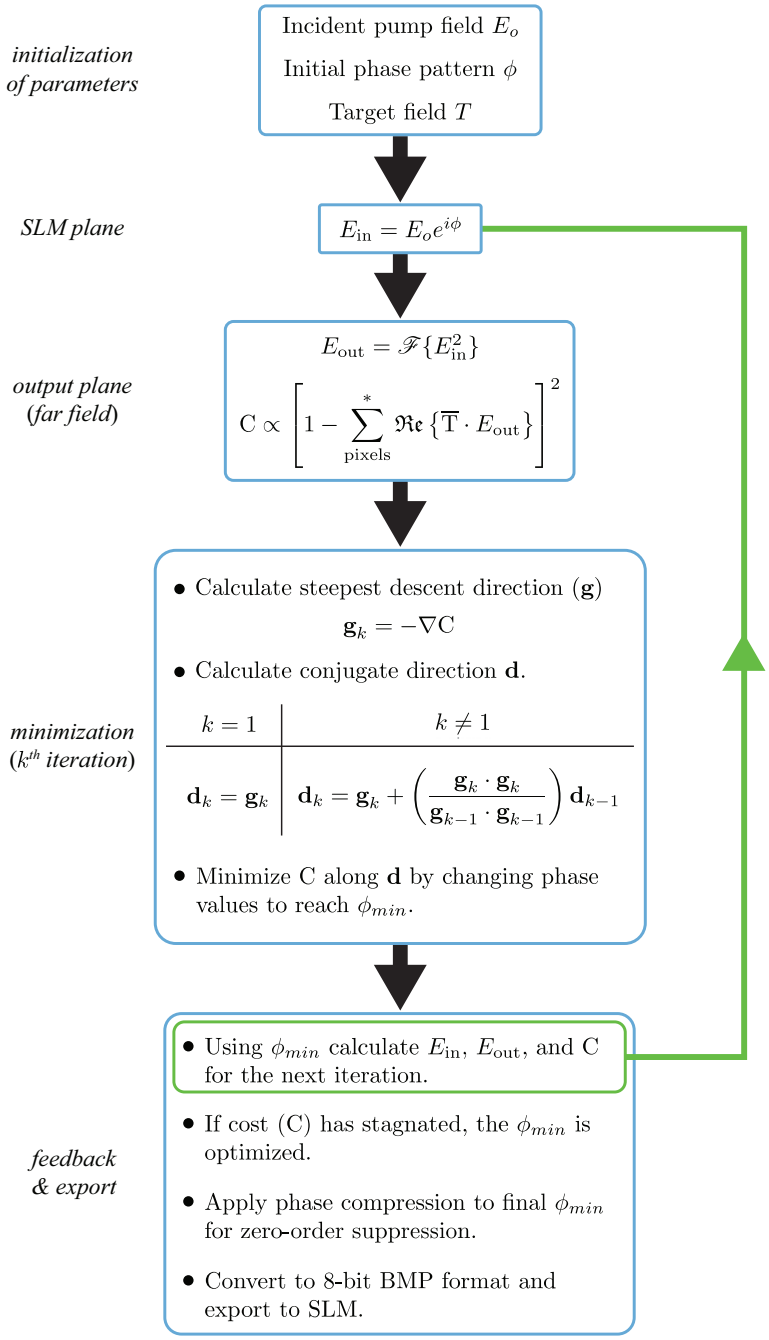

Figure A.1: The flowchart of the computational algorithm used to calculate phase pattern $\phi(\boldsymbol{\rho})$ for given target pattern T. The goal to achieve maximum overlap between E_{out} and T while optimizing ϕ using the conjugate gradient minimization coupled with MRAF algorithm. Beginning with an initial guess phase ϕ and the corresponding E_{out} is compared with T to estimate an initial cost using the cost function C which is then iteratively minimized along various conjugate directions (**d**) until its value stagnates. After an additional phase-compression step to reduce the zero order contribution during SLM reflection, the final phase pattern is converted into bitmap and is applied to the SLM. In the case of an ideal implementation, E_{out} at the far-field plane matches the desired target field T. Figure adapted from [71]. Reproduced with permission.

reduce the cost. A low cost value gives high degree of match between E_{out} and T, and ensures an optimal angular spectrum for the pump field is present at the Rb cell center.

We use a conjugate minimization algorithm [155] coupled with the mixed-region-amplitude-freedom (MRAF) approach to iteratively improve E_{out} matrix values. In MRAF, the transverse plane of target field is divided into a signal and a noise region and the cost function is only evaluated over the signal region while allowing the E_{out} to take any values outside this region. Therefore, any discrepancy between T and E_{out} values in the noise region doesn't affect the cost values. In our implementation of the conjugate gradient minimization algorithm, the cost function (C) has the form

$$\mathrm{C} = 10^n \left(1 - \sum_{\text{pixels}}^{*} \mathfrak{Re} \left(\overline{T} \cdot E_{\text{out}} \right) \right)^2 , \tag{A.7}$$

where $n = 10$, $\overline{T}$ represents complex conjugate of the target field, and $(\cdot)$ operation denotes point-wise multiplication. The cost function in (A.7) is evaluated only over the signal region as indicated by an asterisk over the summation. Based on the spatial discretization of $\boldsymbol{\rho}$ as well as the size of the grid (min/max $\boldsymbol{\rho}$ values) over which phase ϕ is defined, the cost function represents a N^2-dimensional surface for a $N \times N$ grid size. In our implementation, we use a grid size of 512×512.

To achieve a minimization of the cost function with respect to N^2 independent phase values, the gradient of cost function $\partial C/\partial \phi$ is calculated which provides the direction of steepest descent $\boldsymbol{g}$ along the multidimensional cost surface. Based on $\boldsymbol{g}$, a conjugate direction $\boldsymbol{d}$ is determined (see figure A.1). While descending along the conjugate direction $\boldsymbol{d}$, the cost function is reduced in finite size steps until a minimum is reached. We use the final phase value(s) ϕ_{min} to calculate a new gradient and a corresponding conjugate direction and further minimize the cost function C until it stagnates. The large pre-factor of 10^d ($n \sim 10$) in the cost function gives faster optimizations while avoiding local minima [155]. Due to the limited efficiency of our SLM device (especially for higher spatial frequencies), a fraction of the field remains unaltered during reflection and presents itself as a zero-order diffraction in the Fourier plane of the SLM. The phase values in the calculated CGH can be adjusted to suppress contribution from the zero-order. For this, we compress the final ϕ_{min} matrix to reduce the zero-order contribution in the far field [200]. Lastly, the compressed phase value is converted to 8-bit BMP format CGH and is applied to the SLM device. As mentioned in the main text (see chapter 6), the advantage of using phase-only hologram is that it doesn't significantly alter the pump intensity distribution, and therefore, provides a relatively better gain for the FWM process in our experiment. In addition to this, a spatially amplitude-modulated pump would amount to a substantially higher pump background in both the spatial and temporal detection.

APPENDIX B

Fourier transform using MATLAB

MATLAB uses the following definition of Fourier transform (FT) to perform a fast Fourier transform (FFT). The forward FT is

$$F(\xi) = \int_{\xi} e^{-i2\pi\xi x} f(x)\ d\xi\ , \tag{B.1}$$

with the corresponding inverse Fourier transform as

$$f(x) = \int_{x} e^{i2\pi\xi x} F(\xi)\ dx\ . \tag{B.2}$$

Here, a real space $f(x)$ is transformed into a function $F(\xi)$ in the space of spatial frequencies.

Another common definition of a Fourier transform, which is the one used in this dissertation, is

$$F_1(\xi) = \frac{1}{\sqrt{2\pi}} \int_{\xi} e^{-i\xi x} f(x)\ d\xi \tag{B.3}$$

$$f_1(x) = \frac{1}{\sqrt{2\pi}} \int_{x} e^{i\xi x} F(\xi)\ dx\ . \tag{B.4}$$

The variable ξ above is equivalent to spatial angular frequency or k-vector. From (B.1) and (B.3), we get

$$F(\xi) = \sqrt{2\pi} F_1(2\pi\xi). \tag{B.5}$$

In other words, the value of $F(1)$ is assigned to $F_1(2\pi)$ (apart from $\sqrt{2\pi}$ multiplication) and so on. Since MATLAB uses expression in (B.1), the transformation

$$F(\xi) \rightarrow F_1(\xi) \tag{B.6}$$

requires stretching the underlying grid by a factor of 2π, i.e.

$$\xi_{min} : d\xi : \xi_{max} \rightarrow (\xi_{min} : d\xi : \xi_{max}) \times 2\pi\ . \tag{B.7}$$

APPENDIX C

Saturation absorption spectroscopy layout

In our experiments, the single photon detuning of the pump and seed (probe) beams is actively maintained using a PID servo lock based on the saturation absorption (SatAbs) spectroscopy of ^{85}Rb atoms. The overall locking mechanism works by creating upper and lower frequency sidebands (using a electro-optic modulator) on a portion of field and locking one of these sidebands to a fixed ^{85}Rb transition which gives a red or blue detuned locking on the laser frequency. In our implementation, we create the upper and lower sidebands with a specific frequency f ($\sim$ 1.1 GHz, see figure C.1) on a portion of the field at the laser frequency. The lower sideband is then locked to the ^{85}Rb $5\,^2\mathrm{S}_{1/2}, F{=}2 \longrightarrow 5\,^2\mathrm{P}_{1/2}, F'{=}3$ transition. This effectively locks the laser frequency on the blue side of the aforementioned transition with a frequency separation f.

Saturation absorption spectroscopy layout

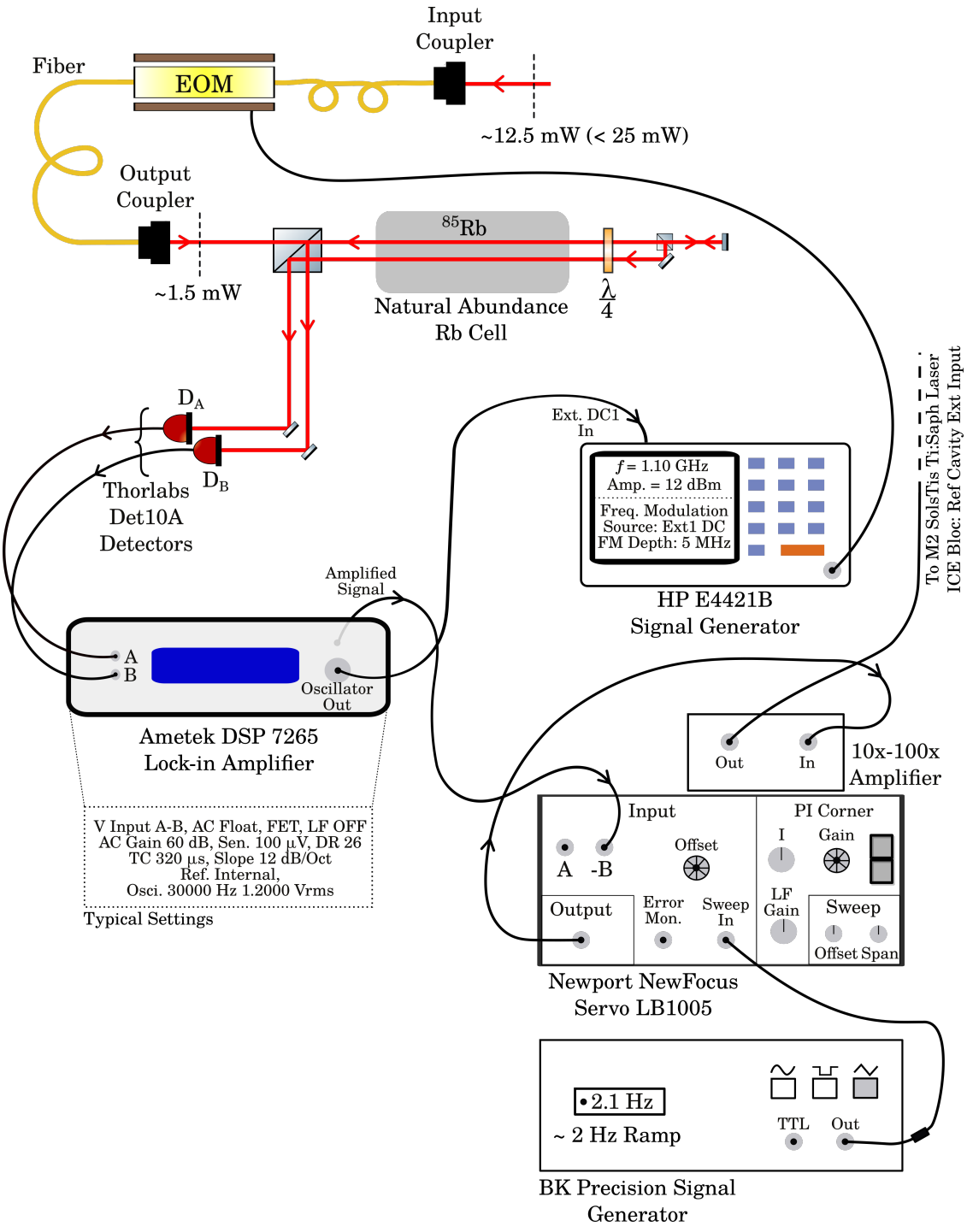

Figure C.1: Ti:Sapphire LASER frequency stabilization using ^{85}Rb spectroscopy.

Bibliography

[1] C. E. Shannon, The Bell System Technical Journal **27**, 379 (1948).

[2] C. H. Bennett and G. Brassard, Theoretical Computer Science **560**, 7 (2014), theoretical Aspects of Quantum Cryptography – celebrating 30 years of BB84.

[3] A. K. Ekert, Phys. Rev. Lett. **67**, 661 (1991).

[4] P. W. Shor and J. Preskill, Phys. Rev. Lett. **85**, 441 (2000).

[5] X. Ma, X. Yuan, Z. Cao, B. Qi, and Z. Zhang, npj Quantum Information **2**, 16021 (2016).

[6] E. Otte, I. Nape, C. Rosales-Guzmán, C. Denz, A. Forbes, and B. Ndagano, J. Opt. Soc. Am. B **37**, A309 (2020).

[7] M. Mirhosseini, O. S. Magaña-Loaiza, M. N. O'Sullivan, B. Rodenburg, M. Malik, M. P. J. Lavery, M. J. Padgett, D. J. Gauthier, and R. W. Boyd, New Journal of Physics **17**, 033033 (2015).

[8] I. Nape, B. Sephton, P. Ornelas, C. Moodley, and A. Forbes, APL Photonics **8**, 051101 (2023).

[9] M. Kolobov, *Quantum Imaging* (Springer New York, 2007).

[10] A. Meda, E. Losero, N. Samantaray, F. Scafirimuto, S. Pradyumna, A. Avella, I. Ruo-Berchera, and M. Genovese, Journal of Optics **19**, 094002 (2017).

[11] G. Brida, M. Genovese, A. Meda, and I. R. Berchera, Phys. Rev. A **83**, 033811 (2011).

[12] M. A. Taylor, J. Janousek, V. Daria, J. Knittel, B. Hage, H.-A. Bachor, and W. P. Bowen, Nature Photonics **7**, 229 (2013).

[13] N. H. Valencia, S. Goel, W. McCutcheon, H. Defienne, and M. Malik, Nature Physics **16**, 1112 (2020).

[14] I. H. Deutsch, PRX Quantum **1**, 020101 (2020).

[15] J. Preskill, Quantum **2**, 79 (2018).

[16] Editorial, Nature Physics **19**, 605 (2023).

[17] J.-Y. Wang, B. Yang, S.-K. Liao, L. Zhang, Q. Shen, X.-F. Hu, J.-C. Wu, S.-J. Yang, H. Jiang, Y.-L. Tang, B. Zhong, H. Liang, W.-Y. Liu, Y.-H. Hu, Y.-M. Huang, B. Qi, J.-G. Ren, G.-S. Pan, J. Yin, J.-J. Jia, Y.-A. Chen, K. Chen, C.-Z. Peng, and J.-W. Pan, Nature Photonics **7**, 387 (2013).

[18] Y. Zhang, Z. Li, Z. Chen, C. Weedbrook, Y. Zhao, X. Wang, Y. Huang, C. Xu, X. Zhang, Z. Wang, M. Li, X. Zhang, Z. Zheng, B. Chu, X. Gao, N. Meng, W. Cai, Z. Wang, G. Wang, S. Yu, and H. Guo, Quantum Science and Technology **4**, 035006 (2019).

[19] J. Yin, Y.-H. Li, L. Shengkai, M. Yang, Y. Cao, L. Zhang, J. Wang, W.-Q. Cai, W.-Y. Liu, S.-L. Li, R. Shu, Y.-M. Huang, L. Deng, L. Li, Q. Zhang, N.-L. Liu, Y.-A. Chen, C.-Y. Lu, X.-B. Wang, and J.-W. Pan, Nature **582**, 1 (2020).

[20] A. D. Ludlow, M. M. Boyd, J. Ye, E. Peik, and P. O. Schmidt, Rev. Mod. Phys. **87**, 637 (2015).

[21] E. A. Burt, J. D. Prestage, R. L. Tjoelker, D. G. Enzer, D. Kuang, D. W. Murphy, D. E. Robison, J. M. Seubert, R. T. Wang, and T. A. Ely, Nature **595**, 43 (2021).

[22] C. Casacio, L. Madsen, A. Terrasson, M. Waleed, K. Barnscheidt, B. Hage, M. Taylor, and W. Bowen, Nature **594**, 201 (2021).

[23] M. Tse, H. Yu, N. Kijbunchoo, A. Fernandez-Galiana, P. Dupej, L. Barsotti, C. D. Blair, D. D. Brown, S. E. Dwyer, A. Effler, M. Evans, P. Fritschel, V. V. Frolov, A. C. Green, G. L. Mansell, F. Matichard, N. Mavalvala, D. E. McClelland, L. McCuller, T. McRae, J. Miller, A. Mullavey, E. Oelker, I. Y. Phinney, D. Sigg, B. J. J. Slagmolen, T. Vo, R. L. Ward, C. Whittle, R. Abbott, C. Adams, R. X. Adhikari, A. Ananyeva, S. Appert, K. Arai, J. S. Areeda, Y. Asali, S. M. Aston, C. Austin, A. M. Baer, M. Ball, S. W. Ballmer, S. Banagiri, D. Barker, J. Bartlett, B. K. Berger, J. Betzwieser, D. Bhattacharjee, G. Billingsley, S. Biscans, R. M. Blair, N. Bode, P. Booker, R. Bork, A. Bramley, A. F. Brooks, A. Buikema, C. Cahillane, K. C. Cannon, X. Chen, A. A. Ciobanu, F. Clara, S. J. Cooper, K. R. Corley, S. T. Countryman, P. B. Covas, D. C. Coyne, L. E. H. Datrier, D. Davis, C. Di Fronzo, J. C. Driggers, T. Etzel, T. M. Evans, J. Feicht, P. Fulda, M. Fyffe, J. A. Giaime, K. D. Giardina, P. Godwin, E. Goetz, S. Gras, C. Gray, R. Gray, A. Gupta, E. K. Gustafson, R. Gustafson, J. Hanks, J. Hanson, T. Hardwick, R. K. Hasskew, M. C. Heintze, A. F. Helmling-Cornell, N. A. Holland, J. D. Jones, S. Kandhasamy, S. Karki, M. Kasprzack, K. Kawabe, P. J. King, J. S. Kissel, R. Kumar, M. Landry, B. B. Lane, B. Lantz, M. Laxen, Y. K. Lecoeuche, J. Leviton, J. Liu, M. Lormand, A. P. Lundgren, R. Macas, M. MacInnis, D. M. Macleod, S. Márka, Z. Márka, D. V. Martynov, K. Mason, T. J. Massinger, R. McCarthy, S. McCormick, J. McIver, G. Mendell, K. Merfeld, E. L. Merilh, F. Meylahn, T. Mistry, R. Mittleman, G. Moreno, C. M. Mow-Lowry, S. Mozzon, T. J. N. Nelson, P. Nguyen, L. K. Nuttall, J. Oberling, R. J. Oram, B. O'Reilly, C. Osthelder, D. J. Ottaway, H. Overmier, J. R. Palamos, W. Parker, E. Payne, A. Pele, C. J. Perez, M. Pirello, H. Radkins, K. E. Ramirez, J. W. Richardson, K. Riles, N. A. Robertson, J. G. Rollins, C. L. Romel, J. H. Romie, M. P. Ross, K. Ryan, T. Sadecki, E. J. Sanchez, L. E. Sanchez, T. R. Saravanan, R. L. Savage, D. Schaetzl, R. Schnabel, R. M. S. Schofield, E. Schwartz, D. Sellers, T. J. Shaffer, J. R. Smith, S. Soni, B. Sorazu, A. P. Spencer, K. A. Strain, L. Sun, M. J. Szczepańczyk, M. Thomas, P. Thomas, K. A. Thorne, K. Toland, C. I. Torrie, G. Traylor, A. L. Urban, G. Vajente, G. Valdes, D. C. Vander-Hyde, P. J. Veitch, K. Venkateswara, G. Venugopalan, A. D. Viets, C. Vorvick, M. Wade, J. Warner, B. Weaver, R. Weiss, B. Willke, C. C. Wipf, L. Xiao, H. Yamamoto, M. J. Yap, H. Yu, L. Zhang, M. E. Zucker, and J. Zweizig, Phys. Rev. Lett. **123**, 231107 (2019).

[24] J. Lough, E. Schreiber, F. Bergamin, H. Grote, M. Mehmet, H. Vahlbruch, C. Affeldt, M. Brinkmann, A. Bisht, V. Kringel, H. Lück, N. Mukund, S. Nadji, B. Sorazu, K. Strain, M. Weinert, and K. Danzmann, Phys. Rev. Lett. **126**, 041102 (2021).

[25] A. Muthukrishnan, M. O. Scully, and M. S. Zubairy, Optics & Photonics News **14**, 59 (2003).

[26] T. H. Maiman, Nature **187**, 493 (1960).

[27] R. E. Slusher, L. W. Hollberg, B. Yurke, J. C. Mertz, and J. F. Valley, Phys. Rev. Lett. **55**, 2409 (1985).

[28] H. J. Kimble, M. Dagenais, and L. Mandel, Phys. Rev. Lett. **39**, 691 (1977).

[29] L. Mandel, Phys. Rev. Lett. **49**, 136 (1982).

[30] J. D. Jackson, *Classical Electrodynamics, 3rd Edition* (Wiley-VCH, New York, 1998).

[31] C. Gerry and P. Knight, *Introductory Quantum Optics* (Cambridge University Press, 2004).

[32] L. Mandel and E. Wolf, *Optical Coherence and Quantum Optics* (Cambridge University Press, 1995).

[33] W. Vogel and D. Welsch, *Quantum Optics* (Wiley-VCH, 2006).

[34] P. A. M. Dirac and N. H. D. Bohr, Proceedings of the Royal Society of London. Series A, Containing Papers of a Mathematical and Physical Character **114**, 243 (1927).

[35] S. Weinberg, Daedalus **106**, 17 (1977).

[36] R. J. Glauber, Phys. Rev. **130**, 2529 (1963).

[37] R. J. Glauber, Rev. Mod. Phys. **78**, 1267 (2006).

[38] L. Mandel, Opt. Lett. **4**, 205 (1979).

[39] D. J. Griffiths, *Introduction to Quantum Mechanics, 3rd Edition* (Cambridge University Press, 2018).

[40] R. J. Glauber, Phys. Rev. **131**, 2766 (1963).

[41] A. M. Fox, *Quantum Optics: An Introduction* (Oxford University Press Inc., New York, 2006).

[42] L. Mandel, Physica Scripta **1986**, 34 (1986).

[43] H.-A. Bachor and T. C. Ralph, *A Guide to Experiments in Quantum Optics* (Wiley-VCH Verlag GmbH & Co. KGaA, 2019).

[44] U. Fano, Phys. Rev. **72**, 26 (1947).

[45] D. Gabor, Journal of the Institution of Electrical Engineers - Part I: General **94**, 58 (1946).

[46] W. P. Schleich, *Quantum Optics in Phase Space* (Wiley-VCH Verlag GmbH, Berlin, 2001).

[47] K. E. Cahill and R. J. Glauber, Phys. Rev. **177**, 1882 (1969).

[48] C. Zachos, D. Fairlie, and T. Curtright, *Quantum Mechanics in Phase Space: An Overview with Selected Papers*, World Scientific series in 20th century physics (World Scientific, 2005).

[49] M. Hillery, R. O'Connell, M. Scully, and E. Wigner, Physics Reports **106**, 121 (1984).

[50] M. Ban, Journal of Mathematical Physics **39**, 1744 (1998).

[51] A. Polkovnikov, Annals of Physics **325**, 1790 (2010).

[52] R. Schnabel, Physics Reports **684**, 1 (2017).

[53] C. M. Caves and B. L. Schumaker, Phys. Rev. A **31**, 3068 (1985).

[54] D. F. Walls, Nature **306**, 141 (1983).

[55] G. S. Agarwal, *Quantum Optics* (Cambridge University Press, 2012).

[56] N. N. Bogoliubov, V. V. Tolmachov, and D. V. Širkov, Fortschritte der Physik **6**, 605 (1958).

[57] G. D'Ariano, M. Rasetti, and M. Vadacchino, Phys. Rev. D **32**, 1034 (1985).

[58] R. A. Fisher, M. M. Nieto, and V. D. Sandberg, Phys. Rev. D **29**, 1107 (1984).

[59] D. R. Truax, Phys. Rev. D **31**, 1988 (1985).

[60] N. Jain, S. R. Huisman, E. Bimbard, and A. I. Lvovsky, Opt. Express **18**, 18254 (2010).

[61] L. Caspani, C. Xiong, B. J. Eggleton, D. Bajoni, M. Liscidini, M. Galli, R. Morandotti, and D. J. Moss, Light, Science & Applications **6** (2017).

[62] M. D. Reid, Phys. Rev. A **40**, 913 (1989).

[63] Z. Y. Ou, S. F. Pereira, H. J. Kimble, and K. C. Peng, Phys. Rev. Lett. **68**, 3663 (1992).

[64] C. Silberhorn, P. K. Lam, O. Weiß, F. König, N. Korolkova, and G. Leuchs, Phys. Rev. Lett. **86**, 4267 (2001).

[65] L.-M. Duan, G. Giedke, J. I. Cirac, and P. Zoller, Phys. Rev. Lett. **84**, 2722 (2000).

[66] F. Acernese, M. Agathos, A. Ain, S. Albanesi, C. Alléné, A. Allocca, A. Amato, C. Amra, M. Andia, T. Andrade, N. Andres, M. Andrés-Carcasona, T. Andrić, S. Ansoldi, S. Antier, T. Apostolatos, E. Z. Appavuravther, M. Arène, N. Arnaud, M. Assiduo, S. A. d. S. Melo, P. Astone, F. Aubin, S. Babak, F. Badaracco, S. Bagnasco, J. Baird, T. Baka, G. Ballardin, G. Baltus, B. Banerjee, P. Barneo, F. Barone, M. Barsuglia, D. Barta, A. Basti, M. Bawaj, M. Bazzan, F. Beirnaert, M. Bejger, V. Benedetto, M. Berbel, S. Bernuzzi, D. Bersanetti, A. Bertolini, U. Bhardwaj, A. Bianchi, M. Bilicki, S. Bini, M. Bischi, M. Bitossi, M.-A. Bizouard, F. Bobba, M. Boër, G. Bogaert, G. Boileau, M. Boldrini, L. D. Bonavena, R. Bondarescu, F. Bondu, R. Bonnand, V. Boschi, V. Boudart, Y. Bouffanais, A. Bozzi, C. Bradaschia, M. Braglia, M. Branchesi, M. Breschi, T. Briant, A. Brillet, J. Brooks, G. Bruno, F. Bucci, O. Bulashenko, T. Bulik, H. J. Bulten, R. Buscicchio, D. Buskulic, C. Buy, G. Cabras, R. Cabrita, G. Cagnoli, E. Calloni, M. Canepa, G. C. Santoro, M. Cannavacciuolo, E. Capocasa, G. Carapella, F. Carbognani, M. Carpinelli, G. Carullo, J. C. Diaz, C. Casentini, S. Caudill, R. Cavalieri, G. Cella, P. Cerdá-Durán, E. Cesarini, W. Chaibi, P. Chanial, E. Chassande-Mottin, S. Chaty, P. Chessa, F. Chiadini, G. Chiarini, R. Chierici, A. Chincarini, M. L. Chiofalo, A. Chiummo, N. Christensen, S. Chua, G. Ciani, P. Ciecielag, M. Cieślar, M. Cifaldi, R. Ciolfi, S. Clesse, F. Cleva, E. Coccia, E. Codazzo, P.-F. Cohadon, A. Colombo, M. Colpi, L. Conti, I. Cordero-Carrión, S. Corezzi, S. Cortese, J.-P. Coulon, J.-F. Coupechoux, M. Croquette, J. R. Cudell, E. Cuoco, M. Curyło, P. Dabadie, T. D. Canton, S. Dall'Osso, G. Dálya, B. D'Angelo, G. Dangoisse, S. Danilishin, S. D'Antonio, V. Dattilo, M. Davier, J. Degallaix, M. De Laurentis, S. Deléglise, F. De Lillo, D. Dell'Aquila, W. Del Pozzo, F. De Matteis, A. Depasse, R. De Pietri, R. De Rosa, C. De Rossi, R. De Simone, L. Di Fiore, C. Di Giorgio, F. Di Giovanni, M. Di Giovanni, T. Di Girolamo, D. Diksha, A. Di Lieto, A. Di Michele, J. Ding, S. Di Pace, I. Di Palma, F. Di Renzo, L. D'Onofrio, T. Dooney, O. Dorosh, M. Drago, J.-G. Ducoin, U. Dupletsa, O. Durante, D. D'Urso, P.-A. Duverne, M. Eisenmann, L. Errico, D. Estevez, F. Fabrizi, F. Faedi, V. Fafone, G. Favaro, M. Fays, E. Fenyvesi, I. Ferrante, F. Fidecaro, P. Figura, A. Fiori, I. Fiori, R. Fittipaldi, V. Fiumara, R. Flaminio, J. A. Font, S. Frasca, F. Frasconi, A. Freise, O. Freitas, G. G. Fronzé, B. Gadre, R. Gamba, B. Garaventa, J. Garcia-Bellido, J. Gargiulo, F. Garufi, C. Gasbarra, G. Gemme, A. Gennai, A. Ghosh, L. Giacoppo, P. Giri, F. Gissi, S. Gkaitatzis, F. Glotin, B. Goncharov, M. Gosselin, R. Gouaty, A. Grado, M. Granata, V. Granata, G. Greco, G. Grignani, A. Grimaldi, D. Guerra, D. Guetta, G. M. Guidi, F. Gulminelli, Y. Guo, P. Gupta, N. Gutierrez, L. Haegel, O. Halim, O. Hannuksela, T. Harder, K. Haris, T. Harmark, J. Harms, B. Haskell, A. Heidmann, H. Heitmann, P. Hello, G. Hemming, E. Hennes, J.-S. Hennig, M. Hennig, S. Hild, D. Hofman, N. A. Holland, V. Hui, G. A. Iandolo, B. Idzkowski, A. Iess, G. Iorio, P. Iosif, T. Jacqmin, P.-E. Jacquet, J. Janquart, K. Janssens, S. Jaraba, P. Jaranowski, P. Jasal, V. Juste, C. Kalaghatgi, C. Karathanasis, S. Katsanevas, F. Kéfélian, G. Koekoek, S. Koley, M. Kolstein, S. L. Kranzhoff, A. Królak, P. Kuijer, S. Kuroyanagi, P. Lagabbe, D. Laghi, M. Lalleman, A. Lamberts, A. La Rana, I. La Rosa, A. Lartaux-Vollard, C. Lazzaro, P. Leaci, A. Lemaître, M. Lenti, E. Leonova, M. Lequime, N. Leroy, N. Letendre, M. Lethuillier, K. Leyde, F. Linde, L. London, A. Longo, M. L. Portilla, M. Lorenzini, V. Loriette, G. Losurdo, D. Lumaca, A. Macquet, C. Magazzù, R. Maggiore, M. Magnozzi, E. Majorana, N. Man, V. Mangano, M. Mantovani, M. Mapelli, F. Marchesoni, D. M. Pina, F. Marion, A. Marquina, S. Marsat, F. Martelli, M. Martinez, V. Martinez, A. Masserot, M. Mastrodicasa, S. Mastrogiovanni, Q. Meijer, A. Menendez-Vazquez, L. Mereni, M. Merzougui, A. Miani, C. Michel, A. Miller, B. Miller, E. Milotti, Y. Minenkov, L. M. Mir, M. Miravet-Tenés, A. L. Mitchell, C. Mondal, M. Montani, F. Morawski, G. Morras, A. Moscatello, B. Mours, C. M. Mow-Lowry, E. Msihid, F. Muciaccia, S. Mukherjee, A. Nagar, V. Napolano, I. Nardecchia, H. Narola, L. Naticchioni, J. Neilson, S. Nesseris, C. Nguyen, G. Nieradka, S. Nissanke, E. Nitoglia, F. Nocera, J. Novak, J. F. N. no Siles, M. Oertel, G. Oganesyan, R. Oliveri, M. Orselli, C. Palomba, P. T. H. Pang, F. Pannarale, F. Paoletti, A. Paoli, A. Paolone, G. Pappas, A. Parisi, D. Pascucci, A. Pasqualetti, R. Passaquieti, D. Passuello, B. Patricelli, R. Pedurand, R. Pegna, M. Pegoraro, A. Perego, A. Pereira, C. Périgois, A. Perreca, S. Perriès, J. W. Perry, D. Pesios, C. Petrillo, K. S. Phukon, O. J. Piccinni, M. Pichot, M. Piendibene, F. Piergiovanni, L. Pierini, G. Pierra, V. Pierro, G. Pillant, M. Pillas, F. Pilo, L. Pinard, I. M. Pinto, M. Pinto, M. Pinto, K. Piotrzkowski, A. Placidi, E. Placidi, W. Plastino, R. Poggiani, E. Polini, E. Porcelli, J. Portell, E. K. Porter, R. Poulton, M. Pracchia, T. Pradier, M. Principe, G. A. Prodi, P. Prosposito, A. Puecher, M. Punturo, F. Puosi, P. Puppo, G. Raaijmakers, N. Radulesco, P. Rapagnani, M. Razzano, T. Regimbau, L. Rei, P. Rettegno, B. Revenu, A. Reza, A. S. Rezaei, F. Ricci, S. Rinaldi, F. Robinet, A. Rocchi, L. Rolland, M. Romanelli, R. Romano, A. Romero, S. Ronchini, L. Rosa, D. Rosińska, S. Roy, D. Rozza, P. Ruggi, E. R. Morales, P. Saffarieh, O. S. Salafia, L. Salconi, F. Salemi, M. Sallé, A. Samajdar, N. Sanchis-Gual, A. Sanuy, A. Sasli, P. Sassi, B. Sassolas, S. Sayah, S. Schmidt, M. Seglar-Arroyo, D. Sentenac, V. Sequino, G. Servignat, Y. Setyawati, N. S. Shcheblanov, M. Sieniawska, L. Silenzi, N. Singh, A. Singha, V. Sipala, J. Soldateschi, V. Sordini, F. Sorrentino, N. Sorrentino, R. Soulard, V. Spagnuolo, M. Spera, P. Spinicelli, C. Stachie, D. A. Steer, J. Steinlechner, S. Steinlechner, N. Stergioulas, G. Stratta, M. Suchenek, A. Sur,

J. Suresh, B. L. Swinkels, A. Syx, P. Szewczyk, M. Tacca, N. Tamanini, A. J. Tanasijczuk, E. N. T. S. Martín, C. Taranto, M. Tonelli, A. Torres-Forné, I. T. e Melo, E. Tournefier, A. Trapananti, F. Travasso, J. Trenado, M. C. Tringali, L. Troiano, A. Trovato, L. Trozzo, K. W. Tsang, K. Turbang, M. Turconi, C. Turski, H. Ubach, A. Utina, M. Valentini, S. Vallero, N. van Bakel, M. van Beuzekom, M. van Dael, J. F. J. van den Brand, C. Van Den Broeck, M. van der Sluys, A. Van de Walle, J. van Dongen, H. van Haevermaet, J. V. van Heijningen, Z. van Ranst, N. van Remortel, M. Vardaro, M. Vasúth, G. Vedovato, P. Verdier, D. Verkindt, P. Verma, F. Vetrano, A. Viceré, J.-Y. Vinet, S. Viret, A. Virtuoso, H. Vocca, R. C. Walet, M. Was, N. Yadav, A. Zadrożny, T. Zelenova, J.-P. Zendri, Y. Zhao, M. Zerrad, H. Vahlbruch, M. Mehmet, H. Lück, and K. Danzmann (Virgo Collaboration), Phys. Rev. Lett. **131**, 041403 (2023).

[67] M. Dowran, A. Kumar, B. J. Lawrie, R. C. Pooser, and A. M. Marino, Optica **5**, 628 (2018).

[68] E. Brambilla, L. Caspani, O. Jedrkiewicz, L. A. Lugiato, and A. Gatti, Phys. Rev. A **77**, 053807 (2008).

[69] P. M. Anisimov, G. M. Raterman, A. Chiruvelli, W. N. Plick, S. D. Huver, H. Lee, and J. P. Dowling, Phys. Rev. Lett. **104**, 103602 (2010).

[70] T. Gehring, V. Händchen, J. Duhme, F. Furrer, T. Franz, C. Pacher, R. F. Werner, and R. Schnabel, Nature Communications **6**, 8795 (2015).

[71] G. Nirala, S. T. Pradyumna, A. Kumar, and A. M. Marino, Science Advances **9**, eadf9161 (2023).

[72] R. N. Alexander, P. Wang, N. Sridhar, M. Chen, O. Pfister, and N. C. Menicucci, Phys. Rev. A **94**, 032327 (2016).

[73] C. González-Arciniegas, P. Nussenzveig, M. Martinelli, and O. Pfister, PRX Quantum **2**, 030343 (2021).

[74] D. Stoler, Phys. Rev. D **1**, 3217 (1970).

[75] D. Stoler, Phys. Rev. D **4**, 1925 (1971).

[76] H. P. Yuen, Phys. Rev. A **13**, 2226 (1976).

[77] C. M. Caves, Phys. Rev. D **23**, 1693 (1981).

[78] L.-A. Wu, H. J. Kimble, J. L. Hall, and H. Wu, Phys. Rev. Lett. **57**, 2520 (1986).

[79] U. L. Andersen, T. Gehring, C. Marquardt, and G. Leuchs, Physica Scripta **91**, 053001 (2016).

[80] H. Vahlbruch, M. Mehmet, K. Danzmann, and R. Schnabel, Phys. Rev. Lett. **117**, 110801 (2016).

[81] R. W. Boyd, *Nonlinear Optics: Third Edition* (Academic Press, Burlington, 2008).

[82] W. H. Louisell, A. Yariv, and A. E. Siegman, Phys. Rev. **124**, 1646 (1961).

[83] C. K. Hong and L. Mandel, Phys. Rev. A **31**, 2409 (1985).

[84] M. O. Scully and M. S. Zubairy, *Quantum Optics* (Cambridge University Press, 1997).

[85] M. T. Turnbull, P. G. Petrov, C. S. Embrey, A. M. Marino, and V. Boyer, Phys. Rev. A **88**, 033845 (2013).

[86] G. Breitenbach and S. Schiller, Journal of Modern Optics **44**, 2207 (1997).

[87] F. A. S. Barbosa, A. S. Coelho, K. N. Cassemiro, P. Nussenzveig, C. Fabre, M. Martinelli, and A. S. Villar, Phys. Rev. Lett. **111**, 200402 (2013).

[88] F. A. S. Barbosa, A. S. Coelho, K. N. Cassemiro, P. Nussenzveig, C. Fabre, A. S. Villar, and M. Martinelli, Phys. Rev. A **88**, 052113 (2013).

[89] A. M. Marino, J. C. R. Stroud, V. Wong, R. S. Bennink, and R. W. Boyd, J. Opt. Soc. Am. B **24**, 335 (2007).

[90] C. S. Embrey, J. Hordell, P. G. Petrov, and V. Boyer, Opt. Express **24**, 27298 (2016).

[91] V. Boyer, A. Marino, R. Pooser, and P. Lett, Science (New York, N.Y.) **321**, 544 (2008).

[92] C. Fabre and N. Treps, Rev. Mod. Phys. **92**, 035005 (2020).

[93] A. Kumar, H. Nunley, and A. M. Marino, Phys. Rev. A **95**, 053849 (2017).

[94] A. Kumar, G. Nirala, and A. M. Marino, Quantum Science and Technology **6**, 045016 (2021).

[95] J. Schneeloch and J. C. Howell, Journal of Optics **18**, 053501 (2016).

[96] R. E. Slusher, B. Yurke, P. Grangier, A. Laporta, and D. F. Walls, Journal of the Optical Society of America B Optical Physics **4**, 1453 (1987).

[97] P. R. Sharapova, G. Frascella, M. Riabinin, A. M. Pérez, O. V. Tikhonova, S. Lemieux, R. W. Boyd, G. Leuchs, and M. V. Chekhova, Phys. Rev. Res. **2**, 013371 (2020).

[98] H. H. Arnaut and G. A. Barbosa, Phys. Rev. Lett. **85**, 286 (2000).

[99] T. B. Pittman, D. V. Strekalov, D. N. Klyshko, M. H. Rubin, A. V. Sergienko, and Y. H. Shih, Phys. Rev. A **53**, 2804 (1996).

[100] M. V. Fedorov, M. A. Efremov, A. E. Kazakov, K. W. Chan, C. K. Law, and J. H. Eberly, Phys. Rev. A **69**, 052117 (2004).

[101] S. P. Walborn, A. N. de Oliveira, R. S. Thebaldi, and C. H. Monken, Phys. Rev. A **69**, 023811 (2004).

[102] A. R. Altman, K. G. Köprülü, E. Corndorf, P. Kumar, and G. A. Barbosa, Phys. Rev. Lett. **94**, 123601 (2005).

[103] G. A. Barbosa and H. H. Arnaut, Phys. Rev. A **65**, 053801 (2002).

[104] M. V. Fedorov, Y. M. Mikhailova, and P. A. Volkov, Journal of Physics B: Atomic, Molecular and Optical Physics **42**, 175503 (2009).

[105] J. Goodman, *Introduction to Fourier Optics*, McGraw-Hill physical and quantum electronics series (W. H. Freeman, 2005).

[106] J. C. Howell, R. S. Bennink, S. J. Bentley, and R. W. Boyd, Phys. Rev. Lett. **92**, 210403 (2004).

[107] P.-A. Moreau, F. Devaux, and E. Lantz, Phys. Rev. Lett. **113**, 160401 (2014).

[108] M. Fadel, T. Zibold, B. Décamps, and P. Treutlein, Science **360**, 409 (2018).

[109] Q. Y. He and M. D. Reid, Phys. Rev. A **88**, 052121 (2013).

[110] A. Einstein, B. Podolsky, and N. Rosen, Phys. Rev. **47**, 777 (1935).

[111] J. S. Bell, Physics Physique Fizika **1**, 195 (1964).

[112] A. Aspect, J. Dalibard, and G. Roger, Phys. Rev. Lett. **49**, 1804 (1982).

[113] G. Weihs, T. Jennewein, C. Simon, H. Weinfurter, and A. Zeilinger, Phys. Rev. Lett. **81**, 5039 (1998).

[114] D. Salart, A. Baas, J. A. W. van Houwelingen, N. Gisin, and H. Zbinden, Phys. Rev. Lett. **100**, 220404 (2008).

[115] A. Hochrainer, M. Lahiri, R. Lapkiewicz, G. B. Lemos, and A. Zeilinger, Proceedings of the National Academy of Sciences **114**, 1508 (2017).

[116] M. D. Reid, P. D. Drummond, W. P. Bowen, E. G. Cavalcanti, P. K. Lam, H. A. Bachor, U. L. Andersen, and G. Leuchs, Rev. Mod. Phys. **81**, 1727 (2009).

[117] S. F. Huelga, C. Macchiavello, T. Pellizzari, A. K. Ekert, M. B. Plenio, and J. I. Cirac, Phys. Rev. Lett. **79**, 3865 (1997).

[118] V. Giovannetti, S. Lloyd, and L. Maccone, Nature Photonics **5**, 222 (2011).

[119] C. S. Embrey, M. T. Turnbull, P. G. Petrov, and V. Boyer, Phys. Rev. X **5**, 031004 (2015).

[120] C. Kim and P. Kumar, Phys. Rev. Lett. **73**, 1605 (1994).

[121] M. Martinelli, N. Treps, S. Ducci, S. Gigan, A. Maître, and C. Fabre, Phys. Rev. A **67**, 023808 (2003).

[122] I. N. Agafonov, M. V. Chekhova, and G. Leuchs, Phys. Rev. A **82**, 011801 (2010).

[123] M. Chekhova, G. Leuchs, and M. Zukowski, Optics Communications **337**, 27 (2015).

[124] M. Taylor, J. Janousek, V. Daria, J. Knittel, B. Hage, H.-A. Bachor, and W. Bowen, Nature Photonics **7** (2012).

[125] M. R. Andrews, M.-O. Mewes, N. J. van Druten, D. S. Durfee, D. M. Kurn, and W. Ketterle, Science **273**, 84 (1996).

[126] K. E. Wilson, Z. L. Newman, J. D. Lowney, and B. P. Anderson, Phys. Rev. A **91**, 023621 (2015).

[127] E. Streed, A. Jechow, B. Norton, and D. Kielpinski, Nature Communications **3**, 933 (2012).

[128] C.-Y. Shih and M. S. Chapman, Phys. Rev. A **87**, 063408 (2013).

[129] F. Nogrette, H. Labuhn, S. Ravets, D. Barredo, L. Béguin, A. Vernier, T. Lahaye, and A. Browaeys, Phys. Rev. X **4**, 021034 (2014).

[130] K. Irie, A. E. McKinnon, K. Unsworth, and I. M. Woodhead, Measurement Science and Technology **19**, 045207 (2008).

[131] T. Woodworth, C. Hermann Avigliano, K. Chan, and A. Marino, EPJ Quantum Technology **9** (2022).

[132] M. P. Edgar, D. S. Tasca, F. Izdebski, R. E. Warburton, J. Leach, M. Agnew, G. S. Buller, R. W. Boyd, and M. J. Padgett, Nature Communications **3**, 984 (2012).

[133] P.-A. Moreau, J. Mougin-Sisini, F. Devaux, and E. Lantz, Phys. Rev. A **86**, 010101 (2012).

[134] P. Kolchin, S. Du, C. Belthangady, G. Y. Yin, and S. E. Harris, Phys. Rev. Lett. **97**, 113602 (2006).

[135] B. Srivathsan, G. K. Gulati, B. Chng, G. Maslennikov, D. Matsukevich, and C. Kurtsiefer, Phys. Rev. Lett. **111**, 123602 (2013).

[136] C. F. McCormick, A. M. Marino, V. Boyer, and P. D. Lett, Phys. Rev. A **78**, 043816 (2008).

[137] A. Kumar and A. M. Marino, Phys. Rev. A **100**, 063828 (2019).

[138] L. Lopez, B. Chalopin, A. R. de la Souchère, C. Fabre, A. Maître, and N. Treps, Phys. Rev. A **80**, 043816 (2009).

[139] D. S. Tasca, S. P. Walborn, P. H. Souto Ribeiro, F. Toscano, and P. Pellat-Finet, Phys. Rev. A **79**, 033801 (2009).

[140] C. K. Law and J. H. Eberly, Phys. Rev. Lett. **92**, 127903 (2004).

[141] M. W. Holtfrerich and A. M. Marino, Phys. Rev. A **93**, 063821 (2016).

[142] B. Ndagano, H. Defienne, A. Lyons, I. Starshynov, F. Villa, S. Tisa, and D. Faccio, npj Quantum Information **6** (2020).

[143] E. Lantz, S. Denis, P.-A. Moreau, and F. Devaux, Opt. Express **23**, 26472 (2015).

[144] A. Marino, R. Pooser, V. Boyer, and P. Lett, Nature **457**, 859 (2009).

[145] M. I. Kolobov, Rev. Mod. Phys. **71**, 1539 (1999).

[146] A. Martin, T. Guerreiro, A. Tiranov, S. Designolle, F. Fröwis, N. Brunner, M. Huber, and N. Gisin, Phys. Rev. Lett. **118**, 110501 (2017).

[147] G. Brida and I. Genovese, M.and Ruo Berchera, Nature Photonics **4**, 227 (2010).

[148] Z. Cao, L. Wang, K. Liang, G. Chai, and J. Peng, Phys. Rev. Appl. **16**, 024012 (2021).

[149] L. Zhou, B.-W. Xu, W. Zhong, and Y.-B. Sheng, Phys. Rev. Appl. **19**, 014036 (2023).

[150] M. P. van Exter, A. Aiello, S. S. R. Oemrawsingh, G. Nienhuis, and J. P. Woerdman, Phys. Rev. A **74**, 012309 (2006).

[151] A. M. Marino, in *Photonics for Quantum 2021*, Vol. 11844, International Society for Optics and Photonics (SPIE, 2021) p. 118440M.

[152] G. Nirala, S. T. Pradyumna, A. Kumar, and A. M. Marino, in *Quantum Information and Measurement VI 2021* (Optica Publishing Group, 2021) p. Th4A.2.

[153] J. Krasinski, D. J. Gauthier, M. S. Malcuit, and R. W. Boyd, Optics Communications **54**, 241 (1985).

[154] D. J. Harter, P. Narum, M. G. Raymer, and R. W. Boyd, Phys. Rev. Lett. **46**, 1192 (1981).

[155] D. Bowman, T. L. Harte, V. Chardonnet, C. D. Groot, S. J. Denny, G. L. Goc, M. Anderson, P. Ireland, D. Cassettari, and G. D. Bruce, Opt. Express **25**, 11692 (2017).

[156] A. Gatti, E. Brambilla, and L. A. Lugiato, Phys. Rev. Lett. **90**, 133603 (2003).

[157] A. K. Jha, *Coherence properties of the entangled two-photon field produced by parametric down conversion*, Ph.D. thesis, University of Rochester (2009).

[158] B. Sephton, A. Valles, I. Nape, M. Cox, F. Steinlechner, T. Konrad, J. Torres, F. Roux, and A. Forbes, Nature Communications **14** (2023).

[159] D. S. Tasca, R. M. Gomes, F. Toscano, P. H. Souto Ribeiro, and S. P. Walborn, Phys. Rev. A **83**, 052325 (2011).

[160] S. Walborn, C. Monken, S. Pádua, and P. S. Ribeiro, Physics Reports **495**, 87 (2010).

[161] C. H. Monken, P. H. S. Ribeiro, and S. Pádua, Phys. Rev. A **57**, 3123 (1998).

[162] P. Boucher, H. Defienne, and S. Gigan, Optics Letters **46**, 4200 (2021).

[163] A. M. Marino, V. Boyer, R. C. Pooser, P. D. Lett, K. Lemons, and K. M. Jones, Phys. Rev. Lett. **101**, 093602 (2008).

[164] L. Cao, J. Du, J. Feng, Z. Qin, A. M. Marino, M. I. Kolobov, and J. Jing, Optics Letters **42**, 1201 (2017).

[165] H. Wang, C. Fabre, and J. Jing, Phys. Rev. A **95**, 051802 (2017).

[166] J. D. Swaim, E. M. Knutson, O. Danaci, and R. T. Glasser, Optics Letters **43**, 2716 (2018).

[167] V. Boyer, A. M. Marino, and P. D. Lett, Phys. Rev. Lett. **100**, 143601 (2008).

[168] D. Casasent, Appl. Opt. **18**, 2445 (1979).

[169] C. Hu, Y. Xiao, Y. He, Y. Hu, G. Xu, and X. Tang, Opt. Express **31**, 6675 (2023).

[170] C. L. Panuski, I. Christen, M. Minkov, C. J. Brabec, S. Trajtenberg-Mills, A. D. Griffiths, J. J. D. McKendry, G. L. Leake, D. J. Coleman, C. Tran, J. St Louis, J. Mucci, C. Horvath, J. N. Westwood-Bachman, S. F. Preble, M. D. Dawson, M. J. Strain, M. L. Fanto, and D. R. Englund, Nature Photonics **16**, 834 (2022).

[171] A. E. Willner, H. Huang, Y. Yan, Y. Ren, N. Ahmed, G. Xie, C. Bao, L. Li, Y. Cao, Z. Zhao, J. Wang, M. P. J. Lavery, M. Tur, S. Ramachandran, A. F. Molisch, N. Ashrafi, and S. Ashrafi, Advances in Optics and Photonics **7**, 66 (2015).

[172] J. Wang, J.-Y. Yang, I. M. Fazal, N. Ahmed, Y. Yan, H. Huang, Y. Ren, Y. Yue, S. Dolinar, M. Tur, and A. E. Willner, Nature Photonics **6**, 488 (2012).

[173] N. Bozinovic, Y. Yue, Y. Ren, M. Tur, P. Kristensen, H. Huang, A. E. Willner, and S. Ramachandran, Science **340**, 1545 (2013).

[174] I. Ruo-Berchera, A. Meda, E. Losero, A. Avella, N. Samantaray, and M. Genovese, Applied Physics Letters **116**, 214001 (2020).

[175] C. Fabre, J. B. Fouet, and A. Maître, Optics Letters **25**, 76 (2000).

[176] A. Forbes, M. de Oliveira, and M. R. Dennis, Nature Photonics **15**, 253 (2021).

[177] A. Yariv and D. M. Pepper, Opt. Lett. **1**, 16 (1977).

[178] J. A. Levenson, I. Abram, T. Rivera, and P. Grangier, J. Opt. Soc. Am. B **10**, 2233 (1993).

[179] Y. Fang and J. Jing, New Journal of Physics **17**, 023027 (2015).

[180] I. V. Dyakonov, P. R. Sharapova, T. S. Iskhakov, and G. Leuchs, Laser Physics Letters **12**, 065202 (2015).

[181] I. B. Bobrov, S. S. Straupe, E. V. Kovlakov, and S. P. Kulik, New Journal of Physics **15**, 073016 (2013).

[182] G. Frascella, R. V. Zakharov, O. V. Tikhonova, and M. V. Chekhova, Laser Physics **29**, 124013 (2019).

[183] H. Di Lorenzo Pires, C. H. Monken, and M. P. van Exter, Phys. Rev. A **80**, 022307 (2009).

[184] C. H. Bennett, G. Brassard, and N. D. Mermin, Phys. Rev. Lett. **68**, 557 (1992).

[185] M. Jasperse, L. D. Turner, and R. E. Scholten, Opt. Express **19**, 3765 (2011).

[186] F. Grosshans and P. Grangier, Phys. Rev. Lett. **88**, 057902 (2002).

[187] U. Vogl, R. T. Glasser, Q. Glorieux, J. B. Clark, N. V. Corzo, and P. D. Lett, Phys. Rev. A **87**, 010101 (2013).

[188] G. Nirala, S. T. Pradyumna, and A. M. Marino, in *Frontiers in Optics + Laser Science 2023 (FiO, LS)* (Optica Publishing Group, 2023) p. JTu5A.45.

[189] B. Brecht, D. V. Reddy, C. Silberhorn, and M. G. Raymer, Phys. Rev. X **5**, 041017 (2015).

[190] V. Ansari, E. Roccia, M. Santandrea, M. Doostdar, C. Eigner, L. Padberg, I. Gianani, M. Sbroscia, J. M. Donohue, L. Mancino, M. Barbieri, and C. Silberhorn, Opt. Express **26**, 2764 (2018).

[191] C. K. Law, I. A. Walmsley, and J. H. Eberly, Phys. Rev. Lett. **84**, 5304 (2000).

[192] A. Bunse-Gerstner and W. B. Gragg, Journal of Computational and Applied Mathematics **21**, 41 (1988).

[193] S. P. Walborn and A. H. Pimentel, Journal of Physics B: Atomic, Molecular and Optical Physics **45**, 165502 (2012).

[194] T. Miatto, F. M.and Brougham and A. M. Yao, The European Physical Journal D **66**, 183 (2012).

[195] V. A. Averchenko, G. Frascella, M. Kalash, A. Cavanna, and M. V. Chekhova, Phys. Rev. A **102**, 053725 (2020).

[196] R. Fickler, R. Lapkiewicz, W. N. Plick, M. Krenn, C. Schaeff, S. Ramelow, and A. Zeilinger, Science **338**, 640 (2012).

[197] B. Ndagano and A. Forbes, Phys. Rev. A **98**, 062330 (2018).

[198] S. Chen and J. Wang, Scientific Reports **7**, 3990 (2017).

[199] G. Nirala, S. T. Pradyumna, A. Kumar, and A. M. Marino, in *Quantum 2.0 Conference and Exhibition* (Optica Publishing Group, 2022) p. QM3C.4.

[200] J. Liang, S.-Y. Wu, F. K. Fatemi, and M. F. Becker, Appl. Opt. **51**, 3294 (2012).